Doctoral Dissertation
Doctoral Program in Chemical Engineering (38th Cycle)

Management of Process Plant and Territories:
Resilient Strategies for Loss of Containment and Early Warning Systems

Morena Vitale
* * * * * *

Supervisors
Prof.ssa Micaela Demichela, Supervisor
Prof. Antonello A. Barresi, Co-Supervisor

Politecnico di Torino
October 24, 2025

This doctoral thesis was written at the conclusion of a doctoral program funded by:
PNRR – Piano Nazionale di Ripresa e Resilienza
Missione 4 – Istruzione e Ricerca
Componente 1 – Potenziamento dell'offerta dei servizi di istruzione: dagli asili nido all'università
Investimento 4.1 – Estensione del numero di dottorati di ricerca e dottorati innovativi per la pubblica amministrazione e il patrimonio culturale
Finanziato tramite Decreto Ministeriale n. 351 del 9 aprile 2022

LOGOS

I declare that the content and structure of this dissertation are entirely my own and have been developed independently, without violating the rights of third parties, including those concerning the confidentiality and security of personal data.

…….....
Morena Vitale
Turin, 24 October 2025

This page is intentionally left

Contents

List of Tables

List of Figures

List of relevant acronyms

AI Artificial Intelligence.

AIDE Adsorption-Induced Dislocation Emission.

AIST National Institute of Advanced Industrial Science and Technology.

AFB Ageing Fishbone

ALOHA Areal Locations of Hazardous Atmospheres.

API American Petroleum Institute.

ARIA Analysis, Research, and Information on Accidents.

ASME American Society of Mechanical Engineers.

BAM Bundesanstalt für Materialforschung und Prüfung.

BN Bayesian Network.

BOG Boil-Off Gas.

BST Baker-Strehlow-Tang.

CARS Coherent Anti-Stokes Raman Spectroscopy.

CCPS Center for Chemical Process Safety.

CFAST Consolidated Model of Fire Growth and Smoke Transport.

CFD Computational Fluid Dynamics.

CFR Code of Federal Regulations.

CMEW-EKNN Condition Monitoring and Early Warning based on the Evidential K-Nearest Neighbor.

CNN Convolutional Neural Network.

CO Carbon monoxide.

CPT Conditional Probability Tables.

CSB Chemical Safety and Hazard Investigation Board.

DGMC Dynamic Graph Monte Carlo.

E Explosions.

EC Environnemental Contamination.

EC&I Electrical, Control and Instrumentation.

EEPs External Emergency Plans.

ETA Event Tree Analysis.

F Fire.

FC Credit Factor.

FD Debit Factor.

FIR Fire Index Risk.

GH2 Gas Hydrogen.

GHS Globally Harmonized System.

HAZOP Hazard and Operability Study.

HE Hydrogen Embrittlement.

HEDE Hydrogen Enhanced Decohesion Mechanism.

HELP Hydrogen Enhanced Local Plasticity.

HF Hydrofluoric Acid.

HRR Heat Release Rate.

HyWAM Hydrogen Wide Area Monitoring.

HTHA High-Temperature Hydrogen Attack.

IAE Institute of Applied Energy.

IEPs Internal Emergency Plans.

IoT Internet of Things.

IPCC Intergovernmental Panel on Climate Change.

IR Infrared.

JRC Joint Research Centre.

LFL Lower Flammability Limit.

LH2 Liquid Hydrogen.

LIDAR Laser Imaging Detection and Ranging.

LOC Loss of Containment.

LNG Liquefied Natural Gas.

LT Level Transmitters.

MAPE Mean Absolute Percentage Error.

MARS Major Accident Reporting System.

MF Multiple Fatalities.

MFL Magnetic Flux Leakage.

MI Multiple Injuries.

MLD Master Logic Diagram.

MM Multi-Prediction.

MMD Minor or Moderate Damage.

MOX Metal Oxide Semiconductor.

MS Multiple Scenarios.

MSR Multi-Prediction with Single Result.

NaTech Natural Hazard Triggering Technological Accidents.

ND No Environmental Contamination.

NEDO New Energy and Industrial Technology Development Organization.

NF No Fatalities.

NFPA National Fire Protection Association.

NH No Hazardous Substances.

NI No Injuries.

NIST National Institute of Standards and Technology.

NOx Nitrogen Oxides.

NRC National Response Center.

NREL National Renewable Energy Laboratory.

OECD Organisation for Economic Co-operation and Development.

OSHA Occupational Safety and Health Administration.

PC Peter-Clark.

PHAST Process Hazard Analysis Software Tool.

PHMSA Pipeline and Hazardous Materials Safety Administration.

PM Particulate Matter.

PPE Personal Protective Equipment.

Pr Index for Waste Storage.

PRESLHY Pre-normative Research for Safe use of Liquid Hydrogen.

PRV Pressure Relief Valve.

PSC Primary Containment System.

PSM Process Safety Management.

Pt Index for processing and treatment processes.

QRA Quantitative Risk Assessment.

RBI Risk Based Inspection.

R-NFC Releases without Further Consequences.

RPM Risk Management Plan

RPT Rapid Phase Transition.

RQ Research Question.

SCC Stress Corrosion Cracking.

SED Serious Environmental Damage.

SF Single Fatality.

SG Scientific Objectives.

SI Single Injury.

SNPA National System for Environmental Protection.

SP Single Prediction.

TDLAS Tunable Diode Laser Absorption Spectroscopy.

TGD Toxic Gas Dispersion.

TNO Netherlands Organisation for Applied Scientific Research.

TNT Trinitrotoluene.

TSB Transportation Safety Board of Canada

TUSL Testo Unico sulla Salute e Sicurezza sul Lavoro.

UAV Unmanned Aerial Vehicles.

UGLD Ultrasonic Gas Leak Detector.

UNECE United Nations Economic Commission for Europe.

VCE Vapour Cloud Explosion.

VOCs Volatile Organic Compounds.

VTOL Vertical Take Off Landing.

Introduction

Resilience was defined as "*the capability to absorb and overcome unexpected, unforeseen, and unknown threatening disturbances that could otherwise result in a catastrophe*" (Pasman and Rogers, 2015). Process plant resilience represents one of the main challenges today in the industrial engineering and management landscape. In a context characterized by high operational complexity and continuous risks, such as failures, supply chain disruptions, natural disasters or cyber-attacks, it is necessary to develop plants that are not only able to withstand these events but also to recover quickly and adapt to new conditions. In a scenario of complex systems that interact with each other with standard procedures and codes, it is necessary to understand the functioning of the socio-technical system to understand how failure can occur (Jain et al., 2017). Industrial resilience goes beyond the mere ability to respond to a critical event: it involves proactive planning, intelligent risk management and the ability to evolve in response to changes (Castro Rodriguez et al., 2025).

The concept of resilience fits into a framework that integrates risk analysis, safe system design and the ability to monitor the plant status in real-time. In the process industry, a resilient framework is a set of practices, technologies and methodologies that allow not only to prevent and mitigate risks but also to ensure continuous operation, minimizing downtime, improving long-term efficiency and optimizing rapid and effective recovery after an incident (Hosseini et al., 2016). Due to the need to explore the concept of resilience in the process industry better, more studies are being conducted on this topic. Hosseini et al. (2016) studied the trend of publications regarding system resilience from 2000 to 2015, noting an almost exponential trend.

Henry and Ramirez-Marquez (2012) studied the delivery function of a system and how it changes when a deviation from normal process conditions occurs, as reported in **Figure 1**. The function F starts from a value F(t0). At the time te the destructive event occurs, it causes the function F to decrease to the value F(td), where the function remains constant until the time ts, then the resilience action occurs, which restores the system. The new state of the system F(tf) can have a value even greater than F(t0).

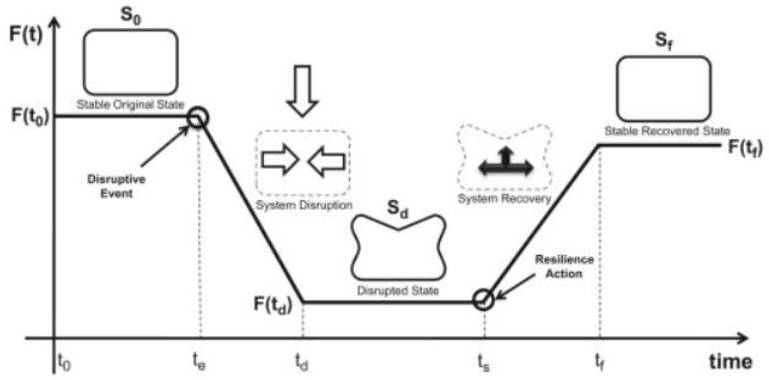

Figure 1: Delivery function of the system during a deviation from normal process conditions (Image taken by Henry and Ramirez-Marquez (2012)).

It should be noted that the value $F(t_0)$ depends on the resilience of the system, the greater the resilience, the greater the value of the function at the original state of the system. Similarly, also for the final value of the system $F(t_f)$ and the system recovery time. Indeed, the study by Pasman et al. (2020) considers two case studies and reports their recovery time following a deviation from normal process conditions:

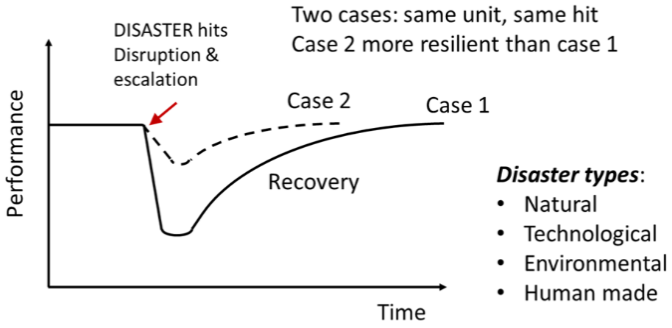

Figure 2: Recovery time following a deviation from normal process conditions (Image taken by Pasman et al. (2020)).

In **Figure 2**, the concept of resilience is applied to two plants with the same units involved. However, case 2 is more resilient than case 1, and it is evident that the recovery time of case 2 is significantly lower than case 1. From this, it can be deduced that a more resilient system has a greater capacity to quickly return to normal operating conditions after a deviation. This result highlights the importance of a resilient approach, which allows plants not only to resist unforeseen events but also to recover in a short time, minimizing the impact of interruptions on the production process.

The study by Pasman et al. (2020) presents the main factors influencing the resilience of a plant, which are illustrated in **Figure 3**.

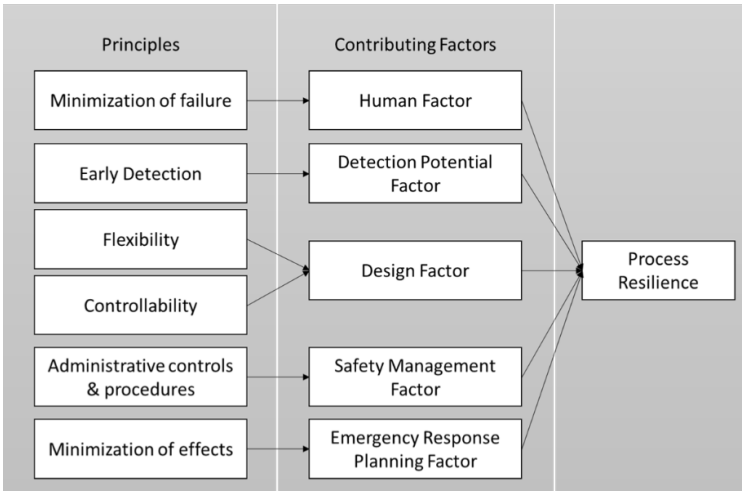

Figure 3: Principles underlying the process of resilience of a process plant (Image taken by Pasman et al. (2020).

It emerges from Figure 1.3 that increasing resilience starts from a series of strategic and technical considerations. First, it is necessary to minimize failure. The techniques used nowadays for the discovery and assessment of risks, such as HAZOP, identify dangerous operating situations in process plants, detect their causes and consequences. Specific methodologies have been developed for each sector, aimed at identifying any failures or malfunctions. However, these techniques do not yet guarantee the identification of all risks, as stated by Jain et al. (2017), which is also due to a disconnection between technical and social factors. Despite great progress made in this area, accidents continue to occur. It is time to adopt a more systemic and comprehensive holistic approach to resilience that emphasizes process safety and risk management. Therefore, it is important to start by studying past accidents in order to learn from them, as stated by Castro Rodriguez et al. (2025). This allows going to the root causes of incidents instead of just stopping at the immediate ones and visible effects. Causes of an incident do not stop at the visible and immediate; they often include process design, organizational culture, communication dynamics, and the risk management systems in use. Therefore, resilience not only involves recovering from an incident but also continuously improving processes and systems with the aim of reducing risks over the longer term. This systemic approach helps organizations gain a deeper understanding of how different parts interact with each other and be more fluent in addressing and mitigating exposures.

Another principle highlighted by Pasman et al. (2020) concerns the importance of early detection of early signs of malfunction, for proactive safety and risk management. Identifying early signs of a potential malfunction allows intervention before the situation becomes critical, reducing the risk of serious accidents and the resulting impact on plants, personnel and the environment. Furthermore, early intervention not only reduces the risk of material and human damage but can also optimize operating costs. Preventing failures through early diagnosis can avoid costly repairs and interruptions in production processes, bringing both economic and operational benefits. For these reasons, it can be important to continuously monitor signals from different sources, such as process control signals. Advanced techniques in signal processing, statistics, machine learning and artificial intelligence are used for the detection and diagnosis of

failures in process variables.

In this context, it is also essential to consider the evolution of the European regulatory framework for industrial safety. Specifically, the Seveso III Directive (2012/18/EU)[1], implemented in Italy in 2015, introduced important innovations in major-accident risk management, including the requirement for scheduled inspections by competent authorities. These inspections are not limited to verifying document compliance but also aim to evaluate the effectiveness of the safety management systems adopted by facilities.

From this perspective, resilience becomes a guiding principle for meeting regulatory expectations: a resilient facility is able to anticipate risks, respond promptly to critical events, and improve over time, demonstrating an adaptive capacity that goes beyond mere compliance. However, while addressing aspects such as material degradation and the release of hazardous substances, the directive does not provide systematic operational tools to address these issues. This highlights the need to integrate advanced technological approaches and continuous monitoring methodologies, capable of supporting proactive risk management and strengthening the resilience of industrial plants.

For this reason, the study will focus on improving the understanding of the relationships between the causes of accidents and their consequences. The research will go beyond the identification of immediate factors that contribute to accidents to explore the systemic and deep causes that may be at the root of failures. Deepening these connections will allow the development of more effective strategies to prevent and mitigate risks, thus improving the ability of a plant to adapt and recover quickly after an accident. Furthermore, the study aims to deepen the technologies and monitoring methodologies for early warning signals, with the aim of reviewing and improving procedures that can promptly detect any signs of malfunction, allowing corrective actions to be taken before the problem evolves into a critical incident. Particular attention is dedicated to the analysis of the potential offered by new technologies and real-time systems to implement solutions that enable the anticipation of risks and allow for timely intervention.

The thesis work aims to increase awareness of industrial risks, analysing the different types of risks present in plants and deepening their dynamics. In this way, the resilient approach not only optimizes the performance of plants but also ensures their operational sustainability in the long term. The study explores innovative technologies for risk monitoring and, at the same time, makes use of tools already consolidated and used in other studies to improve the management of uncertainties and strengthen the capacity to respond to critical events, thus promoting a safer, more reactive and prepared industry to face future challenges.

[1] Directive 2012/18/EU on the control of major-accident hazards involving dangerous substances, amending and subsequently repealing Council Directive 96/82/EC

Research Focus

The research activities conducted in this PhD thesis aim to answer the questions raised above. To facilitate the flow of the exposition, the following paragraph affirms the methodological relationship between the research questions (RQ), the hypothesis and the scientific objectives.

The research questions that guide the work are the following:

RQ1: How can historical incident analysis help identify recurring vulnerabilities related to material degradation, providing useful insights for planning inspections in line with the requirements of the Seveso III Directive?

RQ2: How can material degradation and NaTech risk be integrated into risk assessment, given that current regulations do not systematically address their combined impact on the vulnerability of industrial plants?

RQ3: What are the main challenges in hydrogen leak detection, and how can dynamic monitoring technologies support real-time frequency, overcoming the challenges of traditional approaches?

RQ4: How can predictive analytics methodologies for overpressure estimation support risk assessment and planning prevention measures in industrial environments?

Given the preceding discussion, the need for an integrated approach to technological risk management clearly emerges. Therefore, the aim of this research is to establish theoretical and methodological contributions for the strengthening of the resilience of industrial plants, through the analysis of containment losses, material degradation and NaTech risk.

The aim of this work is to address existing gaps in technological risk management, with particular attention to the critical issues highlighted in the regulatory framework of the Seveso III Directive. Specifically, the directive requires scheduled inspections to also assess material degradation, recognizing its role in the genesis of major accidents. However, no operational guidelines or specific technical criteria are provided to systematically address this issue. This study aims to help filling this gap by providing useful tools and knowledge to support inspection activities and the assessment of material vulnerability. Furthermore, Seveso III introduces quantitative thresholds for hazardous substances present in plants, including hydrogen, a highly flammable gas and particularly critical for industrial safety. For this reason, this work dedicates a specific focus to the issues related to hydrogen leak detection, proposing advanced technological solutions for dynamic monitoring and early diagnosis, in line with the needs of risk prevention and control.

The scientific objectives (SG) associated with each question are:

SG1: Analyse historical industrial accidents to identify recurring vulnerabilities related to material degradation, in order to propose useful technical criteria for inspection planning, in line with the requirements of the Seveso III Directive.

SG2: Develop a methodological approach to integrate material degradation and NaTech risk into risk assessment, filling regulatory gaps and supporting the design of more resilient industrial infrastructure.

SG3: Evaluate the effectiveness of dynamic monitoring technologies for real-time detection of hydrogen leaks, proposing innovative solutions for the prevention and management of the risk associated with highly flammable gases.

SG4: Develop and apply predictive analysis methods for overpressure estimation, in order to improve the planning of prevention measures and support the resilient management of industrial facilities.

Introduction Partial conclusions

In conclusion, the introductory section outlined the conceptual and methodological basis of this research, highlighting the importance of resilience in the management of industrial systems exposed to complex and constantly evolving risks. The need to adopt a systemic and proactive approach, based on continuous monitoring, early identification of anomaly signals and analysis of systemic dynamics that lead to accidents, emerged.

The research questions and related scientific objectives presented in this chapter constitute the backbone of the investigation, oriented to the analysis of the main vulnerabilities of industrial infrastructures, with particular reference to containment losses, hydrogen leak detection, material degradation and NaTech risk. In this context, the Seveso III Directive represents a key regulatory framework: while it requires inspections also for material degradation, it does not provide specific operational tools, highlighting a gap that this research aims to fill through technical and methodological contributions. Furthermore, the directive introduces quantitative thresholds for hazardous substances, including hydrogen, a highly flammable gas of particular importance for industrial safety, which is the subject of specific investigation in this study.

The following chapters will delve deeper into these issues, combining theoretical analyses, historical studies and technological assessments, in order to support the evolution towards safer, more adaptive and sustainable industrial systems.

References Introduction

Castro Rodriguez, D.J, Barresi, A.A., and Demichela, M. (2025b). Resilience-based Framework for Enhancing NaTech Risk Management in Industrial Critical Infrastructures. Environment Systems and Decisions. (under review). PREPRINT available at Research Square https://doi.org/10.21203/rs.3.rs-5937501/v1

Henry, D., and Ramirez-Marquez, J. E. (2012). Generic metrics and quantitative approaches for system resilience as a function of time. Reliability Engineering & System Safety, 99, 114–122. https://doi.org/10.1016/j.ress.2011.09.002

Hosseini, S., Barker, K. and Ramirez-Marquez, J.E. (2016). A review of definitions and measures of system resilience. Reliability Engineering & System Safety 145, 47–61. https://doi.org/10.1016/j.ress.2015.08.006

Jain, P., Pasman, H.J., Waldram, S.P., Rogers, W.J., Mannan, M.S. (2017). Did we learn about risk control since Seveso? Yes, we surely did, but is it enough? A historical brief and problem analysis. Journal of Loss Prevention in The Process Industries, 49, Part A, 5–17. https://doi.org/10.1016/j.jlp.2016.09.023

Pasman, H. J., and Rogers, W. J. (2015). HAZOP: Our Primary Guide in the Land of Process Risks: How can we improve it and do more with its results? TEES Mary Kay O'Connor Process Safety Center, 18th Annual International Symposium, 27–19 October, Texas, College Station, pp. 398–417.

Pasman, H., Kottawar, K., and Jain, P. (2020). Resilience of process plant: what, why, and how resilience can improve safety and sustainability. Sustainability, 12(15), 6152. https://doi.org/10.3390/su12156152

1. Material Degradation: Insights from Historical Accident Data in the Process Industry[2]

As outlined in the introduction, industrial resilience requires a systemic and proactive approach to risk management, capable of integrating continuous monitoring, predictive analytics, and an understanding of the dynamics that lead to incidents. In this context, material degradation represents one of the main vulnerabilities of industrial infrastructure, significantly contributing to loss of containment and the critical evolution of events. Indeed, among the main causes of loss of containment identified in the process industry, failures related to technical integrity represent one of the most significant categories, contributing to approximately 60% of major incidents. Of these, nearly half are exacerbated by infrastructure ageing (Candreva and Houari, 2013). As highlighted by Horrocks et al. (2010), ageing is not a process determined solely by the chronological age of the equipment, but rather by a combination of factors related to operating conditions, management and maintenance methods, and the evolutionary changes that components undergo over time. Ageing manifests itself through the progressive deterioration of materials, which leads to an increased probability of failure throughout the equipment life cycle. This process does not follow a linear evolution, but is strongly influenced by environmental and operating conditions, as well as the effectiveness of the maintenance strategies adopted. The phenomenon affects all categories of physical equipment and begins during the manufacturing or construction phase and continues throughout the asset useful life. Although its evolution can be slowed through targeted maintenance interventions, it cannot be stopped completely (Kelly, 2021).

It is important to distinguish between ageing and obsolescence: the former concerns the progressive alteration of the physical and mechanical properties of components, resulting in an increased risk of failure and loss of containment (Bragatto and Milazzo, 2016); the latter, is linked to the evolution of technical knowledge, regulatory standards, and best practices, may result in the infrastructure no longer complying with current requirements (Milazzo and

[2] Portions of this chapter have been published in preliminary form in:
Vitale, M., Shi, H., Castro Rodriguez, D.J., Barresi, A. and Demichela, M. (2024). Ageing in process industry: Identification of material degradation from past accidents analysis. *IFAC-PapersOnLine* 58(4), 568–573. https://doi.org/10.1016/j.ifacol.2024.07.279.
Vitale, M., Castro Rodriguez, D.J., Shi, H., Barresi, A. and Demichela, M. (2026). Material degradation: Findings from historical accident analysis in process industries. Reliability Engineering & System Safety, 111769. https://doi.org/10.1016/j.ress.2025.111769

Bragatto, 2019).

The issue of infrastructure ageing today represents a significant international concern, particularly in Europe, the United States, and Scandinavian countries, where a significant portion of facilities have exceeded 50 years of operation. In Europe, for example, it is estimated that approximately 50% of plants operate beyond their originally designed useful life (Vairo et al., 2018).

Legislative Decree 105/2015[3], known as Seveso III, implements European Directive 2012/18/EU[4] and regulates the control of hazards associated with major accidents involving certain dangerous substances (Laurent et al., 2021). Although this legislation does not contain explicit provisions regarding the ageing management of industrial plants, it focuses on accident prevention and safety management at sites handling dangerous substances. Specifically, it requires covered facilities to identify and describe the potential deterioration mechanisms of the materials used, thus mandating ageing monitoring to ensure adequate safety management in industrial processes. This approach contributes to the prevention and control of risks associated with material degradation, safeguarding the integrity of the plants (Bragatto et al., 2017). In the United States, although there is no legislation fully analogous to the European Union's Seveso III Directive, there are two important regulatory frameworks governing industrial process safety and the management of hazardous substances: OSHA's Process Safety Management (PSM) and the EPA's Risk Management Plan (RMP) (OSHA, 2025; US EPA, 2025). The PSM system, introduced in 1992, focuses on preventing accidental releases of hazardous chemicals through systematic measures such as hazard analysis, mechanical integrity management, and operational change control. The RMP program, operational since 1996, complements the PSM, requiring industrial facilities to identify potential accident scenarios, assess their consequences, and develop emergency prevention and response plans (Besserman and Mentzer, 2017). While neither standard explicitly addresses the issue of infrastructure ageing or material degradation, both imply the need to manage these phenomena through established inspection practices, scheduled maintenance, and risk-based decision-making approaches. In this scenario, ageing management is integrated into general safety requirements, even if not formally codified as a separate category.

The general principles of safety management are frequently inspired by the Deming Cycle (Plan-Do-Check-Act), as outlined in international standards for environmental management systems. This model involves defining objectives, planning actions, implementing them, verifying results, and finally, adopting any corrective actions. However, a study by Hansler et al. (2022) highlighted that this approach may be inadequate for effective ageing management, as it does not ensure full identification of degradation mechanisms and hazards. According to the study, key aspects such as safety studies, failure analysis, preventive maintenance, periodic inspections, and acceptability criteria have been neglected.

[3] Legislative Decree No. 105 of June 26, 2015, “Implementation of Directive 2012/18/EU on the control of major-accident hazards involving dangerous substances.” Italian Official Gazette General Series No. 161 14/07/2015-Suppl. Ordinary No. 38 (In Italian language).

[4] Directive 2012/18/EU on the control of major-accident hazards involving dangerous substances, amending and subsequently repealing Council Directive 96/82/EC

The Seveso III Directive, through Annex 3, establishes that inspections must consider ageing and corrosion as relevant factors for risk assessment. Annex B requires monitoring of material degradation, mandating systematic monitoring of ageing and corrosion, as well as the adoption of preventive measures to avoid accidents resulting from these phenomena. Annex H, while not providing detailed assessment procedures, offers an inspection checklist, including criteria related to ageing and corrosion (Bragatto et al., 2022).

The Center for Chemical Process Safety (CCPS) also analyses the ways in which industrial structures, equipment, and infrastructure can deteriorate due to prolonged exposure to operational and environmental conditions. The text describes the physical and functional failure mechanisms for various types of equipment, identifying early signs of deterioration and proposing risk-based management strategies. These strategies enable plant managers to make informed decisions and communicate effectively with company management. The safe decommissioning of facilities approaching or exceeding their life cycle is also addressed (Kelly, 2021). API Recommendation Practice 571 (API, 2020) also provides a systematic and detailed classification of damage mechanisms that can occur in process industry equipment. The document represents a fundamental technical reference for identifying, understanding, and managing degradation phenomena, including processes such as generalized and localized corrosion, fatigue cracking, stress corrosion cracking, erosion, high-temperature damage, and other mechanisms related to specific operating conditions.

For effective ageing management, the literature suggests adopting both qualitative and quantitative approaches. In particular, Milazzo and Bragatto (2019) propose the KID (Knowledge, Information, Data) model, which identifies three fundamental elements for assessing and managing the degradation of materials and equipment:

- K (knowledge): A thorough understanding of the deterioration mechanisms, chemical or physical, internal or external, continuous or occasional, that can compromise the integrity of equipment throughout its life cycle. Horrocks et al. (2010) provide a detailed analysis of the main degradation phenomena encountered in the process industry, such as corrosion, erosion, cracking, and others. They reported their onset and manifestation.
- I (information): The availability of complete technical documentation relating to the equipment history, including construction materials, operating conditions, maintenance interventions, and structural modifications made over time.
- D (data): The systematic collection of data from non-destructive testing, useful for monitoring the integrity and functionality of systems. This data, appropriately analysed, forms the basis for a reliable assessment of ongoing degradation.

Scientific literature strongly highlights the importance of a thorough understanding of the ageing and failure mechanisms of plant components, analysed from a physical and chemical perspective, as an essential prerequisite for effective and safe ageing management. A thorough understanding of the operational lifespan of each component, combined with the analysis of historical events such as operational disruptions and past accidents, is essential, as these factors play a significant role in accelerating material degradation. In this context,

historical data from previous tests and inspections represent a fundamental resource for supporting informed decisions in plant integrity management.

To quantify the risk associated with ageing, some studies propose the use of indicator-based methods. Among these, the Ageing Fishbone (AFB) method is noteworthy for its systematic structure, which was subsequently extended to include applications to dynamic systems. Although the index-based approach involves a certain degree of uncertainty compared to more qualitative methods (Martón et al., 2016; Bragatto et al., 2017; Mocellin and Pilenghi, 2023), it allows for a more transparent and replicable assessment of ageing processes.

The method is based on assigning scores to penalizing and compensating factors: if the balance between compensations and penalties is positive or zero, ageing management is considered adequate. The factors are illustrated in the Fishbone diagram shown in **Figure 1.1**. To ensure consistency and objectivity in the assessment, each factor is classified on a four-level scale (1 = low, 2 = medium, 3 = medium-high, 4 = high), with positive signs for compensations and negative signs for penalties. Penalizing factors include equipment age, frequency of shutdowns, failure rates, near-misses, deterioration mechanisms, and damage detected during inspections. Compensating factors include the quality of the management system, inspection planning and effectiveness, audit results, process control, and implemented technical safeguards (Bragatto et al., 2017).

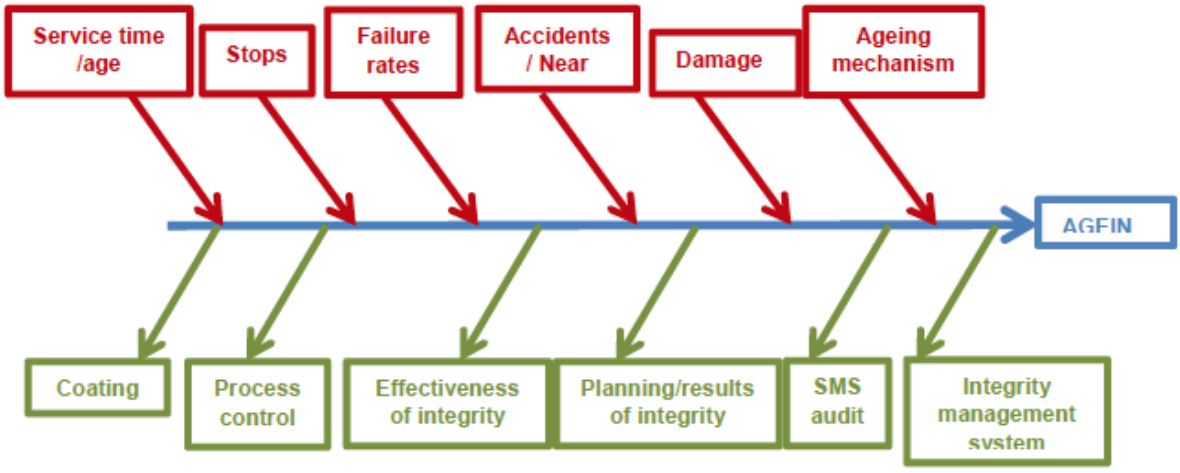

Figure 1.1: Penalizing (in red) and compensating (in green) factors considered in the AFB method. Image taken from Vairo et al. (2018).

Retrospective studies based on the analysis of historical events further contribute to the understanding of failure mechanisms in the process industry. These studies aim to draw lessons from experience to improve risk assessment and inspection planning. However, the limited availability of data, often based on a small number of incidents, constrains the comprehensiveness and reliability of the resulting conclusions (Wintle et al., 2006; Gyenes and Wood, 2016; Bragatto et al., 2022; Hansler et al., 2022, Vitale et al., 2025b). Therefore, it is essential to complement historical analysis with other information sources and complementary methodological approaches.

As part of the retrospective analysis of industrial accidents, this study aims to systematically examine events in which material ageing directly impacted or contributed to the critical evolution of the accident. The investigation is based on

an extensive collection of reports from European and North American open-source databases, updated through 2023, with the aim of identifying the types of equipment most frequently involved and the most recurring accident scenarios. An initial exploratory phase, conducted by Vitale et al. (2024), analysed 546 events extracted from the ARIA database, limiting itself to a preliminary characterization of the raw data and a study of relative frequencies. This analysis formed the basis for a methodological expansion, which integrated additional accident sources and introduced probabilistic modelling tools to address the challenges posed by the uncertainty of the available

data. The approach of Castro Rodriguez et al. (2024) was adopted, and it is structured in two phases: on the one hand, the descriptive analysis of historical data allows for the identification of trends and critical categories, on the other hand, the use of data modelling techniques, such as Bayesian networks, allows for the estimation of plausible scenarios even in the presence of incomplete information. This method enables the exploration of interdependencies between key variables and the formulation of useful predictions for risk management and inspection planning. In this context, an increasingly adopted methodology for managing ageing is Risk-Based Inspection (RBI), described in API Recommended Practice 580 (API, 2023). This methodology prioritizes inspection activities based on the assessed risk of failure, integrating both the probability of degradation mechanisms and the severity of their potential consequences. However, the effectiveness of RBI is strongly dependent on the availability of reliable data on failure mechanisms and incident scenarios. This study aims to provide a quantitative basis useful not only for optimizing inspection planning, but also for integrating the results into multi-hazard analyses in a resilient context, with the ultimate goal of increasing awareness of systemic capabilities and enhancing the ability to respond to unexpected events, thus contributing to a more informed and proactive industrial safety management (Castro Rodriguez et al., 2025). The aim is to contribute to the understanding of material degradation in the process industry, providing a quantitative basis for decision-making in inspection and maintenance. The analysis focuses specifically on the most vulnerable equipment categories and the most frequent failure scenarios, with the aim of strengthening prevention strategies and improving the resilience of industrial systems.

1.1 Materials and Methods

As described by Castro Rodriguez et al. (2024), the analysis is developed through a structured approach consisting of two complementary macro-phases.

The **First Phase** consists of the systematic collection of data relating to industrial accidents, extracted from various sector databases that document significant events in the process industry. The primary objective of this phase is to ensure a sufficiently large and representative sample, capable of providing a comprehensive overview of the different types of events and the conditions in which they occur.

Subsequently, the **Second Phase** involves processing and analysing the collected data using graphical, statistical, and mathematical models. This phase

aims to identify recurring patterns, correlations between variables, and significant trends, with the purpose of deepening our understanding of the dynamics that characterize accidents and the factors that influence their evolution.

The methodological division into two phases allows the construction of a solid information base, useful for developing more effective and targeted prevention strategies, thus contributing to the improvement of risk and safety management in industrial plants.

1.1.1 Source

To conduct the analysis, the main open-source scientific databases were examined, with the aim of identifying all reports in which ageing and material degradation played a decisive role or contributed, even secondarily, to the escalation of the accident.

Database exploration was conducted using specific keywords, listed in **Table 1.1**. To ensure maximum coverage, searches were also performed in the original language of each database: in particular, for the ARIA database, French-language keywords were also included. The keywords were also combined with terms such as "plant," "industry," and "establishment" to limit the analysis to the context of the process industry.

Table 1.1: Keywords used in the database analysis.

English Keyword	French Keyword
Ageing	Vieillissement
Corrosion	Corrosion
Erosion	Erosion
Vibration	Vibration
Wear	Usure
Embrittlement	Fragilisation
Creep	Fluage
Fatigue	Fatigue
Degradation	Dégradation

This approach allowed the construction of a structured repository of accident events, as reported by Castro Rodriguez et al. (2023). Each report included in the dataset documents a single incident, providing detailed information such as geographic location, event date, technical description of the incident, consequences in terms of human losses, and environmental impact in the event of a release of hazardous substances.

The databases consulted come from both European and US sources and include:

i)Analysis, Research and Information on Accidents (ARIA) database (BARPI, 2022), managed by the French Ministry of the Environment, ARIA is a key resource for collecting data on industrial accidents. Designed to improve the management of industrial risks, it contains a large collection of reports on

accidents, near misses and anomalies from different industrial sectors. At the end of 2023, the database included over 59,000 cases, with an annual increase of approximately 1,200-1,500 new events.

ii)Major Accident Reporting System (eMars, 2022), managed by the European Commission, it is dedicated to the recording of significant accidents in high-risk industries, as required by the Seveso Directive. The system aims to improve the prevention and management of major accidents, providing a tool to analyse their causes and consequences. By the end of 2023, eMARS had registered over 1,200 cases, with continuous updates coming from the reports sent by Member States.

iii)Hydrogen Incident and Accident (JRC HIAD) Database (JRC,2022), managed by the Joint Research Centre (JRC) of the European Commission, it focuses on accidents and hazardous situations related to the use of hydrogen. This repository is key to improving safety in hydrogen applications and collects detailed reports of events, analysing their causes, dynamics and impacts. By the end of 2023, the database counted more than 700 records, with regular updates following new incidents reported globally.

iv)National Response Center (NRC) database (NRC, 2022), managed by the U.S. Coast Guard on behalf of the federal government, it is the official clearinghouse for all reports of hazardous substance releases and environmental incidents in the United States. The NRC receives and archives reports of oil spills, chemical, radiological, biological releases, and other

events that may compromise environmental and public safety. The collected data is forwarded to the appropriate authorities for analysis and response. The database, updated daily, contains hundreds of thousands of records and is a critical resource for monitoring and preventing environmental incidents nationwide.

v)Chemical Safety and Hazard Investigation Board (CSB) database (CSB, 2022), an independent agency of the United States government, the CSB collects and analyses serious chemical incidents that occurred in industrial facilities and laboratories. This repository is designed to identify the root causes of events, promote chemical safety, and prevent future incidents. Since 2020, with the enactment of the federal mandatory reporting regulation for accidental releases, the CSB has received hundreds of reports, many of which have been documented in detailed reports. The volumes published to date include dozens of incidents with significant impacts on workers, communities, and the environment, and are regularly updated with new investigations and summaries.

vi) The Transportation Safety Board of Canada (TSB) is an independent body of the Canadian government responsible for investigating accidents in various sectors of transportation, including civil aviation, merchant marine, trains, road transport and conditions of navigation in Canadian waters. The TSB is committed to determining the causes and circumstances of accidents to improve transport safety. TSB investigations are conducted independently of regulators and transport operations management authorities, and the results of the investigations are made public to promote transparency and facilitate learning to prevent future accidents (TSB, 2022).

1.1.2 Database Structure

The database structure presented in **Figure 1.2**. The classification of the collected data was organized into different areas, with the aim of providing a detailed view of the industrial events and their main characteristics.

First, the **Source** was recorded, which represents the origin of the report.

Then, the **Macro sector** was identified, which specifies the type of plant where the event occurred. Process plants were divided into main categories: Chemical & Petrochemical, Bioprocess, Manufacturing, Pipeline, Power Production, Storage & Warehouse, and Transportation as highlighted by Ricci et al. (2021).

Another fundamental aspect of the classification is the **Outcome**, which describes the type of industrial event that occurred. Categories include Accidents, Incidents, Loss of Containment (LOC) and Near-miss, with specific definitions provided by Ricci et al. (2021) and the inclusion of the "Near-miss" category described by Gnoni et al. (2013).

The **Final Scenario** refers to the impacts resulting from the accident and includes various types of consequences, such as toxic gas dispersion (TGD), environmental contamination (EC), releases without further consequences (R-NFC), fires (F), explosions (E) or complex scenarios combining several events (MS), as defined by Ricci et al. (2021).

The **Cause** of the accident refers to the main deterioration mechanisms:

i)Corrosion is a degradation phenomenon that affects the surface of materials, caused by chemical reactions with the surrounding environment. The material vulnerability to this process depends on the characteristics of its environment, while the corrosiveness of the environment itself is influenced by the type of material exposed (Davis, 2000). This category also includes events related to high-temperature hydrogen attack (HTHA), a process that occurs when steel is

subjected to high temperatures in the presence of hydrogen. Under these circumstances, the carbon contained in the steel can react with gases such as methane, generating hydrogen and causing surface or internal decarburization of the material (Poorhaydari, 2021). HTHA can permanently compromise the mechanical properties of the material, making it brittle and less resistant. Due to its chemical nature and the degradation mechanism involving reactions between hydrogen and carbon, this phenomenon was included in the study within the category of corrosion. This classification is consistent with what is reported in technical literature and in previous studies (Hansler et al., 2022).

ii) Fatigue is a progressive material degradation mechanism triggered by cyclical or repeated stresses over time. During these loading and unloading cycles, the material can develop microcracks that, as the cycles progress, tend to expand until they cause failure. This process is strongly influenced by environmental and operational factors, such as variations in temperature, pressure, and applied load intensity. This category also includes the phenomenon of brittleness, which describes the loss of toughness and increased susceptibility to fracture of a material. This condition can be induced by prolonged exposure to high temperatures, ionizing radiation, or continuous mechanical stress. Brittleness

compromises the material's ability to absorb energy before breaking, making it more vulnerable to sudden failure.

iii) Erosion is a process of surface material removal caused by the mechanical action of external agents, such as solid particles transported by moving fluids, whether liquid or gas (Horrocks et al., 2010). This phenomenon is particularly common in systems where flows containing particles pass through pipes, ducts, or equipment, causing progressive deterioration of exposed surfaces. This same category also includes wear, a damage mechanism that occurs when two surfaces in contact move relative to each other. The relative movement generates friction and abrasion, causing the gradual loss of material from one or both of the surfaces involved. This process can alter the geometry, dimensions, and surface characteristics of components, compromising their functionality over time.

iv)Hydrogen embrittlement (HE) has been treated as an autonomous category, given its specific nature and critical implications for the mechanical properties of materials. This phenomenon occurs when hydrogen atoms penetrate the crystal lattice of the metal, compromising its tensile strength, fracture toughness, and fatigue resistance, both at the macroscopic and microscopic levels. Despite the extensive scientific literature on the subject, the mechanisms underlying HE are still not fully understood (Li et al., 2020).

v)Vibrations are also considered a significant factor in the deterioration of materials and equipment. They can be generated by various sources, such as moving machinery, motors, rotating equipment, or other mechanical processes. Vibrations can cause undesirable effects such as accelerated wear, structural damage, noise emissions, and, in some cases, pose a risk to operational safety.

vi)Unspecified material degradation was used to describe cases where a specific failure could not be identified.

According to Horrocks et al. (2010), different types of industrial equipment are particularly vulnerable to material degradation. Therefore, the **Equipment Involved** can be divided into four main categories:

i)Primary Containment System (PCS), this includes all components designed to safely contain hazardous substances within the facility. These include both static and dynamic elements, such as tanks, piping, pumps, and turbines, which are subject to severe operating conditions and potential corrosion, erosion, or fatigue.

ii) Control & mitigation system, this is a set of devices, procedures, and components designed to manage critical or abnormal situations. These systems play a vital role in preventing and limiting the effects of undesirable events, contributing to the safety and reliability of the facility.

iii) Electrical, control, and instrumentation (EC&I), this includes equipment and systems related to electrical management, process control, and instrumentation. These elements represent a form of active safeguard, as they include detection, alarm, and automatic response systems, which are essential to ensuring operational continuity and safety.

iv)Structures, this category includes the structural components of the plant infrastructure, which provide physical support for equipment and operational activities. These elements can also be subject to degradation over time, impacting

the stability and overall integrity of the plant.

Regarding the **Classification of the substances involved**, reference was made to the Globally Harmonized System of Classification and Labelling of Chemicals (UNECE, 2021), which categorizes substances based on physical, health and environmental hazards. In addition, two categories were added: "NH", for substances without significant risks, and "Multiple hazards", for those that present more than one type of risk.

Losses were divided into three main areas: human, economic and environmental.

Economic losses were classified into four categories, depending on the extent of the damage: up to $100,000, between $100,000 and $1 million, between $1 million and $10 million, and over $10 million, following a classification consistent with previous studies.

Environmental losses are divided into two main categories: serious environmental damage (SED) and minor or moderate damage (MMD), in accordance with the Seveso III Directive (European Commission, 2015) and the criteria of the Ministry of Public Works (Ministero dei Lavori Pubblici, 2001). When there was no environmental contamination, it was identified as ND.

Human losses were classified separately according to severity, dividing them into deaths and injuries. For deaths, the following categories are adopted: Multiple Fatalities (MF), Single Fatality (SF) and No Fatalities (NF). Similarly, for injuries, the categories are used: Multiple Injuries (MI), Single Injury (SI) and No Injuries (NI).

This study introduces two additional categories, aiming to broaden the interpretative framework for incidents. The first category, **Action Taken**, refers to the measures adopted following an incident, as proposed by Marrazzo and Vazzana (2021). Specifically, three types of response were considered:

i)Inspections: This occurs when, following the event, the frequency of inspections is increased, highlighting a previous monitoring deficit.

ii)Treatments: This includes the adoption of technical interventions on the affected materials, aimed at improving their performance or resistance, to reduce the probability of future failures.

iii)No action implemented: This refers to scenarios in which, after the incident, no changes are made to the maintenance plan or routine inspection procedures.

The second category is the **Age of the installation**, defined as the operational age of the structure or infrastructure involved in the event. The classification adopted is based on the study by Hansler et al. (2022) and distinguishes three time periods:

i)Old: plants in operation for over 25 years.

ii)Medium: plants active for 5 to 25 years.

iii)New: plants with less than 5 years of operation.

However, this information is not always explicitly reported in accident reports. For this reason, it was necessary to supplement the analysis with additional information sources, such as the type of production site and geographical location, to estimate the age of the affected infrastructure. **Figure 1.2**

illustrates the classification performed within the database developed for this study, including all the categories considered in the analysis. The repository was structured to optimize the systematic collection, analytical processing, and subsequent consultation of data relating to material degradation phenomena. This organization allows for efficient information management, facilitating the identification of recurring patterns and supporting the interpretation of results from a comparative and multidisciplinary perspective.

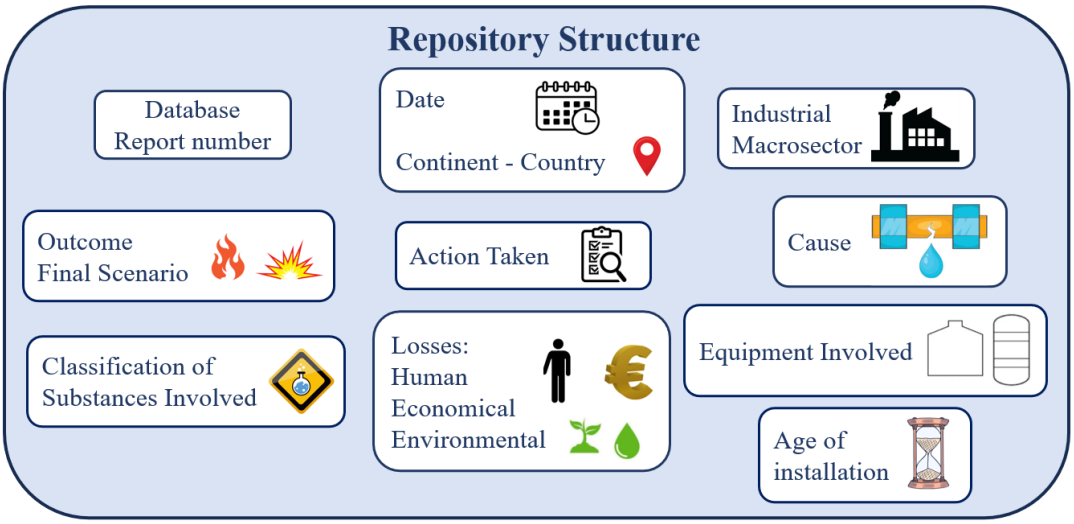

Figure 1.2: Database structure.

1.1.3 Data Accuracy

It is important to note that the data extracted from the analysed reports frequently contains information gaps or inaccuracies. These critical issues stem primarily from the lack of uniform regulatory standards for incident reporting, particularly in databases like the NRC, which rely on anonymous reports from citizens. To address this structural limitation and ensure methodological consistency with previous studies, a specific category called 'Unknown' was introduced. This additional classification allows for the systematic inclusion of cases characterized by partial, ambiguous, or unverifiable information, while still allowing for a structured and comparable analysis (Cozzani et al., 2010; Krausmann et al., 2011; Ricci et al., 2021).

During the database construction phase, particular attention was paid to removing duplicates and selecting the most reliable reports. The validation process focused on three main criteria: the date of the event, the geographic location, and the specific type of incident reported. This approach allowed the prioritization of the clearest and most detailed sources, significantly contributing to preserving the quality, consistency, and overall integrity of the repository.

1.1.4 Data Examination

The second phase of the investigation, dedicated to data processing and interpretation, is divided into two distinct but complementary parts:

Part 1 - Exploratory and descriptive data analysis:

In this first phase, the collected data is represented through tables, graphs, and visual diagrams, with the aim of facilitating the immediate identification of correlations, trends, and anomalies among the variables considered. The visual approach allows for a concise yet effective understanding of the distribution and relationships between the data, serving as the basis for subsequent quantitative analyses. The analysis of the HE case was discontinued at this stage, as the amount of uncertain data found in this context was limited and did not justify the application of further levels of analytical depth.

Part 2 - Risk modelling and quantitative analysis (QRA):

Following the preliminary analysis, we proceed with the quantitative risk assessment using advanced modelling tools. Among these, Event Tree Analysis (ETA) is used to graphically represent causal sequences that can lead to failures or accidents, offering a structured view of possible risk scenarios (Čepin, 2011).

Subsequently, Bayesian Networks (BN) are employed, are applied to model the probabilistic dependencies among variables and to estimate the conditional likelihood of specific events (Giudice et al., 2023). This approach allows the quantification of event occurrence rates and facilitates a deeper understanding of the interactions between risk factors. In this study, the construction of the Bayesian model was supported by the Peter-Clark (PC) algorithm, used to explore the network structure. The model skeleton was defined through conditional independence tests, while the directionality of the links was learned by combining causal rules embedded in the algorithm with expert domain knowledge. Thanks to the use of a large data set, this methodology has highlighted the conditional interdependencies between key attributes, supporting both predictive modelling and probabilistic reasoning under uncertainty (Castro Rodriguez et al., 2024).

The introduction of this second level of analysis is particularly useful for addressing the critical issues related to the incompleteness and fragmentation of historical accident data. Specifically, it allows for the inference of significant relationships even in the presence of partial information, contributing to a more robust understanding of the systemic vulnerabilities associated with material degradation phenomena.

1.2 Results and Discussion

The analysis is based on a total of 3,830 reports collected between 1966 and 2023, in which material degradation was identified as the main cause of the escalation of accident events (Vitale et al., 2025a). **Figure 1.3** shows the distribution of sources from which the examined reports originate. The majority of documents (81%) were extracted from the NRC database, followed by ARIA with 14%.

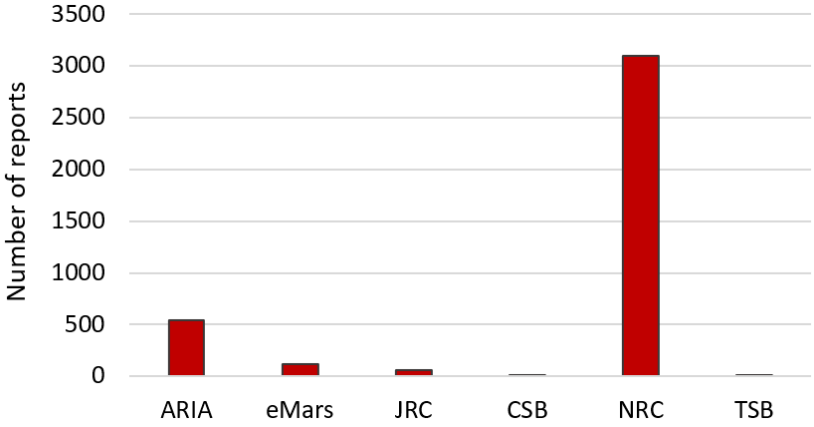

Figure 1.3: Sources of the 3,830 reports analysed.

Given the high number of reports from the NRC database, which, as discussed previously, primarily collects spontaneous reports from citizens, often characterized by limited detail and inconsistent information quality, it was deemed appropriate to present the results separately. The analysis was therefore conducted separately for reports from the NRC and those from other sources, such as ARIA, JRC, CSB, TSB and eMars, which generally provide more structured and verified data.

It is also important to highlight the different geographical distribution of the reported events. All cases from the NRC database refer to events that occurred in North America, while 92% of the events collected from other sources occurred in Europe. Overall, the geographical distribution of the analysed events shows that 84.9% occurred in North America, 14.9% in Europe, and the remainder is attributable to events that occurred in Asia. **Figure 1.4** shows the trend of the reported events over the years.

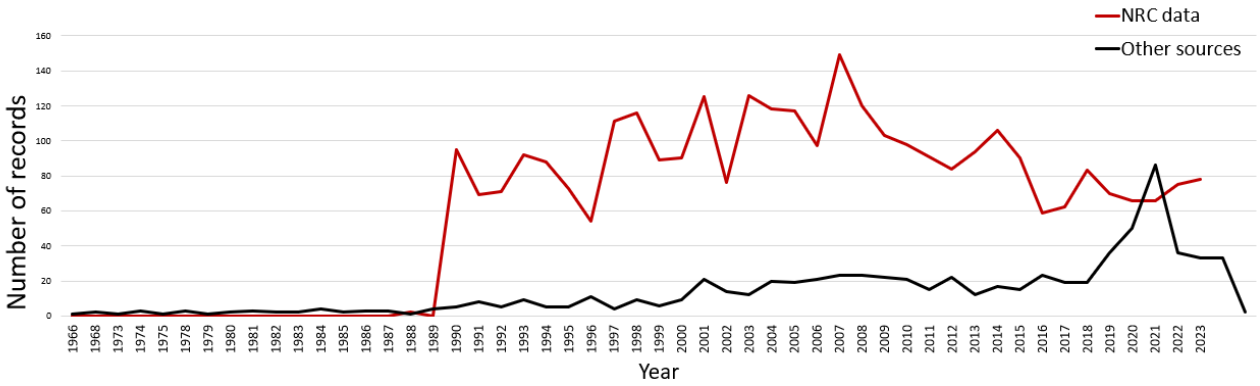

Figure 1.4: Time trend of recorded events, based on data collected between 1966 and 2023.

The NRC database has been operational since 1990, although a single prior event, dating back to 1988, is present. Analysis of data for the period 1990-2023 shows a generally stable trend in the number of annual reports, with a slight decrease in the average number of cases recorded since 2016. This reduction coincides with the adoption of more stringent regulations, the introduction of advanced technologies, and increased investment in industrial safety. Indeed, in the United States, significant regulatory updates have been implemented to mitigate material degradation and strengthen the reliability of critical

infrastructure. In particular, the Pipeline and Hazardous Materials Safety Administration (PHMSA) has introduced more stringent requirements for inspection, maintenance, and corrosion control (Cazenave et al., 2024). In parallel, the American Society of Mechanical Engineers (ASME) revised the Boiler

Pressure Vessel Code, including new materials and protection techniques to more effectively manage degradation processes (Fehring and Reynolds, 2021).

Regarding other sources, a progressive increase in the number of recorded events has been observed since 2000, a phenomenon coinciding with the advent of the fourth industrial revolution. Another significant factor is the high number of European plants, built primarily after World War II and currently in operation for over half a century. This condition exposes infrastructure to problems related to structural and functional ageing. Between 2000 and 2016, the number of reports remained relatively stable, while starting in 2016, significant growth was recorded, with a peak in 2019. This increase occurred just a few years after the entry into force of the Seveso III Directive (2012/18/EU) in Europe, which placed greater emphasis on the role of material degradation and ageing in industrial settings, encouraging more careful identification of such phenomena. In 2020, the spread of the COVID-19 pandemic led to a widespread slowdown in industrial activities globally, and a reduction in reported events was registered in the same year. This also coincided with the publication of new guidelines for assessing material degradation and preventing accidents, including those proposed by Milazzo and Bragatto (2019).

1.2.1 Part 1: Analysis of Functional Attribute

The 3,830 records analysed were classified based on the failure mechanism that led to the escalation of the incident. **Figure 1.5** presents the distribution of the number of events for each identified mechanism, sorted by data source. The analysis indicates that corrosion constitutes the most prevalent failure mechanism among the records examined, with a particularly high incidence in reports originating from the NRC database. This finding highlights the need for more effective prevention and monitoring strategies and more appropriate treatments for corrosion control in industrial systems. Other relevant mechanisms include mechanical vibration, material fatigue, and erosion, which also significantly contribute to equipment deterioration and the triggering of critical events.

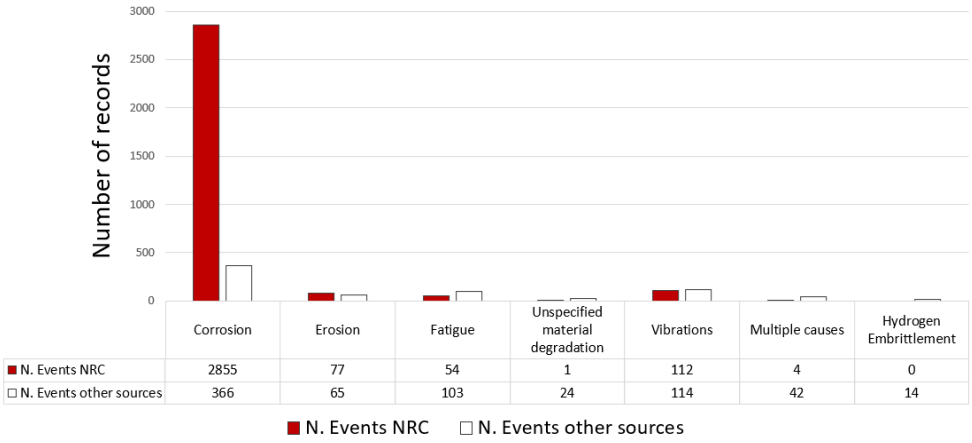

	Corrosion	Erosion	Fatigue	Unspecified material degradation	Vibrations	Multiple causes	Hydrogen Embrittlement
N. Events NRC	2855	77	54	1	112	4	0
N. Events other sources	366	65	103	24	114	42	14

Figure 1.5: Distribution of the number of events by failure mechanism, divided by data source. The red bar represents the NRC database records, the white bar represents ARIA, JRC, CSB, TSB and eMars database.

The analysis also examined the main industrial macro-sectors and the types of equipment involved in incidents. As highlighted in **Figure 1.6**, the most recurring sectors are the Chemical & Petrochemical industries, Pipelines, and, to a lesser extent, Storage & Warehousing. In the former case, typical operating conditions can generate mechanical stresses that can accelerate degradation. Conversely, pipelines are also affected by external environmental conditions, which directly impact their structural integrity.

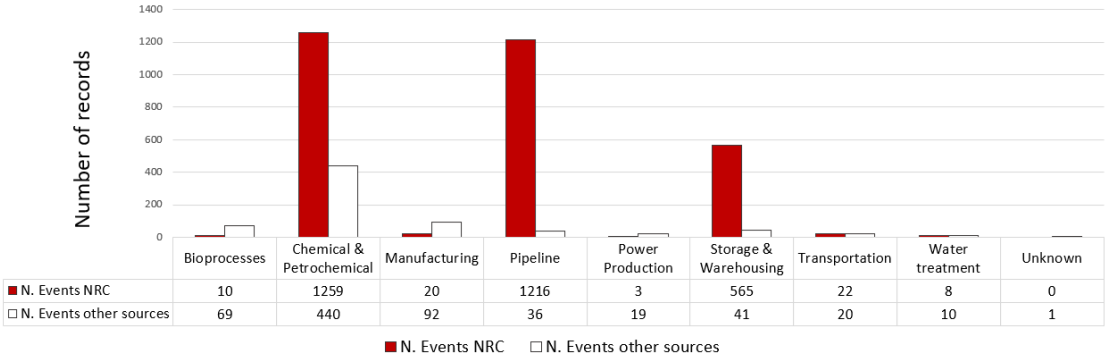

	Bioprocesses	Chemical & Petrochemical	Manufacturing	Pipeline	Power Production	Storage & Warehousing	Transportation	Water treatment	Unknown
N. Events NRC	10	1259	20	1216	3	565	22	8	0
N. Events other sources	69	440	92	36	19	41	20	10	1

Figure 1.6: Distribution of events by industrial macro-sector involved. The red bar represents the NRC database records, the white bar represents ARIA, JRC, CSB, TSB and eMars database.

The geographical analysis highlighted significant differences between continents: in America, the Chemical & Petrochemical and Pipeline sectors are almost equally affected, with a distribution of events of 40% and 39%, respectively, while the remaining approximately 20% is attributable to Storage & Warehousing. In Europe, however, the Chemical & Petrochemical sector clearly dominates with approximately 60% of events, followed by Manufacturing (13%) and Storage & Warehousing (6%). These results suggest that, in the North American context, pipeline transport is more subject to material degradation phenomena than in the European context, where problems related to industrial processes within the plants prevail.

The analysis of the equipment involved, shown in **Figure 1.7**, in the incidents highlighted a marked incidence of Primary containment system, which is the most frequently affected component. This result can be explained by considering

multiple contributing factors. First, the composition and chemical-physical properties of the transported fluids are critical: particularly reactive or aggressive substances can accelerate the degradation of materials. Furthermore, these systems often operate under non-stationary operating conditions, subject to temperature and pressure variations that generate cyclic stresses and structural fatigue. These conditions, if prolonged, can compromise the mechanical integrity of the system and increase the likelihood of failures or leaks. The Control & mitigation system and Structures categories also show a certain recurrence in the analysed data, but with much lower recurrence. It is particularly significant to note that Control & mitigation system are involved in a higher number of events than static Structures, despite the latter also being subject to environmental factors and mechanical stresses. However, it is interesting to note that Structures present a higher incidence than EC&I Systems. This type of equipment has a lower impact than dedicated control and mitigation systems, presumably due to more intense and systematic preventative maintenance. This approach significantly contributes to reducing the incidence of failures attributable to material degradation.

Regarding the distribution of event outcomes, a substantial majority, amounting to 89%, resulted in LOC. Events categorized as accident and incident each accounted for 3% of the total, whereas near-miss occurrences represented only 1%. These data are summarized in **Figure 1.8**, which shows that LOC is the primary cause of material degradation. Specifically, the data for the American context indicate a prevalence of LOC of 94%, with a negligible percentage of events classified as incidents (0.4%). In contrast, in Europe, the distribution of outcomes is more varied: 67% of events are classified as LOC, while accidents and incidents represent 13% and 16%, respectively. Consequently, in the United States, the frequency of events other than LOC is approximately 235 times lower, while in Europe, LOC occurs approximately four times more frequently than incidents and five times more frequently than accidents. These differences can be attributed to a variety of factors, including operational practices, safety management systems, and plant infrastructure, which vary significantly between the two contexts. Differing regulatory frameworks also play a key role: in the United States, the NRC adopts a voluntary reporting system, which can lead to a higher incidence of events classified as LOC. In Europe, however, the Seveso III Directive imposes structured reporting requirements for certain industrial installations, which can lead to increased reporting of incidents and near-misses.

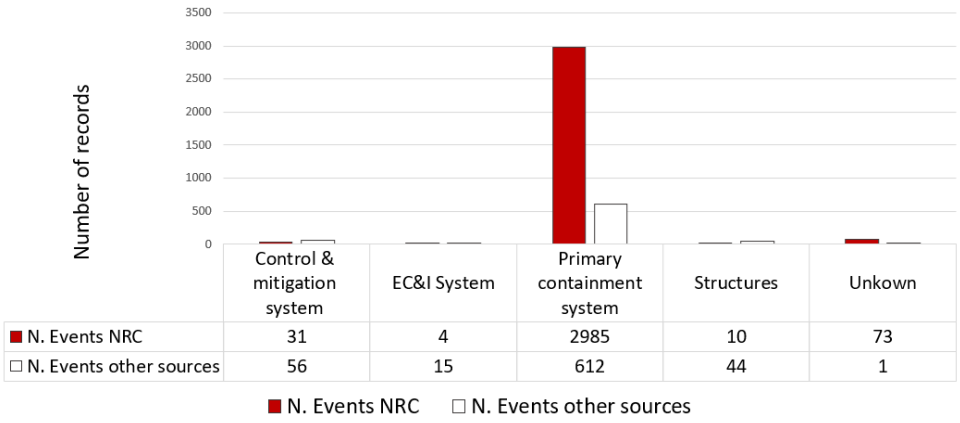

Figure 1.7: Distribution of material degradation events according to the type of equipment involved. The red bar represents the NRC database records, the white bar represents ARIA, JRC, CSB, TSB and eMars database.

Interestingly, according to the literature (Cooper, 2018), near-misses tend to occur more frequently than more serious events. However, in the analysed dataset, these events are significantly underrepresented. This discrepancy may be due to the lack of specific regulatory requirements for their reporting in some jurisdictions, inconsistencies in data collection systems between operators and competent authorities, resulting in underreporting. This limitation highlights the need to promote a culture of reporting even for minor events, to improve the early identification of precursors to serious incidents and prevent their escalation.

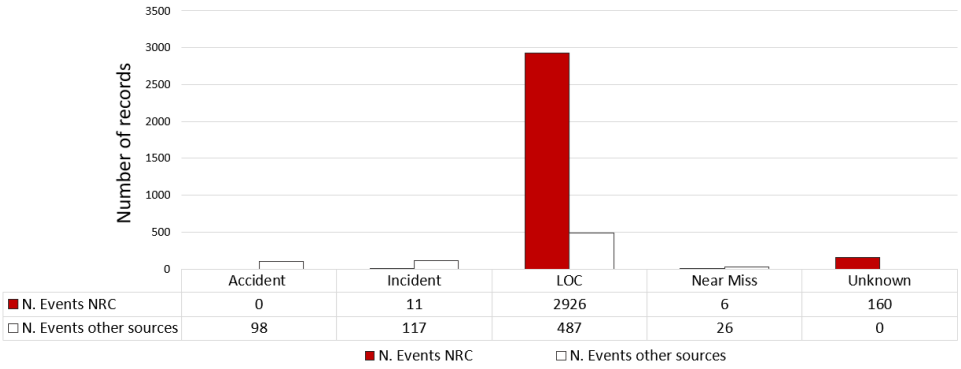

Figure 1.8: Percentage distribution of the outcomes of the analysed events. The red bar represents the NRC database records, the white bar represents ARIA, JRC, CSB, TSB and eMars database.

Numerous studies, including that of Casal (2008), highlight how containment losses are one of the main causes of major accidents in the process industry. This data underscores the urgency of adopting effective preventative measures to contain such losses and limit the progression of events to more serious scenarios.

To further analyse the failure mechanisms, **Figures 1.9a** and **1.9b** were developed, illustrating the different outcomes associated with the main degradation phenomena. The division into two graphical representations was adopted for greater visual clarity, as events attributed to corrosion numerically predominate compared to other mechanisms.

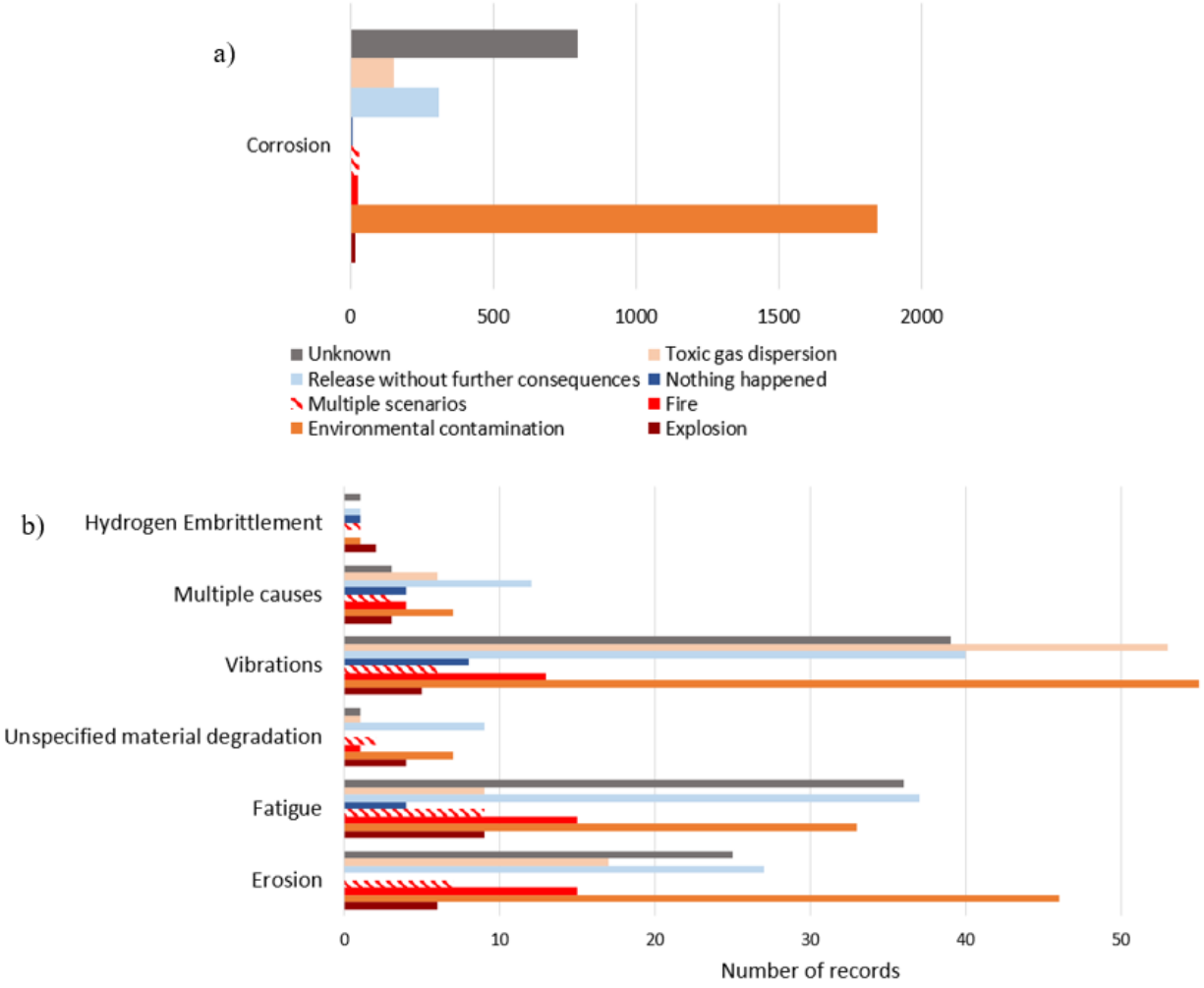

Figure 1.9: Distribution of final outcomes by failure mechanism. A) Corrosion. B) All other mechanisms.

The analysis reveals significant differences between the various phenomena. Corrosion is responsible for environmental contamination in 58% of cases, primarily due to the chemical aggressiveness of the substances contained, which accelerate the deterioration of the materials. A further 10% of corrosion events result in releases without significant environmental impacts, generally in the presence of non-hazardous substances or thanks to effective event management, which may include containment, neutralization, and securing the area. However, the frequency of these scenarios is significantly lower than those with environmental impacts, highlighting the need for enhanced inspection activities and targeted protective treatments. Vibrations are also a critical mechanism, with 24% of events resulting in environmental contamination and 23% resulting in the dispersion of toxic gases. This is attributable to the formation of microcracks or holes in components, which facilitate the release of hazardous substances. Fatigue and erosion, both mechanical in nature, exhibit distinct behaviours. Fatigue, caused by cyclic stresses, predominantly leads to releases without serious consequences (24%), thanks to the non-reactive nature of the failure and the timely operational response. Erosion, however, while not directly related to the hazardous nature of the substances, is responsible for environmental contamination in 32% of cases. It is important to note that approximately 30% of events that result in fires or explosions are associated with fatigue and erosion

phenomena. Vibrations contribute significantly to these scenarios, as they can generate sparks in the presence of flammable substances. A specific case is hydrogen embrittlement, which leads to explosions in 29% of cases and fires in the remaining 50%. This behaviour is attributable to the dynamics of hydrogen release following structural failures, which can generate explosive atmospheres under favourable conditions. Finally, there is a significant presence of data classified as "unknown," particularly regarding corrosion, where the second most frequent scenario has not been defined. This highlights a criticality in the information collection and classification systems, which could compromise the accuracy of the analyses and suggests the need to improve the quality and completeness of the available data.

Figure 1.10 illustrates the substances involved in the events, divided by their respective hazardous categories. The analysis shows that a significant portion of these substances, approximately 74%, are characterized by multiple hazards. In particular, many of these substances exhibit corrosive or otherwise aggressive behaviour toward the materials they come into contact with, thereby accelerating their degradation. **Table 1.2** lists the substances identified as belonging to more than one hazard class. Noteworthy is that 92% of events involving multi-class substances are associated with physical hazard. Another interesting aspect is the marginal presence, approximately 2%, of substances classified as non-hazardous (NH). This data can be interpreted considering that material degradation is not necessarily attributable exclusively to the chemical nature of the substances present in the system but can also be influenced by external or operational factors. These include environmental conditions and the mechanical stresses to which the materials are subjected. For instance, phenomena such as atmospheric corrosion, induced by humidity, the presence of pollutants, or proximity to the sea, and corrosion under insulation, which occurs when water becomes trapped under insulating materials, represent recurring degradation mechanisms even in the absence of hazardous chemical substances.

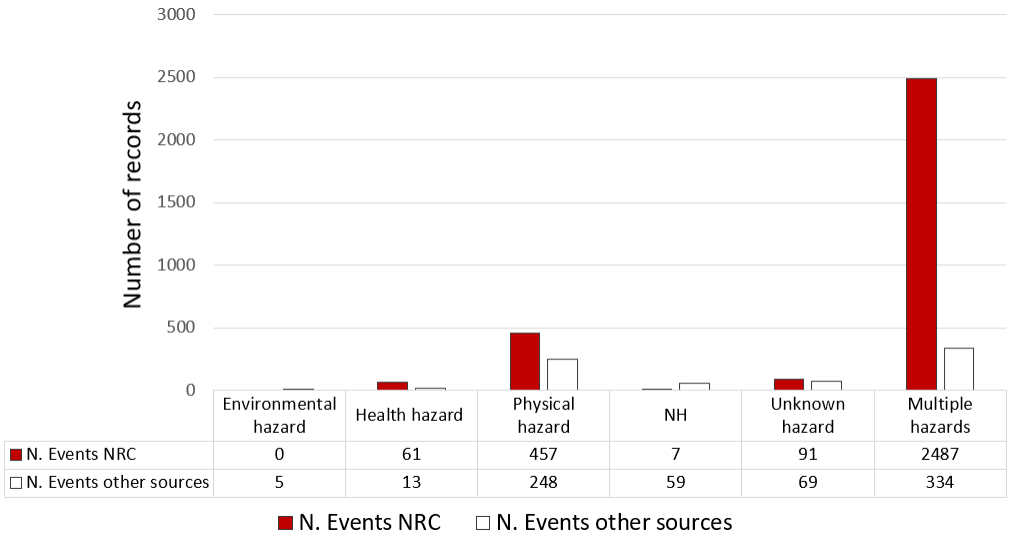

Figure 1.10: Distribution of substances involved in accidents by hazard category. The red bar represents the NRC database records, the white bar represents ARIA, JRC, CSB, TSB and eMars database.

Table 1.2: Substances classified as multiple hazards according to UNECE (2021).

Multiple hazard	N. Events	%
Health hazard and Environmental hazard	220	7.8
Health hazard and Environmental hazard and Physical hazard	2348	83.2
Health hazard and Physical hazard	238	8.4
Physical hazard and Environmental hazard	15	0.5

To further deepen the analysis, where available, the age of the systems involved was also considered. Specifically, it was possible to trace the construction date of the plant or the age of the equipment involved for a total of 461 events. **Figure 1.11** represents the distribution of this data, highlighting that 70% of the incidents involved systems that can be classified as Old, meaning more than 25 years in operation. This finding is consistent with Vairo et al. (2018), who reported that approximately 50% of European industrial plants continue to operate beyond their designed useful life, often exceeding 25 years. This finding helps explain the high incidence of events in older systems observed in the dataset. However, a small percentage (approximately 6%) concerns systems less than 5 years old. This suggests that operational age, while a significant factor, is not the only determining factor in material degradation: a combination of technical, environmental, and management variables must also be considered, as they influence system performance and material integrity.

A comparative analysis of the age of plants in relation to their geographic location was also conducted. This analysis highlighted a limitation in the available data: while European databases frequently provide information on the age of plants, the NRC does not provide this information. CSB and TSB reports include this data, making the comparison less homogeneous. Nevertheless, a common trend emerges in both Europe and the United States: older plants are more likely to be involved in incidents, followed by those of intermediate age, while newer plants show a lower incidence.

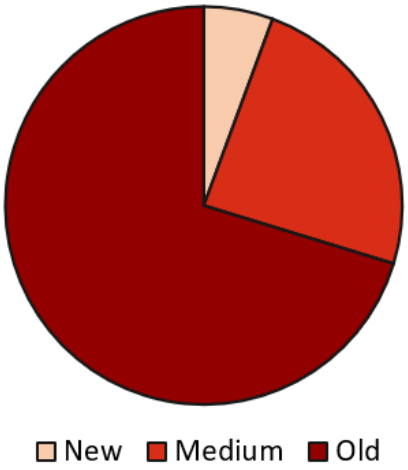

Figure 1.11: Distribution of events by plant age.

For cases where additional information was available, the type of corrective actions taken following the event was also collected, with particular attention to the revision of inspection plans. This data was collected for 377 events. As shown

in **Figure 1.12**, in 91% of cases, the inspection plan was revised, resulting in an increase in inspection frequency. This data highlights how existing inspection plans are often inadequate, underscoring the need for more effective approaches. In particular, it highlights the importance of implementing risk-based inspection strategies, replacing traditional fixed-interval approaches that do not take into account the specific vulnerabilities of components (Rasmussen, 1997; Bragatto et al., 2009). This highlights the need for a more advanced management and control system, capable of dynamically adapting to operating conditions and actual risk factors. In approximately 7% of the events analysed, no post-incident corrective measures were implemented. This data suggests that, although in some cases, high-frequency inspection plans were already in place, these measures were not sufficient to prevent the event, highlighting the inadequacy of some current inspection practices. This finding underscores the urgent need to develop more effective guidelines and operating procedures that ensure not only frequent but also thorough and targeted inspections. Therefore, it is necessary to promote the adoption of innovative inspection methodologies that not only increase the frequency of inspections but also improve their quality, enhancing the ability to identify critical conditions early and intervene promptly to prevent them from escalating into failures. In a small percentage of cases (2%), however, the use of specific treatments on materials aimed at improving their resistance to degradation was reported. These treatments should be carefully selected during the design and commissioning phase of the system or introduced later if they were not initially available. The lack of adequate protective treatments can be traced back to a poor risk assessment, which has led to an underestimation of degradation phenomena and, consequently, the omission of key preventative measures.

To effectively address these critical issues, a deeper understanding of material deterioration mechanisms, as well as monitoring and predictive maintenance techniques, is essential. A deeper understanding of these aspects enables the implementation of more effective management strategies, reducing the risk of failures, production losses, and safety impacts. The adoption of advanced prevention systems, combined with ongoing updates to inspection and maintenance techniques, is key to mitigating the negative effects of degradation. This integrated approach contributes not only to improving plant safety but also to ensuring their long-term reliability, reducing the costs associated with corrective interventions and unplanned downtime.

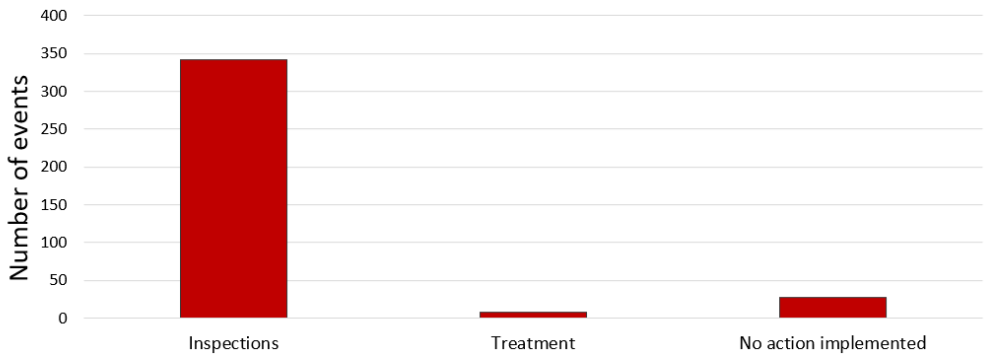

Figure 1.12: Corrective actions taken after analysed events.

Another aspect analysed concerns losses associated with accidents. **Figure**

1.13 summarizes the results, distinguishing between human (light red), economic (dark red), and environmental (red) losses. The acronyms shown in the figure identify the different categories of events, while the numbers indicate the relative frequency for each category. It is clear that the number of events for which data on consequences is available is significantly lower than the total number of incidents analysed. Only 4% of cases report economic losses, 7.3% mention impacts on people, and 29.2% document environmental effects. This distribution may reflect both a lack of detailed data in the databases consulted and a greater focus on some types of consequences than others.

Regarding economic losses, the four categories considered show a relatively uniform distribution, with the exception of events with damages exceeding ten million dollars, which are slightly less frequent.

Regarding environmental contamination, the majority of events are classified as ND, followed by cases of mild or moderate contamination (MMD). Incidents with severe environmental impacts (SED) are significantly fewer.

Regarding human losses, the analysis shows that the most frequent category is no fatalities (NF), followed by no injuries (NI) and multiple injuries (MI). The categories of single injury (SI), multiple fatalities (MF), and single fatality (SF) are less recurrent. These results indicate that, in most cases, incidents involve releases without serious consequences for people.

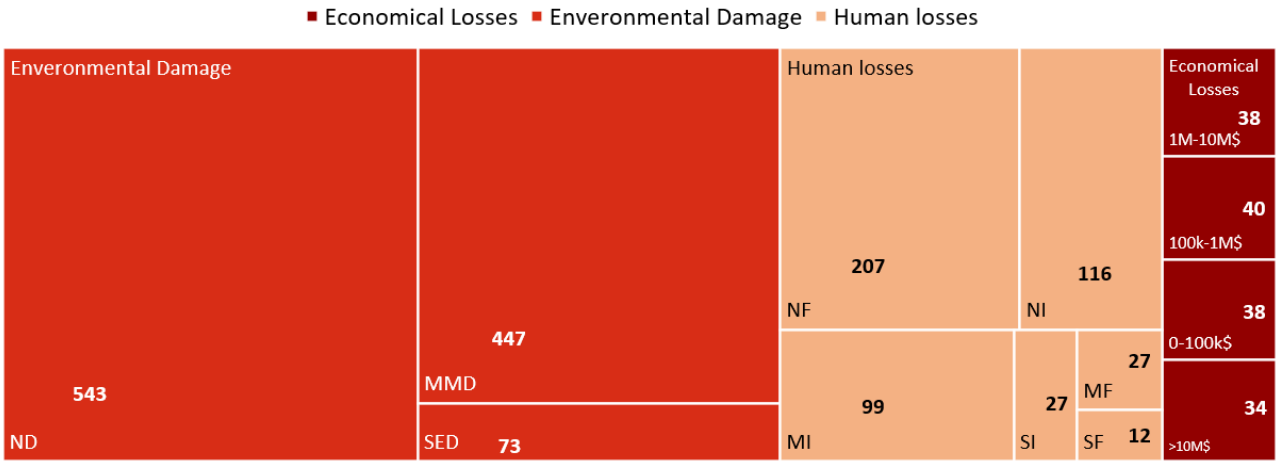

Figure 1.13: Losses resulting from the incident are categorized by type. Environmental pollution is shown in red, human losses in light red, and economic losses in dark red.

To contextualize the results related to human losses, a comparison was made with the historical study by Ricci et al. (2021), which analysed a database of 9,100 NaTech (Natural Hazard Triggering Technological Accidents) events, also including information on human consequences (Valente et al., 2025). In the study, data relating to human losses are available for 210 events, equal to 2.3% of the total, while in the analysis focused on material degradation, such information is present in 276 reports, corresponding to 7.3%. **Figure 1.14** presents the results of this comparison. "Available data" refers to the percentage of reports that include information on human losses compared to the total number of events analysed. The figure also distinguishes between single and multiple injuries, as well as single and multiple fatalities, comparing the two studies: the red bars represent data from the material degradation study, while the white bars are published in the

NaTech study. The comparative analysis shows that, in absolute terms, the number of reports containing information on human losses is similar in the two studies. However, in relative terms, the material degradation study has greater data availability, suggesting potentially more detailed documentation than the NaTech events.

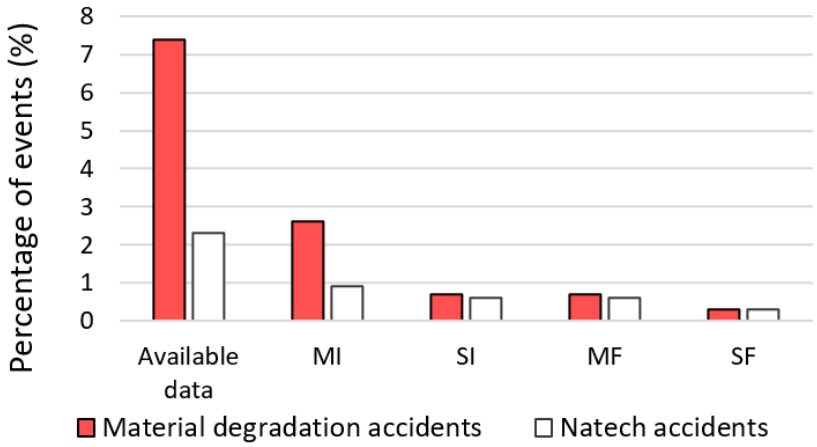

Figure 1.14: Comparison of data availability on human losses between NaTech and material degradation studies (Ricci et al., 2021). The red bars represent the material degradation study, while the white bars represent the NaTech study, with differences in occurrence rate. MI indicates Multiple Injuries, SI Single Injury, MF Multiple Fatalities and SF Single Fatality.

1.2.2 Part 2: Risk Modelling and Quantitative Analysis

This section presents the results obtained through the combined use of event trees and Bayesian networks, two fundamental tools for modelling complex systems with dependencies between variables. Event trees provide a structured representation of the possible evolutions of an initial failure, outlining the sequences of events that may result. However, the analysis highlighted a significant data gap, particularly regarding the final outcomes of accident scenarios, as illustrated in **Figure 1.9**. This information gap limits the predictive capacity of event trees, necessitating the introduction of a complementary approach.

To address this gap, Bayesian networks were adopted, which allow conditional relationships between variables to be inferred even in the presence of incomplete or uncertain information. BNs offer a probabilistic representation of uncertainties and allow plausible values to be assigned to final scenarios not documented in historical records. This second level of analysis is particularly useful for addressing the inherent uncertainty of open-source data, which is often fragmented or unverifiable. Furthermore, the Bayesian approach supports more robust predictive reasoning, facilitating the identification of system vulnerabilities and the prioritization of inspection and maintenance strategies.

Event Tree Analysis

Considering that 84% of the analysed events were caused by corrosion, the event tree analysis was constructed based on this type of failure. Equipment

corrosion can cause leaks of hazardous substances, which, depending on their nature, can trigger fires or explosions. The trigger can occur immediately or with a certain delay, and the timing of the trigger determines the development of different scenarios, as highlighted by Vílchez et al. (2011). The ETA structure is shown in **Figure 1.15**. The conditional probability of a specific scenario occurring is given by the product of the estimated frequency of occurrence of the events leading to that scenario:

$$P(S_i) = \prod F(B_k) \quad (1.1)$$

where S_i is the i scenario while B_k is the k branch; therefore, $P(S_i)$ is the conditional probability of the i scenario and $F(B_k)$ is the frequency of occurrence of branch k at scenario i.

Using this framework, it is possible to estimate the conditional probabilities of specific scenarios. For instance, the conditional probability of a fire scenario occurring following an immediate ignition, indicated as $P(F|II)$, can be calculated by **Equation 1.2:**

$$P(F|II) = F(F|II) \times F(II) \times F(R) \times F(C) \quad (1.2)$$

where:

$P(F|II)$ is the conditional probability that a fire will occur due to an immediate ignition of a release due to corrosion.

$F(F|II)$ is the frequency of occurrence of the ignition scenarios after an immediate ignition.

$F(II)$ is the frequency of occurrence of immediate ignition.

$F(R)$ is the frequency of occurrence of a release.

$F(C)$ is the frequency of occurrence of corrosion.

Replacing:

$$P(F|II) = 0.68 \times 0.01 \times 0.949 \times 0.85 = 0.006$$

Likewise, it is possible to determine the conditional probabilities associated with the other scenarios outlined in the event tree. The graphical analysis clearly shows that the event with the highest probability of occurrence is environmental contamination, represented by the red line in **Figure 1.15**. The probability of this scenario occurring can be estimated by applying **Equation 1.3**:

$$P(EC|\overline{DI}) = F(EC|\overline{DI}) \times F(\overline{DI}) \times F(\overline{II}) \times F(R) \times F(C) \quad (1.3)$$

where:

$P(EC|\overline{DI})$ is the probability of environmental contamination, assuming there is no delayed ignition, occurring as a result of a release due to corrosion.

$F(EC|\overline{DI})$ is the frequency of occurrence of environmental contamination, if there is no delayed ignition.

$F(\overline{DI})$ is the frequency of non-occurrence of a delayed ignition.

$F(\overline{II})$ is the frequency of non-occurrence of an immediate ignition.

Replacing:

$$P(EC|\overline{DI}) = 0.794 \times 0.98 \times 0.78 \times 0.949 \times 0.85 = 0.49$$

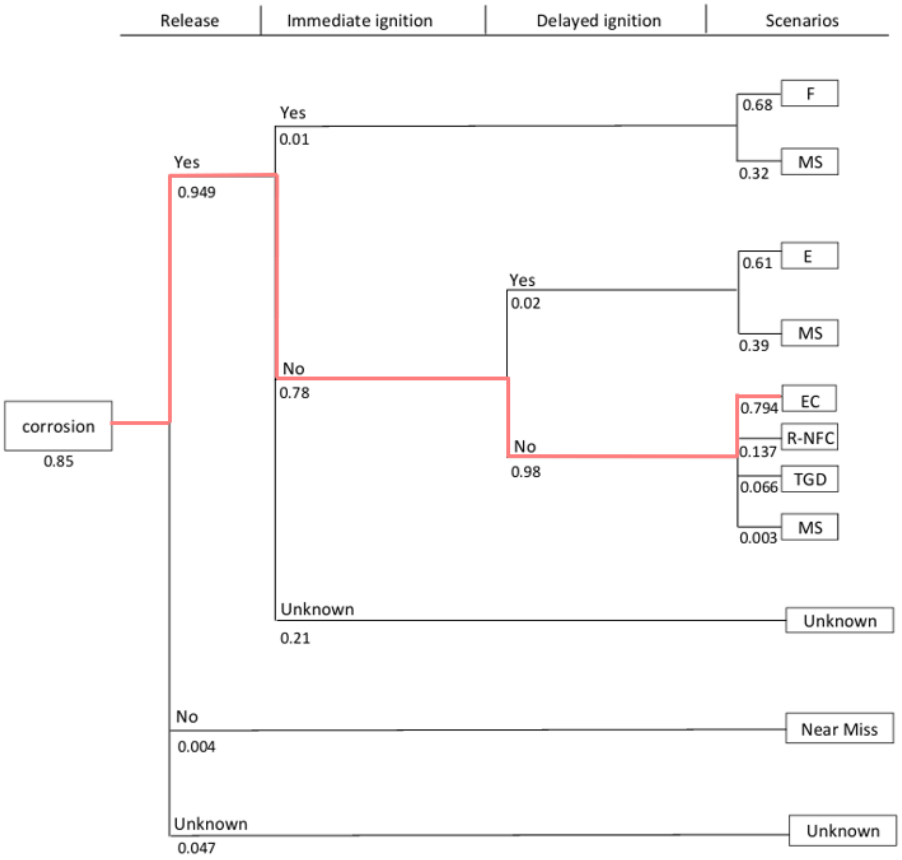

Figure 1.15: Event tree developed to analyse the possible outcomes of corrosion-related incidents. Environmental contamination, highlighted in red, is the most frequently observed scenario in the analysed data.

The analysis of the dataset shows that, in scenarios where industrial components were subjected to corrosion, approximately 50% of incidents resulted in environmental contamination. This value represents a conditional probability, calculated exclusively on the subset of corrosion-attributed events in the database, and not an absolute probability for the entire population of operating equipment. Therefore, this value represents the observed proportion of corrosion events that generated an environmental impact, and not a predictive estimate of the failure rate for a specific time period, plant, or individual equipment. It is crucial to emphasize that this probability reflects the observed frequency within a sample of real incidents, in which corrosion was identified as the primary cause. Consequently, the resulting value represents a mitigated risk, that is, the residual risk after the implementation of operational safety measures at the time of the event. This distinction is crucial for correctly interpreting the results.

To apply the proposed method, two real-world case studies were selected from the developed accident database, with the aim of validating the model and demonstrating its operational effectiveness.

Case Study 1 refers to ARIA database report no. 44683, relating to an accident that occurred on December 9, 2013, at a paper mill. On that occasion, abnormal noises and vibrations occurred in the black liquor steam generator, which normally operates at negative pressure, but which at that moment recorded a positive pressure of between 20 and 30 mbar. After some fluctuations, the parameters returned to normal. An external visual inspection revealed no

anomalies, but the cause was hypothesized to be a falling block of sodium sulphate. To remove the deposits, the fuel oil supply was activated. During the night, a water leak was detected in the boiler, accompanied by abnormal humidity and low temperature. The water level became unstable, and there was a sudden increase in flow, causing the boiler to drain and the building to be isolated. All production facilities were shut down. The inspection, repair, and restart operations took several weeks, with economic losses estimated between €2 and €3 million. The inspection detected a hole in a coated steel pipe, attributed to corrosion-erosion caused by air turbulence. In response, the SIR department decided to revise the boiler inspection plan, increasing the frequency of checks.

The case study highlights a corrosion-erosion event with water release into the surrounding environment, classified as a release without further consequences. No injuries or environmental contamination occurred, but the economic losses were significant. In **Figure 1.16**, the path corresponding to this scenario is highlighted in red within the event tree.

The conditional probability of the case study was calculated following Equation 1.1:

$$P(R - NFC|\overline{DI}) = F(R - NFC|\overline{DI}) \times F(\overline{DI}) \times F(\overline{II}) \times F(R) \times F(C) = 0.137 \times 0.98 \times 0.78 \times 0.949 \times 0.85 = 0.084$$

where:

$P(R - NFC|\overline{DI})$ is the probability of release without further consequences, assuming there is no delayed ignition, occurring as a result of a release due to corrosion.

$F(R - NFC|\overline{DI})$ is the frequency of occurrence of release without further consequences, if there is no delayed ignition.

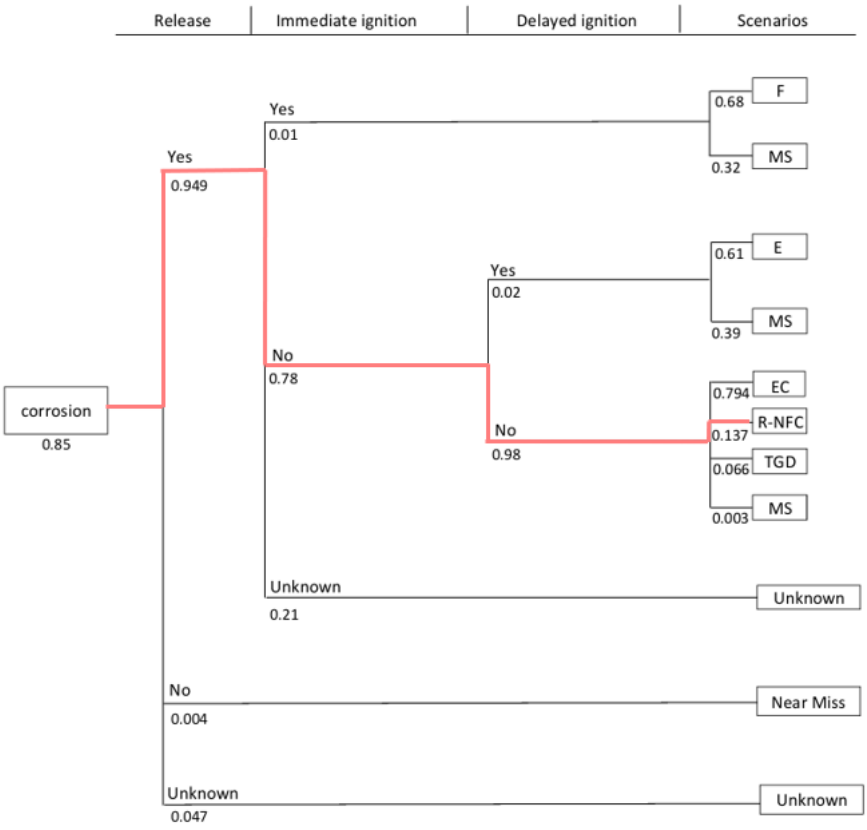

Figure 1.16: Event tree for corrosion-related incidents. The branch highlighted in red represents the path followed in Case Study 1, where a corrosion-erosion phenomenon caused a release without further consequences.

Case Study 2 is based on CSB Report No. 2019-04-I-PA, which documents an accident that occurred on June 21, 2019, at a hydrofluoric acid (HF) alkylation unit. That morning, a pipe elbow ruptured, releasing a cloud of flammable vapours composed primarily of propane and HF. The cloud ignited two minutes later, generating a large fire and three explosions, one of which involved a tank, projecting metal fragments up to 600 meters. The fire was extinguished only the following day. The investigation conducted by the Chemical Safety Board identified the primary cause as accelerated corrosion of the elbow, which was made of carbon steel with nickel and copper, materials notoriously susceptible to attack by HF. The deterioration led to thinning of the metal and subsequent fracture. Aggravating factors identified included the lack of thorough inspections of carbon steel components, the lack of remotely activated emergency isolation valves, the failure of the water mitigation system (unable to be activated due to electrical and structural damage), and inadequate general safety measures. The accident resulted in the release of approximately 2,300 kg of HF, 1,400 kg dispersed into the atmosphere, and 300,000 kg of hydrocarbons, of which 270,000 kg burned. Six people were injured, including five workers and a firefighter. Metal fragments fell near tanks containing toxic and flammable substances, increasing the risk of escalation. Property damage was estimated at approximately $750 million, making the event the third costliest refinery accident worldwide since 1974. The case study highlights a corrosion event with the release of flammable vapours, which led to a fire and explosion, with significant economic, environmental, and safety consequences. In **Figure 1.17**, the path corresponding

to this scenario is highlighted in red within the event tree.

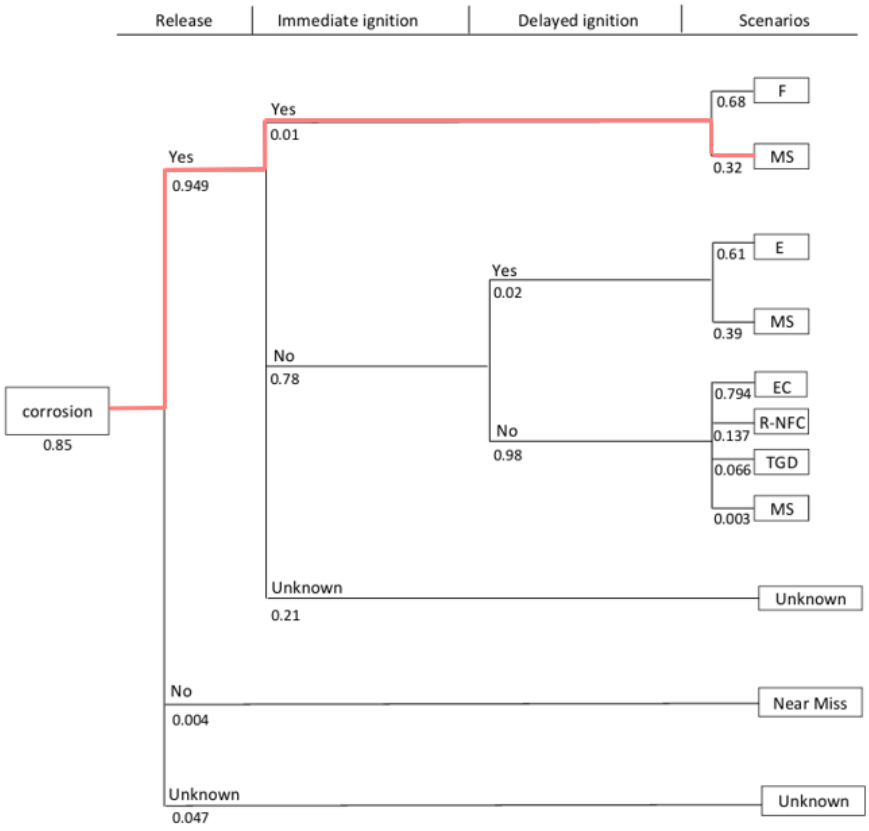

Figure 1.17: Event tree for corrosion-related incident scenarios. The branch highlighted in red represents the path followed in Case Study 2, where corrosion of a pipe caused the release of flammable vapours, resulting in a fire and explosion.

The conditional probability of the case study was calculated following **Equation 1.1**:

$$P(MS|II) = F(MS|II) \times F(II) \times F(R) \times F(C) = 0.32 \times 0.01 \times 0.949 \times 0.85 = 0.003$$

where:

$P(MS|II)$ is the probability of multiple scenarios, assuming there is immediate ignition, occurring as a result of a release due to corrosion.

$F(MS|II)$ is the frequency of occurrence of multiple scenarios, if there is immediate ignition.

$F(II)$ is the frequency of immediate ignition.

To integrate the model results into an operational decision-making system, a 3x3 risk matrix was developed, combining two key dimensions:

The conditional probability of the event, obtained through event tree analysis.

The severity of the consequences is assessed based on three criteria: economic damage, environmental impacts, and human losses.

The proposed matrix represents an integrative tool for qualitative and quantitative risk assessment, based on the intersection between the probability of occurrence and the severity of the consequences, following the approach suggested by Duijm (2015). The classification thresholds are as follows:

Probability:

- Low: $P < 0.01$

- Medium:$0.01 \leq P < 0.05$
- High: $P \geq 0.05$

Consequences:

- Low: limited economic losses, no injuries or fatalities, no environmental impact.
- Medium: significant economic losses, injuries, but no fatalities, moderate environmental contamination.
- High: high economic losses, deaths and injuries, severe environmental contamination.

The intersection of these two dimensions allows each scenario to be classified into one of three risk categories: low, medium, or high. This classification can be used to support operational decisions such as determining inspection frequency and prioritizing maintenance interventions.

Unlike the thresholds proposed by Duijm (2015), which are based on absolute frequencies, this study adopted more permissive thresholds for probability. This choice is justified by the use of conditional models based on historical accident data, rather than deterministic approaches or annual failure frequencies. These probabilities reflect the residual risk in the presence of safety barriers already in place and are influenced by selection bias, as the dataset includes only events that actually occurred and were reported. Therefore, the adoption of more permissive thresholds allows for a more realistic assessment of residual risk, in line with the objective of the BN-ETA model: to support operational decisions in complex contexts characterized by high uncertainty.

The two selected cases were positioned within the risk matrix, as illustrated in **Figure 1.18**:

i)AIR Case 44683: it presents a high conditional probability, but the consequences are limited to economic losses. Therefore, the scenario is classified as medium risk.

ii)CSB Case 2019-04-I-PA: despite it has a low conditional probability, it is characterized by serious consequences (explosion, injuries, environmental contamination, and significant material damage), also falling into the medium risk category.

The integration of conditional probability and severity of consequences allows for a

systematic assessment of the risk associated with specific scenarios. The matrix provides a concise yet informative representation of the criticality, useful for prioritizing inspection and maintenance activities, focusing attention on assets or scenarios classified as medium or high risk.

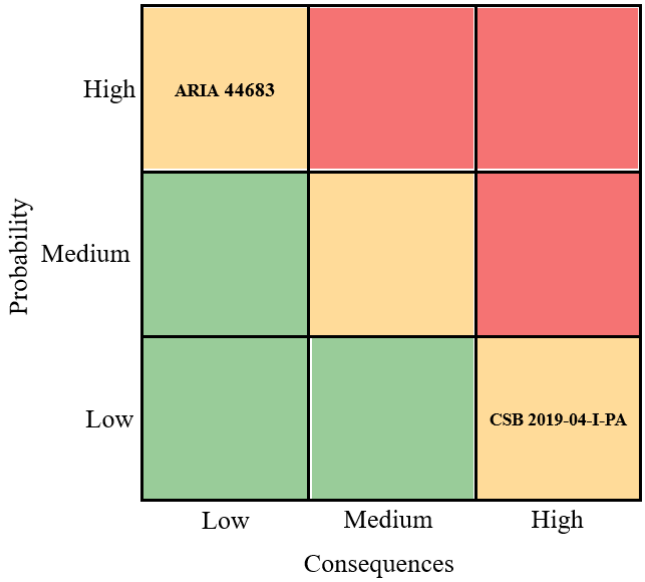

Figure 1.18: A 3x3 risk matrix developed for the classification of accident scenarios. The two case studies are highlighted.

The following insights were identified:

i)Risk equivalence between different events: despite the differences between the two scenarios in terms of facility, dynamics, and probability, both are medium risk. This highlights how rare but catastrophic events can have a comparable impact to more frequent but less severe events.

ii)Presence of barriers does not eliminate risk: both cases included active safety measures, technical barriers, inspections, and mitigation systems, underscoring the need for more robust prevention strategies.

iii)Limitations of historical data: the probabilities used are derived from historical datasets, which may contain errors, omissions, or non-standardized descriptions. The quality and detail of the information vary, introducing a certain degree of subjectivity.

iv)Potential predictive application: although in this study, severity was assessed based on real events, in a predictive context, it could be estimated using surrogate indicators (type of equipment, property of the substance, quantity released, proximity to sensitive targets). This would make the risk matrix a useful tool even in the preventive phase, in the absence of complete historical data.

Bayesian Network Analysis

To address the high degree of uncertainty and significant amount of missing data found in historical incident records, as highlighted in the previous analysis conducted using ETA, a complementary modelling approach based on BN was introduced. The primary objective of this section is to provide a second level of analysis, capable of integrating and interpreting partial or missing information by deducing conditional probabilistic relationships between key system variables. Bayesian Networks are particularly effective in contexts characterized by incomplete

or uncertain data, as they allow the representation and the quantification of dependencies between variables, despite incomplete or uncertain information.

This allows for an inferential view of the system, useful for identifying vulnerabilities and supporting strategic decisions regarding inspection and maintenance.

Each node in the network represents a variable of interest, a functional attribute, while the arcs connecting the nodes describe the conditional independence relationships between the variables. This framework allows not only predictive reasoning but also the dynamic updating of probabilities as available evidence changes, making the approach particularly suitable for risk management under conditions of uncertainty. This section is dedicated to the analysis of the NRC database, with the aim of building a Bayesian Network-based model for interpreting accident dynamics. The variables selected for modelling include "Equipment Involved", "Cause", "Outcome", "Macro-sector", "Substance Involved", and "Final Scenario". The network structure was defined through a hybrid approach that combines structural learning algorithms with expert knowledge to ensure a consistent and meaningful representation of the system. To train the BN model, the dataset was divided into a training set and a validation set, adopting the K-fold cross-validation technique with K = 5. This choice, as suggested by Marcot and Hanea (2021), represents a good compromise between accuracy and computational complexity, proving adequate for most BN applications. In each of the five iterations, four subsets were used for training and one for validation. The average score obtained from the five iterations was considered an indicator of the model's overall performance, defined as the K-validation score. **Figure 1.19** shows the structure of the Bayesian network learned from the training set, highlighting good stability across iterations.

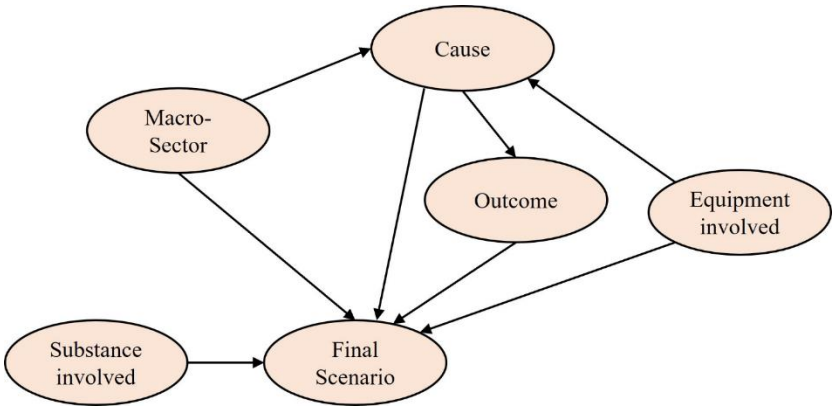

Figure 1.19: Bayesian network structure for material degradation.

A preliminary analysis of the structure shows that the cause of the event is influenced by the industrial macro-sector and the equipment involved. The final accident scenario is determined by a broader set of variables, including the macro-sector, the equipment, the degradation mechanism, and the chemical-physical nature of the substance. Numerous network configurations emerged during the modelling process, but to ensure greater readability and applicability of the model, we chose to focus on the most significant dependencies. This approach allowed for a more concise and interpretable model structure, focusing on the connections that have a significant impact on the evolution of the event. To validate the Bayesian Network model generated in each iteration, the prediction accuracy of

the Final Scenario was considered as the evaluation metric, conditioned by the evidence provided by other system variables. However, some of these variables can take on multiple values, increasing the complexity of the predictive process. For example, an equipment may be associated with substances classified as both a Health Hazard and a Physical Hazard. In this scenario, the model makes multiple predictions, treating each value as a separate input.

To account for this variability, three prediction scenarios were defined, shown in **Table 1.3**:

- Single Prediction (SP): each input variable takes on a single value, simplifying the inference process. This case is the most represented in the dataset. Prediction accuracy remained stable across the five cross-validation iterations, with an average score of 85.58%.
- Multi-Prediction with Single Result (MSR): In this scenario, the input variables can contain multiple values (e.g., Health Hazard and Physical Hazard), each treated as a separate node in the network. Despite the multiplicity of inputs, the model returns a single predictive outcome. This approach reflects more realistic operating conditions and improves the model's interpretability. Although less common than Case S, this scenario achieved a higher accuracy of 90.71%.
- Multi-Prediction with Multi-Result (MM): in multi-prediction, the combination of multiple inputs can generate different predictive outcomes. This is the least common configuration. Validation is based on verifying that at least one of the predicted outcomes includes the true reference value (involvement).

Table 1.3: Results from model validation using a 5-part K-fold cross-validation approach.

Case	**Iteration**	I1	I2	I3	I4	I5	Score
SP	Case No.	782	770	783	752	736	85.58%
	Accuracy	85.29%	86.49%	85.95%	84.18%	86.01%	
MSR	Case No.	162	170	159	167	187	90.71%
	Accuracy	91.98%	92.94%	87.42%	89.22%	91.98%	
MM	Case No.	4	2	6	9	1	100%
	Involvement	100%	100%	100%	100%	100%	

As shown in **Table 1.3**, the predictive accuracy of the BN model for a single prediction is around 86%, while for multiple predictions with a unique outcome, the accuracy reaches approximately 91%. This result is particularly significant, as this demonstrates the model capability to generate accurate and dependable forecasts, even when confronted with complex or ambiguous input data. In general, an accuracy above 80% is considered satisfactory in highly uncertain contexts, such as those related to industrial risk management.

Tables 1.4 and **1.5** present the results of the probabilistic analysis conducted using Bayesian networks. Specifically, **Table 1.4** reports the conditional probability tables (CPT) for the cause of the event and the final scenario, while **Table 1.5** shows the probability distribution associated with the equipment

involved and the final scenario. To facilitate comparison with the results obtained in the previous analysis (**Section 1.1.1**), the observed occurrence frequencies are indicated in parentheses. These values are calculated on the entire database, which also includes events with an unknown final scenario due to missing information in the incident reports. Consequently, the sum of the reported conditional probabilities is not equal to 1, since a portion of the events is associated with final outcomes classified as "Unknown". Some probabilities have been rounded to zero, as they are less than three decimal places. This choice was made to simplify the model structure and improve its interpretability, while maintaining consistency with available data. However, it is recognized that such simplification may reduce the visibility of rare but potentially high-impact scenarios. The analysis conducted using Bayesian networks highlighted a significant increase in the probability of environmental contamination and toxic gas release compared to the initial data. In particular, a rise of approximately 50% was observed in both conditional probabilities. Conversely, scenarios such as near-misses, fires, explosions, and releases with no consequences show a reduction in occurrence. Regarding the equipment involved, the results obtained are consistent with those observed for the causes of the events. However, Structures exhibit a rising incidence of near-misses, fires, and toxic releases is observed, while the probability of environmental contamination and release without further consequences decreases. For control and mitigation systems, an increase in the occurrence of environmental contamination has been observed. Finally, for the EC&I system, the occurrence probability of environmental contamination was approximated to 1, while for all other scenarios, the values are three orders of magnitude lower and were approximated to zero.

Table 1.4: CPT representing the relationship between Causes and Final Scenario.

Cause/Final scenario	Corrosion	Erosion	Fatigue	Vibrations
Near-miss	0.002 (0.004)	0 (0.019)	0 (0.032)	0.005 (0.047)
EC	0.875 (0.581)	0.644 (0.323)	0.675 (0.222)	0.511 (0.242)
F	0 (0.012)	0 (0.097)	0 (0.108)	0 (0.089)
R-NFC	0.055 (0.101)	0.104 (0.206)	0.036 (0.266)	0.103 (0.191)
TGD	0.067 (0.048)	0.252 (0.129)	0.289 (0.076)	0.380 (0.242)
E	0 (0.010)	0 (0.045)	0 (0.070)	0 (0.021)

Table 1.5: CPT representing the relationship between Equipment Involved and Final Scenario.

Equipment/Final Scenario	Control & mitigation system	EC&I system	Primary containment system	Structures
Near-miss	0 (0.024)	0 (0)	0.002 (0.007)	0.091 (0.065)
EC	0.304 (0.274)	1 (0.235)	0.875 (0.538)	0 (0.026)
F	0 (0.036)	0 (0.059)	0.001 (0.023)	0.545 (0.152)
R-NFC	0.036 (0.238)	0 (0.294)	0.055 (0.113)	0 (0.239)
TGD	0.661 (0.202)	0 (0.294)	0.067 (0.058)	0.364 (0.130)

E	0 (0.024)	0 (0)	0 (0.015)	0 (0.065)

Bayesian networks also prove effective in predicting the final scenario based on specific input configurations. **Table 1.6** presents an application example: considering the variables "Pipeline", "Primary Containment System", "Environmental Contamination", "Corrosion", and "LOC", it is possible to calculate the conditional probability of the different final scenarios. The scenario with the highest probability is the predictive outcome of the model.

Table 1.6: Application of a Bayesian Network for predictive analysis.

Input	**Joint probability of the Final Scenario**		**Prediction result**
	Value	Probability	
{Pipeline, Primary containment system, Environmental hazard, Corrosion, LOC}	Near-miss	0	EC
	EC	**0.976**	
	F	0.001	
	R-NFC	0.014	
	TGD	0.009	
	E	0	

Further analytical evidence is presented using heat maps, which provide a visual representation of the conditional probability distributions, as illustrated in **Figure 1.20**. This technique allows for the immediate identification of areas characterized by greater probabilistic intensity, thus facilitating data interpretation and the emergence of relevant patterns. **Figure 1.20a** shows the heat map of the conditional probabilities of system age with respect to the causes of failure. The results show that, in older or intermediate-age systems, corrosion is the predominant failure mechanism, suggesting a slow and progressive degradation process. Conversely, more recently installed systems show a higher incidence of vibration-related failures, a phenomenon that manifests itself more quickly. In older systems, in addition to corrosion, a relatively uniform distribution of vibration, erosion, and fatigue is observed. For plants classified as medium-aged, fatigue and vibration follow corrosion in terms of occurrence, while erosion is less significant, indicating a lower incidence of this mechanism compared to younger or older plants. **Figure 1.20b** shows the distribution of conditional probabilities for the various industrial macro-sectors in relation to material degradation phenomena. The sectors most subject to corrosion are Pipelines and Storage & Warehousing. However, corrosion remains the most common phenomenon in all sectors except Power Production, where corrosion and fatigue exhibit equal probability. In the Bioprocess and Transportation sectors, vibration is the second most common mechanism.

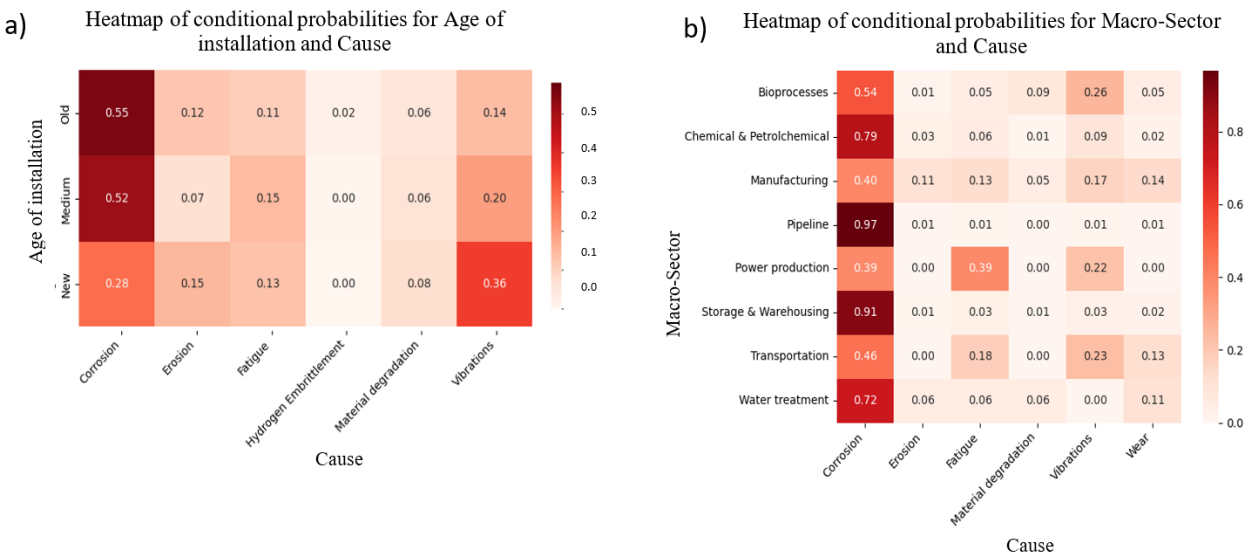

Figure 1.20: Heatmaps showing conditional probability patterns. A) Correlation between plant age and failure mechanisms. B) Macro-sector distribution of failure causes.

These observations provide a probabilistic reinterpretation of partial historical data that would otherwise have remained unexplored. By offering an integrative perspective, they help to uncover aspects, strengthening the decision-making process in managing industrial vulnerability related to material degradation. It is worth highlighting some limitations of the dataset used, however: key information such as plant age, economic losses, human consequences, and environmental impact is only available for a portion of the recorded events. This incompleteness may reduce the depth of analyses on critical variables. The use of Bayesian Networks has made it possible to manage the uncertainty associated with missing data, but it is recognized that the lack of complete information may impact the robustness of inferences in specific areas. Finally, it is important to emphasize that the probabilities used in the model, both in the event tree analysis and in the BNs, are derived from historical data collected over a long period. Consequently, they represent an empirical synthesis of observed frequencies in the past. As also highlighted in **Figure 1.4**, the frequency and nature of incidents vary over time, occurring in parallel with the introduction of new regulations, technological innovations, and structural organizational changes. Therefore, these probabilities should not be interpreted as static estimates, but as historical indicators useful for understanding general trends and supporting comparative analyses between scenarios.

Chapter 1 Partial Conclusions

Chapter 1 explored the topic of material degradation in the process industry, analysing 3,830 historical events between 1966 and 2023. This study identified the most recurring failure mechanisms, the most vulnerable equipment, and the most frequent consequences, with a particular focus on corrosion, vibration, and fatigue.

The historical analysis confirmed that loss of containment is the most frequent scenario, with significant environmental impacts. A strong correlation emerged between equipment age and the probability of failure, reinforcing the need for predictive maintenance and risk-based inspection strategies. The application of probabilistic models such as Event Tree Analysis and Bayesian Networks allowed the estimation of scenarios even in the presence of incomplete data, contributing to a more robust management of uncertainty.

The results show that most of the data comes from the NRC database, with a predominance of events recorded in North America. In Europe, an increase in events was observed after 2000, peaking in 2019. Corrosion is the most common failure mechanism, followed by vibration and fatigue. The most affected industrial sectors are the chemical and petrochemical industries and the pipeline industry, with a higher incidence of LOCs in the Americas than in Europe. The most vulnerable equipment is primary containment systems, and over 90% of events resulted in a loss of containment. Corrosion is often associated with environmental contamination, while vibration is also linked to the release of toxic gases. Most of the substances involved present multiple risks, increasing the complexity of risk management. Over 70% of events involved facilities older than 25 years, and in 90% of cases, inspection plans were revised after the event, indicating a lack of preventive controls. The analysis showed that the likelihood of LOCs increases in older facilities, while vibrations are more common in newer ones. The two case studies analysed, despite presenting different scenarios, were both classified as medium risk, demonstrating that rare but catastrophic events can have a risk comparable to more frequent but less severe events.

The results obtained fit fully into the theoretical framework outlined in the introduction, which highlighted the importance of industrial resilience as a systemic approach to risk management. These findings directly address RQ1 and RQ2 presented in the introduction, providing a quantitative basis for classifying material vulnerabilities. Furthermore, the chapter contributes to SG1 and SQ2 by proposing operational tools to improve the resilience of industrial infrastructure.

Finally, the constructed database and the adopted methodology offer a replicable framework for future studies, with potential application in different geographical contexts and high-risk industrial sectors. The work done in this chapter represents a step towards an integrated technological risk assessment, in line with the objectives of the Seveso III Directive and the needs of a safer, more adaptive and sustainable industry.

Chapter 1 References

API (2020). American Petroleum Institute Recommended Practice 571: Damage Mechanisms Affecting Fixed Equipment in the Refining Industry. 3rd ed. Washington, DC: American Petroleum Institute.

API (2023). American Petroleum Institute Recommended Practice 580: Risk-Based Inspection 4th ed. Washington, DC: American Petroleum Institute.

BARPI (2022). The ARIA database [WWW Document]. The French Bureau for Analysis of Industrial Risks and Pollutions (BARPI). URL, https://www.aria.developpement-durable.gouv.fr/the-barpi/the-aria-database/?lang=en. (Accessed 12/2023).

Besserman, J., and Mentzer, R. A. (2017). Review of global process safety regulations: United States, European Union, United Kingdom, China, India. Journal of Loss Prevention in the Process Industries, 50, 165-183. https://doi.org/10.1016/j.jlp.2017.09.010

Bragatto, P.A., Pittiglio, P., and Ansaldi, S. (2009). The management of mechanical integrity inspections at small-sized "Seveso" facilities. Reliability Engineering & System Safety, 94(2), 412-417. https://doi.org/10.1016/j.ress.2008.04.005

Bragatto, P., and Milazzo, M.F. (2016). Risk due to the ageing of equipment: Assessment and management. Chemical Engineering Transactions, 53, 253–258. https://doi.org/10.3303/CET1653043

Bragatto, P., Delle Site, C., and Milazzo, M.F. (2017). Audit of ageing management in plants at major accident hazard. In: Proceedings of 2nd International Conference on System Reliability and Safety (ICSRS), 20-22 December 2017, pp. 400–404. IEEE, USA. https://doi.org./ 10.1109/ICSRS.2017.8272855

Bragatto, P., Milazzo, M.F., Vairo, T., Hansler, R., and Bellamy, L. J. (2022). Control of plant ageing at Seveso sites: Achievements in research and transfer to current practice. Chemical Engineering Transactions, 90, 703–708. https://doi.org/10.3303/CET2290118

Candreva, F., and Houari, M. (2013). Plant screening for ageing impact in the process industry. Chemical Engineering Transactions, 31, 253–258. https://doi.org/10.3303/CET1331043

Casal, J., 2008. Evaluation of the Effects and Consequences of Major Accidents in Industrial Plants. Industrial safety series, Vol. 8. Else vier. https://doi.org/10.1016/C2016-0-00740-4

Castro Rodriguez, D.J., Tufano, C., Vitale, M., Mietkiewicz, J., Baldissone, G., Barresi, A.A., and Demichela, M. (2023). Dataset of NaTech events triggered by lightning within the Process Industry, Mendeley Data, V2. https://doi.org/10.17632/fff64w3rzn.2

Castro Rodriguez, D.J., Mietkiewicz, J., Vitale, M., Baldissone, G., Barresi, A.A., and Demichela, M. (2024). NaTech triggered by lightning: Novel insights from past events in the process industry. Heliyon, 10, e31610. https://doi.org/10.1016/j.heliyon.2024.e31610

Castro Rodriguez, D.J, Barresi, A.A., and Demichela M. (2025). Resilience-based framework for enhancing NaTech risk management in industrial critical infrastructures. Environment Systems and Decisions, submitted.

Cazenave, P., Jimenez, K., Krishnamurthy, R., and Shall, Z. (2024). Improvement of ILI sizing accuracy for problematic corrosion profiles: A PRCI/PHMSA project. Proceedings of the 2024 15th International Pipeline Conference. Volume 2B: Pipeline and Facilities Integrity. Calgary, Alberta, Canada. September 23–27, 2024. V02BT03A042. ASME. https://doi.org/10.1115/IPC2024-134089

Čepin, M. (2011). Event Tree Analysis. In: Assessment of Power System Reliability, pp 89–99. Springer, London. https://doi.org/10.1007/978-0-85729-688-7_6

Cooper, M.D. (2018). The safety culture construct: Theory and practice. In: C. Gilbert, B. Journé, H. Laroche and C. Bieder, eds. Safety Cultures, Safety Models. SpringerBriefs in Applied Sciences and Technology. Cham: Springer. https://doi.org/10.1007/978-3-319-95129-4_5

Cozzani, V., Campedel, M., Renni, E., and Krausmann, E. (2010). Industrial accidents triggered by flood events: Analysis of past accidents. Journal of hazardous materials, 175(1–3), 501–509. https://doi.org/10.1016/j.jhazmat.2009.10.033

CSB (2022). Chemical Safety Board Investigations Database. U.S. Chemical Safety and Hazard Investigation Board. [WWW Document]. URL, https://www.csb.gov/investigations/ (Accessed 12/2023).

Davis, J.R. (2000). Corrosion: Understanding the Basics. ASM International, Chapter 2: Basic Concepts Important to Corrosion. https://doi.org/10.31399/asm.tb.cub.9781627082501

Duijm, N.J. (2015). Recommendations on the use and design of risk matrices. Safety science, 76, 21-31. https://doi.org/10.1016/j.ssci.2015.02.014

eMARS (2022). Europa - eMARS accidents search - European commission [WWW Document]. URL, https://emars.jrc.ec.europa.eu/en/emars/accident/search. (Accessed 12/2023).

JRC (2022): HIAD 2.1. European Commission, Joint Research Centre (JRC) Dataset [WWW Document]. URL: http://data.europa.eu/89h/1d6b06e9-3a89-4ec2-b051-3fb8a28eab9f (Accessed 10.23).

Fehring, T., and Reynolds, T. (2021). Boiler and Pressure Vessel Safety. Chronicles of Mechanical Engineering in the United States (Ed.Fehring,

TH, and Reynolds, TS.). ASME,2021. pp. 93-124. https://doi.org/10.1115/1.356056_ch4

Giudice, E., Kuipers, J., and Moffa, G. (2023). The dual PC algorithm and the role of Gaussianity for structure learning of Bayesian networks. International Journal of Approximate Reasoning, 161, 108975. https://doi.org/10.1016/j.ijar.2023.108975

Gyenes, Z., and Wood, M.H. (2016). Lessons learned from major accidents relating to ageing of chemical plants. Chemical Engineering Transactions, 48, 733-738. https://doi.org/10.3303/CET1648123

Hansler, R.J., Bellamy, L.J., and Akkermans, H.A. (2022). Ageing assets at major hazard chemical sites–The Dutch experience. Safety Science, 153, 105788. https://doi.org/10.1016/j.ssci.2022.105788

Horrocks, P., Mansfield, D., Parker, K., Thomson, J., Atkinson, T., Worsley, J., and Park, B. (2010). Managing ageing plant. HSE, Warrington, UK, Technical Report 823.

Kelly, B.D. (2021). Challenges to managing aging process equipment and infrastructure. Process Safety Progress, 40(4), 266–271. https://doi.org/10.1002/prs.12244

Krausmann, E., Renni, E., Campedel, M., and Cozzani, V. (2011). Industrial accidents triggered by earthquakes, floods and lightning: lessons learned from a database analysis. Natural Hazards, 59, 285–300. https://doi.org/10.1007/s11069-011-9754-3

Laurent, A., Pey, A., Gurtel, P., and Fabiano, B. (2021). A critical perspective on the implementation of the EU Council Seveso Directives in France, Germany, Italy, and Spain. Process Safety and Environmental Protection, 148, 47–74. https://doi.org/10.1016/j.psep.2020.09.064

Li X., Ma X., Zhang J., Akiyama E., Wang Y., and Song X. (2020). Review of hydrogen embrittlement in metals: Hydrogen diffusion, hydrogen characterization, hydrogen embrittlement mechanism and prevention, Acta Metallurgica Sinica (English Letters), 33, 759–773.

Marcot, B.G., Hanea, A.M. (2021). What is an optimal value of k in k-fold cross-validation in discrete Bayesian network analysis? Computational Statistics, 36, 2009–2031. https://doi.org/10.1007/s00180-020-00999-9

Marrazzo, R., and Vazzana, F. (2021). The aging challenge of hazardous installations in Italy accidents result of inspections and good practices. In: Proceedings of the 31st European Safety and Reliability Conference (ESREL), 19-23 September 2021, pp 2548–2554. https://doi.org/10.3850/978-981-18-2016-8 444-cd

Martón, I., Martorell, P., Mullor, R., Sánchez, A. I., and Martorell, S. (2016). Optimization of test and maintenance of ageing components consisting of multiple items and addressing effectiveness. Reliability Engineering &

System Safety, 153, 151-158. https://doi.org/10.1016/j.ress.2016.04.015

Milazzo, M.F., and Bragatto, P. (2019). A framework addressing a safe ageing management in complex industrial sites: The Italian experience in «Seveso» establishments. Journal of Loss Prevention in the Process Industries, 58, 70–81. https://doi.org/10.1016/j.jlp.2019.01.005

Mocellin, P., and Pilenghi, L. (2023). Semi-quantitative approach to prioritize risk in industrial chemical plants aggregating safety, economics and ageing: A case study. Reliability Engineering & System Safety, 237, 109355. https://doi.org/10.1016/j.ress.2023.109355

NRC (2022). USCG National Response Center Home Page [WWW Document]. URL, https://nrc.uscg.mil/. (Accessed 12/ 2023).

OSHA (2025). Occupational Safety and Health Administration, Process Safety Management of Highly Hazardous Chemicals (29 CFR 1910.119). U.S. Department of Labor. URL,https://www.osha.gov/laws-regs/regulations/standardnumber/1910/1910.119 (Accessed June 2025)

Poorhaydari, K. (2021). A comprehensive examination of high-temperature hydrogen attack—A review of over a century of investigations. Journal. of Materials Engineering and Performance, 30, 7875–7908. https://doi.org/10.1007/s11665-021-06045-z

Rasmussen, J. (1997). Risk management in a dynamic society: a modelling problem. Safety science, 27(2–3), 183–213. https://doi.org/10.1016/S0925-7535(97)00052-0

Ricci, F., Casson Moreno, V., and Cozzani, V. (2021). A comprehensive analysis of the occurrence of Natech events in the process industry. Process Safety and Environmental Protection, 147, 703–713. https://doi.org/10.1016/j.psep.2020.12.031

TSB (2022). The Transportation Safety Board of Canada [WWW Document]. URL, https://www.tsb.gc.ca/eng/ (Accessed 12/2023).

UNECE (2021). Globally harmonized system of classification and labelling of chemicals (GHS), ST/SG/AC.10/30/Rev.9. United Nations Economic Commission for Europe (UNECE).

US EPA (2025). United States Environmental Protection Agency, Risk Management Plan Rule (40 CFR Part 68). U.S. Environmental Protection Agency. URL, https://www.epa.gov/rmp (Accessed June 2025).

Vairo, T., Reverberi, A.P., Milazzo, M.F., and Fabiano, B. (2018). Ageing and creeping management in major accident plants according to Seveso III directive. Chemical Engineering Transactions, 67, 403–408. https://doi.org/10.3303/CET1867068

Valente, M., Ricci, F., and Cozzani, V. (2025). A systematic review of resilience engineering applications to NaTech accidents in the chemical and process

industry. Reliability Engineering & System Safety, 255, 110670. https://doi.org/10.1016/j.ress.2024.110670

Vílchez, J. A., Espejo, V., and Casal, J. (2011). Generic event trees and probabilities for the release of different types of hazardous materials. Journal of Loss Prevention in the Process Industries, 24(3), 281–287. https://doi.org/10.1016/j.jlp.2011.01.005

Vitale, M., Shi, H., Castro Rodriguez, D.J., Barresi, A., and Demichela, M. (2024). Ageing in process industry: Identification of material degradation from past accidents analysis, IFAC-PapersOnLine 58(4), 568-573. https://doi.org/10.1016/j.ifacol.2024.07.279

Vitale, M., Castro Rodriguez, D. J., Barresi, A., and Demichela, M. (2025a). Database of material degradation event within process industry, Mendeley Data, V1. https://doi.org/10.17632/6hd3xky6kb.1

Vitale, M., Rodriguez, D. J. C., Barresi, A. A., and Demichela, M. (2025b). Hydrogen Safety in Process Industry: Systematization of Past Lessons. Chemical Engineering Transactions, 116, 403-408. https://doi.org/ 10.3303/CET25116068

Wintle, J., Moore, P., Henry, N., Smalley, S., and Amphlett, G. (2006). Plant ageing: Management of equipment containing hazardous fluids or pressure. HSE, Warrington, UK, Scientific Report RR509.

2. Material Degradation and NaTech Risk: Bidirectional Vulnerability in Industrial Systems[5]

The previous chapter outlined a systematic framework of degradation mechanisms in materials used in critical industrial infrastructure, with particular attention to ageing dynamics and the effects of deterioration on structural functionality and reliability. The analysis highlighted how a thorough understanding of degradation processes is an essential prerequisite for assessing system vulnerability and guiding inspection and maintenance strategies with a view to operational resilience.

Continuing with these considerations, this chapter aims to deepen the analysis of multiple factors on material degradation, including the characteristics of the substances contained in the systems, environmental conditions, and the service life of the infrastructure. In this perspective, and with specific reference to NaTech-related issues, the findings from the historical analysis suggest the need to investigate these relationships in real-world contexts in order to understand the interactions between structural vulnerabilities and external stresses.

To this end, an emblematic case study was selected, characterized by the interaction between a latent structural defect and an extreme natural event. The analysis is conducted using consolidated tools and supported by quantitative data from a database of degradation events. The case study highlights how deterioration mechanisms can not only increase the vulnerability of infrastructure to natural events, but also be accelerated by these stresses, generating critical operating conditions. This case study sheds light on the intricate interplay between structural degradation and environmental stressors, revealing how vulnerability emerges and evolves within complex operational contexts. The results highlight how vulnerability is not a static property, but a dynamic phenomenon that evolves over time as a function of operating and environmental conditions

The chapter contributes to the achievement of scientific objective SG2 by proposing an interpretative model aimed at integrating the bidirectionality between material degradation and natural risk in vulnerability assessment.

[5] The following work was presented at NaTech 2024, 8th International Symposium on Natural Hazard-Triggered Technological Accident, Trondheim 1-2 July 2024.
Portions of this chapter have been published in preliminary form in:
Vitale M., Barresi A.A., Demichela M. (2025). Material Degradation and NaTech Risk: A Case-Study to Discuss Bidirectional Vulnerability in Industrial Systems. *Applied Sciences.* Under review.

Specifically, it aims to answer research question RQ2 by exploring how knowledge of deterioration mechanisms can support the development of prevention strategies and resilience-building in industrial infrastructure.

In this way, the chapter consolidates the systemic and adaptive perspective of industrial resilience, consistent with the theoretical and methodological framework outlined in the introduction and contributes to the development of interpretative tools useful for the integrated management of technological risk in contexts exposed to environmental stresses.

Considering the above, the focus is on NaTech (Natural Hazard Triggering Technological Accidents) events, which represent a particularly relevant area for the integrated analysis of structural degradation and environmental risk.

NaTech events simultaneously involve natural phenomena and technological risks, generating significant impacts on the environment and public safety. Krausmann et al. (2011) highlighted how such events represent an increasing criticality for industrial plants, while Valente et al. (2025) analysed the application of resilience engineering to improve risk management in complex scenarios. Several recent studies have addressed the topic of NaTech risk with complementary approaches. Cruz et al. (2017) proposed structural measures to reduce the impact of natural events on industrial plants. Naderpour and Khakzad (2018) analysed the domino effects triggered by natural disasters, highlighting systemic vulnerability. Ibrion et al. (2020) offered a life-cycle analysis perspective, studying structural resilience in nuclear contexts. Laor and De Vivo (2022) introduced predictive methods for environmental risk management, based on deterministic approaches. Ju and Xing (2024) integrated machine learning and GIS techniques for spatial risk mapping. Finally, Reichstein et al. (2025) proposed an artificial intelligence-based framework for early warning in complex climate scenarios. In the European panorama, the inclusion of the evaluation of NaTech scenarios in Seveso plants was introduced by the third revision of the Directive (2012/18/EU). Already in previous version the Directive required to provide detailed information on the meteorological conditions of the area, along with a chronological record of any past geophysical and hydrogeological event for the companies that had to prepare a safety report (Upper Tier). In this last version, these requirements have been deepened, requiring to identify and describe major accidents that may occur, including natural causes such as earthquakes and floods. NaTech risks were also explicitly addressed within the aspect to control in the Safety Management Systems, that pertains non only to Upper Tier plants, but also to Lower Tier Ones.

The increasing frequency and complexity of NaTech events has stimulated scientific interest, highlighting the need to delve deeper into the dynamics of interaction between extreme natural phenomena and technological vulnerability. Several studies have focused on historical incidents, with the aim of identifying relations and connections between the industrial sectors affected by the natural phenomena and the substances involved in these events. In the classification described by Ricci et al. (2021), NaTech events are divided into four categories. The research collected a set of data including 9100 incidents that occurred in the previous 70 years, with the aim of analysing the trend of NaTech events, their

geographical distribution, the technological scenarios involved and the related consequences. The study highlights that meteorological events represent the most recurring category, while the geophysical ones are responsible for the greatest losses, both in human and economic terms. This approach aims to provide a deeper understanding of the risk patterns and dynamics that characterize such incidents. Ricci et al. (2023) studied the impacts of cold waves within the process industry. In detail, they examined the categories and specific elements most influenced, investigating the recurring causes, the losses recorded, and the substances involved in these situations. Furthermore, their work included an indepth analysis of safety barriers, assessing the likelihood of these barriers to fail in the presence of cold waves. Castro Rodriguez et al. (2023) have developed a repository that collects all accidents, caused by lightning, present in the main available databases. Likewise, Castro Rodriguez et al. (2024) conducted an analysis of previous lightning accidents, providing a notable contribution to the design, risk assessment, inspection, and implementation phases of lightning protection measures.

Equipment conditions can amplify the consequences of these events. Material degradation emerges as a crucial element in NaTech risk assessment and management. Despite this, an aspect that has received limited attention in the literature is the link between material degradation and NaTech events. The concept of bidirectional vulnerability describes the mutual influence between degradation and natural stresses: indeed, structural deterioration can amplify the infrastructure vulnerability to external events, while environmental stresses can accelerate degradation processes, generating critical and potentially unstable operating conditions. Over time, infrastructures undergo structural deterioration due to factors like corrosion, wear, tear, and material fatigue. Such degradation reduces structural resistance to natural hazards like earthquakes or storms, increasing the likelihood of failure (Majidian and Di Sarno, 2025). Older infrastructures may lack effective design considerations for handling NaTech events, emphasizing the need to assess and enhance their resilience to such scenarios. This approach is critical to ensure the safety of infrastructures in an context of everevolving Natech risks. In addition to triggering technological failures, NaTech events can intensify existing degradation processes, increasing the likelihood of structural failure. For example, floods or overflows can cause rapid corrosion or physical damage to the infrastructure, further increasing the risk of structural failure. The interplay between NaTech events and material ageing is complex and must be integrated into risk assessment procedures to enable effective prevention. Indeed, Pilone et al. (2022) proposed to use a NaTech index based on two factors, one of which concerns the vulnerability of each element and includes obsolescence.

Despite the growing attention to NaTech scenarios and the everincreasing availability of industrial accident databases, the scientific literature still lacks an integrated framework that explicitly addresses the dynamic interaction between material degradation and natural hazards. Most studies tend to treat these phenomena separately: degradation is often analysed in the context of ageing or mechanical failure managing, while NaTech risk is predominantly addressed from

a perspective focused on the initiating event or its consequences. This fragmentation limits the ability to capture the synergistic effects that occur when structural deterioration and environmental stresses occur simultaneously, representing a methodological limitation in understanding industrial vulnerability. The research problem addressed in this study concerns precisely the lack of an integrated framework that considers the dynamic interaction between environmental stresses and structural defects. The integration of these two areas in a conceptual framework allows for a more realistic representation of systemic vulnerability and supports the early identification of critical conditions. This chapter aims to fill this gap by proposing an interpretative model that integrates material degradation into the assessment of vulnerability to NaTech events, with the goal of improving the understanding of the mechanisms that generate bidirectional vulnerability. This dynamic interaction, often overlooked in traditional models, represents a key factor in defining systemic risk in industrial contexts exposed to environmental stresses.

From an applied perspective, the proposed approach offers a contribution to industrial risk management, enabling the integration of degradation indicators into NaTech vulnerability models, the early identification of systemic risk conditions, and the development of prevention strategies to strengthen infrastructure resilience. The study also explores the influence of multiple factors on material degradation, including the characteristics of the substances contained in the systems, the environmental conditions, and the service life of the infrastructure. By adopting a bidirectional perspective, the research contributes to the development of a holistic and operational approach to industrial risk management in environments exposed to natural stresses, consolidating a systemic and adaptive vision of resilience, consistent with the aim of the thesis.

2.1 Case Study and Analytical Approach

To illustrate the bidirectional interaction between material degradation and NaTech risk, the chapter presents the analysis of a representative case study relating to a critical energy infrastructure. The selected event combines a latent structural defect, developed during construction, with an extreme natural event, offering a concrete example of how degradation and environmental stress can interact. The case was chosen from the inventory of ageing events in which structural deterioration occurred in conjunction with extreme natural events. The aim is to use the case study to highlight how degradation mechanisms can amplify NaTech risk, and vice versa.

2.1.1 Case Study Selection

Among the events identified in the inventory (Vitale et al., 2025) analysed in **Chapter 1**, a representative case involving a cold-triggered failure due to latent degradation was selected. A detailed description is provided in **Section 2.2.1**.

The selection was guided by criteria of technical relevance, availability of detailed information, and clarity in reconstructing the causal dynamics. The selected event offers important insights into the vulnerability of industrial

infrastructure and their ability to respond to complex scenarios. Specifically, the observed dynamics can provide useful insights to better understand the implications of material degradation in terms of loss of containment and operational resilience, thus contributing to the construction of a more integrated view of risk in contexts exposed to NaTech events.

2.1.2 Root Cause Analysis

To carry out an accurate analysis, a detailed reconstruction of the selected case study was initially conducted, with the aim of identifying the causes that contributed to the accident and understanding the dynamics that led to the escalation of the event. In this phase, a fishbone diagram, also known as Ishikawa or cause-and-effect diagram, was used. This technique is useful for visually representing the possible causes of a specific problem, organizing them into logical categories that branch out from a central axis, where the unwanted effect is reported. The diagram reveals how different variables interact, providing a systemic view and helping identify critical areas for further investigation (Slameto, 2016).

Subsequently, a more in-depth analysis was conducted to investigate the relations between material degradation and natural hazards. In this phase event historical analysis was conducted, a process that involves the examination of incidents that have occurred in similar industrial settings to identify correlations, recurring trends, and a raw estimation of expected frequencies. This approach allows the determination of the root causes, circumstances, and dynamics that led to the event, providing useful insights for improving risk management and preventing the recurrence of similar scenarios.

Finally, further analysis was carried out to explore how material degradation and natural events can influence each other. The goal was to delve deeper into the effect of structural deterioration on infrastructure vulnerability and, consequently, understand how this vulnerability can alter the risk profile in NaTech scenarios. This integrated approach allows for a more complete and nuanced view of the complexity of risk, offering useful insights for future considerations regarding the resilience of industrial facilities.

The choice of the Ishikawa diagram as a root cause analysis tool is motivated by its ability to visually and systematically represent the causal relationships between technical, operational, and environmental factors. This approach highlights the interactions between latent defects and external conditions, facilitating the identification of structural vulnerabilities. Event historical analysis was selected for its effectiveness in exploiting lessons learned from occurred accident dynamics based on historical data in similar contexts. The integration of these methods allows for a multidimensional interpretation of the event, consistent with the aim of this study to analyse bidirectional vulnerability in multifactorial scenarios.

2.1.3 Summary of the Interpretative Model

The interpretative model proposed in this study is based on a conceptual

framework that integrates two complementary analytical tools, the root cause analysis and the factor analysis, into a methodology for assessing bidirectional vulnerability in industrial systems.

- Root cause analysis, using Ishikawa diagrams, allows the construction of the causal dynamics of the event, highlighting the interactions between latent defects, operating conditions, and environmental factors.
- Factor analysis identifies and classifies the internal and external factors that influence material degradation, providing a basis for assessing structural vulnerability.

These tools are not used separately, but in synergy within the conceptual framework. In this integrated approach, the conceptual framework guides the systemic interpretation, the factor analysis supports the understanding of the critical variables, and the causal diagram allows the visualization of the connections between the different elements. Together, they form an integrated methodological approach, useful for diagnosing vulnerability and planning preventive and resilient strategies.

2.2 Case Study Results and Interpretative Insights

The analysed event, extracted from the Transportation Safety Board of Canada database (TSB, 2022), is examined in relation to the operating conditions, the technical characteristics of the system involved, and the environmental context, to highlight the interaction between structural degradation and natural stresses in the genesis of the failure.

The analysis focuses on the sequence of events that led to the failure, with particular attention to the material degradation mechanisms and the role played by natural stresses. Through a technical reconstruction and an assessment of the root causes, the aim is to provide an integrated interpretation of the event, useful for understanding the interactions between structural and environmental factors in NaTech scenarios.

2.2.1 Event description

At approximately 01:15 Central Standard Time on January 25, 2014, a natural gas pipeline rupture and ignition occurred in the vicinity of Otterburne, Manitoba, Canada. As a result, a crater approximately 24 meters long and 12.5 meters wide was formed, caused by an explosion, with debris projected approximately 100 meters from the crash site (**Figure 2.1**). The technical data of the Otterburne case are reported in **Table 2.1**, which also summarises the main parameters and the evidence emerging from the analysis.

Figure 2.1: Uplift of the valve and pipeline section following rupture and explosion. Photo credit: courtesy of Transportation Safety Board of Canada (2014).

Table 2.3: Parameters and evidence of the Otterburne case analysed.

Parameter	Value / Description
Event Date	January 25, 2014
Location	Otterburne, Manitoba (Canada)
Infrastructure Type	Natural gas pipeline
Age of facility	Installed in 1960, 54 years old at the time of the event
Current operating pressure	6330 kPa
Ambient temperature	–26°C, coldest winter since 1898
Defect Type	Hydrogen embrittlement
Deterioration Mechanism	Hydrogen embrittlement and mechanical fatigue
Natural trigger	Cold wave
Consequences	Pipe rupture, explosion, 12-hour fire, evacuation of 5 homes
Previous Inspections	MFL in 2001 and 2009; excavation in 1997–1999; no post-installation inspection of the defect
Components Affected	Valve and 11-meter section of pipe

The natural gas continued to burn for about 12 hours. In response to the event, five homes in the immediate vicinity were evacuated, and the provincial road remained closed until the fire was completely extinguished. Fortunately, no injuries were reported. Before the event, the system was operating normally, with an operating pressure at the event site of approximately 6330 kPa. The maximum

operating pressure for this section of the system was 7030 kPa. The event happened in an agricultural land; the area was sparsely populated. Due to lack of customer demand, gas flow in the pipeline was interrupted starting January 5, 2014. However, static pressurized gas was still present in the line between the two closed valves. The line had undergone hydrostatic testing when the pipeline was originally placed in service in 1960. No other pressure tests had been performed since then. Records of welding and non-destructive testing dating back to the commissioning had not been retained. Internal inspections of the line were performed as follows: in 2001, the pipeline was inspected using a gage instrument and a high-resolution magnetic flux dispersion (MFL) instrument. In 2009 the pipeline was inspected again using a high resolution MFL instrument. The following integrity-related activities were conducted in proximity of the incident: in 1997, a single excavation was performed 9 meters downstream of the line to inspect for external corrosion. Subsequently, in 1998, 1999, and 2009, a series of investigative excavations took place in adjacent sections of the valves to confirm the presence of external corrosion and stress corrosion cracking (SCC). The nearest excavation site was situated approximately 3 km downstream from the line. As a result of the 1999 excavations, a 38-meter segment of the pipeline located on the line was cut and replaced due to the identification of SCC. The line rupture occurred around 1 meter north of the first valve, resulting from a brittle fracture originating in a pre-existing crack. This crack is presumed to have developed during the pipeline construction phase due to an inadequate welding procedure and poor welding quality, leading to hydrogen cracking. In this context, the hydrogen is not related to the transported substance, which was methane, but was introduced locally during welding operations, where it remained trapped in the metal structure, generating HE cracks. Amazingly, the weld defect remained stable for over 50 years before failing. As a result of the failure, the first valve and an 11-meter-long section of pipe to the south rose, causing a sharp bend at a circumferential weld at the top of the pipe, thus causing a secondary failure. The release of natural gas from the pipeline triggered an explosion, and the resulting fire lasted about 12 hours.

During the accident, the recorded temperature was –26°C, accompanied by light winds coming from the north. That winter, southern Manitoba was facing extreme weather, marking one of the coldest winters since 1898. Following the accident, a thorough examination of the site was conducted, which revealed the following considerations: the ground support in the vicinity of the site may have suffered weakening due to repeated excavation and backfilling activities over the years, as part of the facility standard repair and maintenance practices. Due to the extremely low temperatures recorded during the exceptionally cold winter experienced in southern Manitoba, frost in the ground likely penetrated deeper than normal. Maintenance work carried out in January 2014 in and around the site may have helped push the frost even deeper into the ground. Finally, thermal contraction may have taken place as the pipeline, without gas flow for 20 days, cooled. The accident was triggered by an initial crack generated during the welding process due to hydrogen. The section of pipe involved exhibited a significantly higher level of hardness, giving it greater brittleness than the base

steel. Further minor cracks were also identified in other points of the pipe. The movement of the ground and the cold wave caused the pipe to collapse, leading it to rise and causing the gas to escape, generating an explosion and a consequent fire.

The Otterburne case occurred in a rural area of southern Manitoba, characterized by extreme climate conditions and low population density. This location contributed to the underestimation of environmental risk during the design phase, particularly regarding protection against cold spells. The main problem that emerged was the presence of a latent structural defect, caused by inadequate welding, which remained undetected for over fifty years. The event highlighted how the lack of post-installation checks and targeted preventive strategies can compromise the resilience of the infrastructure. Operational implications suggest the need to integrate obsolescence and environmental vulnerability criteria into inspection and maintenance programs, with particular attention to infrastructure exposed to extreme climate conditions.

2.2.2 Contributing Factors Analysis

The Otterburne accident highlights the importance of considering materials degradation during a NaTech event, as the combination of both led to the pipe explosion. The cause-and-effect diagram depicted in **Figure 2.2** provides a clear illustration of the causes of the accident. The Ishikawa diagram for the Otterburne pipeline accident classifies the causes into four main categories, each represented by a branch highlighting specific contributing factors:

- Maintenance and inspection: Maintenance activities carried out prior to the accident caused soil displacement, altering stability and contributing to mechanical stress on the structure.
- Environmental conditions: An exceptional cold snap caused frost to penetrate the ground, amplifying the material fragility and promoting crack propagation.
- Operational factors: Gas loading and unloading cycles generated pressure fluctuations that increased mechanical stress on the pipeline.
- Construction and quality: During the construction phase, poor quality procedures were employed, including inadequate welding practices and deficient post-installation inspections, which promoted hydrogen embrittlement and the presence of latent defects.

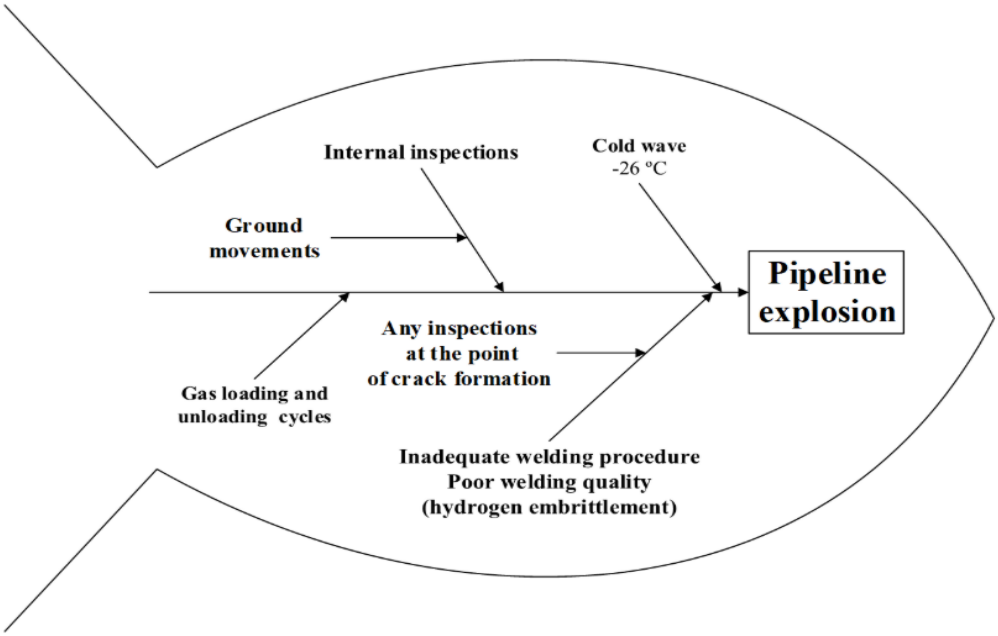

Figure 2.2: Fishbone diagram illustrating the root causes and contributing factors of the Otterburne pipeline accident.

Hydrogen embrittlement (HE), although it had occurred 50 years earlier, had not caused significant damage during the years. However, it was the natural event that triggered the breakup. In this situation, it emerges that although the inspections were conducted, their effectiveness was limited and they were incomplete, as the fracture dates to the construction period of the pipe, which was not adequately monitored after the installation. Furthermore, the lack of protection systems against extreme natural events is highlighted. This is a deficiency that should have been carefully evaluated during the design phase, especially considering the harsh climatic conditions of the area in which the infrastructure is located. Additionally, the accident underscores the significance of substances interacting with the material, as certain materials can expedite the degradation process. Indeed, in this scenario, the failure could have been avoided by adopting appropriate welding procedures and performing post-installation checks. Poor quality control during construction allowed a latent defect to remain undetected for over fifty years, eventually failing under extreme environmental stress. This highlights how quality management during the construction phase represents a crucial element in preventing long-term failures, especially in infrastructure exposed to extreme environmental risks.

To further explore the interaction between internal and external factors in the failure process, it is useful to distinguish the specific contribution of welding defects and extreme environmental conditions. The welding defect, generated during the construction phase, represented a latent structural weakness that remained stable for over fifty years. However, the extreme natural event acted as a trigger, inducing thermal contractions and mechanical stresses that favoured crack propagation. Although the Otterburne case is well documented, there are no specific quantitative models describing the coupling effect between material degradation and environmental stresses. This is mainly due to the retrospective nature of the event and the lack of detailed and continuous operational data over

time, such as thermal stress measurements, pressure variations, or structural inspection parameters. Furthermore, the welding defect was latent and unmonitored, making predictive modelling based on historical data difficult. The literature proposes probabilistic approaches and vulnerability indices that integrate structural and environmental parameters, such as the NaTech index proposed by Pilone et al. (2022), which considers obsolescence as a vulnerability factor, but does not include specific environmental variables such as the frequency of temperature excursions. For real cases such as Otterburne, integrated models based on multi-source data (historical, climatic, structural) and predictive analytics techniques would be necessary.

To explore the causes in more depth, an analysis was performed on past incidents related to material deterioration. Hydrogen embrittlement is a process in which hydrogen penetrates the interior of a material, compromising its ability to resist fracture under stress (Li et al., 2020). Once inside the structure of the material, hydrogen can cause the formation of micro-fractures and cracks, which can lead to sudden failure or breakage of the material.

According to Vitale et al. (2026) the hydrogen embrittlement is an autonomous category among material degradation mechanisms, highlighting its specificity and relevance in critical contexts. However, the data show that this phenomenon represents only 0.3% of the total events analysed. This limited occurrence is likely due to the current low level of hydrogen utilization as an energy carrier in the process industry, thus limiting systemic exposure to this risk. Despite this, HE occurs predominantly in highly critical components: 93% of the events involved Primary containment system, while 7% involved Control & Mitigation Measures. From a sectoral perspective, the phenomenon is mainly concentrated in the Chemical & Petrochemical (71%), followed by Manufacturing (21%) and, to a much lesser extent, Pipeline (8%). This specific finding is especially noteworthy when considered in conjunction with the case study discussed: indeed a transport infrastructure was subjected to a structural failure attributable to a hydrogen embrittlement mechanism.

In the case study, the pipeline cracked during installation, but the raising of the equipment occurred after 50 years. This behaviour is also confirmed by the data from the analysed database. Indeed, among the reports in which hydrogen embrittlement was identified as the cause of the event, 43% did not indicate the age of the plant. However, considering only the cases for which such information is available, 63% of the events occurred in plants older than 25 years. This data reinforces the hypothesis that hydrogen embrittlement, while potentially originating during the construction phase, tends to manifest itself critically only after long periods of operation, in the presence of environmental or operating conditions favourable to the propagation of the damage.

The gas flow on Line 400-1 was interrupted on January 5, 2014, due to reduced demand, as reported in the official incident record. Although gas was not flowing at the time of the event, the pipeline was still under static pressure between the closed valves. However, over the operational life of the infrastructure, the pipeline was subject to pressure fluctuations related to demand variability, which may have contributed to the onset of long-term mechanical fatigue. These

cycles could have contributed to stressing the material over time, favouring the occurrence of failure. This phenomenon is a deterioration mechanism known as material fatigue and has been identified in the analysis of past events as being involved in only 4% of previous incidents, but its implications are significant and should not be overlooked. The industrial sectors most affected by fatigue are the Chemical & Petrochemical and Storage & Warehousing, which account for 72% of reports. Only 7% of events involve Pipeline. It is important to note that fatigue is not determined by the chemical nature of the substances involved but is a mechanical phenomenon. Among the mechanisms analysed, this is the only one whose most common final result is release without further consequences. This further highlights the mechanical aspect of fatigue, which develops over time. Indeed, more than half of the plants where the fatigue phenomenon occurred are more than 25 years old.

The incidental event examined in this study also involves an extreme natural event, as shown in **Figure 2.2**, the anomalous cold waves. Ricci et al. (2023) highlighted that industrial sites are more susceptible to cold climate impacts than to heat waves. Low temperatures are the third leading cause of NaTech accidents in Europe, following lightning and floods. It is important to note that the perceived risk related to such accidents is significantly underestimated by the European population. In the industrial context, the Chemical & Petrochemical sector is particularly vulnerable to accidental events caused by cold waves (38% of events), mainly due to the widespread use of dangerous substances. Pipes represent the component of the system most affected by cold waves, contributing to 39% of recorded events. Furthermore, the transportation sector, especially through pipelines, is identified as the second most affected category (18% of events). This frequency is attributed to the significant impact of cold waves in causing accidents during the transportation of hazardous substances, confirming the high vulnerability of transportation systems and infrastructure to the effects of these adverse weather conditions. Extreme weather conditions linked to cold waves add further risk factors, such as ice formation on transport infrastructure. The study highlights several major direct causes of NaTech events occurring during cold spells in the process industry, included in the analysed dataset. These include equipment failures caused by low temperatures exceeding the brittle transition temperature of some materials, contributing to 16% of recorded events. Through the phenomenon known as cold fatigue, materials can be impacted over time. This process of degradation occurs when materials are subjected to repeated cycles of mechanical loading under low-temperature conditions, particularly during cold waves. As in the Otterburne pipeline accident, during a cold wave, materials can become more brittle, making them susceptible to fracture even under relatively modest mechanical stresses.

The previously analysed event clearly highlights that the management of material degradation and NaTech risk are currently not adequately handled, with insufficient inspections and a lack of preventative approaches. Indeed, the accident was caused by a latent welding defect that had not been detected or adequately monitored. This confirms that even localized imperfections, if neglected, can interact with extreme natural stresses and lead to catastrophic

failures even decades later. The case thus illustrates the central message of this work: material degradation and NaTech risks must be assessed together, as their bidirectional interaction can critically amplify the vulnerability of infrastructure. Indeed, structures that are not adequately monitored and maintained to prevent material degradation could be more vulnerable and prone to failures in natural event situations. This gap in material degradation management is a critical factor that should be explicitly addressed in NaTech risk assessments. These two factors can interact synergistically, contributing to an increase not only in magnitude, as the deterioration of infrastructure could intensify the severity of such incidents, making them more dangerous or difficult to manage, but also in frequency. Indeed, it is important to consider the consequences of accidental events caused by material degradation, as they can have a significant impact on the environment. The quantitative data discussed Vitale et al. (2026) provide context for interpreting this case. For example, loss of containment accounts for over 90% of degradation-related events, and 60% lead to environmental contamination. Accidental releases of hazardous substances may result in soil, air, and water contamination, posing long-term environmental risks. This form of environmental contamination can generate long-term impacts on the climate. These data demonstrate that degradation-related failures are not isolated anomalies, but part of a systemic framework with significant implications. Integrating this evidence into NaTech risk models allows for more realistic vulnerability assessments and better targeting of inspection priorities. This contributes to a more informed and systemic approach to industrial safety, oriented towards prevention and resilience.

As widely debated in scientific literature, climate change is related to an increase in the frequency and intensity of such events, contributing to making natural risk more significant and alarming.

This is depicted in **Figure 2.3**, which shows the scheme devised in the study conducted by Pilone et al. (2017), integrating the notion of material degradation and its influence on NaTech risk.

Figure 2.3 represents the conceptual model of bidirectional vulnerability, enriched with graphical elements that enhance its analytical capacity. The three main domains are color-coded: orange highlights the effects of environmental contamination, blue highlights those associated with NaTech risk, and red highlights those resulting from material degradation. The directional arrows represent the causal relationships between model domains and vary in thickness to indicate the intensity of their influence. Specifically, thicker arrows correspond to high-intensity interactions, i.e., phenomena that generate immediate and significant effects on the system, such as the accidental release of hazardous substances or the NaTech escalation. Conversely, thinner arrows represent low-intensity influences, typically associated with slow, cumulative, or indirect processes, such as progressive corrosion or the alteration of the mechanical properties of materials over time. This visual coding allows for the distinction between acute and chronic impact mechanisms. and supports the integration of degradation indicators into NaTech vulnerability models, providing a foundation for future quantitative developments.

Moreover, the diagram emphasizes the cyclical and interconnected nature of

the three domains. Each element can act as both cause and effect, generating a systemic vulnerability loop. Environmental contamination can increase the frequency and intensity of extreme natural events, which accelerate material degradation processes. Degradation, in turn, can compromise the structural resistance of infrastructure and contribute to the release of hazardous substances, further fuelling environmental contamination and closing the cycle.

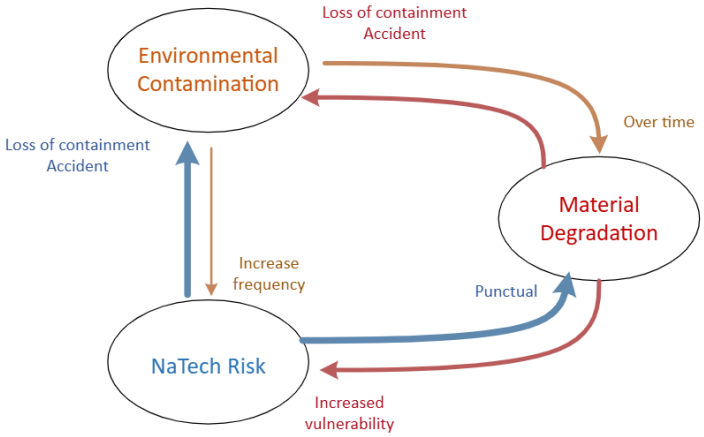

Figure 2.3: Conceptual model of the bidirectional relationship between material degradation and NaTech risk. The colours distinguish the risk domains; the thickness of the arrows represents the intensity of the causal influence, from indirect effects to acute impacts.

Therefore, from **Figure 2.3** emerges that natural events can influence material degradation in short timescales, material degradation can influence natural events, but the impact on frequency occurs much more slowly and gradually. Therefore, during the risk analysis, it is essential to consider the state of infrastructure on the consequences of natural events. Consequently, it is crucial to incorporate this factor into the NaTech risk assessment.

As mentioned before, Pilone et al. (2022) developed a NaTech index to evaluate the risk associated with natural events that can cause technological accidents. This index is based on two main factors, one of which concerns the vulnerability of infrastructure elements. This vulnerability is assessed by considering several factors, including the location of the infrastructure, its exposure to risks from earthquakes, floods, storms, and fires, as well as the obsolescence of the infrastructure. However, the calculation methodology adopted is limited to a binary evaluation (presence/absence), without taking into account all the conditions that could influence the deterioration of the material to which the element is subject. The degree of potential deterioration of the material over time, based on the conditions to which it is exposed, should be incorporated into the analysis. Assessing material degradation and planning an inspection program requires a comprehensive understanding of the interactions between the materials used and the surrounding environment, incorporating both factors internal and external to the plant, as shown in **Figure 2.4**. The graph was developed in line with previous research (Castro Rodriguez et al., 2022). From the diagram it emerges that the factors positioned in the upper part can have a negative impact on

the degradation of the material. Internal factors include the operating conditions of the process, the nature of the materials used in the plant and their age, and the substances contained. In the Otterburne case, for example, pressure variations due to the discontinuity of the gas flow contributed to the mechanical stress of the material, favouring crack propagation. On the other hand, external factors are related to the geographical location of the facility. These include the environmental conditions of the surrounding area and potential exposure to natural events.

Spells and frost penetration into the ground, can accelerate material degradation; in the case analysed, extreme climatic conditions acted as catalysts, inducing thermal contractions and stresses that led to structural failure.

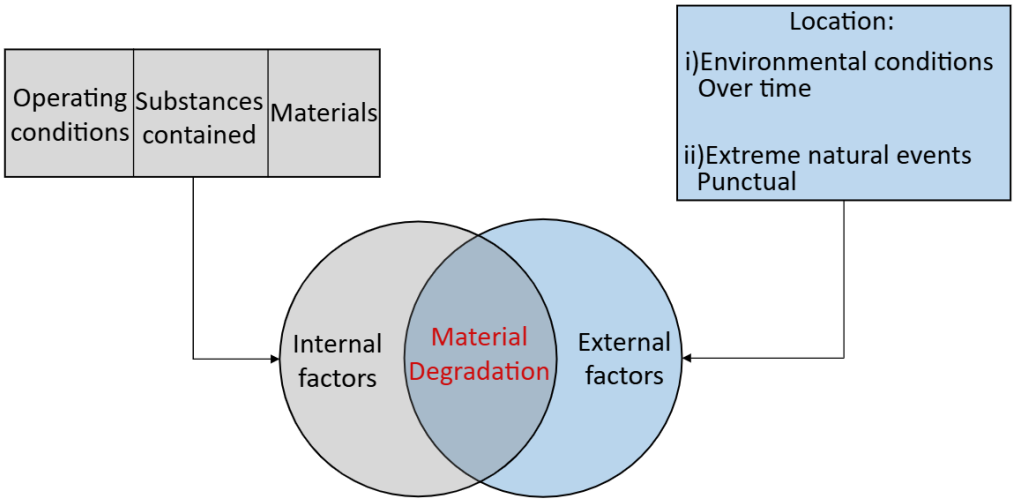

Figure 2.4: Internal and external factors contributing to material degradation in industrial infrastructures.

Thus, internal factors are intrinsic to the process and materials of the plant itself, while external factors are linked to the geographical location and surrounding environmental conditions, including natural events. A thorough understanding of both is essential for a complete and accurate assessment of the risk of material degradation and for the design of preventive maintenance programs. This approach improves the resilience of industrial structures to NaTech events, effectively reducing the risk of failures and significantly contributing to general operational safety.

2.2.3 Internal Factors

As previously discussed, material degradation can be accelerated by factors internal to the plant. Three key components are identified as significant contributors to this accelerated process: i) the operating conditions, ii) the structure materials and iii) the substances contained in the plant.

Operating conditions refer to the process variables within the plant, such as temperature, pressure, flow rate and other operating parameters. These conditions and their variation can significantly affect the durability and integrity of the materials used. As highlighted in the previous work, primary containment systems are the equipment most frequently involved in degradation events, accounting for over 90% of the cases analysed. These systems are subject to cyclic stress due to

fluctuating operating conditions. Furthermore, the analysis by industrial macro-sector shows that the Chemical & Petrochemical sectors, as well as Pipeline, are particularly vulnerable to these mechanisms, precisely because of the complexity of the processes and the aggressive nature of the substances handled.

In the analysis, it is essential also to consider the materials selected for the system and their age, since they can interact in various ways with the surrounding environment and respond differently to external stresses. Therefore, for effective safety management, it is essential to conduct a detailed study of the material used, fully understanding all its characteristics. However, in the Otterburne case, detailed technical data on the metallurgical properties of the material used or its evolution over time are not available. This limitation prevented an indepth quantitative analysis of the material behaviour, necessitating a qualitative approach based on official sources and historical data.

The chemical and physical nature of the substances treated in the plant represents another critical internal factor in material degradation processes. The analysis conducted in Vitale et al. (2026) highlighted a significant correlation between the characteristics of the substances contained in the systems and the observed degradation mechanisms. The case study analysis confirms this trend: the substances contained within or in contact with the equipment played a decisive role in triggering or amplifying the degradation phenomenon, highlighting the need to carefully consider the compatibility between materials and process substances during the design and management of the plants.

As illustrated in **Section 2.2.2**, HE is a critical degradation mechanism with a low occurrence frequency. This process, widely documented in the literature, involves complex mechanisms of physical and chemical absorption, as well as hydrogen dissolution within the crystalline structure of metals, with significant effects on tensile strength, fatigue, and fracture toughness (Dwivedi and Vishwakarma, 2018). This characteristic makes hydrogen a particularly difficult substance to store and manage safely, especially in facilities subject to mechanical or environmental stress. In the Otterburne case, the failure was triggered by HE phenomena that developed during the welding process. Although the pipeline transported natural gas and not hydrogen, the fracture, originated during the pipe construction, remained stable for decades, until it propagated under extreme environmental stresses. This demonstrates how degradation mechanisms generated during construction can manifest themselves many years later, under unfavourable environmental conditions.

2.2.4 Environmental and Geographical Influences

The geographic location of an industrial facility is a key factor in assessing the risk and durability of infrastructure, although it often receives less attention than other technical factors (OECD et al., 2024). However, the environmental and climatic context in which a facility is located can significantly influence the degradation mechanisms of materials and the overall weakness of the system.

Different geographic areas are subject to variable environmental conditions, such as extreme temperatures, high humidity, temperature fluctuations, or

recurring natural events such as floods, earthquakes, and cold waves. These factors can accelerate corrosion, embrittlement, or erosion, compromising the structural integrity of equipment. For example, in cold climates or climates subject to cold spells, as demonstrated in the Otterburne case, materials may be more vulnerable to embrittlement, while higher corrosion rates are observed in hot and humid environments. In marine or coastal environments, the presence of salty air and constant humidity promotes atmospheric corrosion, while in arid areas, wind erosion can damage exposed surfaces. Urban air pollution can also contribute to degradation through the action of aggressive chemical agents.

Furthermore, the nature of the soil and proximity to seismic faults can increase structural risk, affecting the stability of foundations and the dynamic response of the facility. Infrastructure located in flood-prone areas faces challenges related to soil saturation, loss of bearing capacity, and accelerated corrosion due to prolonged contact with water.

Geographic location also affects the likelihood and intensity of NaTech events, amplifying exposure to complex accidental scenarios. Mesa-Gómez et al. (2021) highlight a critical gap in current NaTech quantitative risk analysis methodologies, emphasizing that the geographical location of the plant is not adequately considered in the risk assessment process, despite its direct influence on exposure and vulnerability. Therefore, a truly holistic risk assessment must integrate both chronic environmental factors, which act over the long term, and acute factors related to extreme natural events. This approach allows for the development of more effective prevention and management strategies, improving the structural and operational resilience of facilities over time.

2.2.5 Systemic Vulnerability

In light of the evidence presented in the previous Sections, it is clear that structural vulnerability cannot be considered a static attribute, but rather a dynamic condition that evolves over time (IPCC, 2023) as a function of the interaction between internal and external factors. The case study analysis has shown how the degradation of materials, often latent and progressive, can significantly amplify the effects of extreme natural events, generating complex and highly severe accident scenarios. In this context, vulnerability emerges as the result of two pressures: on the one hand, the operating conditions and intrinsic characteristics of the system; on the other, the environmental and geographical context in which the infrastructure is located, which can expose it to recurrent or exceptional natural phenomena.

In the context of NaTech risk, vulnerability represents the convergence between system exposure and fragility. It manifests not only in the presence of acute events but can also derive from chronic pressures that act over time, progressively compromising the ability of the system to resist and adapt. For this reason, its assessment requires a systemic approach capable of integrating information on the life cycle of materials, operating conditions, and the evolution of the local context.

Recent studies have shown that the combination of corrosion and subsequent

seismic stresses (aftershocks) can drastically reduce the structural resilience of industrial plants, doubling the annual damage rate and significantly increasing life cycle costs (Majidian and Di Sarno, 2025). In particular, structural components subject to corrosion are more prone to collapse than nonstructural components, highlighting the urgency of targeted and timely maintenance strategies.

Managing vulnerability requires early identification through monitoring, predictive maintenance, and resilient design. Only an integrated view of internal and external factors can reduce systemic risk and strengthen the infrastructure ability to withstand adverse events. In this sense, adopting predictive maintenance techniques during the design phase, as suggested by Kubba (2010), allows for the early identification of structural and environmental criticalities, reducing intervention costs and increasing operational sustainability.

Therefore, it is essential to recognize how material degradation can amplify the consequences of extreme or prolonged events. This highlights the need for effective risk management strategies and targeted interventions to preserve structural integrity over time and prevent serious damage in critical situations. Although the analysis conducted does not aim to define operational guidelines, it provides useful elements to guide future methodological and applicative reflections, contributing to the construction of a more informed and systemic interpretative framework of industrial vulnerability in contexts exposed to NaTech risk.

The main contribution of this study lies in the integration of material degradation and NaTech risk, which enables a systemic understanding of technological risk in contexts exposed to extreme natural events.

However, the study has some limitations: the retrospective nature of the case, the lack of continuous quantitative data, and the absence of specific predictive models for degradation in critical environmental conditions.

Going forward, it will be necessary to validate the model in other industrial contexts, develop quantitative vulnerability indicators, and propose regulatory updates that include obsolescence and degradation parameters in risk assessment criteria. These elements are essential to strengthening the resilience of industrial infrastructure and improving risk management in multifactorial scenarios.

2.2.6 Application of the Bidirectional Vulnerability Model to the Otterburne Case

The conceptual model presented in **Figure 2.3** describes bidirectional vulnerability as the dynamic interaction between material degradation and NaTech risk. Applying this framework to the Otterburne case, it is possible to observe how a latent defect made the infrastructure vulnerable for decades. The extreme natural event acted as an external trigger, accelerating the failure process.

The accident cannot therefore be interpreted as a simple causal sequence, but rather as the result of an evolving vulnerability, developed over time under the influence of internal and external factors. The bidirectional approach allows the interpretation of the incident not as a simple chain of causes, but as the result of a systemic vulnerability that has matured over time.

While the Otterburne case represents a prime example, the proposed interpretative model can be extended to other industrial contexts, such as chemical plants, reaction vessels, storage systems, and pipelines. In these facilities, bidirectional vulnerability manifests itself in different ways yet maintaining the same systemic structure: internal factors interact with external factors, amplifying the risk.

For example, in storage vessels, degradation can be accelerated by temperature variations and atmospheric phenomena such as hail or floods, while in chemical reactors, the combination of high pressures and aggressive substances can generate critical conditions in the presence of seismic events or fires. Pipelines, as shown in the case study, are particularly sensitive to mechanical and thermal stress induced by extreme weather events.

Analysis of historical data highlights that degradation mechanisms and the types of NaTech events vary depending on the sector, but the principle of bidirectional interaction remains valid. Specifically, studies conducted by Vitale et al. (2026), Ricci et al. (2021) and Ricci et al. (2023) report statistical data on the frequency of occurrence of events related to material degradation, NaTech accidents and extreme natural events such as cold waves, in different sectors of the process industry. These results support the extensibility of the proposed model to different plant contexts, confirming its validity in multifactorial scenarios and the versatility of the model, which can be adapted by integrating plant-specific parameters. This adaptability makes the model a useful tool for assessing vulnerability in complex and multifactorial scenarios.

Chapter 2 Partial Conclusions

This chapter explores the bidirectional relationship between material degradation and NaTech risk. A representative case study was selected and analysed, allowing for a concrete observation of the dynamics of interaction between structural deterioration and extreme environmental stresses. In particular, the Otterburne case showed how a welding defect, latent for over fifty years, can be triggered by an extreme natural event, leading to a sudden rupture and an explosion. The analysis highlighted the correlation between the age of the plant, the lack of post-installation inspections, and structural vulnerability, These findings confirm the trends observed in historical data on hydrogen embrittlement and mechanical fatigue, and demonstrate how material degradation can be a determining factor in the genesis and escalation of complex accidents.This study provides useful insights for the design, and operational management of industrial facilities exposed to NaTech risk. First, integrating material degradation into vulnerability assessment models represents a fundamental step towards moving beyond the traditionally static approach to structural safety. During the design phase, this requires adopting material selection criteria and construction solutions that consider not only operational stresses, but also potential exposure to extreme natural events and the synergistic interactions between these factors.

The results obtained support future methodological and applicative developments. From a scientific perspective, the developed interpretative model can be further validated through the analysis of case studies in different industrial contexts, contributing to the development of more robust predictive tools for the integrated management of technological risk in complex and multifactorial scenarios.

Considering the results obtained, some recommendations are proposed to improve technological risk management in NaTech scenarios:

- Regulatory update: Integrate explicit structural obsolescence parameters into the Seveso Directive, such as the age of the system, maintenance history, and exposure to critical environmental factors. These parameters should be included in safety reports and risk assessment criteria.
- Vulnerability-based inspections: Adopt targeted inspection strategies, prioritizing critical components (such as primary containment systems) exposed to extreme environmental conditions or subject to latent degradation mechanisms. The use of predictive models based on historical data and climate simulations can support intervention planning.
- Integrated risk indicators: Develop analytical tools that include key variables such as the timescale of degradation, the intensity of environmental exposure, and the frequency of natural events. These indicators can transform the conceptual model into an operational tool for quantitative vulnerability assessment.

These recommendations aim to strengthen the resilience of industrial

infrastructure, overcoming the currently prevalent fragmented approach and promoting a systemic and adaptive vision of safety.

In terms of contribution to research, the work directly addresses RQ2 by proposing the integration of material degradation phenomena and NaTech risk in vulnerability assessment processes. Furthermore, it contributes to the achievement of scientific objective SG2 by offering a useful interpretative model to support the design and management of more resilient industrial infrastructures. This approach lays the foundation for future methodological and applicative developments, oriented towards increasingly aware, systemic and preventive technological risk management.

Chapter 2 References

Castro Rodriguez, D.J., Mietkiewicz, J., Vitale, M., Baldissone, G., Barresi, A.A., and Demichela, M. (2024). NaTech triggered by lightning: Novel insights from past events in the process industry. Heliyon, 10, e31610. http://doi.org./ 10.1016/j.heliyon.2024.e31610

Castro Rodriguez, D.J., Tufano, C., Vitale, M., Mietkiewicz, J., Baldissone, G., Barresi, A.A., Demichela, M. (2023). Dataset of NaTech events triggered by lightning within the Process Industry 3. https://doi.org/10.17632/fff64w3rzn.3

Castro Rodríguez, D.J.C., Benítez, O.G., Acosta, J.B., Rodíguez, J.P., Rabassa, D.R., Ribot, O.V., Pérez, E.C., Chiampo, F., Godio, A., Demichela, M. (2022). Resilient Safer Approach to cope the oily waste generation in industrial facilities: lessons learned from Cuban installations. Chemical Engineering Transactions 90, 589–594. https://doi.org/10.3303/CET2290099

Cruz, A. M., Krausmann, E., Kato, N., and Girgin, S. (2017). Reducing Natech risk: structural measures. In: Krausmann, E., Cruz, A.M. and Salzano, E. (eds.) Natech risk assessment and management: Reducing the risk of natural-hazard impact on hazardous installations. Amsterdam: Elsevier, pp. 205–225.

Dwivedi, S.K., Vishwakarma, M. (2018). Hydrogen embrittlement in different materials: A review. International Journal of Hydrogen Energy 43, 21603–21616. https://doi.org/10.1016/j.ijhydene.2018.09.201

Ibrion, M., Paltrinieri, N., and Nejad, A. R. (2020). Learning from non-failure of Onagawa nuclear power station: an accident investigation over its life cycle. Results in Engineering, 8, 100185. https://doi.org/10.1016/j.rineng.2020.100185

IPCC (2023). Climate Change 2023: The Physical Science Basis. Contribution of Working Group I to the Sixth Assessment Report of the Intergovernmental Panel on Climate Change. In: Masson-Delmotte, V., Zhai, P., Pirani, A., Connors, S.L., Péan, C., Berger, S., Caud, N., Chen, Y., Goldfarb, L., Gomis, M.I., Huang, M., Leitzell, K., Lonnoy, E., Matthews, J.B.R., Maycock, T.K., Waterfield, T., Yelekçi, O., Yu, R. & Zhou, B. (eds.). Cambridge University Press, Cambridge, United Kingdom and New York, NY, USA. https://doi.org/10.1017/9781009157896

Ju, W., and Xing, Z. (2024). A novel technology for unraveling the spatial risk of Natech disasters based on machine learning and GIS: a case study from the city of Changzhou, China. Earth Science Informatics, 17(6), 5751-5770. https://doi.org/10.1007/s12145-024-01484-3

Krausmann, E., Cozzani, V., Salzano, E., and Renni, E. (2011). Industrial accidents triggered by natural hazards: an emerging risk issue. Natural Hazards and Earth System Sciences, 11(3), 921-929.

https://doi.org/10.5194/nhess-11-921-2011, 2011

Kubba, S. (2010). Green Construction Project Management and Cost Oversight. 1st ed. Burlington, Massachusetts: Butterworth-Heinemann. ISBN: 978-1-85617-676-7.

Laor, E. and De Vivo, B. (2022). Disaster prediction and civil preparedness. In: Panza, G., Kossobokov, V.G., Laor, E. and De Vivo, B. (eds.) Earthquakes and Sustainable Infrastructure: Neodeterministic (NDSHA) Approach Guarantees Prevention Rather Than Cure. Amsterdam: Elsevier, pp. 77–95

Li X., Ma X., Zhang J., Akiyama E., Wang Y., and Song X. (2020). Review of hydrogen embrittlement in metals: Hydrogen diffusion, hydrogen characterization, hydrogen embrittlement mechanism and prevention, Acta Metallurgica Sinica (English Letters), 33, 759–773.

Majidian, A., and Di-Sarno, L. (2025). Seismic risk assessment of an existing oil refinery subjected to earthquake swarms. Reliability Engineering & System Safety, 111482. https://doi.org/10.1016/j.ress.2025.111482

Mesa-Gómez, A., Casal, J., Sánchez-Silva, M. and Muñoz, F. (2021). Advances and gaps in Natech quantitative risk analysis. Processes, 9(1), p.40. https://doi.org/10.3390/pr9010040

Naderpour, M., and Khakzad, N. (2018). Texas LPG fire: Domino effects triggered by natural hazards. Process Safety and Environmental Protection, 116, 354-364. https://doi.org/10.1016/j.psep.2018.03.008

OECD, UNECE and JRC (2024). Managing Risks from Natural Hazards to Hazardous Installations (Natech): A Guide for Senior Leaders in Industry and Public Authorities. OECD Series on Chemical Accidents. OECD Publishing, Paris. [WWW Document]. URL, https://unece.org/environment-policy/publications/managing-risks-natural-hazards-hazardous-installations-natech (Accessed 07/2025).

Pilone, E., Demichela, M., Camuncoli, G. (2022). Na-Tech Risk: a New Challenge for Local Planners. Chemical Engineering Transactions 90, 223–228. https://doi.org/10.3303/CET2290038

Pilone, E., Demichela, M., Camuncoli, G. (2017). Seveso Directives and LUP: The mutual influence of natural and anthropic impacts. Journal of Loss Prevention in the Process Industries, 49, 94–102. https://doi.org/10.1016/j.jlp.2017.02.027

Reichstein, M., Benson, V., Blunk, J., Camps-Valls, G., Creutzig, F., Fearnley, C. J., Han B., Kornhuber K., Rahaman N., Schölkopf B., Tárraga J.M., Vinuesa R., Dall K., Denzler J., Frank D., Martini G., Nganga N., Maddix D.C.and Weldemariam, K. (2025). Early warning of complex climate risk with integrated artificial intelligence. Nature Communications, 16(1), 2564. https://doi.org/10.1038/s41467-025-57640-w

Ricci, F., Casson Moreno, V., Cozzani, V. (2023). Natech accidents triggered by

cold waves. Process Safety and Environmental Protection 173, 106–119. https://doi.org/10.1016/j.psep.2023.03.022

Ricci, F., Casson Moreno, V., Cozzani, V. (2021). A comprehensive analysis of the occurrence of Natech events in the process industry. Process Safety and Environmental Protection 147, 703–713. https://doi.org/10.1016/j.psep.2020.12.031

Slameto (2016). The Application of Fishbone Diagram Analisis to Improve School Quality. Dinamika Ilmu 16, 59–74. https://doi.org/10.21093/di.v16i1.262

Transportation Safety Board of Canada (2014). Pipeline investigation report P14H0011 [WWW Document]. URL https://www.tsb.gc.ca/eng/rapports-reports/pipeline/2014/p14h0011/p14h0011.pdf (Accessed 02.24)

TSB (2022). The Transportation Safety Board of Canada [WWW Document]. URL, https://www.tsb.gc.ca/eng/(Accessed 12/2023).

Valente, M., Ricci, F., and Cozzani, V. (2025). A systematic review of resilience engineering applications to NaTech accidents in the chemical and process industry. Reliability Engineering & System Safety, 255, 110670. https://doi.org/10.1016/j.ress.2024.110670

Vitale, M., Castro Rodriguez, D. J., Barresi, A., and Demichela, M. (2025). Database of material degradation event within process industry, Mendeley Data, V1. https://doi.org/10.17632/6hd3xky6kb.1

3. Loss of Containment: Causes, Monitoring Technologies and Risk Management Strategies

As highlighted by the historical analysis presented in Chapter 1, over 90% of material degradation events lead to a loss of containment (LOC), with significant consequences for plant safety, the environment, and human health. This strong correlation between equipment failures and LOC justifies a specific study of this phenomenon, recognized as one of the most critical outcomes in industrial risk scenarios. Consistent with research questions RQ3 and RQ4, this chapter analyses the causes, dynamics, and prevention strategies of LOC, with particular attention to monitoring technologies and leak detection methods. These aspects represent the methodological link between the historical analysis in Chapter 1 and the development of innovative monitoring approaches, which will be explored in greater depth in subsequent chapters.

Casal (2008) declares that major accidents are frequently caused by loss of containment (LOC), highlighting the importance of such events in the context of industrial safety. Kletz (2009) defines containment losses as the major hazard in the context of the process industry. Losses of containment of toxic, flammable or pressurized materials in chemical plants pose a significant hazard to human health and the environment, with the potential to cause major accidents, including exposures to hazardous substances, fires and explosions (Vílchez et al., 2011). These incidents could have a devastating impact on the population, the infrastructure and the environment, resulting in significant direct and indirect economic impacts. Direct damages include all immediate costs incurred in managing the incident, including costs related to the treatment of injuries and fatalities, recovery and clean-up actions implemented at contaminated sites. Indirect losses involve long-term costs resulting from the interruption of production activities, loss of trust by customers and business partners and even potential legal and regulatory sanctions. Therefore, to effectively manage these risks, it is necessary to define the characteristics of a major incident.

Although this notion does not have a univocal definition in international risk and safety regulations, at the European level it is clearly established by the Seveso III Directive (2012/18/EU)[6]. According to this directive, a major accident is described as an “occurrence such as a major emission, fire, or explosion resulting from uncontrolled developments in the course of the operation of any

[6] Directive 2012/18/EU on the control of major-accident hazards involving dangerous substances, amending and subsequently repealing Council Directive 96/82/EC.

establishment covered by this Directive and leading to serious danger to human health or the environment, immediate or delayed, inside or outside the establishment, and involving one or more dangerous substances". A single major accident can generate several scenarios at the same time. For example, a fire can cause harm to people and surrounding structures and can cause the release of toxic substances into the atmosphere. Furthermore, major accidents can trigger domino effects, a phenomenon where an accident in one industrial unit propagates to adjacent units, amplifying the initial impact through a series of cascading events, leading to even more serious accidents, such as fires and explosions (Zeng et al., 2020). The complexity of industrial environments, characterized by intricate networks of pipelines and equipment operating at high pressure, increases the likelihood of these scenarios. Statistical analysis of chemical domino accidents by Kourniotis et al. (2000) shows that these events not only occur more frequently than non-domino accidents but also cause significantly more severe overall damage. Furthermore, Alencar et al. (2005) highlight that domino effects can generate secondary accidents that frequently result in more destructive consequences than the primary events. This underlines the importance of adopting comprehensive risk assessments, which consider the potential for propagation and cascading failures, to prevent the propagation of damage and to minimize economic and social losses.

3.1 Cause and scenario of Loss of Containment

According to research by Bellamy et al. (2013), Lisbon et al. (2012) and Dharmavaram and Klein (2010), the main causes of loss of containment (LOC) in chemical plants are multiple and often interconnected. Equipment condition failures emerge as one of the predominant causes, mainly due to the lack or inadequate maintenance of the equipment, structural defects, and deterioration , which compromise the strength of the materials and increase the risk of failure. Equipment management plays a key role in failures; inappropriate design or improper use of components can reduce the effectiveness of safety barriers. If incorrectly designed or insufficiently maintained, such safety barriers are more likely not to perform their function correctly, thus increasing the risk of accidents. Gaps in the monitoring of process parameters, such as pressure and flow, help to hide deviations that, if not detected in a timely manner, can evolve into critical situations. Furthermore, human errors, which are responsible for approximately 50% of accidents, are often the result of a lack of adequate training, poor operational discipline and incorrect application of safety procedures. Therefore, all these factors, including equipment condition failures, inadequate safety barriers, human errors and operational management defects, lead to LOC events, as indicated by the studies conducted. Maintenance should be preventive, there should be strict application of safety procedures, and process parameters should be constantly monitored to reduce the risk of such incidents.

For safe risk management in chemical industries, it is important to analyse all possible scenarios of accidents due to the release of substances, which constitute the broadest category of hazardous events. These scenarios range from the

simplest, involving non-hazardous materials, to major accidents involving toxic, flammable or pressurised substances, which are dangerous for humans and the environment. In the risk analysis, it is also necessary to consider minor releases, since even small spills of flammable substances can result in more serious consequences than larger leaks of non-hazardous materials (Dharmavaram and Klein, 2010). The accurate assessment of these scenarios is important to identify potential vulnerabilities and their implications for public health and the environment.

3.2 Risk Assessment and Mitigation Strategies for Loss of Containment

To mitigate and prevent the risks associated with loss of containment, several strategies have been developed. Several studies have developed risk assessment methods for identifying leak scenarios and understanding their impacts on human health. Studies in the literature suggest that the assessment of the risks associated with loss of containment in process plants can be achieved through inspections, quantitative assessments, smart systems, targeted risk management strategies and comprehensive safety management programs. Milazzo et al. (2015) evaluated the use of quantitative risk assessment (QRA) as a decision-support tool in the chemical industry, focusing on the management of risk arising from pipeline spills. Their study also analyzed the uncertainties present in contemporary risk analysis models, such as fault trees, considering both possible variations in input data and simplifications introduced into the models. They assessed how these uncertainties could affect the reliability of the results and, consequently, decisions regarding risk prevention and mitigation measures. The extended risk assessment approach was then used in a case study to show the necessity of considering and managing these uncertainties to optimize decisions on preventive and mitigation measures, thus helping to improve the effectiveness of protection strategies and reduce the risk of loss of containment. Vianello et al. (2019) propose an innovative approach for safety management in chemical and petrochemical plants, focusing on the prevention of failures and loss of containment of process equipment. The adopted approach is the API Risk Based Inspection (RBI), which allows a significant reduction of maintenance costs while improving plant reliability and availability. To support this methodology, the Inspection Manager software has been developed, which facilitates the cost-benefit analysis and the selection of preventive measures needed to avoid accidental events that could lead to the release of hazardous materials. Ansaldi and Bragatto (2019) analyse the safety benefits of adopting the Internet of Things (IoT) and smart systems technologies in chemical and oil and gas plants. The main objective is to assess how the application of such technologies to critical equipment can improve safety by reducing the probability of incidents related to the loss of containment of hazardous materials or by mitigating their consequences. A method based on specific criteria is proposed to help employers and regulators evaluate the effectiveness of innovative smart systems for safety. A risk mitigation approach, in order to reduce the magnitude and therefore the consequences of the event,

consists of the implementation of robust secondary containment systems, designed to stop the spills and protect the external environment from the release of hazardous materials. Using ethanol as a hazardous substance, Horiguchi and Numazawa (2023) highlighted the need for detailed risk assessments, such as in the case of liquid toxic spills, to identify vulnerabilities and choose adequate safety devices. Papazoglou et al. (2023) propose a combined assessment of the risk of a release in hazardous installations, combining technical and management models. It uses a master logic diagram (MLD) to analyse the causes of containment losses and calculate the frequency of events. The management model examines the quality of primary business activities. The interface between the two models allows for risk adjustment based on the quality of the management system. This method is applied in an ammonia storage plant for risk evaluation resulting from containment loss. Finally, Rahmawati (2024) highlights the need to consider secondary containment structures, chemical compatibility measures between substances, and emergency response procedures in the design of storage facilities.

3.3 Consequence Analysis and Emergency Preparedness

In support of risk analysis, another area of interest concerns the understanding of the consequences arising from the release of materials classified as hazardous, important for emergency preparedness. Different approaches are proposed in the literature. Vílchez et al. (2011) propose a systematic set of generic event trees for loss of containment scenarios, involving different types of hazardous materials. These event trees are based on generic assumptions and are associated with the hazardous properties of the materials (flammability, volatility, toxicity) and CE labelling categories. The paper also includes probabilities of occurrence, based on a literature review and expert experience. In order to focus on the release of hazardous materials such as acrylonitrile, Chen et al. (2021) proposed a dynamic methodology, the Dynamic Graph Monte Carlo (DGMC), which aims to model and evaluate multi-hazard accident scenarios in the chemical industry. The model permits consideration of the simultaneous application of different hazards, acute toxicity, fire and explosion, and their potential nonlinear spatiotemporal evolution leading to cascading effects. Paculescu et al. (2022) review the use of modelling software to simulate pressure vessels containing hazardous materials. ALOHA and Phast QRA are used to simulate the consequences of such events. The modelling allows the analysis of the plant layout and the prediction of the effects of toxic release on the surrounding population. The study compares the results obtained by the two software, highlighting inconsistencies. Mohd Shariff and Zaini (2013) developed a design tool that integrates the PETRONAS iCON process simulator with a toxic release consequence analysis model, built using MS-Excel. The main objective is to prevent or minimise toxic release incidents in process plants. The tool allows the assessment of the potential consequences of a toxic release from the preliminary design stage. In case the project does not meet the established safety criteria for the release of toxic substances, it is possible to intervene, adopting intrinsic safety solutions to prevent or reduce the impact of the

consequences. Nicotra et al. (2024) studied the behaviour of flange leaks using computational fluid dynamics. Subsequently, they proposed operating rules for leak identification and event response methodologies to enable the continued operation of the system. Mizuta et al. (2020) present an evacuation model for chemical release events in a plant, offering recommendations for the implementation of efficient evacuation strategies. These studies are particularly relevant after the repercussions of historical events such as the Bhopal disaster, which caused thousands of fatalities, underscoring the need for more strict safety measures, as highlighted by Nyberg et al. (2011). Therefore, releases of hazardous substances from process plants result in severe effects - acute toxicity, fire and explosions and other cascading effects which affect human safety and infrastructure. Such events call for comprehensive risk assessment and safety measures, as well as emergency planning, to mitigate their effects.

3.4 Leak Detection and Continuous Monitoring Technologies

At the same time, leak detection technologies have made significant progress, improving the ability to instantly identify leaks at an early stage. Fahimipirehgalin et al. (2020) propose an inspection system based on thermographic video and motion pattern detection to identify liquid leaks, enable quick interventions and prevent serious damages. Takeda (2020) proposed a leak detection method based on measuring temperature differences at different points in a tank. Since the leakage of a gas or liquid, especially if under pressurized or cryogenic conditions, typically generates localized thermal anomalies, monitoring the temperature at the bottom and top of the tank allows for the indirect detection of such anomalies. However, since the installation of sensors at the bottom can be complex due to the presence of ventilation channels, which have the function of ensuring air exchange and avoiding the accumulation of dangerous vapours, the study proposes simplified configurations, which use the air temperature at the inlet of the channels in combination with other measurements inside the tank. In this way, even without direct access to the lower part of the structure, it is possible to infer the presence of a leak through the detection of anomalous thermal variations. Ichimiya et al. (2021) demonstrate that hybrid emergency ventilation systems are effective in controlling the concentration of contaminants emitted during chemical leakage incidents. Wang et al. (2021) propose a novel technique for real-time monitoring of the leak rate of containment at nuclear power plants as against traditional methods that require days of data accumulation before the leak rate can be evaluated. The technique employs a convolutional neural network (CNN) with data acquired on a daily basis from the monitoring systems of the plants. This methodology allows for the timely identification of containment leakage during the reactor startup phase. Choi and Jo (2023) focus on improving the early leakage detection and effectiveness of secondary containment systems to prevent the dispersion of hazardous liquids and minimize casualties in the event of a chemical accident. Computational fluid dynamics (CFD) simulations are conducted on tanks with different heights, comparing the detection times between level

transmitters (LTs) and leakage sensors. The results show that the combined use of these devices significantly speeds up the detection, compared to using a single sensor alone. The study by Geyer and Stellmach (1995) focuses on the importance of implementing a combined leak detection and secondary containment system for storage tanks, both underground and above ground. Despite advances in leak detection systems, the study highlights that soil or groundwater contamination cannot be prevented by the use of leak detection alone. Other research has delved into the use of advanced chemical sensors for leak detection and identification, aiming to improve safety and reduce risks associated with the dispersion of hazardous substances. Kim et al. (2024) and Burgués and Marco (2020) emphasize the new advances in chemical sensor technologies, being able to monitor hazardous materials in real-time within industrial setups. These sensors, thanks to their ability to rapidly detect the presence of hazardous substances in the environment, enable a timely response in the event of a leak, limiting the potential impact on human health, the environment, and industrial operations. These studies suggest that effective containment leak detection can be achieved through advanced modelling techniques such as convolutional neural networks, real-time monitoring systems, integration of level transmitters with leak sensors, and non-destructive assessment methods.

Considering the prevention strategies and detection technologies analysed, it is clear that the ability to anticipate a critical event is a key element in industrial risk management. In this context, continuous monitoring of process parameters plays a central role. It's not just about detecting an anomaly once it has already occurred but also intercepting the weak signals that may precede a loss of containment. The integration of real-time monitoring systems, supported by intelligent technologies, allows for strengthening plant resilience, improving response and prevention capabilities.

Continuous monitoring is important in operational safety and efficiency in most process industries: chemical, oil and gas, and food industries. Real-time monitoring of critical process parameters can often give signals to observe anomalies or deviations from standard values. Such monitoring assumes great importance in accident prevention, as warning signals are issued long before any serious incidents occur. Continuous monitoring also allows the detection of early warnings, i.e. indicators that suggest the possibility of a significant deviation from normal process parameters, anticipating the occurrence of anomalous events. Thanks to these signals, it is possible to intervene promptly to prevent the situation from worsening, blocking the escalation of a potential accident.

As cited by Zhang et al. (2019), numerous existing studies in the literature deal with the problem of early warning detection in industrial processes. Among all processes, oil refining has been recognized as one of the most high-risk processes because of the complicated raw materials, products and processes; thus, the authors proposed an early warning method based on monitoring trends in critical parameters for possible future deviations from these parameters to prevent some critical events. Similarly, Chen et al. (2018) proposed a new method for monitoring and detecting early signals of warnings in complex and sensitive industrial systems such as power plants by utilizing the Condition Monitoring and

Early Warning based on the Evidential K-Nearest Neighbor. (CMEW-EKNN) method-condition monitoring and early warning based on the Evidence Theory. Benson et al. (2021) proposed a digitalized methodology for early warning detection to effectively capture warning signals using contemporary technology, thus reducing the possible risk of human error while increasing efficiency in the monitoring process. A variety of techniques have been used for safe and reliable industrial systems against accident occurrences.

Chapter 3 Partial Conclusions

This chapter explored the phenomenon of loss of containment, highlighting its causes, consequences, and prevention and mitigation strategies. It emerged that LOC represents a major source of risk in process plants, with potentially serious impacts on human health, the environment, and the integrity of industrial infrastructures.

The analysis showed that the causes of LOC are often multifactorial and interconnected, including mechanical failures, human errors, design flaws, and deficiencies in monitoring systems. In this context, continuous monitoring and early identification of anomaly signals are key tools for accident prevention. Furthermore, the evolution of sensing technologies, such as smart sensors, IoT systems, and artificial intelligence techniques, offer new opportunities to improve the effectiveness of safety systems.

The chapter also highlighted the importance of adopting an integrated approach to risk management, including quantitative assessments, dispersion simulations, and the implementation of secondary containment barriers. These tools, if appropriately combined, can help reduce the probability and severity of LOC events, strengthening the overall resilience of industrial plants.

The complexity of risk management increases further when dealing with particularly critical substances, such as those that are highly flammable, toxic, or subject to material degradation. In these scenarios, even small leaks can lead to highly serious accident scenarios, requiring integrated approaches and advanced tools for risk assessment and mitigation.

In conclusion, the chapter outlines the state of the art on containment losses, highlighting their main causes, resulting scenarios, and prevention and detection strategies. The analysis confirms that continuous monitoring and early detection of anomalies are essential tools for strengthening the resilience of industrial plants, in line with the scientific objectives SG3 and SG4. The theoretical and methodological framework presented thus provides the basis for addressing issues related to dynamic monitoring and leak management of high-risk substances, which will be explored in greater depth in subsequent chapters. Thus, **Chapter 3** provides the methodological link between the historical analysis of failure mechanisms and the development of innovative approaches for monitoring and integrated management of technological risk.

Chapter 3 References

Alencar, J. R., Souza, J., and Barbosa, R. A. (2005). Evaluation of accidents with domino effect in LPG storage areas. Revista De Engenharia Térmica, 4(1), 08–12. https://doi.org/10.5380/reterm.v4i1.3541

Ansaldi, S. M., and Bragatto, P. (2019). Reducing accident hazard in chemical and petrol industries, through smart safety systems. In 2019 IEEE International Conference on Environment and Electrical Engineering and 2019 IEEE Industrial and Commercial Power Systems Europe (EEEIC/I&CPS Europe) (pp. 1-5). IEEE.

Bellamy, L., Mud, M., Manuel, H., and Oh, J. (2013). Analysis of underlying causes of investigated loss of containment incidents in Dutch Seveso plants using the Storybuilder method. Journal of Loss Prevention in The Process Industries, 26(6), 1039–1059. https://doi.org/10.1016/J.JLP.2013.03.009

Benson, C., Argyropoulos, C. D., Dimopoulos, C., Mikellidou, C. V., and Boustras, G. (2021). Safety and risk analysis in digitalized process operations warning of possible deviating conditions in the process environment. Process Safety and Environmental Protection, 149, 750–757. https://doi.org/10.1016/j.psep.2021.02.039

Burgués, J., and Marco, S. (2020). Environmental chemical sensing using small drones: A review. Science of the Total Environment, 748, 141172. https://doi.org/10.1016/j.scitotenv.2020.141172

Casal, J. (2008). Evaluation of the Effects and Consequences of Major Accidents in Industrial Plants. 1st ed. Amsterdam: Elsevier B.V.

Chen, C., Reniers, G., and Khakzad, N. (2021). A dynamic multi-agent approach for modeling the evolution of multi-hazard accident scenarios in chemical plants. Reliability Engineering & System Safety, 207, 107349. https://doi.org/10.1016/j.ress.2020.107349

Chen, X. L., Wang, P. H., Hao, Y. S., and Zhao, M. (2018). Evidential KNN-based condition monitoring and early warning method with applications in power plant. Neurocomputing, 315, 18–32. https://doi.org/10.1016/j.neucom.2018.05.018

Choi, M., and Jo, S. (2023). New developments in detector and bund wall standards to mitigate the risk of hazardous liquid leaks. Processes, 11(11), 3179. https://doi.org/10.3390/pr11113179

Dharmavaram, S., and Klein, J. (2010). Using hazards assessment to prevent loss of containment. Process Safety Progress, 29(4), 308–312. https://doi.org/10.1002/prs.10410

Fahimipirehgalin, M., Vogel-Heuser, B., Trunzer, E., and Odenweller, M. (2020). Visual leakage inspection in chemical process plants using thermographic videos and motion pattern detection. Sensors, 20(22), 6659.

https://doi.org/10.3390/s20226659

Geyer, W. B., and Stellmach, W. A. (1995). Secondary containment and leak detection: A great marriage. Environmental Protection, 6(4).

Horiguchi, A. and Numazawa, S. (2023). Development of a risk assessment method for the detailed consideration of the effects of liquid toxic substance leakage incidents on the human body: ethanol as a model substance. The Journal of Toxicological Sciences, 49(1), 37–47. https://doi.org/10.2131/jts.49.37

Ichimiya, S., Murga, A., Yoo, S. J., Sumiyoshi, E., Harashima, H., Long, Z., and Ito, K. (2021). Hybrid emergency ventilation system for controlling inhaled contaminant dose in the case of chemical leakage. Indoor and Built Environment, 31(3), 696–709. https://doi.org/10.1177/1420326x211026360

Kim, Y., Jeon, Y., Na, M., Hwang, S., and Yoon, Y. (2024). Recent trends in chemical sensors for detecting toxic materials. Sensors, 24(2), 431. https://doi.org/10.3390/s24020431

Kletz, T. (2009). Chapter 7 - Leaks. In: T. Kletz, ed.,What Went Wrong? Case Histories of Process Plant Disasters and How They Could Have Been Avoided. 5th ed. Oxford: Butterworth-Heinemann, pp.131–148. https://doi.org/10.1016/B978-1-85617-531-9.00007-X

Kourniotis, S. P., Kiranoudis, C. T., and Markatos, N. C. (2000). Statistical analysis of domino chemical accidents. Journal of Hazardous Materials, 71(1-3), 239–252. https://doi.org/10.1016/S0304-3894(99)00081-3

Lisbona, D., Johnson, M., Millner, A., McGillivray, A., Maddison, T., and Wardman, M. (2012). Analysis of a loss of containment incident dataset for major hazards intelligence using storybuilder. Journal of Loss Prevention in The Process Industries, 25(2), 344–363. https://doi.org/10.1016/J.JLP.2011.11.004.

Milazzo, M. F., Vianello, C., and Maschio, G. (2015). Uncertainties in QRA: Analysis of losses of containment from piping and implications on risk prevention and mitigation. Journal of Loss Prevention in The Process Industries, 36, 98–107. https://doi.org/10.1016/j.jlp.2015.05.016

Mizuta, Y., Sumino, M., Kunito, Y., Shiota, K., Izato, Y., and Miyake, A. (2020). Emergency evacuation model assuming leakage of toxic substances in a chemical plant. Journal of Loss Prevention in The Process Industries, 68, 104287. https://doi.org/10.1016/j.jlp.2020.104287

Mohd Shariff, A., and Zaini, D. (2013). Using integrated toxic release consequences analysis tool for inherently safer design of process plant at preliminary design stage. Clean Technologies and Environmental Policy, 15, 851–858. https://doi.org/10.1007/s10098-012-0572-4

Nicotra, G., Ripepi, A., Tortora, A., Ponteggia, L., Cincotta, S., Pozzi, N.,

Lombardi, D., Rocchi, A., Pisani, E., and Fani, A. (2024). A Structured Approach for Weeps and Seeps Identification, Verification and Control. In SPE International Conference and Exhibition on Health, Safety, Environment, and Sustainability, Abu Dhabi, UAE, 10 September. https://doi.org/10.2118/220342-MS

Nyberg, A., Stricklin, D., and Sellström, Å. (2011). Mass casualties and health care following the release of toxic chemicals or radioactive material contribution of modern biotechnology. International Journal of Environmental Research and Public Health, 8(12), 4521–4549. https://doi.org/10.3390/ijerph8124521

Papazoglou, I. A., Bellamy, L. J., Hale, A. R., Aneziris, O. N., Ale, B. J. M., Post, J. G., and Oh, J. I. H. (2003). I-Risk: development of an integrated technical and management risk methodology for chemical installations. Journal of Loss Prevention in The Process Industries, 16(6), 575–591. https://doi.org/10.1016/j.jlp.2003.08.008

Pasculescu, V. M., Ghicioi, E., Tuhut, L. I., Simon-Marinica, A. B., and Pasculescu, D. (2022). Discharge and atmospheric dispersion modelling in case of hazardous material releases. In MATEC Web of Conferences 354, 9. EDP Sciences. https://doi.org/10.1051/matecconf/202235400009

Rahmawati, F. (2024). Design of an integrated temporary storage for hazardous and toxic material wastes 4.0 case study in the department of industrial chemical engineering. Iptek the Journal of Engineering, 10(1), 61. https://doi.org/10.12962/j23378557.v10i1.a19252

Takeda, H. (2020). Helium leak detection methods using temperatures of a canister bottom and air at an inlet. Nuclear Engineering and Design, 362, 110576. https://doi.org/10.1016/j.nucengdes.2020.110576

Vianello, C., Milazzo, M. F., and Maschio, G. (2019). Cost–benefit analysis approach for the management of industrial safety in chemical and petrochemical industry. Journal of Loss Prevention in The Process Industries, 58, 116–123. https://doi.org/10.1016/j.jlp.2019.02.006

Vílchez, J. A., Espejo, V., and Casal, J. (2011). Generic event trees and probabilities for the release of different types of hazardous materials. Journal of Loss Prevention in The Process Industries, 24(3), 281–287. https://doi.org/10.1016/j.jlp.2011.01.005

Wang, H., Liu, J., Xie, G., Zhong, X., and Fan, X. (2021). A method of containment leakage rate estimation based on convolution neural network. Frontiers in Energy Research, 9, 637283. https://doi.org/10.3389/fenrg.2021.637283

Widarsson, B., and Dotzauer, E. (2008). Bayesian network-based early-warning for leakage in recovery boilers. Applied Thermal Engineering, 28(7), 754-760. https://doi.org/10.1016/j.applthermaleng.2007.06.016

Zeng, T., Chen, G., Yang, Y., Chen, P., and Reniers, G. (2020). Developing an

advanced dynamic risk analysis method for fire-related domino effects. Process Safety and Environmental Protection, 134, 149-160. https://doi.org/10.1016/j.psep.2019.11.029.

Zhang, L., Cai, S., and Hu, J. (2019). An adaptive pre-warning method based on trend monitoring: Application to an oil refining process. Measurement, 139, 163-176. https://doi.org/10.1016/j.measurement.2019.03.013

4. Hydrogen and industrial resilience[7]

The previous three chapters have highlighted how integrated industrial risk management, focusing on loss of containment (LOC) and material degradation, is essential to ensuring plant safety and sustainability. This approach has addressed the main critical issues related to infrastructure reliability and accident prevention, placing the resilience of production systems and the ability to respond to adverse events at the centre of the analysis.

In this context, one of the emerging challenges concerns the introduction of new energy carriers, including hydrogen, which is a key element in the transition to a decarbonized economy. In recent years, scientific research has focused on developing increasingly efficient and economically sustainable methods for hydrogen production from renewable sources, such as wind, solar, and hydroelectric power, with the aim of reducing dependence on fossil fuels (Xiao et al., 2011). Hydrogen obtained by water electrolysis powered entirely by renewable energy represents a concrete solution to contribute to the decarbonization of the industrial and transport sectors, with significant potential for mitigating climate-altering emissions (Acar and Dincer, 2019; Demirbas, 2017).

In addition to being a low-emission energy carrier, hydrogen offers advantages in terms of flexibility of use in various fields and increased energy resilience. However, its unique physical and chemical properties, such as high flammability, high diffusivity, and difficulty in detecting leaks, pose significant challenges for the safety of industrial plants. Added to these critical issues are the complexities associated with storage, transportation, and the need for advanced monitoring systems, making careful assessment essential, including from a regulatory perspective.

Hydrogen, due to its low density (0.0899 kg/m³), is an extremely light gas. This characteristic makes it particularly susceptible to dispersion into the environment, especially in the presence of leaks. Furthermore, with a wide flammability range of 4 to 75% by volume and an extremely low minimum ignition energy of 0.017 mJ (Chemsafe, 2024; Gong et al., 2022), hydrogen can

[7] Portions of this chapter have been published in preliminary form in:

Vitale, M.; Demichela, M.; Barresi, A. (2024). Hydrogen leak detection: Monitoring and control methodologies. Book of abstracts of the RETURN Dissemination Workshop pp. 275-276. Fondazione Return - ELETTRONICO. Torino, Italy 1-2 February 2024. https://dx.doi.org/10.5281/zenodo.1059800

Vitale, M., Barresi, A., and Demichela, M. (2024). The Use of Aerial Platforms for Identification of Loss of Containment. *Chemical Engineering Transactions*, 111, 73-78. https://doi.org/10.3303/CET24111013

Vitale, M., Rodriguez, D. J. C., Barresi, A. A., and Demichela, M. (2025). Hydrogen Safety in Process Industry: Systematization of Past Lessons. *Chemical Engineering Transactions*, 116, 403–408. https://doi.org/10.3303/CET25116068

accumulate in the environment in flammable mixtures with air, significantly increasing the risk of fire in the event of a leak.

Another critical issue is the ability of hydrogen molecules to escape rapidly through equipment. Because hydrogen molecules are so small, it is difficult for containment structures to prevent their escape, increasing the possibility of accidental leaks. Once released, hydrogen can give rise to dangerous phenomena such as jet fires, which are concentrated flames that arise from leaks of pressurised gas. These jet fires, while extremely dangerous, are particularly difficult to detect, as they are invisible to the human eye, especially in sunlight, as illustrated in **Figure 4.1**. This exposes plant personnel to potential serious injury or death.

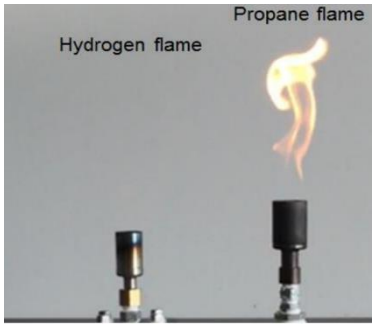

Figure 4.1: Comparison between propane flame and hydrogen flame. Hydrogen flame is not visible in daylight. Image taken from Okino et al. (2017).

The presence of liquid hydrogen with storage temperatures below -253 °C (hydrogen liquefaction temperature) could cause complex and dangerous consequences, considering the physical and chemical characteristics of the gas, as extensively described by Alfarizi et al. (2023). Once released, hydrogen tends to form an intense two-phase jet composed of liquid and gaseous phases. The orientation and flow of the release determine the possibility of forming a pool of liquid hydrogen, with a particular probability of forming a pool fire if the release is oriented vertically downwards. Released liquid hydrogen poses significant safety risks, including freezing and potential asphyxiation. In fact, the low temperatures of liquid hydrogen can cause oxygen and nitrogen to solidify, resulting in highly dangerous mixtures.

In addition, if the concentration of hydrogen in the air reaches a critical level, a deflagration or detonation explosion can occur. Deflagration, which generates subsonic shock waves, can occur even at low hydrogen concentrations (4%-11% by volume in air), while detonation, which involves supersonic combustion with high-velocity shock waves, is more likely at hydrogen concentrations between 11% and 59% by volume. It has been demonstrated that the mixture of liquid hydrogen and solid air that forms above the liquid hydrogen pool can switch from deflagration to detonation in the presence of an ignition source, especially if the concentration of solid oxygen in the mixture exceeds 50%, with potentially devastating explosive consequences for the surrounding environment.

Therefore, safe handling of hydrogen in industrial facilities requires careful design of equipment and constant surveillance to prevent any leakage. The physical and chemical characteristics of this gas, if not managed properly, can pose considerable safety risks.

For the reasons listed, one of the problems of hydrogen is storage and

transportation with current technologies. In addition, hydrogen has a good energy density by weight, but a poor energy density by volume compared to hydrocarbons (Roes and Patel, 2011). There are several ways to store hydrogen, as reported by Dutta (2014):

- The most common hydrogen storage system is pressurized using high-pressure cylinders, typically up to 20 MPa (Züttel, 2004). Cylinders that can withstand up to 80 MPa have recently been developed, allowing a significant decrease in the volumetric density of hydrogen. To compensate for the higher diffusivity of hydrogen, modifications to the seals are sometimes necessary. Therefore, despite its simplicity and reliability at the laboratory level, the high-pressure storage method has two main drawbacks: the low density of hydrogen and the need for high-pressure storage systems.
- As cryogenic liquid. Due to hydrogen very low boiling point (-253°C at 1 bar), liquefaction requires a lot of energy. However, the advantage of storing energy at an extremely high storage density at atmospheric pressure through liquefaction is obviously significant (Andersson and Grönkvist, 2019). Therefore, liquid hydrogen has been considered a viable solution for distribution, due to its high energy density compared to other storage methods.
- Chemical storage, in which hydrogen is bound to chemicals for storage and release when and where needed.
- Physical storage, in which hydrogen is absorbed or adsorbed in porous materials (e.g., carbon-based) for storage and subsequent use.

Each storage method has its own advantages and disadvantages. The choice, however, depends on the specific application needs and on safety and cost considerations.

4.1 Regulatory Framework

Hydrogen is in gaseous form at room temperature and pressure. According to the Globally Harmonized System (GHS) (UNECE, 2021), a flammable gas is defined as a gas that can ignite easily, being capable of forming a flammable mixture with air. This mixture must be within a specific concentration range, which is measured at 20°C and 101.3 kPa (standard reference conditions). Since hydrogen has a flammability range that makes it susceptible to ignition under these conditions, it is classified as a flammable gas according to the GHS.

The III Seveso Directive[8] (2012/18/UE) regulates activities in Europe involving the use of dangerous substances, including hydrogen, in order to prevent major accidents and minimize risks to human health and the environment. The directive establishes that installations that treat, store or use hydrogen must be classified according to the quantity of gas present and the risk that such activity entails.

Seveso III divides installations into two main categories based on the quantity

[8] Directive 2012/18/EU on the control of major-accident hazards involving dangerous substances, amending and subsequently repealing Council Directive 96/82/EC.

of hydrogen stored or treated. The directive distinguishes between lower and upper thresholds of quantities of dangerous substances, with different safety measures for each case:

- Lower threshold: If the quantity of hydrogen present in the installation exceeds the lower threshold established by Seveso III, the installation is subject to safety requirements, but these are less stringent than those foreseen for higher quantities. In this case, the installation must adopt basic safety measures for the prevention and management of risks, such as continuous monitoring and the adoption of standardized operating procedures.
- Upper threshold: If the amount of hydrogen exceeds the upper threshold, the installation is subject to more stringent safety requirements. In this case, more complex safety measures must be implemented, including the requirement to have detailed emergency and safety plans. These plans must include specific actions in the event of major accidents, such as gas leaks, fires or explosions. In addition, the competent authorities carry out regular checks to verify compliance with the higher safety standards.

Conversely, if the amount of hydrogen stored or processed in an installation is below both the lower threshold sets out in the Seveso III Directive, the establishment is classified as non-Seveso. However, even if the installation does not fall under the Seveso classification, this does not exempt the employer from complying with other regulations on occupational safety and environmental protection.

There are numerous codes and standards applicable to hydrogen systems, which are designed to ensure the safety, reliability and efficiency of these technologies (Qanbar and Hong, 2024). These documents address different areas of hydrogen systems, such as design, installation, operation, maintenance, testing and inspection. However, many of these documents do not provide specific guidance on risk management, such as leak prevention and reduction. The international standard ISO/TR 15916:2015[9] provides guidance for the use of hydrogen in gaseous and liquid forms, as well as for its storage in these and other forms. The document identifies the main safety risks, associated hazards and the characteristics of hydrogen that are relevant to the safe handling of its applications. Although ISO/TR 15916 covers the risks and properties of hydrogen in a general way, specific safety requirements for individual applications are addressed separately in other international standards.

The Canadian Hydrogen Installation Code, regulated in CAN/BNQ 1784-000[10], establishes requirements for the installation of equipment used in the generation of hydrogen for non-process purposes, including distribution systems, storage vessels and hydrogen pipelines. This code applies to all gaseous and liquid hydrogen applications, with the exception of the production or use of hydrogen in

[9] ISO/TR 15916:2015, *Basic considerations for the safety of hydrogen systems*, 2nd edition, International Organization for Standardization, Geneva, Switzerland, December 2015.
[10] CAN/BNQ 1784-000/2022, *Canadian Hydrogen Installation Code*, Bureau de normalisation du Québec (BNQ), approved as a National Standard of Canada by the Standards Council of Canada (SCC), 2nd edition, 31 May 2022.

petroleum refineries and chemical plants as a feedstock directly into process production and industrial facilities where hydrogen is produced, handled and stored for external end-use.

In the United States, there is no centralized regulatory framework for hydrogen. There are several regulations that treat hydrogen as a flammable gas. Many of these regulations are dated and obsolete; the introduction of unified codes would be necessary, especially for the growing interest as an energy carrier. The safety standards for the transportation and distribution of gas in the United States are established by PHMSA. 49 CFR 192[11] and 193[12] are the standards that regulate flammable gases in pipelines. 49 CFR 173[13] and 177[14] regulate cryogenic hydrogen tanks and compressed hydrogen cylinders. The American Society of Mechanical Engineers (ASME) code B31.12[15] covers certain types of hydrogen piping. ASME B31.12 applies to piping and tubing designed to handle gaseous hydrogen and gaseous hydrogen mixtures, as well as liquid hydrogen. It covers all piping up to the point of connection to pressure vessels and related equipment, but does not apply directly to the vessels or equipment themselves. It also includes specifications for the location and type of structural supports for the piping, but does not address the actual structure to which these supports are attached. There is also the Occupational Safety and Health Administration (OSHA) standard 29 CFR 1910.103[16], which includes regulations for the storage of compressed gases, including gaseous hydrogen (Bade and Tomomewo, 2024). Finally, NFPA 2, developed by the National Fire Protection Association (NFPA), provides essential safety measures for the safe handling of hydrogen, whether in the form of compressed gas (GH2) or cryogenic liquid (LH2). This standard covers all aspects of the generation, installation, storage, distribution, use, and handling of hydrogen in both its physical states.

4.1.1 In Italy

The Preliminary Guidelines of the National Hydrogen Strategy, published by the Ministry of Economic Development, outline the vision and objectives for the integration of hydrogen into a decarbonized economy. The goal is to achieve a 2% penetration of hydrogen in final energy demand by 2030, with applications in transport, heavy industry and refineries. By 2050, the share will increase to 20%, with applications also in the energy and residential sectors. Investments of up to 10 billion euros are needed between 2020 and 2030. The strategy includes three

[11] 49 CFR Part 192, *Transportation of Natural and Other Gas by Pipeline: Minimum Federal Safety Standards*, Pipeline and Hazardous Materials Safety Administration (PHMSA), U.S. Department of Transportation, current as of May 2025.
[12] 49 CFR Part 193, *Liquefied Natural Gas Facilities: Federal Safety Standards*, Pipeline and Hazardous Materials Safety Administration (PHMSA), U.S. Department of Transportation, current as of May 2025.
[13] 49 CFR Part 173, *Shippers – General Requirements for Shipments and Packagings*, Pipeline and Hazardous Materials Safety Administration (PHMSA), U.S. Department of Transportation, current as of May 2025.
[14] 49 CFR Part 177, *Carriage by Public Highway*, Pipeline and Hazardous Materials Safety Administration (PHMSA), U.S. Department of Transportation, current as of May 2025.
[15] ASME B31.12-2019, *Hydrogen Piping and Pipelines*, The American Society of Mechanical Engineers (ASME), New York, NY, United States, 2019 Edition.
[16] 29 CFR 1910.103, *Hydrogen*, Occupational Safety and Health Administration (OSHA), U.S. Department of Labor, Code of Federal Regulations, Title 29 – Labor, Part 1910 – Occupational Safety and Health Standards, Subpart H – Hazardous Materials, current as of May 2025.

green hydrogen production models with the goal of reducing emissions by 8 Mton of CO2 equivalent by 2030 (International Energy Agency, 2021).

The management of hazardous substances in plants in Italy, regulated by Legislative Decree of 9 April 2008, n. 81[17] Testo Unico sulla Salute e Sicurezza sul Lavoro (TUSL) is essential to ensure the protection of workers' health and safety. The TUSL establishes a series of provisions that impose precise obligations on the employer and define specific measures for the protection of workers.

In particular, Article 223 of the TUSL obliges the employer to carry out an assessment of the risks arising from the use of hazardous chemical substances, including flammable ones. This assessment must consider the chemical properties of the substances, the methods of use, the quantities used, the working conditions and the interactions with other agents present in the environment. The assessment must be continuous and updated to ensure that the risks are monitored and reduced in real time.

Article 224 requires that the employer adopt adequate preventive and protective measures to eliminate or minimize risks arising from the use of dangerous substances. These measures may include the adoption of personal protective equipment (PPE), the installation of ventilation systems, the introduction of technologies that reduce the emission of dangerous substances and the implementation of safe working procedures. In addition, constant monitoring of working conditions and control of the presence of dangerous substances in the environment is required.

Article 225 establishes that workers must be informed and trained on the risks associated with the dangerous substances with which they come into contact. Training must include information on specific risks, the prevention and protection measures to be adopted, and emergency procedures in the event of an accident. Workers must also be trained in the use of PPE and the application of safety measures.

Finally, the TUSL includes specific provisions in Title XI for protection from explosive atmospheres, a significant risk in environments where combustible gases, vapours or dust are present. The measures envisaged concern the classification of areas at risk of explosion, the use of explosion-proof equipment and the adoption of emergency procedures to deal with possible explosions.

Previously, the Ministerial Decree of March 10, 1998, known as DM 10/03/1998[18], in Italy had established the "Criteri generali di sicurezza antincendio e per la gestione delle emergenze nei luoghi di lavoro", a regulation for the prevention and management of fires in the workplace. This decree defined the essential requirements for active and passive protection against fires, as well as the procedures necessary to ensure the safety and protection of people in the event of an emergency.

[17] Legislative Decree No. 81 of April 9, 2008, *Implementation of Article 1 of Law No. 123 of August 3, 2007, concerning the protection of health and safety in the workplace*, published in the Official Gazette No. 101 of April 30, 2008 – Ordinary Supplement No. 108, as amended and supplemented (In Italian language).

[18] Ministerial Decree of 10 March 1998, *General fire safety criteria and emergency management in workplaces*, issued by the Ministry of the Interior, published in the Official Gazette of the Italian Republic No. 81 of 7 April 1998 – Ordinary Supplement No. 64 (In Italian language).

The decree distinguished fire protection into two main categories: active protection and passive protection. Active protection refers to all measures and devices that intervene directly in the event of a fire to contain the flames and prevent their spread. Among these devices, we find extinguishing systems such as sprinklers, portable and wheeled extinguishers, and alarm systems. DM 10/03/1998 required that these devices be regularly checked and maintained, to ensure that they are always ready to intervene promptly. Furthermore, the decree established that, in some cases, automation technologies should be adopted to speed up intervention in the event of a fire.

Passive protection, on the other hand, covered all structural measures designed to limit the spread of fire. These measures included the use of fireproof building materials, thermal insulation of structures, and the division of environments into fire compartments. The aim of passive protection was to slow down the spread of fire, thus allowing more time for the evacuation of workers and for rescue operations.

The Ministerial Decree of 10/03/1998 also provided for the development of evacuation procedures in the event of fire, requiring the creation of detailed evacuation plans that had to be known by all workers. These plans included clearly marked emergency exits, safe escape routes and assembly points outside the building. It was essential that these plans were regularly tested with evacuation simulations to ensure that workers were prepared to respond appropriately in the event of an emergency.

Ministerial Decree 10/03/1998 was subsequently replaced by the Ministerial Decree of 02/09/2021[19], which introduced updated criteria for managing fire safety in the workplace. The new decree places greater emphasis on organizational and management aspects, emergency planning, training and qualifications of firefighters, and the integration of fire risk management into the broader corporate prevention system, in accordance with Legislative Decree 81/2008.

4.2 Hydrogen Embrittlement

One of the critical aspects in the use of hydrogen is the phenomenon of hydrogen embrittlement (HE), which can occur due to the extremely small size of hydrogen molecules. These molecules have the ability to penetrate materials, as shown in **Figure 4.2**, altering their fundamental mechanical properties, such as tensile strength, fatigue resistance and fracture toughness (Dwivedi and Vishwakarma, 2018).

[19] Ministerial Decree of 2 September 2021, Criteria for the management of fire safety in workplaces, issued by the Ministry of the Interior, published in the Official Gazette of the Italian Republic No. 237 of 4 October 2021 (In Italian language).

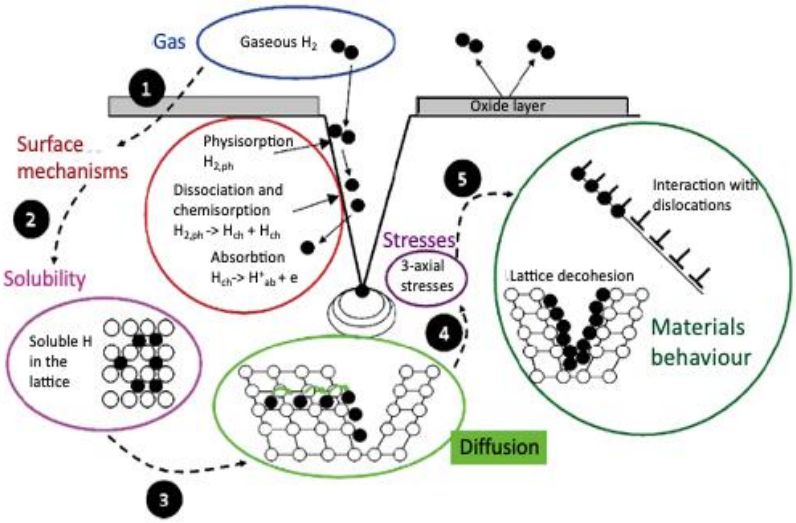

Figure 4.2: Hydrogen diffusion mechanism in materials. Image taken from Li et al. (2020).

This is a complex phenomenon that involves different mechanisms, including the physical and chemical absorption of hydrogen, as well as its dissolution within the material matrix. This process can lead to a significant reduction in the performance of the material, with possible serious consequences, including the reduction of its strength and durability. As a result, situations of structural failure or sudden fracture can occur, putting the integrity of the structure itself at risk. A concrete example of the consequences of hydrogen embrittlement was analysed in **Chapter 2**, where material contact with hydrogen, which occurred during an improperly performed welding operation, led to the formation of a crack and subsequent structural failure. In that case, hydrogen was present in low concentrations within a gaseous mixture used as a protective atmosphere, and not as a fuel. Although the exposure was limited in time, the thermal conditions and the transient nature of the process favoured the surface absorption of the gas, highlighting how even brief interactions can generate localized mechanical degradation effects in materials. Laadel et al. (2022) analyse in detail the HE phenomenon to identify the materials less susceptible to this degradation. Among the main degradation mechanisms identified, HELP (Hydrogen Enhanced Local Plasticity), HEDE (Hydrogen Enhanced Decohesion Mechanism) and AIDE (Adsorption-Induced Dislocation Emission) have been found; however, none of these phenomena offers a comprehensive explanation of the embrittlement process. The HE phenomenon is influenced by multiple factors, including environmental and operational conditions and the intrinsic characteristics of the materials.

In relation to the resistance of materials, the study highlights that permeation barriers, with particular reference to surface coatings, represent effective solutions to prevent hydrogen diffusion. Furthermore, the effectiveness of permeation barriers can be further improved through advanced deposition techniques. The adoption of multiple surface treatments, such as multilayer coatings, together with the introduction of innovations in the design and production of structural materials, can help to optimize the performance and economic competitiveness of the proposed solutions.

Therefore, to ensure the safety and reliability of applications using hydrogen, it is important to adopt preventive measures that address the risk of material fragility. This involves a thorough analysis of the potentially harmful effects of hydrogen on materials, together with the management of containment losses, which could have consequences on the plant and the surrounding environment. Proper management of these factors serves to ensure the proper functioning and durability of equipment and systems operating with hydrogen.

4.2.1 Historical Analysis

For effective leakage monitoring and accurate risk assessment, it is necessary to identify the most vulnerable points within the plant, i.e. the areas where failures or leaks are most likely to occur. This requires a thorough understanding of hydrogen-induced degradation mechanisms, such as corrosion and embrittlement, which can compromise the integrity of structures and equipment (Vitale et al., 2025b). A useful method to gain such knowledge is the analysis of previous incidents in the hydrogen industry, which provides data on where and how failures occur, which equipment is most vulnerable, and which operating conditions have favoured such events (Vitale et al., 2024b). Such analysis also enables the verification of the effectiveness of the adopted safety measures and helps identify areas in need of improvement. Furthermore, it provides an overview of the economic and environmental damages caused by incidents, facilitating the development of strategies to reduce risks and the overall impact. The results obtained can support inspections, contributing to safer hydrogen management. Ultimately, the main objective is to examine in detail how hydrogen can affect the degradation of materials used in industrial plants. This insight allows the identification of the main factors that, if not properly managed, could cause serious events such as loss of containment, fires or explosions. The analysis of degradation mechanisms can support understanding how to prevent these risks, optimize the design of structures and improve maintenance practices, in order to implement safer and more reliable solutions, ensuring the protection of both people and the environment, and reducing the potential damage caused by accidents.

4.2.2 Materials and Methods

The analysis presented in this section is based on the methodology described in **Chapter 1.3**, where is discussed in detail. In summary, the approach is divided into two main phases:

i)Data Collection: a targeted selection was made from the database constructed in Chapter 1 to extract a subset of reports involving hydrogen. Events were included where hydrogen was present as a substance contained in the plant, either as a main component or in a mixture with other substances, or generated as a byproduct of industrial processes, such as welding operations or corrosion. Indeed, as discussed in **Chapter 2**, the welding process can involve either the direct use of hydrogen in low concentrations within protective gas mixtures or its local generation in the presence of unfavourable environmental conditions. In both

cases, at high temperatures, hydrogen can diffuse into the material, favouring the activation of embrittlement mechanisms. The selected reports came exclusively from three open-source databases: ARIA (BARPI, 2022), eMARS (eMars, 2022), and JRC HIAD (JRC, 2023). The American databases did not contain any hydrogen-related events.

ii)Data Analysis: the selected reports were processed using descriptive tools and probabilistic models, with the aim of identifying recurring patterns, correlations between variables, and critical scenarios. The classification of events follows the structure already adopted in **Chapter 1**, outlined in **Figure 1.2**. Unlike the analysis already conducted, Quantitative Risk Assessment (QRA) methodologies were not integrated to manage uncertainty, as the available data, coming exclusively from European sources, are already structured and sufficiently complete for an exploratory analysis based on trends and distributions.

The purpose of this section is to specifically analyse the subset of events in which hydrogen played a significant role, in order to understand the relationships between hydrogen embrittlement (HE) phenomena and the types of equipment and systems most affected. The observations emerging from this analysis can provide useful support for planning inspections, contributing to the early identification of vulnerabilities and the improvement of risk management strategies in industrial contexts where hydrogen is present or can be generated.

4.2.3 Results

In this section, a database of 84 events related to the use of hydrogen in the process industry is examined, with particular attention to material degradation. From **Figure 4.3**, it is clear that the JRC database contains the highest number of recorded events, amounting to 74%.

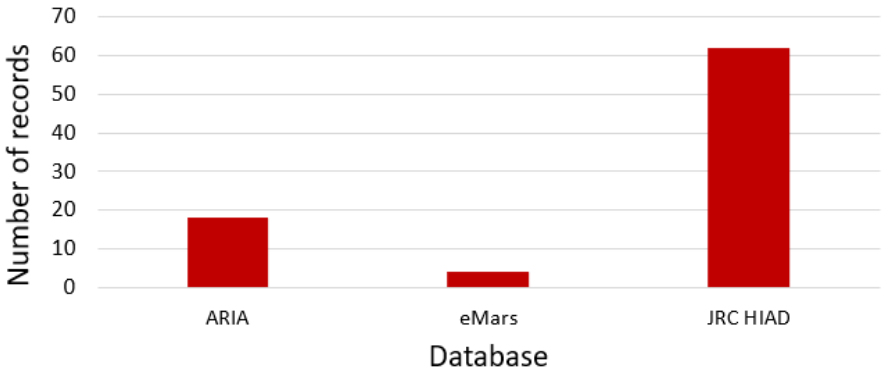

Figure 4.3: Number of reports collected for each database analysed.

This result can be attributed to the characteristic of the JRC, which is specifically focused on hydrogen-related accidents. Next, it is observed that the ARIA database has a significant number of reports, equal to 21%, probably due to its wide coverage of different industrial sectors. Finally, the eMARS database appears to have a much lower number of events than the other two, probably because eMARS focuses mainly on severe accidents in high-risk sectors and, therefore, collects a lower number of reports. **Figure 4.4** shows the geographical distribution of the collected events related to accidents caused by the degradation

of materials in the presence of hydrogen. It is interesting to note that, although the analysed databases are of European origin, a significant part of the events is located outside Europe: 26% were recorded in the American continent and 10% in Asia. This data highlights how the high reactivity and dangerousness of hydrogen have led to the documentation of relevant events also in non-European contexts, often known internationally and therefore included in the databases for their technical and scientific relevance.

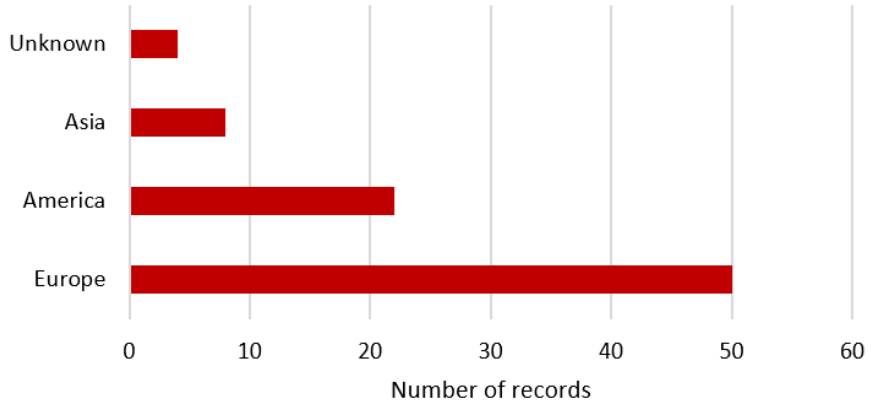

Figure 4.4: Geographical distribution of the collected events.

The events were recorded between 1971 and 2022. **Figure 4.5a** shows how the number of accidents varies annually, with small fluctuations over time. Despite these fluctuations, an increase in the annual average of accidents can be seen in the first few years. **Figure 4.5b**, on the other hand, illustrates the average number of accidents in different time periods, calculated by dividing the total number of events recorded in each period by the number of years in that period. For the temporal analysis, the events were divided into regular ten-year blocks from 1970 to 2019, while the period 2020–2022 was considered separately as the final interval, as it does not cover a full decade. The analysis reveals that the average of accidents increased until the decade 2000-2009 and then decreased thereafter. The initial increase coincides with several factors, such as the spread of the Internet in industry and the increased interest in hydrogen as an alternative to fossil fuels, in response to the growing need for more sustainable solutions. The subsequent reduction in accidents coincides temporally with the introduction of the Seveso III Directive (2012/18/EU) in 2012, which established stricter regulations for the management of accidents involving dangerous substances, thus helping to improve safety and reduce the number of accidents through more effective preventive measures.

The data showed, as illustrated in **Figure 4.6**, that 77% of the incidents related to hydrogen-related material degradation occurred in the chemical and petrochemical sector, making it the most affected sector overall. This result can be explained by the fact that hydrogen is widely used in these sectors, both for the production and processing of various chemicals and petrochemicals. Then, with 7% of the incidents, there is the manufacturing sector, followed by 6% in the power generation sector. Both of these sectors, despite having a lower incidence of events, use hydrogen in processes, making its presence in their plants still relevant.

Regarding the equipment involved, shown in **Figure 4.7**, pipelines were the most affected component, with 52% of the incidents. This result could reflect the extensive use of pipelines in various industrial plants and their exposure to operating conditions that promote material degradation, such as pressure or corrosion. Process equipment is in second place with 18%, followed by machinery (17%) and storage equipment (10%). Interestingly, electrical equipment and the "other" category are affected in a very low percentage of 1.5% each. It is worth noting that storage equipment, despite being frequently exposed to hydrogen and may seem particularly vulnerable to hydrogen embrittlement, does not appear to be among the most affected categories. This could be due to the adoption of advanced technologies and more stringent safety measures in this type of equipment, such as the use of resistant materials or more rigorous monitoring systems. These factors could have contributed to a lower incidence in relation to storage equipment, compared to other components such as piping or process equipment.

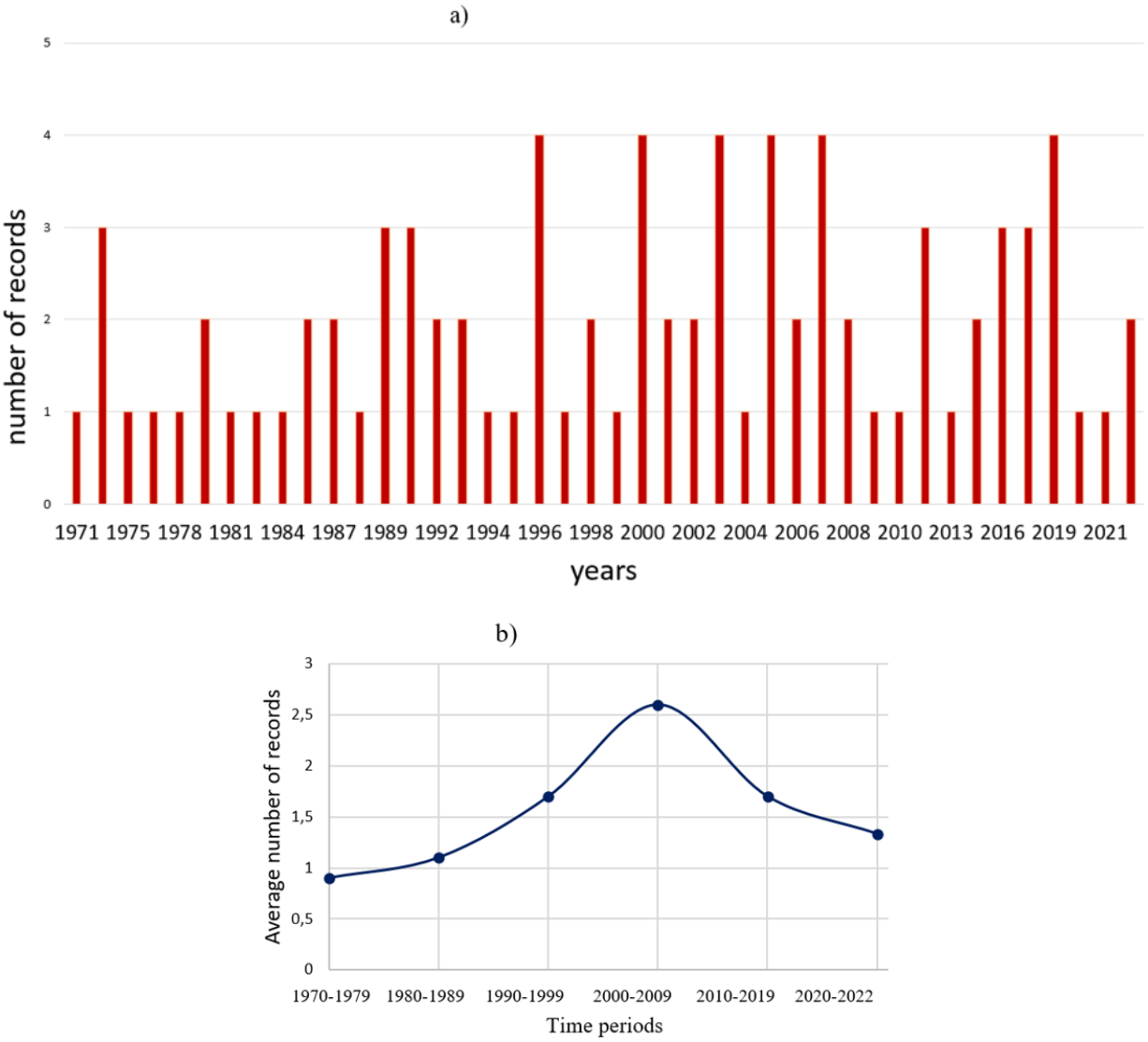

Figure 4.5: Time course of events due to material degradation in the presence of hydrogen. A) Number of reports for each year. B) Average number of incidents in different time periods, indicated on the x-axis.

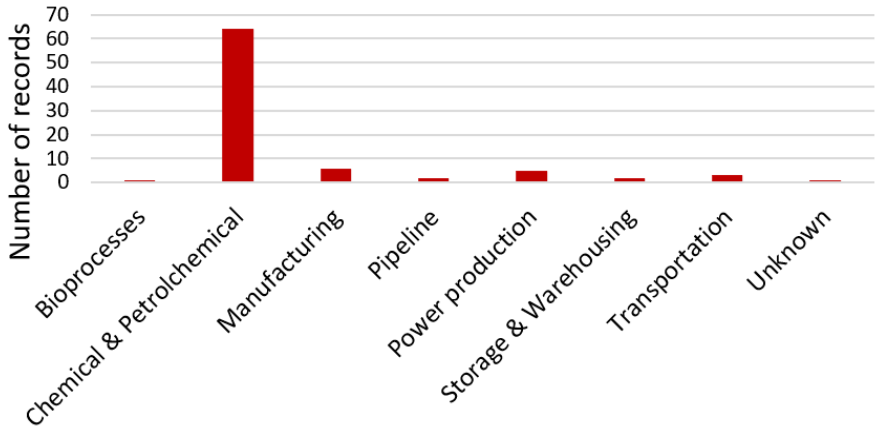

Figure 4.6: The incidence of events in the industrial sectors analysed.

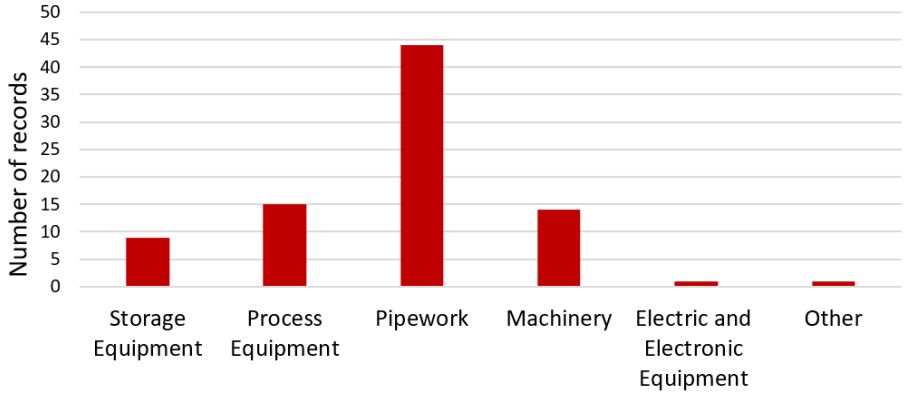

Figure 4.7: The equipment involved in the events.

Figure 4.8 presents the results of the analysis of 84 examined reports, through which the most frequent degradation mechanisms in industrial environments in the presence of hydrogen were identified. The three main mechanisms found are corrosion, hydrogen embrittlement and vibrations. Corrosion and hydrogen embrittlement are particularly relevant in contexts where hazardous substances are present in the equipment, since these substances can accelerate the deterioration of materials, promoting corrosion and structural damage. Instead, the high number of events associated with vibrations could be attributed to the mechanical stresses generated by the vibrations themselves, which can cause the formation of micro holes in the materials, with the consequent release of gas, particularly in the presence of hydrogen due to the size of its molecules.

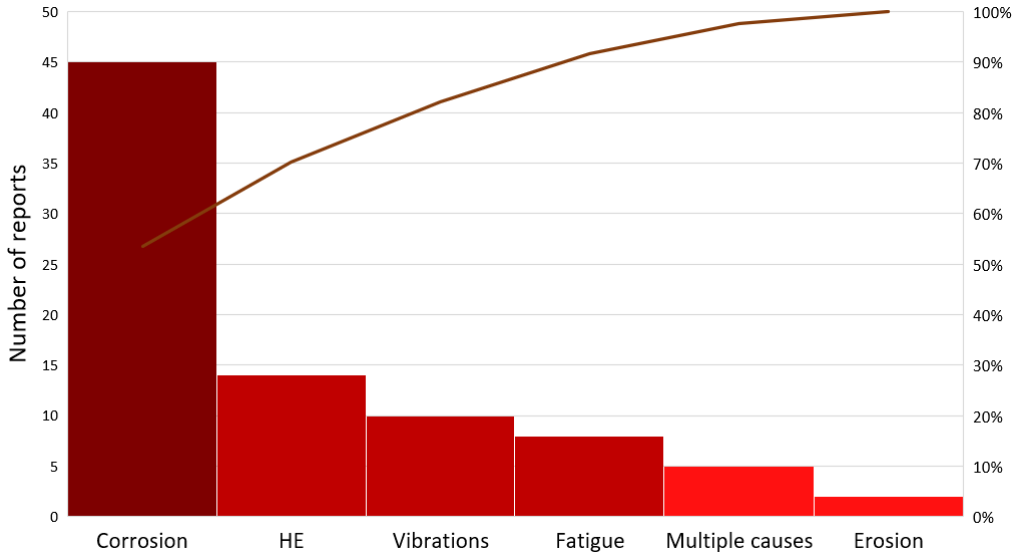

Figure 4.8: Degradation mechanisms in the 84 reports analysed.

The analysis reveals that in 12% of the reports, hydrogen was not initially present in the system, but was generated as a by-product of corrosion processes, which can be induced by both internal and external factors or due to welding operations. This phenomenon highlights the importance of considering the risks related to the presence of hydrogen even in systems where it is not initially expected. Hydrogen can be formed unexpectedly during the corrosion of metallic materials, where the chemical reaction with the environment produces hydrogen as a by-product, or during the welding process, where the high temperature can lead to the dissociation of molecules and the formation of hydrogen. Failure to take this possibility into account significantly increases the risk of undesirable events, as hydrogen is a highly flammable gas, capable of compromising the structural integrity of materials, causing leaks and, in the most serious cases, fires and explosions.

The analysis of the data, shown in **Figure 4.9**, highlighted that 36% of the recorded events were classified as accident and 39% as incident. It is important to underline that, in both cases, a fire always occurred, indicating that every time an event with significant consequences occurred in the presence of hydrogen, a fire was always involved. In the remaining 25%, the events were divided into two categories: 19% involved losses of containment, while a smaller portion was represented by near miss, a situation in which a potential risk occurred without generating actual damage.

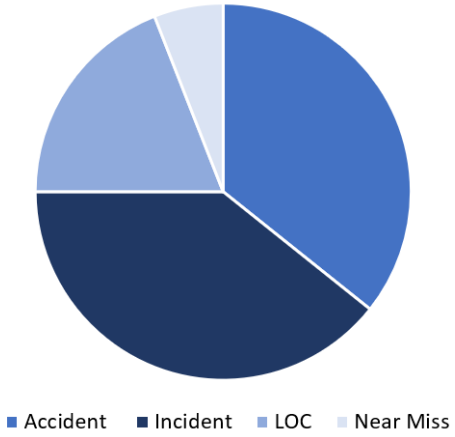

Figure 4.9: Outcome in the analysed records.

The relevant data of this scenario concerns the high flammability of hydrogen. This implies that even small gas leaks can be particularly dangerous, as the presence of an ignition source could trigger a fire or an explosion. Therefore, it is of fundamental importance to limit and control hydrogen leaks through adequate detection and intervention systems to prevent the occurrence of serious accidents.

Figure 4.10 presents the causes of the events in relation to the final scenarios. Among the main scenarios that emerged in the analysed accidents, there are explosions, fires and situations in which both an ignition and an explosion occur. These results are consistent with the intrinsic characteristics of hydrogen, which is known for its high flammability. However, some points require further reflection. In particular, in the cases of corrosion, it was noted that the release of hydrogen had no consequences in as many cases as those in which fires or explosions occurred. This phenomenon, defined as R-NFC, suggests that not all hydrogen leaks lead to accidents, despite the intrinsic risk. This scenario occurs with all degradation mechanisms. Furthermore, in the context of hydrogen embrittlement, the second most recurrent scenario is the nothing happened, so despite the deterioration of the material, the accident has not occurred. It is interesting to note that, in the cases of erosion and fatigue, phenomena related to factors internal or external to the plant but not to the substances contained, the most frequent scenarios are fires and explosions. These data suggest that the current safety measures may not be completely adequate. Although a number of events without consequences have been recorded, the presence of hydrogen leaks indicates the need to improve the safety system to reduce risks.

Finally, losses reported in the events analysed were examined. 20% of the incidents resulted in injuries, 7% caused fatalities, while 40% did not report any human losses. Regarding economic losses, only 28% of the reports provided specific data. Of these, 24% reported losses exceeding 1 million euros, while 4% reported losses below this figure. Regarding environmental impacts, 88% of the reports did not report any pollution. This may be attributed to the fact that gaseous hydrogen is not considered toxic or harmful to the environment. However, it should be noted that in 40% of the events, hydrogen is present together with other hazardous substances. These data highlight that economic impacts are the main effects of these events.

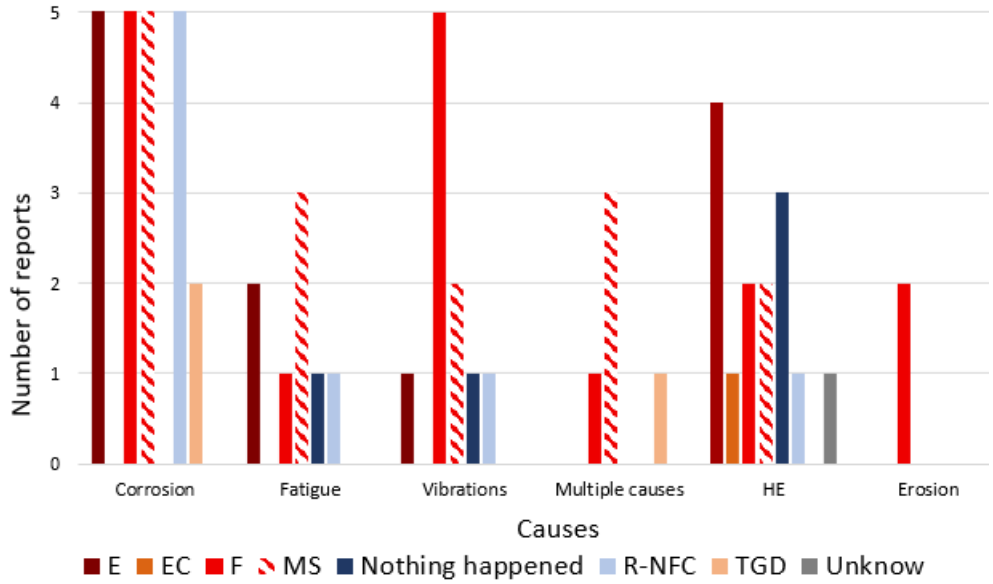

Figure 4.10: Degradation mechanisms of the studied events, in relation to the reported scenario.

The analysis highlights the need to implement safety measures, particularly in the chemical and petrochemical sectors, which have been found to be the most vulnerable to hydrogen. This exposure arises from the dependence of these sectors on plants and pipeline networks that are subject to corrosion and degradation due to hydrogen. The introduction of stricter regulations, such as those foreseen by the Seveso III Directive, can help reduce the number of accidents. It is important that the risk assessment also considers the possibility of hydrogen production, even in the absence of hydrogen within the plant, as it can be generated by processes such as corrosion or non-compliant welding. For this reason, it is necessary to take preventive measures and conduct a thorough risk analysis related to corrosion and hydrogen embrittlement, which are the main causes of potentially disastrous events, such as explosions or fires.

4.3 Monitoring of Hydrogen Leaks: Critical Review

Hydrogen leaks occur when hydrogen, commonly stored or transported in tanks or pipelines, escapes from the system. These leaks can occur for a variety of reasons, including both large holes and the molecular nature of hydrogen itself, which can easily escape from equipment. Large hole leaks are those caused by openings or structural defects in the equipment or transport pipelines. In this case, leaked hydrogen can be detected more easily as the breakdown of the material is visible. On the other hand, hydrogen leaks caused by its molecular nature, characterized by extremely small molecules, represent another challenge. Due to its small molecular size, hydrogen can penetrate through porous materials or seals, escaping from equipment even in the absence of obvious holes or structural defects (Vitale et al., 2024a). This type of leak can be particularly difficult to detect because hydrogen is a colourless and odourless gas. As a result, when a hydrogen leak occurs, there is no warning, making it more difficult to detect its presence in the surrounding environment. In addition, leaks from very small holes can easily generate jet fires, a sort of narrow and directional flame, since hydrogen

is highly flammable. This gas, indeed, has a wide flammability range and a low ignition energy level, which means that it can ignite and burn very easily; in these scenarios, even simple friction with the walls of the equipment can act as a trigger. The critical problem with these small fires is that they are not easily detectable in sunlight, as shown in **Figure 4.1**. Okino et al. (2017) conducted a study on the hydrogen flame, analysing its spectrum with the support of a spectrometer. The results showed that the hydrogen flame has an emission peak around 310 nm, a value that falls into the ultraviolet and not the visible. Consequently, if this phenomenon occurs in a process plant, operators or nearby personnel may not immediately realize that a fire is in progress. This lack of timely detection significantly increases the risk of accidents, as dangerous situations may arise. Therefore, it may be useful to use specialized detection technologies to continuously monitor the presence of hydrogen and prevent the occurrence of jet fires or other dangerous events.

For the reasons mentioned above, several studies have investigated methodologies to detect hydrogen leaks and study their characteristics. Wang et al. (2022) conducted a series of experiments to test a fluid dynamic model, using the Schlieren method and supported by a high-speed camera, as shown in **Figure 4.11**. During these tests, the focus was on the detection of hydrogen leaks, showing variations in the shape of the hydrogen flow in relation to the increase in pressure.

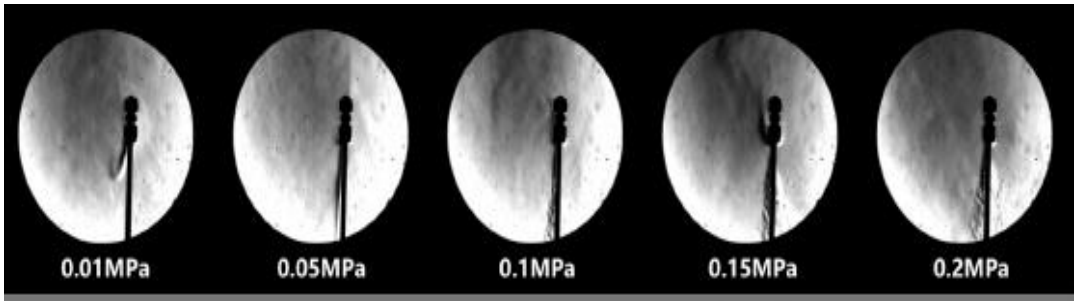

Figure 4.11: Schlieren method for detecting hydrogen leaks at various pressures in the pipeline upstream of the leak outlet: P = 0.01, 0.05, 0.1, 0.15, and 0.2 MPa. Image taken from Wang et al. (2022).

The grey gradient indicates the hydrogen gas flow. At pressures below 0.1 MPa, the hydrogen flow initially develops as a downward-directed, momentum-dominated jet, followed by a laminar flow phase. The flow shifts to the left due to interaction with the ambient air, with a crosswind speed between 0 and 1 m/s. When the pressure reaches 0.05 MPa, the hydrogen flow still appears as a laminar jet, with momentum being the main determining factor. However, when the pressure exceeds 0.1 MPa, the hydrogen jets start to interact with the surrounding air, inducing the formation of various types of turbulence and resulting in a transition from laminar to turbulent flow. When the pressure exceeds 0.15 MPa, the hydrogen flow enters a turbulent phase, generating a "tail-sweeping" phenomenon due to the atmospheric pressure directing the hydrogen flow towards the surface of the tube. Sugimoto et al. (2021) investigated the use of Raman scattering to measure hydrogen gas using Coherent Anti-Stokes Raman Spectroscopy (CARS), a nonlinear optical method that uses photon scattering. They found that this technology allows for faster detection of hydrogen leaks,

with a concentration range of 200 ppm up to 100% by volume, compared to other technologies that have longer response times and narrower detection ranges. Han et al. (2014) used a thin laser beam to pass through the central line of a hydrogen jet carrying Al2O3 particles. The particles were excited by the laser light, allowing the hydrogen jet to be visualized. The hydrogen concentration was determined by sampling the gas at five points along the central line of the jet. The authors simulated different configurations by varying the pressures and diameters of the exit holes. Experimental data showed discrepancies with the isentropic predictions presented by Birch et al. (1984), with measured values consistently lower than those estimated by the isentropic model. Roberts et al. (2006) focused on characterizing the hazards associated with hydrogen jet releases. They conducted controlled hydrogen release experiments with release pressures ranging from 1 to 15 MPa. During the experiments, hydrogen concentration measurements were taken to determine the extent of the flammable cloud that forms during the release. The data obtained from the tests were then compared with predictions generated by the HGSYSTEM model, previously developed and validated for hydrocarbon jet releases. The results showed that, in 8 of the 23 releases analysed, the experimental data were in excellent agreement with the model predictions. Campari et al. (2023) investigate the optimization of the positioning of ultrasonic sensors for hydrogen leak detection. Ultrasonic gas leak detectors (UGLD) detect acoustic ultrasound generated by the release of pressurized gas by detecting the pressure wave propagating at the speed of sound from the leak source to the sensor, thus enabling the detection of the gas leak. The study considers two distinct scenarios: release from a nearly empty tank and release from a tank under overpressure. The optimization of the UGLD placement was performed using a genetic algorithm, which simulated a set of possible configurations and identified the spatial arrangement of the sensors that ensures the maximum coverage area. Elaoud et al. (2010) propose a procedure for the detection, quantification and localization of leaks in a rigid pipeline carrying hydrogen or natural gas mixtures, based on the transient analysis of pressure and discharge time. The analysis is performed by solving a system of coupled nonlinear hyperbolic partial differential equations, using the method of specified time intervals, which allows an effective simulation of transient flows in the presence of leaks. The results show that the pressure signal is more effective in detecting leaks in the case of hydrogen than in natural gas. Russo et al. (2020) analyse hydrogen jet fires resulting from the immediate ignition of pressurized gas releases, with the support of a thermal imaging camera, evaluating the parameters that influence the potential damage, including the diameter of the release orifice and the gas pressure, through a large-scale experimental campaign. The experimental tests allowed to characterize the jet flame morphology and the associated thermal radiation, highlighting that for pressures above 300 bar and orifices with diameters between 3 and 5 mm, the flame can reach 8 meters in extension, determining potentially lethal conditions. In particular, a flame generated by a 3 mm orifice at 320 bar can cause second-degree burns up to 2 meters away, while a 5 mm orifice is associated with a 1% lethality risk.

Some studies, instead, have conducted experiments with the aim of

identifying temporal and spatial correlations for the formation of the hydrogen cloud and the flame. Hecht et al. (2019), performed cryogenic hydrogen release experiments with pressures ranging from 2 to 6 bar and temperatures up to -295°C, using exit holes with diameters of 0.75 mm, 1 mm and 1.25 mm to simulate low-flow releases, with a mass flow rate range between 0.1 g/s and 0.7 g/s. The study analysed, for each of the simulated conditions, the maximum ignition distance, which depends on the hydrogen pressure, the temperature and the diameter of the exit hole. A correlation between the variables was obtained, highlighting the dependence of the maximum ignition distance, x_{ign}, on the temperature and the diameter of the exit hole, D, given by **Relation 4.1**:

$$x_{ign} = 0.430D\sqrt{\frac{\rho_0}{\rho_\infty}} \quad \textbf{(4.1)}$$

where ρ_0 is the density of the gas in the chamber e ρ_∞ is the density of the release gas.

Gong et al. (2022) conducted experiments to model the release of hydrogen at sub-ambient temperatures and moderate pressures above atmospheric conditions, with the aim of analysing the concentration profile of the leak. Through the analyses conducted, the authors identified a correlation between the volumetric concentration of hydrogen CH2 (%Vol) and the distance from the release point x, demonstrating that this relationship depends on several key parameters. In particular, the concentration was expressed as a function of the diameter of the outlet orifice D, the air density ρ_a and the density of hydrogen at the nozzle ρ_a:

$$\frac{1}{c_{H_2}} = 0.000188\left(\frac{x}{D}\right)\sqrt{\frac{\rho_0}{\rho_a}} + 0.0064 \quad \textbf{(4.2)}$$

The diameter of the outlet orifice directly affects the rate of release, determining the amount of hydrogen released into the environment. The density of the ambient air plays an important role in the dispersion of the gas, since air has a higher density than hydrogen; therefore, it favours the expansion of the cloud. From **Formula 4.2**, it is possible to determine the distances at which the gas concentration falls within the flammability limits, thus the distances from the outlet hole corresponding to a concentration of 4% and 75%. The distances of interest are reported in **Table 4.1**. This allows the identification of the threshold beyond which the gas concentration no longer falls within the flammability range, ensuring safety conditions.

Table 4.1: Expressions of the distance from the release point to the point where the desired hydrogen concentration is present in space. Image taken from Gong et al. (2022).

The key hydrogen concentration	Expression
4% (the lower flammable limit)	$x_{4\%} = 1295.74 \cdot D \cdot \left(\frac{\rho_a \cdot R_{H_2} \cdot T}{p}\right)^{-0.5}$
75% (the upper flammable limit)	$x_{75\%} = 36.88 \cdot D \cdot \left(\frac{\rho_a \cdot R_{H_2} \cdot T}{p}\right)^{-0.5}$
4%– 75% (flammable length)	$L_f = 1258.87 \cdot D \cdot \left(\frac{\rho_a \cdot R_{H_2} \cdot T}{p}\right)^{-0.5}$
11% (the lower detonability limit)	$x_{11\%} = 449.52 \cdot D \cdot \left(\frac{\rho_a \cdot R_{H_2} \cdot T}{p}\right)^{-0.5}$
1% (a quarter of the LFL)	$x_{1\%} = 5285.11 \cdot D \cdot \left(\frac{\rho_a \cdot R_{H_2} \cdot T}{p}\right)^{-0.5}$

Computational Fluid Dynamics (CFD) is widely used to investigate and study accidental hydrogen releases and related dispersion phenomena, providing detailed information on jet behavior, buoyancy effects, and the interaction between hydrogen plumes and the surrounding environment, including the presence of obstacles and complex geometries. Numerous studies have demonstrated that CFD simulations are an effective tool for supporting the design and optimization of hydrogen safety and leak detection systems, enabling, for example, the identification of critical accumulation zones and the definition of optimal sensor placement strategies (Koutsourakis et al., 2023; Giannissi et al., 2020; Giannissi et al., 2015; Makarov et al., 2009). More recent studies have further highlighted the role of CFD in analyzing the consequences and assessing the risk associated with hydrogen releases. In particular, Calabrese et al. (2024) showed that advanced CFD models can more accurately describe hydrogen leakage phenomena than simplified empirical models, highlighting their potential for analyzing hazardous areas and supporting safety decisions. Similarly, the work of Portarapillo et al. (2025) analyzes hydrogen release scenarios through high-resolution CFD simulations, highlighting the influence of operating conditions and geometric configurations on the distribution of concentrations and residence times of the gas in confined or partially confined environments.

Although CFD represents a powerful tool for understanding hydrogen leakage mechanisms, its direct application for real-time leak detection and monitoring is generally limited by its high computational requirements, the need to accurately define boundary conditions, and the requirement for advanced skills in setting up, running, and interpreting simulation results. For this reason, CFD is more widely used in an offline context, where it can significantly contribute to define representative release scenarios by assessing the expected performance of detection systems and the associated risk. In this context, CFD-based analyses can be effectively integrated with real-time monitoring technologies, supporting their design, positioning, and validation.

4.3.1 Static vs Dynamic Monitoring

The reviewed studies aim to identify hydrogen leaks in order to improve system safety. In particular, leak monitoring is mainly conducted in static mode, that is, through the collection of data in stable operating conditions and without

significant variations over time or in the environment (Campari et al., 2023). This approach is commonly used to assess the state of a system at a precise point in space at a given time. Alternatively, monitoring can be performed in dynamic mode, which involves the collection and analysis of data in real time during normal system operation or under variable load conditions (Yang et al., 2018; Burgués et al., 2019). This approach exploits advanced sensors for the detection of process anomalies, allowing a continuous assessment of the plant status and an early identification of potential failures, thus improving operational reliability. The two monitoring methods are complementary to ensure the safety and efficiency of industrial plants. While static monitoring provides a picture of the operating conditions at a given point in the plant at a certain moment in time, dynamic monitoring allows for real-time performance analysis, allowing timely interventions in the event of anomalies or critical conditions.

In the case of hydrogen, static monitoring has already been widely discussed in the literature; on the contrary, dynamic monitoring has been little explored but could represent a valid alternative for the instantaneous detection of leaks in industrial environments. This type of monitoring can be carried out with the aid of platforms capable of obtaining data, such as photographs and/or videos, from different altitudes and consequently with a different spatial-temporal resolution. The aerial platforms used today are drones, aeroplanes, satellites or alternatively terrestrial types such as trucks and tractors (Pillosu, 2020). With these systems, it is possible to monitor the environment and infrastructures more or less accurately and at different time intervals depending on the chosen technology:

- monitoring large areas over time allows you to check any changes in the site, which may be caused by fluid leaks, comparing conditions day by day or at previously chosen time intervals. The platforms that are suitable for obtaining information over time are satellites, whose data present a global view of the Earth's surface but with lower precision. Obtaining data and post-processing, in this case, are not very complex.
- instantaneous inspection allows you to study small areas of the site, obtaining more accurate information. This type of inspection is in real time, so the data collected reveals the current condition of the area of interest. The platforms that are suitable for obtaining similar information are mainly drones, which cover limited areas with higher resolution data. When using drones, it is necessary to install a device that allows you to obtain information. This instrument is a sensor that can have as its objective the detection of released gases or small fires that are not easily identifiable, with the acquisition of photos and/or videos at a safe distance. Or it can calculate the concentration of the gas in the atmosphere.

Figure 4.12 shows the main monitoring platforms used, highlighting their respective flight altitudes. In particular, satellites operate at an altitude of about 600 km, manned systems reach approximately 200 m, while drones fly up to 150 m.

.

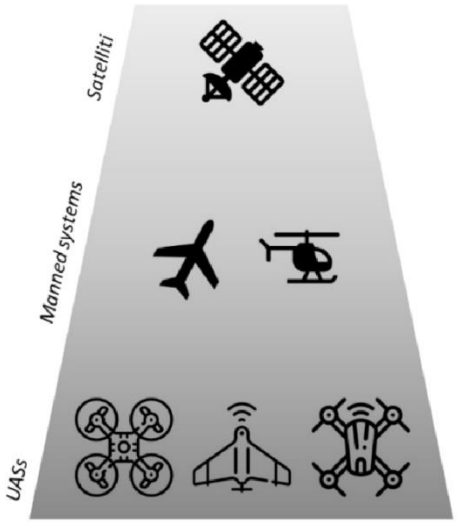

Figure 4.12: Aerial platforms that can be used for area monitoring. Image taken from Casabona (2020).

Several studies have applied the listed methodologies, both to support precision agriculture to maximize yields (Hu et al., 2022; Rejeb et al., 2022; Pillosu, 2020; Daponte et al., 2019; Spalevic et al., 2018; Murugan et al., 2017) and to monitor sites where containment losses can be found (Li et al., 2023; Bel Hadj Ali et al., 2020; Burgués et al., 2019).

The present study aims to detect small-scale containment losses; therefore, the most suitable platforms for the analysis are those with higher resolution and therefore traveling at lower altitudes. Drones, also known as unmanned aerial vehicles (UAV), are vehicles that can operate without the need for human operators on board (Greenwood et al., 2019). These platforms cover limited areas, which means that the data has greater precision and resolution, and is more flexible and versatile than satellites. Drones are piloted from the ground by an operator, who can program the flight plan in advance or adjust the direction, altitude and speed during the flight itself. There are three types of drones:

- Fixed Wing: Fixed-wing drones, in **Figure 4.13**, have a configuration similar to that of traditional aeroplanes, with a fixed wing that provides lift during flight. These platforms are optimal for prolonged missions and for covering large areas, such as for surveillance, research and environmental monitoring activities.
- Rotary wing: these platforms, in **Figure 4.14**, are equipped with multiple rotors, usually four or more, which allow vertical take-off and manoeuvrability in narrow spaces. They are mainly used for aerial photography, video, mapping and inspections.

Figure 4.13: Example of a fixed wing drone. Image taken from Greenwood et al. (2019).

Figure 4.14: Example of rotary wing drone. Image taken from Greenwood et al. (2019).

- Vertical Take-Off Landing (VTOL): these aircraft, in **Figure 4.15**, combine the peculiarities of multirotors and fixed-wing aircraft, allowing them to take off and land vertically like a multirotor, but to transform into a fixed wing for high-speed flight and long-distance coverage.

Figure 4.15: Example of VTOL drone. Image taken from Greenwood et al. (2019).

The choice depends on the application. Drones are widely used for the control and management of civil infrastructures, but recent studies have also implemented these platforms in the industrial sector, both for visual analysis (Druart et al., 2021; Watremez et al., 2018; Casabona, 2020) and for the detection of gas leaks (Burgués et al., 2022; Burgués and Marco, 2020; Barchyn et al., 2019; Yang et al., 2018). For example, Taj et al. (2020) use a drone to obtain images to detect cracks on the wall of a tank containing water. The study compares colour and thermal images. While Casabona (2020) uses data obtained from drones and satellites to train neural networks in order to monitor portions of land of variable size.

4.3.2 Sensors

The use of drones requires the integration of a data acquisition system to enable information retrieval during operation. The sensors strictly depend on the application. For the study of leaks, the sensor can have the purpose of:

- calculating the concentration of the gas in the atmosphere. To obtain this type of information, the drone needs to fly in contact with the dispersed gas; in this way, the sensor will be able to calculate its quantity. Different studies have implemented this type of sensor for the calculation of the concentration of chemical substances. Burgués et al. (2019) use MOX (metal oxide semiconductor) to calculate the concentration of ethanol present in the chamber. Koval et al. (2017) instead use a catalytic sensor for the detection of methane. No studies on the detection of hydrogen using drones equipped with dedicated sensors have been identified. However, different types of sensors are available that can detect this gas (Qanbar and Hong, 2024).
- detecting released gases or small fires that are not easily identifiable, by acquiring photos and/or videos from a safe distance. Therefore, this methodology is more suitable for flammable or corrosive substances that could deteriorate or cause the equipment to fail. For this technology, no studies were found for the application in the case of hydrogen. An application for leak detection is presented in the study by Druart et al. (2021), who used a drone equipped with an infrared camera to detect methane emissions from a storage tank. The test was conducted at three different flight heights: 80 m, 40 m and 20 m, with gas leaks of 200 g/s, 10 g/s and 1 g/s, respectively. The results obtained (represented in **Figure 4.16**) demonstrated that even the smallest methane leaks can be clearly identified already at 80 m of height. This type of surveillance has advantages in terms of speed in

obtaining real-time data, the ability to detect gas leaks safely, and the possibility of quantifying their concentration. However, not all cameras are suitable for this analysis; they must be equipped with an optical filter that absorbs the spectral bands of the gas analysed.

Li et al. (2023) identified gaseous emissions using a multispectral camera. Their study monitored the emissions of NH_3, SF_6, CH_4, and SO_2 (**Figure 4.17**) at a distance of 50 m, demonstrating that a surveillance system based on multispectral infrared cameras is able to detect gases even at long distances, up to several tens of meters and up to kilometres away.

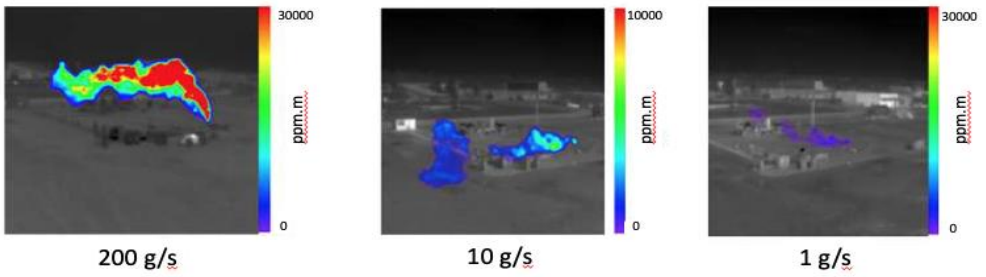

Figure 4.16: Images obtained from an infrared camera for the detection of methane leaks, at different heights, from right to left at 20m, 40m and 80m. Images taken from Druart et al. (2021).

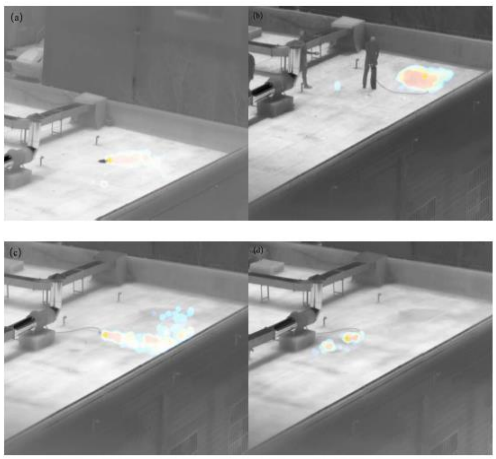

Figure 4.17: Images obtained from a multispectral camera to detect: (a) Ammonia (NH_3); (b) Sulfur hexafluoride (SF_6); (c) Methane (CH_4); (d) Sulfur dioxide (SO_2). Image taken from Li et al. (2023).

Watremez et al. (2018) and Doz et al. (2018) detected a methane cloud with a high-resolution hyperspectral camera and an infrared camera, managing to identify the cloud at 100m away and calculating its concentration. The study was implemented with a LIDAR, an absorption laser used to measure atmospheric gases capable of quantifying their flow rate.

A literature analysis was conducted on the type of instrument that can be used on the hydrogen detection platform (Post et al., 2021). The sensors that can be used include different types of instruments, characterized by different operating principles. The operating principle of an instrument is the mechanism or physical phenomenon on which its operation is based to perform a measurement. This principle determines how the instrument converts a physical quantity (e.g. pressure, temperature, force) into a readable signal or into a useful measurement. Based on an analysis of the scientific literature and the instruments currently

available on the market, the devices identified as the most suitable for the detection of hydrogen are reported below:

- *Concentration detectors* have been used in scientific literature for hydrogen leak monitoring. However, a limitation of this methodology is that the drone must fly in proximity to the gas, which entails safety risks. Indeed, the hydrogen cloud is in continuous movement and, consequently, an area that initially appears safe with low gas concentrations can, in a very short time, transform into an area with high concentrations, putting the vehicle and equipment at risk (Burgués et al., 2022). The most common typologies for hydrogen detection are: i) semiconductor hydrogen detectors that exploit the variation of the electrical conductivity of semiconductor materials in the presence of hydrogen. The interaction of hydrogen with the semiconductor material causes a modification of its electrical resistance, which can be detected and measured to determine the concentration of hydrogen in the environment. ii) Electrochemical hydrogen detectors that include electrodes that react with hydrogen, generating an electrical signal proportional to the hydrogen concentration present. These sensors often use an electrolyte to facilitate the electrochemical reaction, thus improving the detection efficiency. iii) Catalytic hydrogen detectors, which employ a catalyst that facilitates the reaction of hydrogen with another chemical, causing a change in the electrical or optical properties of the sensor (Buttner et al., 2011). This change can be detected and measured to determine the presence and concentration of hydrogen in the environment. Some examples: i) NLBN Detector, ii) Detector Boldringroup, iii) Detector Drawing Cad, iv) Detector it sensor
- *The Schlieren method* is based on the principle that light is bent when it passes through regions of fluid with different refractive indices. The Schlieren method uses a light beam that is parallelized through a collimator (usually a lens). The light beam then passes through hydrogen (Wang et al., 2022), which has variations in refractive index (e.g., due to temperature or density gradients). These variations cause the light to bend, and the parabolic mirror collects and reflects the bent light back to a focal point. The next step is to use an iris diaphragm to block the light that has not been bent, allowing only the light that has been bent by the fluid to pass through. This helps to improve contrast and highlight differences in density or temperature gradients. Finally, a high-resolution camera or other imaging system (e.g., a high-speed video camera) is used to capture the image that shows the variations in the refractive index of the hydrogen, which manifest as bright or dark lines in the final image. Therefore, a collimating lens, a parabolic mirror, a diaphragm and a camera or display system are needed. The problem with this method is that the equipment needed is not suitable for industrial use, due to its complexity.
- *CO_2 detection camera* as a tracer, but this technology is valid for

hydrogen storage with significant CO_2 concentrations, therefore not in the case of pure hydrogen: link. These instruments are based on infrared (IR) spectroscopy, exploiting the ability of CO_2 molecules to selectively absorb infrared radiation. In particular, CO_2 has characteristic absorption bands in the mid-infrared range, generally between 4.2 and 4.3 µm (Hosch, 2019). The camera uses an array of IR sensors to measure spatial variations in the absorption of infrared radiation, thus allowing the generation of a representative image of CO_2 distribution in the observed area.

- *Thermal imaging camera* that uses an infrared sensor to capture the infrared radiation emitted by objects in the observation area. Indeed, every body with a temperature above absolute zero (-273.15 °C) emits electromagnetic radiation in the infrared range. The intensity and wavelength are determined by the temperature of the body and its emissive properties, such as emissivity and the nature of the material. This can be used to detect flames generated by hydrogen combustion (Russo et al., 2020), as the thermal imaging camera is sensitive to the temperature variations associated with the flame. When hydrogen is released into the environment and ignites, the thermal imaging camera detects the heat produced by the flame, displaying the high temperature. From simulations conducted using the PHAST software, it was observed that, when hydrogen is released into the atmosphere through holes of sufficiently small dimensions, approximately 1 mm in diameter, in the absence of ignition, the temperature at the exit of the hole can drop below 0°C, creating a thermal gradient with respect to the ambient temperature. **Figure 4.18** shows the temporal profile of the temperature at the exit hole as a function of the hydrogen storage pressure inside the tank.

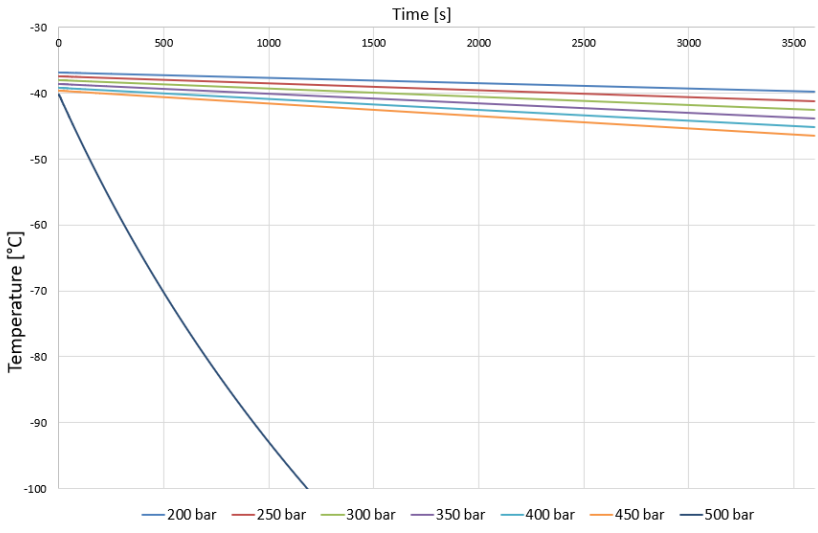

Figure 4.18: Temperature trend over time at the hydrogen outlet hole in the absence of ignition, as the storage pressure varies.

It is observed that, at the time of release, despite the storage temperature being set equal to the ambient temperature, the temperature at the exit hole is lower than -30°C for all the pressures

considered and then decreases further over time. For pressures between 200 and 450 bar, the temperature decreases gradually over time, following a similar trend. However, at 500 bar, a more marked and sudden change in temperature is observed. This behaviour may be attributed to more intense release phenomena due to the high pressure, which may generate accelerated cooling due to the Joule-Thomson effect (Chae et al., 2020), a thermodynamic phenomenon that describes the temperature change of a real gas when expanded under a constant enthalpy. This deviation suggests that, beyond a certain pressure threshold, the thermal behaviour of cryogenic release no longer follows a linear trend. Examples of instruments are: i) Thermal camera Flame, ii) Thermal camera between -20°C and 350°C.

- *Ultrasonic Gas Detector (UGLD)* is an instrument used to detect leaks of compressed gases, including hydrogen stored under pressure, by using the technology of detecting the high-frequency sound produced by gas leaks. Ultrasonic detectors for detecting hydrogen releases are particularly effective in open, well-ventilated environments where wind can disperse the gas, making it difficult to detect with traditional concentration-based sensors. In these conditions, a UGLD instantly detects the ultrasonic sound generated by the escaping pressurized gas. The sound wave travels to the detector, which senses it and activates the alarm signal. UGLDs are designed to filter out audible noise, detecting only ultrasonic frequencies between 25 kHz and 70 kHz. This feature allows small leaks to be identified without the interference of background noise in the audible frequencies. The overall response time of a UGLD is determined by the intrinsic detection delay, which can vary between 10 and 30 seconds, and the ultrasonic propagation time, which is in the order of milliseconds. The sensor coverage also depends on the ultrasonic background noise, the minimum leak rate to be detected, and the pressure of the released gas (Post et al., 2021; Campari et al., 2023). However, the industrial environment in which these detectors are used is often characterized by a high level of ambient noise from machinery, production processes, and other sources of sound. This background noise can interfere with the sensors acoustic ability to distinguish signals produced by gas leaks, altering the accuracy of the data and making it more difficult to accurately detect leaks of hydrogen or other compressed gases.
- *Ultrasonic camera,* although there are no specific studies on the use of this technology for hydrogen detection, ultrasonic cameras could still offer advantages over traditional detectors. The camera is based on ultrasonic acoustic sensors, which are designed to detect high-frequency sound waves, generally above 20 kHz, and therefore inaudible to the human ear. Unlike traditional microphones, which typically operate in the audible frequency range (20 Hz – 20 kHz), ultrasonic acoustic sensors are able to detect frequencies above 20

kHz, suitable for applications that require high sensitivity and precision in capturing physical events. The signal collected by the sensors is then processed by the camera processor, which analyses the intensity, frequency and arrival time. The processing results are finally displayed via a sound map or a thermal image, which provides information on the location and intensity of the detected sound, allowing the identification and monitor of anomalous acoustic events in real time. Although these cameras do not directly measure the gas concentration, they can help locate the leak. The main advantage over ultrasonic detectors is the ability to view the equipment in real time, making the analysis more intuitive. Tool examples can be: i) Ultrasonic camera Cs-Instruments, ii)Ultrasonic camera Flir, iii) Ultrasonic camera Fluke.

- *Tunable Diode Laser Absorption Spectroscopy (TDLAS)* is an advanced technology that can be used to detect gases such as hydrogen, particularly to identify leaks in industrial sites. Tunable diode laser absorption spectroscopy is a technique in which a laser with a frequency (wavelength) tuned to a specific absorption line is used to measure the intensity of light passing through the sample. The measurement system is simple and comprises a laser, a detector and the sampling volume between the two. The diode laser is a compact and robust light source, ideal for spectroscopy, as it operates at room temperature and provides intense monochromatic light. The diode lasers used in TDLAS can be tuned to emit at specific wavelengths by varying the temperature or laser injection current. In TDLAS, the laser wavelength is scanned across the absorption band of a target gas to record the complete spectral profile. Gas absorption is observed as a variation in the transmitted light intensity, with an absorption peak corresponding to the resonant frequency of the target molecule (Lackner, 2007). A TDLAS imager represents an advanced application of TDLAS technology, integrated with imaging techniques (spatial visualization). This combination allows the acquisition of spectral data related to gas concentration and the generation of spatial images representing the distribution of gases in a specific environment. The adoption of this technology allows real-time monitoring and analysis of hydrogen leaks, optimizing operational efficiency and promoting the climate benefits associated with the production and use of hydrogen as an energy source. However, this technology, similarly to the Schlieren method, presents difficulties in industrial application due to its operational complexity and the large areas to be monitored, which complicate its large-scale adoption.

4.3.3 Hydrogen and Infrared

Hydrogen cannot be detected effectively by infrared (IR) spectroscopy because of its unique spectral characteristics, which differ significantly from those

of other gases commonly detected by this technique, such as CO_2, methane, or water vapour. Hydrogen is a light, symmetric molecule. One of the main reasons why it does not have significant absorption bands in the infrared is its molecular symmetry and vibrational structure. Hydrogen molecules, being symmetrical, do not have permanent dipole moments strong enough to interact with infrared radiation. More specifically, infrared light does not induce significant vibration in the H-H bond that can lead to absorption of radiation. The vibrations that occur in the hydrogen molecule are very weak and not strong enough to interact effectively with infrared light. Infrared wavelengths, which are commonly used in IR sensors for gas detection, are absorbed by molecules that have vibrations and rotations strong enough to interact with IR light. Hopfield and Dieke (1926) detected the absorption spectrum of molecular hydrogen in the extreme ultraviolet.

Gases such as CO_2, methane, and water vapour have very different spectral characteristics. These molecules have vibrations and rotations that are activated by infrared radiation, causing strong absorptions at specific wavelengths. For instance, CO_2 has a prominent absorption band in the infrared near 4.3 μm (Ferriso, 1962; Howard et al., 1956), which coincides with a stretching vibration of the C=O bond. This vibration is strong enough to interact with IR light, making its detection possible. The same is true for methane, which has absorption bands in different regions of the infrared spectrum (Byrom and Shine,2022). Water vapour also has strong absorption bands in the infrared, especially in the regions around 1.4 μm and 2.7 μm, related to the stretching and bending vibrations of the O-H bond. The presence of these absorption peaks allows for very sensitive detection of water vapour, even at low concentrations (Hosch, 2019).

4.4 PHAST Simulations

A simulation plan has been developed that includes the use of software specialized in the analysis of consequences, with the aim of reproducing and studying different phenomena related to emergency situations. Specifically, the plan aims to examine hydrogen release, simulating gas dispersion dynamics and the effects of any accumulation, in order to assess the risks of explosion or the formation of explosive mixtures. These simulations are also instrumental in the development of advanced leak detection systems, providing useful data for the calibration and validation of these models. In addition, the behaviour of the gas or vapour cloud is analysed to understand its propagation and to identify the risk areas. As discussed in **Section 4.3**, CFD simulations are a useful tool for analyzing hydrogen dispersion and defining representative release scenarios, but they have some limitations. Based on these considerations, this analysis focuses on the use of consequence modeling tools that are easily implemented in an industrial setting and offer significantly reduced computation times to support hydrogen leak detection strategies. PHAST software was chosen, as it allows for rapid simulations on a large number of scenarios, providing reliable results for risk assessment and the design of safety measures. The software also allows the examination of the radiation emitted by a possible jet fire, that is, a directional fire caused by a release of flammable gases at high pressure (Palacios and Rengel,

2020), and to determine the intensity and extension of the affected area. Another aspect studied concerns the areas that could be affected by a flash fire, that is, a rapid and intense fire that develops following the ignition of a mixture of air and a flammable substance dispersed in the environment (Shelke and Wen, 2020), with the aim of identifying the critical areas and predicting the propagation of the fire. Finally, the plan includes the analysis of the overpressure waves generated by a possible explosion, to determine the impact of the shock waves on structures and people. In general, the use of this software allows the modelling and quantification of the effects of dangerous scenarios, providing useful information for the risk assessment and the definition of targeted intervention plans.

PHAST Software

PHAST (Process Hazard Analysis Software Tool) is an advanced tool designed to support the analysis and modelling of risks related to chemical accidents in industrial plants. It allows the simulation and the analysis of complex scenarios, such as the release of hazardous substances, and to study their interactions with the surrounding environment, considering variables such as weather conditions, topography and other relevant factors.

The software offers a range of useful functions to assess and model risks in detail. The input data required for simulations depends on the type of equipment being considered. For instance, in the case of tanks and pipes, information must be provided regarding the type of equipment, its dimensions, the characteristics of the release, the material contained and the operating conditions at the time of the incident. When the data has been processed, PHAST generates a range of simulation results, including concentration-time and concentration-space curves for hazardous substances, temperature and pressure graphs, curves representing the thermal radiation of fires and overpressure curves, useful for assessing the risks associated with explosions. It also provides dose curves that quantify the health hazards arising from exposure to toxic substances.

PHAST is able to simulate the dispersion of chemicals released into the environment during an accident, considering atmospheric factors that influence propagation, such as wind speed and atmospheric stability. For combustion, the software calculates the combustion speed, flame length and composition of combustion products. In explosion simulation, PHAST evaluates the intensity of the overpressure wave generated, a crucial element to determine the impact on people and structures. Furthermore, it is able to analyse the effect of toxic substances on human health, considering the risks arising from prolonged exposure.

All simulation results are documented and can be exported to Word or Excel files for easier management and subsequent analysis. In summary, PHAST presents itself as an extremely versatile tool for industrial risk assessment, allowing companies to improve safety management and ensure safer working environments through accurate simulations and an in-depth assessment of chemical risk scenarios (DNV, 2018).

The decision to use PHAST software for industrial risk assessment was influenced by various factors, both theoretical and practical, supported by

numerous scientific studies and field experience.

Several comparative works have examined the reliability and performance of PHAST compared to other simulation tools used for the analysis of the consequences of industrial accidents. These studies have highlighted the main strengths of the software, such as its high accuracy in predicting the outcomes of risk scenarios and its ability to model complex industrial scenarios in detail, including those involving the release of hazardous substances, explosions and fires. Recent research (Khorram, 2020; Ekerold, 2014; Lee et al., 2018) has shown that PHAST provides accurate and reliable predictions of outcomes in various scenarios, making it a valuable tool for consequence analysis in emergency situations.

Another reason for choosing PHAST is its widespread use in the industrial sector. Many companies use it as a primary tool for safety management and risk analysis, especially for determining safety distances and assessing the impacts of the consequences of incident events. PHAST's ability to simulate complex events in a realistic way and to provide crucial data for emergency management makes it a prime option for industrial safety analysis. Finally, one aspect that contributed to the choice of PHAST is its user interface, which is designed to be particularly intuitive. This allows operators, even those with limited experience in the field of risk modelling, to use it effectively. The accessibility of the software, combined with the robustness of its analytical capabilities, makes it a useful and easily implementable tool even in industrial environments where resources may vary.

Khodadadi-Mousiri et al. (2023) focused on consequence modelling and root cause analysis of a real explosion of a pressure vessel containing methane in the separation unit of a gas refinery in Iran. The main objective of this study was to model the incident using PHAST software and determine a confidence interval for the safety distance, with the aim of reducing the impact and severity of consequences of future events. The results showed that methane use in various settings is associated with significant safety risks, and the consequence modelling results closely matched the range of damage observed in real situations. MacNguyen (2023) reviewed and evaluated the main flammable hazards associated with emissions of common hydrocarbon fuels (CH4 gas, LNG, LPG) and hydrogen. At equivalent pressure and temperature, large emissions (150 mm holes) of hydrogen gas were observed to disperse over shorter distances than methane. However, for smaller emissions (25 mm holes), hydrogen leaks resulted in longer dispersion distances than methane. Additionally, at equivalent pressures and temperatures, jet fires caused by hydrogen gas leaks had shorter flame lengths and thermal hazard distances than those caused by methane leaks. The flame velocities of hydrogen were significantly higher than the hydrocarbon fuels studied. The results also indicated that hydrogen generated smaller pool fire hazard zones than equivalent emissions of hydrocarbon fuels. Wang and Ma (2021) used PHAST software to simulate hydrogen diffusion, explosion, and jet fire radiation safety distance in a hydrogen refuelling station, considering a pressure range of 20 MPa to 43.8 MPa and release holes of 10 mm to 18 mm. The results showed that the diffusion of the combustible gas cloud occurs very rapidly, and as the release pressure and hole size increase, the required safety distance also

increases. The cloud dispersion distance and jet fire radiation were evaluated at wind speeds of 1.5, 3, and 5 m/s, with an atmospheric stability class of D. The results indicated that under high wind speeds, it is necessary to increase the safety distance between hydrogen refuelling stations and surrounding areas.

This shows that the PHAST software has already been used in the literature to simulate hydrogen release scenarios; most studies have focused on large-scale releases or standard operating conditions. In this work, however, the simulations were applied to small-scale releases, difficult to detect with traditional methods, and under variable environmental conditions. The goal is not only to validate the software but also to extract quantitative parameters to be integrated into a predictive model for the localization of the release source. No previous studies explicitly validating PHAST for hydrogen releases were identified, for this reason a validation phase was conducted. To this end, the results obtained were compared, when available, with experimental data reported in the literature. Where no experimental studies were found, validation was performed by comparing the PHAST results with CFD simulations already published and validated by the authors, thus ensuring that the results were reliable even without directly performing CFD simulations in this work. This approach supports the development of a dynamic monitoring methodology using drones, which represents an innovative contribution compared to existing studies. The simulation results provide the operational basis for defining safe flight trajectories and improving emergency response strategies.

4.4.1 Validation PHAST Software for Gaseous Hydrogen

Validation simulations reproduced two distinct scenarios: hydrogen gas releases under pressure and releases at sub-ambient thermal conditions, replicating the experimental conditions described by Gong et al. (2022) and Han et al. (2014). Both studies provide experimental data relating to the spatial distribution of hydrogen concentration along the jet axis. These results were used as a reference to compare the concentration profiles obtained with the PHAST software, considering the maximum concentration over time as a function of the distance from the release point. The values used in the simulations are reported in **Table 4.2**. Three simulations were performed at a pressure of 5 bar, with variable outlet diameters of 1 mm, 1.5 mm and 2 mm. For each outlet diameter, three different temperatures were simulated, equal to 200K, 250K and 300K. Three other release scenarios were simulated at room temperature, with an outlet diameter of 1 mm, in a tank subjected to pressures of 200, 300, and 400 bar respectively.

Table 4.2: Simulations of hydrogen releases from storage tanks as pressure, storage temperature and outlet hole diameter vary.

Simulation number	Equipment	Pressure [bar]	Hole Diameter [mm]	Height of the release [m]	Temperature [K]		
1	Storage tank	5	1	1	200	250	300
2	Storage tank	5	1.5	1	200	250	300

3	Storage tank	5	2	1	200	250	300
4	Storage tank	200	1	1	288		
5	Storage tank	300	1	1	288		
6	Storage tank	400	1	1	288		

For each simulation, the maximum gas concentration along the axis of the exit point was plotted in relation to the downwind distance. The wind speed was set to 1.5 m/s, a common value for atmospheric dispersion simulations. Furthermore, an atmospheric stability of type F was considered, which represents a very stable atmospheric condition, according to the classification of Kahl and Chapman (2018). This type of atmospheric stability suggests calm and little turbulent air, which favours the slow dispersion of gases and is often used in consequence assessment simulations for industrial plants, where gas dispersion conditions can have a significant impact on safety.

Simulation results at sub-ambient temperature

In order to validate the reliability of the PHAST software in simulating hydrogen release scenarios, the experimental study by Gong et al. (2022) was used as a reference. However, this study does not report the experimental data, but only proposes an empirical correlation derived from them. Therefore, the results obtained from the PHAST simulations were directly compared with this correlation, as it represents the only quantitative reference available for validation. The mean absolute percentage error (Hyndman and Koehler, 2006) between the experimental results obtained by Gong et al. (2022) and those obtained by PHAST was calculated according to **Formula 4.3**:

$$MAPE = \frac{1}{n}\sum_{i}^{n}\frac{Y_i - y_i}{Y_i}100 \quad \textbf{(4.3)}$$

where n represents the total number of Y_i concentration values simulated by the PHAST software, while y_i is the expected concentration value, obtained from the experimental data. **Formula 4.3**, which is used to compare the simulated values with the experimental ones, allows the evaluation of the difference between the simulated and expected values, in order to quantify the accuracy of the simulation with respect to the real data. **Table 4.3** reports the values of the average absolute percentage error, in which the average error between all the simulations is equal to 3.416%:

Table 4.3: Mean absolute percentage error (MAPE) calculated by comparing the values of the simulations performed with PHAST and the relation proposed by Gong et al. (2022), obtained from experimental data.

Hole diameter [mm]	Temperature [K]	MAPE%
1	200	4.07
	250	2.13
	300	1.72
1.5	200	5.23

	250	2.60
	300	1.35
2	200	9.39
	250	3.06
	300	1.17

A MAPE value of 3.416% highlights good model accuracy, with a small average deviation between predicted and observed values. This result is considered satisfactory in the literature for similar applications, where thresholds lower than 4.5% are considered indicative of good predictive capacity (Prakash et al., 2011; Lee et al., 2006). A lower MAPE percentage corresponds to a better performance of the prediction model demonstrating its reliability in several applications, such as environmental modelling. A MAPE of 3.416% not only reflects an efficient prediction model, but also suggests its validity in real-world scenarios, where accuracy is crucial. The obtained results indicate that PHAST provides a more accurate description of the gas release behaviour at room temperature. Indeed, an increase in error is observed with decreasing temperature. Furthermore, the error increases with increasing hole diameter, suggesting a relationship between increasing outlet flow rate and prediction accuracy. Therefore, it can be inferred that the PHAST model more accurately describes low-flow gas releases, while being less accurate for high-flow gas releases.

The scenario with the largest error corresponds to the 2 mm hole release scenario at 200K, where the MAPE is equal to 9.386%. This indicates that the predictions obtained by the model differ from the experimental data more than in other scenarios. In support of this observation, the two curves in **Figure 4.19** are reported, from which it emerges that, although the two curves are more separated, the one deriving from the software model overestimates the experimental data; therefore, it is more conservative. In other words, the model tends to provide higher values than the real data, which could be advantageous in contexts where it is necessary to adopt precautionary estimates. The result obtained is in line with the study of Ganci et al. (2011), who calculated the hydrogen concentration in the space downstream of a release from an 11 mm hole, with hydrogen stored at 10 bar. The experimental data obtained were then compared with the values predicted by the PHAST software. The results showed that, with the increase of the distance from the release point, the values provided by PHAST progressively deviate from the experimental ones, showing an overestimation.

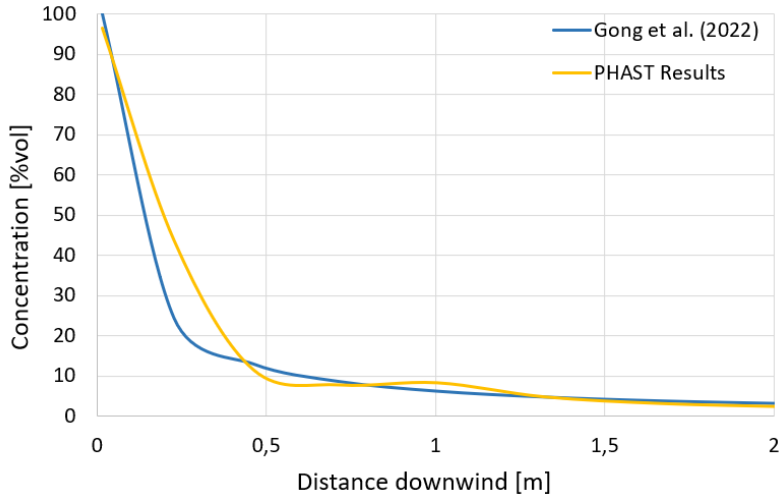

Figure 4.19: Concentration profiles following a release of hydrogen from a 2 mm hole from a 5-bar and 200K storage tank. In blue the curve obtained from the experimental data of Gong et al. (2022), in orange the results of the PHAST software.

Subsequently, the concentration results obtained from PHAST were analysed. **Figure 4.20** shows the results obtained by PHAST, which shows the concentration curves as a function of the distance downwind on the gas outlet axis with a storage pressure of 5 bar and a hole diameter of 2 mm, corresponding to simulation number 3 from **Table 4.2**. The figure shows that the concentration near the gas outlet point is almost 100% by volume, then decreases very quickly, reaching 10% by volume in just 0.5 m. The concentration reaches close to zero in less than 2 m. However, compared to the experimental curve, the simulation shows a less rapid decrease in the initial phase and presents a ripple in the concentration distribution along the trajectory.

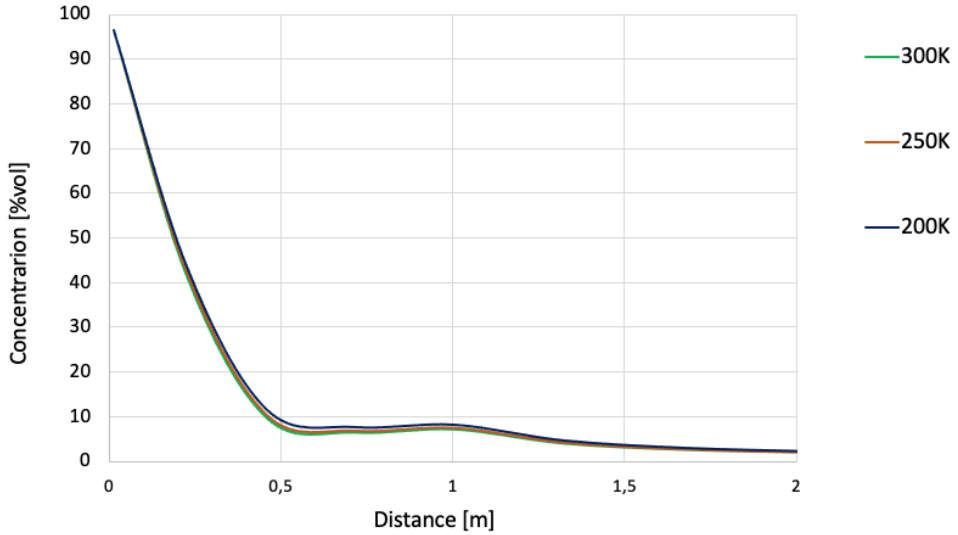

Figure 4.20: Maximum concentration as a function of distance following a release of hydrogen from a 2 mm hole from a 5-bar storage tank at three different temperatures. In green 300K, in red 250K and in blue 200K. Simulation performed with the PHAST software.

The trend of the three curves is the same; the only difference to be highlighted is that the graph shows that the lower the temperature, the higher the concentration; therefore, at the same storage pressure, the concentration in space is greater as the storage temperature decreases. In particular, it is possible to

calculate how much the concentration value at 200K differs from that at 300K (room temperature) by following **Formula 4.4** (Cole and Altman, 2017):

$$\Delta\% = \frac{(C_{200K} - C_{300K})}{C_{300K}} \quad \textbf{(4.4)}$$

Where $\Delta\%$ is the percentage difference between the results obtained at room temperature and at 200K, C_{200K} is the concentration at 200K at a given point in space, and C_{300K} is the concentration at 300K at the same point in space. **Table 4.4** shows the comparison between the concentration values, showing how they differ as a function of the distance downwind, and highlights how the difference between the concentration values increases as the distance from the point of origin of the release increases. The first column shows the distance from the point of release, while the second column shows the percentage difference between the concentration measured at 200K and that at 250K. The third column, instead, indicates how much the concentration at 200K is greater than that at 300K. It is observed that the difference between $\Delta\%_{200K-300K}$ and $\Delta\%_{200K-250K}$ remains nearly constant, with the former being approximately twice the latter. This behaviour is consistent with what was experimentally observed by Gong et al. (2022).

Table 4.4: Percentage difference between concentrations in space following a release from a 5-bar tank with a 2mm diameter hole at 200K and 250K in the second column. Percentage difference between concentrations at 200K and 300K in the third column, at a distance from the release point reported in the first column.

Distance [m]	$\Delta\%_{200°K-250°K}$	$\Delta\%_{200°K-300°K}$
0.01	0.08	0.14
0.23	3.04	5.47
0.46	11.2	21.17
0.72	11.46	21.66
1.00	9.11	16.97
1.32	11.33	21.5
1.67	12.1	23.14
2.06	12.5	24.03

The same percentage analysis was extended to the other hole diameters analysed. Detailed results are reported in the **Annex 1**.

The percentage differences between simulated concentrations at different temperatures were reported to quantify the effect of temperature on hydrogen dispersion. Specifically, they highlight how, for the same pressure and release geometry, the gas concentration along the jet axis increases significantly as the temperature decreases. This behaviour is attributable to the increased density and mass flow rate of hydrogen at lower temperatures.

Subsequently, the analysis was extended while keeping the temperature constant by studying the effect of the hole diameter on the distribution of hydrogen concentration along the jet axis. This second phase of the study allows isolating the influence of geometric parameters on the release behaviour on the

release behaviour, providing a complementary insight to what was previously observed. The results, reported in **Figure 4.21** at 200K, show that as the hole diameter increases, there is an increase in concentration and a greater extension of the cloud, an expected result, as a larger hole determines a higher mass flux. The curves relating to the other temperatures have not been reported, as they show a similar trend.

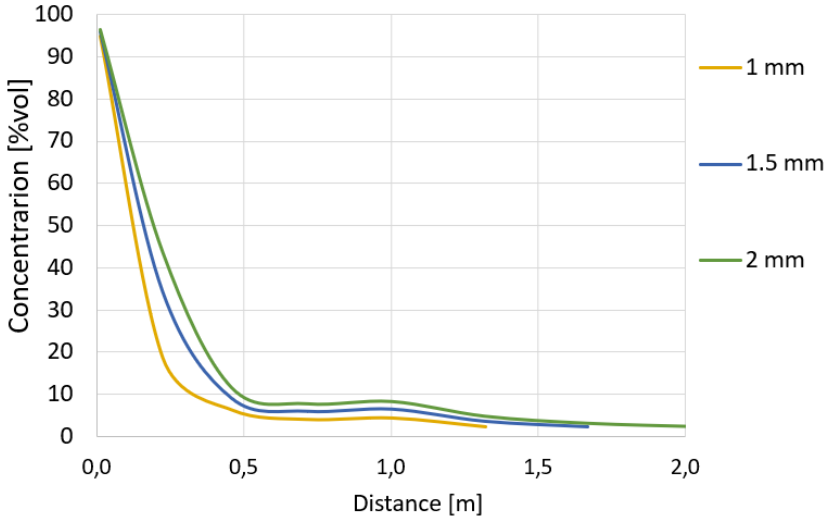

Figure 4.21: Maximum concentration as a function of distance following a release of hydrogen from a 5-bar and 200K storage tank, at three different hole diameters. In orange 1 mm, in blue 1.5 mm and in green 2 mm. Simulation conducted with the PHAST software.

Under-pressure simulation results

The results of the two pressure tank simulations were compared with the results obtained by Han et al. (2014). **Figure 4.22** shows the results for a storage pressure of 200 bar. **Figure 4.22a** shows the concentration profile on the release axis as a function of distance obtained by PHAST and the profile reported by the study by Han et al. (2014).

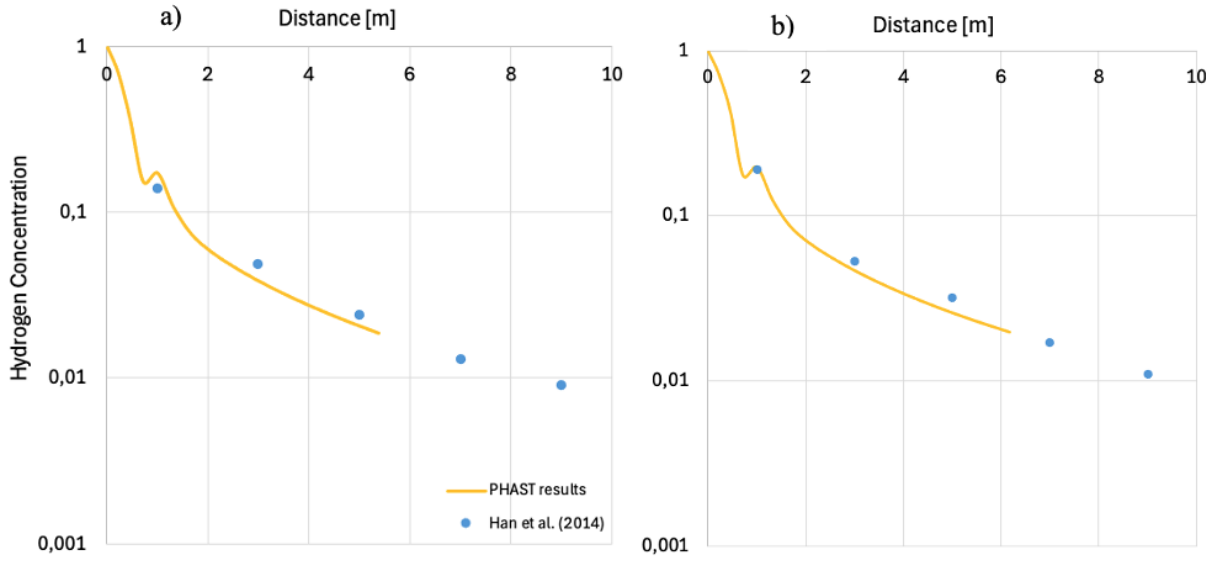

Figure 4.22: Concentration versus distance following a hydrogen release from a 1 mm

hole in a storage tank, PHAST predictions in orange and experimental data from Han et al. (2014) in blue. A) Comparison at 200 bar. B) Comparison at 300 bar.

PHAST and experimental data show a hydrogen concentration that decreases rapidly with distance from the source, displaying similar trends. However, PHAST shows an increase in gas concentration approximately one meter from the release point. From the experimental data, it is not possible to determine with certainty whether this peak is actually present, since the concentration was not measured continuously along the distance. Although no investigations explicitly document this phenomenon, the PHAST technical documentation (DNV, 2025) and model sensitivity study (Pandya et al., 2008) suggest that the software does not simulate the near-orifice region in detail but applies conservative simplifications to ensure numerical stability. Therefore, the observed peak should likely be considered a modelling artifact, rather than a real physical phenomenon. The comparison shows that the concentration obtained experimentally is slightly higher than that predicted by the PHAST software. This behaviour differs from what was previously observed at sub-ambient temperatures, where the software tended to overestimate the concentrations compared to the experimental data. The discrepancy could be attributed to differences in the dispersion models used by the software. The same behaviour is also observed in **Figure 4.22b** at a pressure of 300 bar.

The study conducted by Han et al. (2014) introduces the relative dispersion distance, defined as the ratio between the distance at which the hydrogen cloud reaches a concentration of 2% (half of the lower flammability limit) and the diameter of the hole. This parameter allows a normalized comparison of the propagation of the cloud in scenarios with different geometric and operating conditions. From the analysis of the results reported in **Figure 4.23**, it clearly emerges that the dispersion distances simulated with the PHAST software are systematically lower than those obtained experimentally.

This discrepancy was quantified by calculating the MAPE, according to **Formula 4.3**. The values obtained indicate an underestimation by the numerical model equal to 11.3%, 20% and 15.6% for operating pressures of 200, 300 and 400 bar, respectively. These results suggest that, although PHAST is a consolidated tool for gas dispersion modelling, it tends to underestimate the cloud extension in high-pressure conditions, highlighting the need for a more accurate calibration or integration with experimental data for critical scenarios.

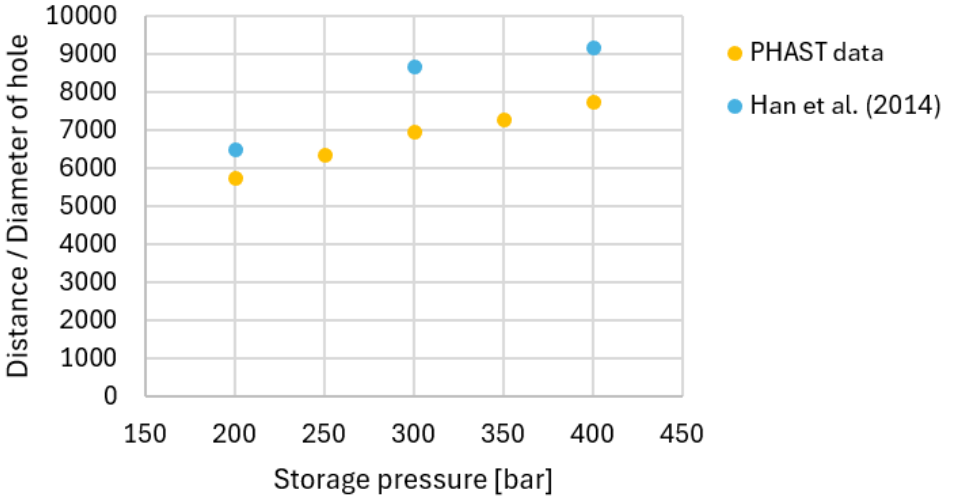

Figure 4.23: Comparison between the relative dispersion distances obtained experimentally by Han et al. (2014) in blue and those simulated with PHAST in orange, for pressures of 200, 300 and 400 bar.

4.4.2 Hydrogen Cloud Analysis

To support the study of hydrogen leak detection using an aerial platform, the PHAST consequence modelling software was employed. This tool was used to analyse the safe areas for the drone flight, with the aim of determining a safe height that would guarantee a safe flight. Although ATEX-certified drones exist, their adoption is limited mainly due to their high costs, which make their use difficult in industrial scenarios. Therefore, the main objective of this study is to investigate the dispersion of the hydrogen cloud generated by small-sized releases, which are difficult to detect with the naked eye, especially in industrial environments. Such leaks could occur from small holes, which would not be easily detectable through traditional monitoring methods. The analysis using PHAST allows for an estimation of the hydrogen cloud propagation, thus providing information to define safe flight trajectories. In this study, the hydrogen cloud analysis was conducted using maximum concentrations in space, as provided by the PHAST software. This approach was adopted as a conservative measure to safeguard equipment integrity and to ensure a precautionary estimation of both the cloud geometry and the release source location. Maximum concentrations represent the most critical value that can be detected during the overflight and allow flight trajectories and detection strategies to be defined under maximum safety conditions. Future developments will include the analysis of the characteristic time with which local hydrogen concentrations vary and the comparison with the drone response times, in order to evaluate the validity of the static approach and quantify any dynamic effects.

For this purpose, a simulation plan reported in **Table 4.5** was conducted. The scenarios were all analysed in relation to storage tanks, since PHAST allows the simulation of tank and pipeline releases, but the results obtained were similar in both scenarios. The pressure was varied between 200 and 500 bar, keeping the ambient temperature constant. The outlet hole was varied between 0.3 mm and 2 mm. The environmental conditions were kept at default values, with wind speeds of 1.5 m/s and 5 m/s, and atmospheric stability of class F (very stable), typical of

night-time conditions, and class D (less stable), which represents a more common situation during the day (Kahl and Chapman, 2018).

Table 4.5: Simulations performed with PHAST to study the hydrogen cloud released from small holes in storage tanks.

Equipment	Pressure [bar]			Temperature [°C]	Exit hole [mm]					Weather
Tank	200	250	300	15	0.3	0.35	0.4	0.45	0.5	1.5F
	350		400		0.6	0.7	0.8	0.9	1	1.5D
	450		500		1.2	1.5		1.7	2	5D

From these simulations, the following were evaluated:

i. The height of the cloud from the release point at 20,000 ppm
ii. The height of the cloud from the release point at 500 ppm
iii. The length of the cloud at 20,000 ppm
iv. The length of the cloud at 500 ppm
v. The length of the jet fire flame
vi. The distance to which the jet fire radiation reaches
vii. The maximum jet fire radiation and the distance from the release of such radiation
viii. The time between the start of the release and a possible explosion
ix. The distances to which the overpressures of 0.02068 bar, 0.1379 bar, and 0.2068 bar reach in the case of explosion.

The overpressure values of 0.02068 bar, 0.1379 bar, and 0.2068 bar were selected in accordance with the criteria established by the Ministry of Public Works (Ministero dei Lavori Pubblici, 2001), which define increasing damage thresholds in the event of an explosion. Specifically, these values correspond to minor, moderate, and severe damage to structures, respectively. The analysis therefore focuses on the distances at which these overpressure thresholds are reached, in order to assess the potential impact on the surrounding environment. Furthermore, the flammability range of hydrogen is wide, ranging from 4% to 75% by volume, which means that its concentration in air can be dangerous in a wide range of conditions. However, the Ministry of Public Works has adopted as a precautionary value half of the lower flammability limit, corresponding to 2% by volume or 20,000 ppm. This value has been chosen as a reference for the evaluation of the height and safety distance, as it represents a threshold at which the risk of ignition and fires is considerably reduced. However, following a study of the sensors available on the market, which are able to detect hydrogen concentrations up to 1000 ppm with an accuracy of 1 ppm, it was considered appropriate to also adopt a more conservative value of 500 ppm. This choice is motivated by the need to ensure a safety distance greater than the flammability range, reducing the risk to a minimum. In this way, it is ensured that the equipment used never enters a potentially dangerous area, even in conditions of error or uncertainty in the detections. Therefore, the adoption of a wider safety margin, such as that of 500 ppm, is a prudential measure that aims to safeguard the safety of the entire system, avoiding any compromise in terms of operational

safety and accident prevention.

Concentration results

The results for the cloud height at 20,000 ppm and 500 ppm are presented below, as shown in **Figure 4.24** and **Figure 4.25**, respectively. In both graphs, the cloud height is plotted as a function of the distance from the exit hole, with the vertical position of the gas expressed relative to the orifice itself. This approach eliminates the influence of the absolute height of the release point, allowing for a normalized comparison across different configurations, taking into account that this representation implies a negligible influence of the distance from the ground on the dispersion dynamics.

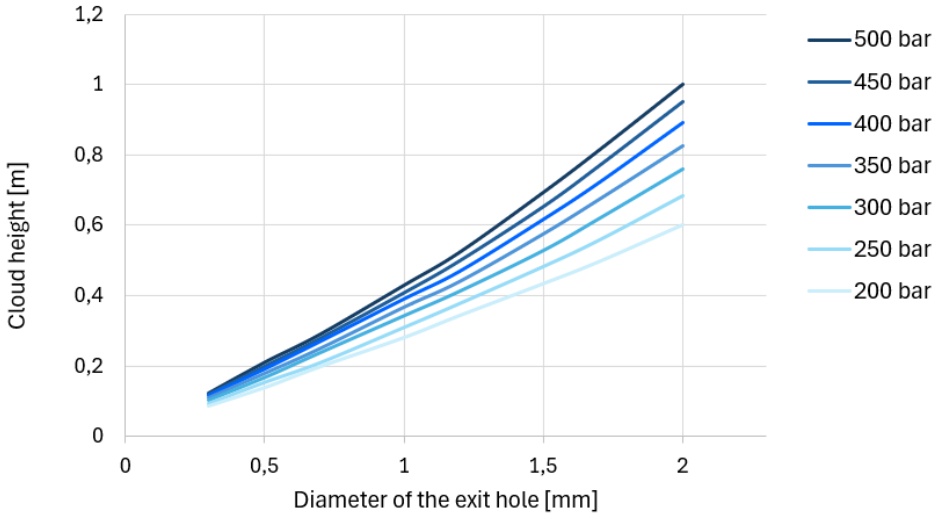

Figure 4.24: Trend of the height of the cloud at 20,000 ppm as the diameter of the outlet hole and the storage pressure vary, under 1.5D atmospheric conditions.

Each curve represents a different pressure, while the diameter of the exit hole is an unknown variable in the real case. The curves show the results of simulations conducted under 1.5D atmospheric conditions, that is, neutral stability and a wind speed of 1.5 m/s, corresponding to the most representative weather scenario. The results obtained for smaller hole diameters indicate that atmospheric turbulence has a negligible influence on the vertical dispersion of the cloud. However, in the presence of stronger winds, the cloud tends to be lower in height. On the contrary, as the hole diameter increases, more turbulent atmospheric conditions and lower intensity winds determine the formation of a higher cloud.

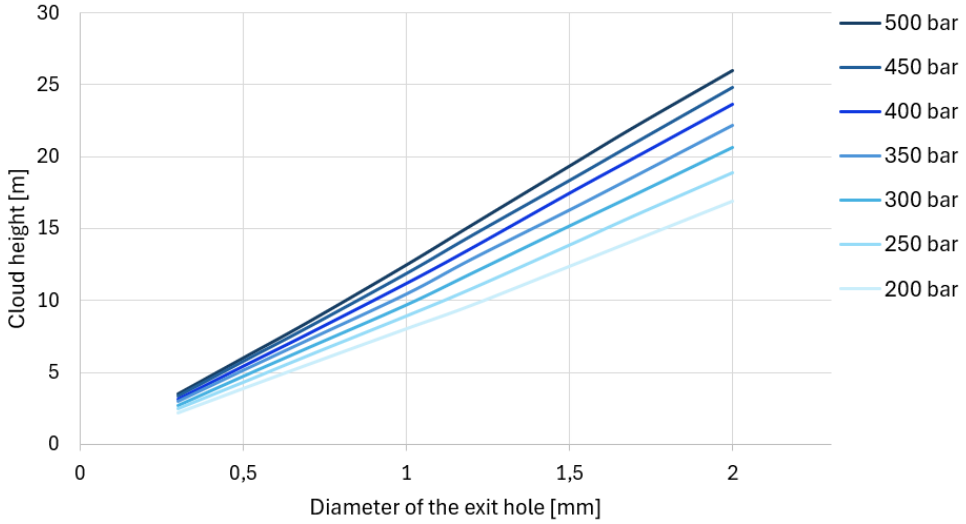

Figure 4.25: Trend of the height of the cloud at 500 ppm as the diameter of the outlet hole and the storage pressure vary, under 1.5D atmospheric conditions.

It is interesting to note that, for the same diameter, the height of the cloud varies differently with the pressure, depending on the hydrogen concentration. Indeed, for clouds at 20,000 ppm, at diameters of 0.3 mm, the height increases by about 0.45 times from 200 bar to 500 bar, while for diameters equal to 2 mm, the height increases by 0.66. On the contrary, for clouds at 500 ppm, at diameters of 0.3 mm, the height increases by 0.6 times, while at 2 mm in diameter, the increase is just over 0.5. This highlights that, for higher hydrogen concentrations, the height of the cloud is more influenced by the storage pressure with the increase in the diameter of the hole. On the contrary, for lower concentrations, the influence of the pressure on the height of the cloud decreases with the increase in the diameter of the gas outlet. This behaviour is also observed in relation to the diameter. At 200 bar, the height of the cloud increases 6.1 times when the diameter increases from 0.3 mm to 2 mm at a concentration of 20,000 ppm, and 6.6 times at 500 ppm. For a diameter of 2 mm, the increase is 7.1 times at 20,000 ppm and 6.3 times at 500 ppm. This suggests that, as the pressure increases, the influence of the hole diameter on the vertical extent of the cloud becomes more pronounced at higher concentration levels, specifically those approaching the flammability threshold.

However, overall, the analysis shows that the change in diameter has a much more significant impact on the height of the cloud compared to the pressure.

Another interesting aspect to observe concerns the rapid diffusion of hydrogen. Indeed, while the cloud with a concentration of 20,000 ppm reaches a maximum of only 1 meter in height, the cloud with a concentration of 500 ppm extends up to 26 meters. This different behaviour can be explained by the density of hydrogen, which is significantly lower than that of air. Being a lighter gas, hydrogen tends to rise quickly and disperse more easily in the atmosphere, especially when the concentration is high. At high concentrations, such as 20,000 ppm, hydrogen is in a more concentrated form and it tends to disperse quickly in a limited area, without expanding much in height. On the other hand, at lower concentrations, such as 500 ppm, the lower density allows for a wider dispersion in height, since hydrogen has a greater possibility of mixing with the surrounding

air, occupying a much larger area. This phenomenon highlights the importance of the density of the gas in determining its propagation and its ability to disperse, which implies that at low concentrations, hydrogen spreads over larger horizontal and vertical distances, increasing the area potentially at risk.

Subsequently, the distance of the cloud from the release point was analysed, as shown in **Figure 4.26** for the concentration of 20,000 ppm and in **Figure 4.27** for 500 ppm. Similar to the height of the cloud, the length of the cloud also increases as two parameters vary: the diameter of the exit hole and the release pressure. These two factors influence the propagation of the gas and, consequently, the distance that the cloud travels from the release point. In both scenarios, a longer cloud extent was observed under more turbulent atmospheric conditions, specifically in class D stability, compared to the more stable class F conditions. Indeed, the turbulent atmosphere favours a more extensive horizontal dispersion of the gas, increasing the length of the cloud. This behaviour is in line with expectations, since more turbulent atmospheric conditions cause a greater mixing of the hydrogen with the surrounding air, extending the diffusion zone of the gas. On the contrary, with more stable atmospheric conditions, class F, the length of the cloud tends to reduce. The influence of wind speed on hydrogen dispersion is strongly dependent on the gas release rate. In the presence of small holes, and therefore low flow rates, stronger winds tend to generate larger clouds, since they favour the horizontal transport of the gas before it is significantly diluted. On the contrary, in release conditions with high flow rates (larger holes), situations characterized by low ventilation determine larger clouds. In these cases, the gas dilution is slowed down, allowing the cloud to maintain high concentrations over greater distances.

Furthermore, it was observed that, with smaller exit diameters, the cloud length is maximum right on the axis of the release point, but as the diameter and the exit gas flow increase, the maximum cloud length moves to a greater height. Again, the cloud length shows different behaviours depending on the hydrogen concentration. For a concentration of 20,000 ppm, at exit diameters of 0.3 mm, the cloud length increases by about 0.47 times from 200 bar to 500 bar pressure. On the contrary, at exit diameters equal to 2 mm, the increase in length is equal to 0.7. This indicates that the increase in hole diameter and storage pressure has a significant impact on the horizontal dispersion of the cloud. For the concentration of 500 ppm, the situation is different: at an outlet diameter of 0.3 mm, the cloud length increases by 0.62 times when moving from 200 bar to 500 bar, while at diameters of 2 mm, the increase is more modest, equal to 0.48. These data suggest that, for lower concentrations, the influence of the storage pressure on the cloud length decreases with the increase in the diameter of the outlet hole. This behaviour is also observed in relation to the cloud diameter. In particular, at a pressure of 200 bar, when the diameter increases from 0.3 mm to 2 mm, the cloud height increases by 5 times at a concentration of 20,000 ppm and by 4.6 times at 500 ppm. If the initial diameter is already 2 mm, the increase in height is even more marked, with an increase of 5.9 times at 20,000 ppm and 4.1 times at 500 ppm. These data suggest that, as the pressure increases, the diameter has a greater impact on the height of the cloud, especially when the concentration is high,

especially near the lower flammability limit. Thus, for high concentrations such as 20,000 ppm, the cloud size is strongly influenced by both the storage pressure and the hole diameter, with both parameters increasing. On the contrary, for lower concentrations, the increase in diameter reduces the impact of pressure on the cloud length, suggesting that in these conditions the dispersion is less sensitive to pressure variations. These results also highlight another aspect: at higher concentrations, closer to the lower flammability limit, the cloud size tends to increase with the increase in pressure and diameter. On the contrary, at lower concentrations, the increase in cloud size becomes less significant with increasing pressure and diameter.

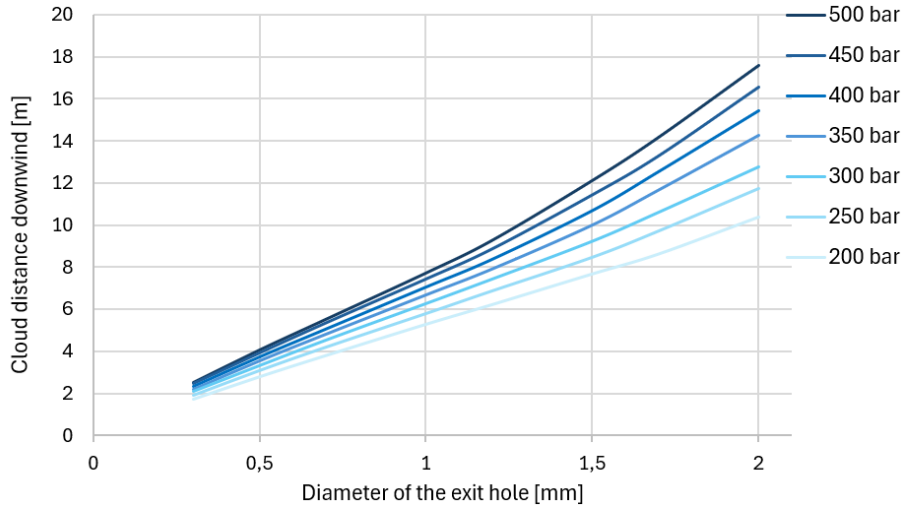

Figure 4.26: Trend of the length of the cloud at 20,000 ppm as the diameter of the outlet hole and the storage pressure vary, under 1.5D atmospheric conditions.

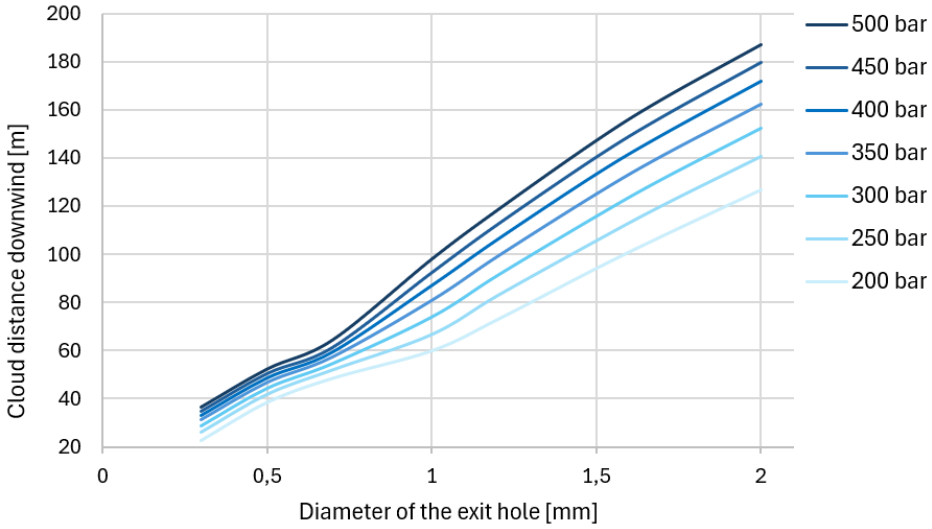

Figure 4.27: Trend of the length of the cloud at 500 ppm as the diameter of the outlet hole and the storage pressure vary, under 1.5D atmospheric conditions.

To clarify the cloud geometry and support subsequent analyses of the release point location, the planar footprints of the hydrogen cloud at constant concentration, observed at different detection heights, were plotted. Specifically, **Figure 4.28** shows the cloud footprint at 500 ppm, measured from the release point up to 5 meters above sea level, while **Figure 4.29** represents the cloud footprint at 20,000 ppm, measured from the release point up to 0.2 meters, as it is

not detectable at higher altitudes. All simulations were conducted at a pressure of 300 bar, a 1 mm hole, and class 1.5D atmospheric conditions.

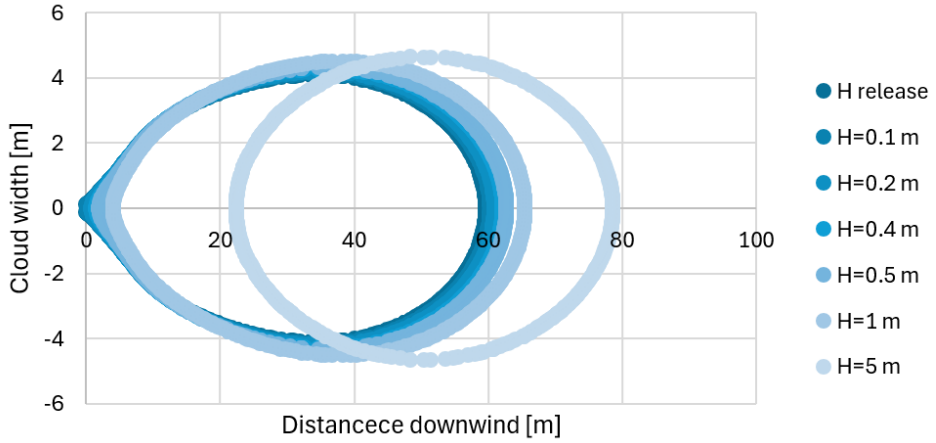

Figure 4.28: Hydrogen cloud footprint at 500 ppm, simulated release from a 300 bar pressure tank, 1 mm hole, and 1.5D atmospheric conditions. Detection from 0 to 5 m height from the release point.

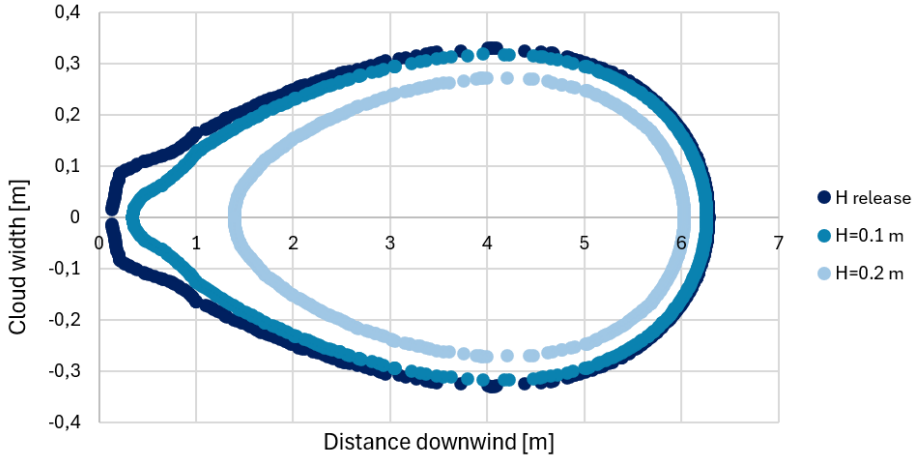

Figure 4.29: Hydrogen cloud footprint at 20,000 ppm, simulated release from a 300 bar pressure tank, 1 mm hole, and 1.5D atmospheric conditions. Detection from 0 to 0.2 m height from the release point.

Comparing the two footprints reveals a different spatial evolution of the cloud as a function of concentration and detection height. In **Figure 4.28**, for a concentration of 500 ppm, the curves are very close, indicating a compact and consistent distribution of the cloud at the different heights considered. It can also be seen that, as height increases, the curves gradually shift in the direction of the wind, as expected. The curve at 5 metres shows a slightly more pronounced shift, likely attributable to the combined effect of the wind and the greater vertical distance, which leads to an increase in horizontal displacement. In **Figure 4.29**, for a concentration of 20,000 ppm, the curves show a more uniform shift in the direction of the wind as height increases. In this case, the cloud is only detectable at very low altitudes (up to 0.2 m), and the area of influence is more restricted, suggesting predominantly horizontal dispersion and greater dilution, consistent with the high density of the cloud at high concentrations.

Jet Fire Results

For the jet fire, the flame length, the maximum radiation and the distance they can reach have been studied. **Figure 4.30** shows the trend of the flame length in relation to the diameter and the storage pressure. From the analysis, it emerges that the flame length is predominantly influenced by the diameter of the exit hole, while the effect of the storage pressure is less significant. This behaviour may be explained by the increased gas flow rate associated with a larger orifice diameter, which favour the formation of a more extended flame. However, despite the maximum diameter considered being 2 mm, with a limited flow rate of released gas, the flame length can reach significant values, up to 4.3 m. This extension represents a potential risk in industrial environments, where the flame could come into contact with structures, systems or flammable materials, increasing the probability of accidents. Conversely, atmospheric stability appears to have a negligible effect on flame length, unlike the wind, which shows a more noticeable, though still limited, influence. It is important to note that, similarly to what was observed for the height and length of the cloud, the influence of pressure on the flame length becomes more significant for larger diameter holes. For smaller diameters, the effect of pressure is less relevant: for instance, for a 1 mm hole, the flame length increases on average by only 7 cm for every 100 bar of pressure increase. In contrast, for larger diameters of 2 mm, the effect of pressure is much more marked, with an average increase in flame length of 45 cm for every 100 bar.

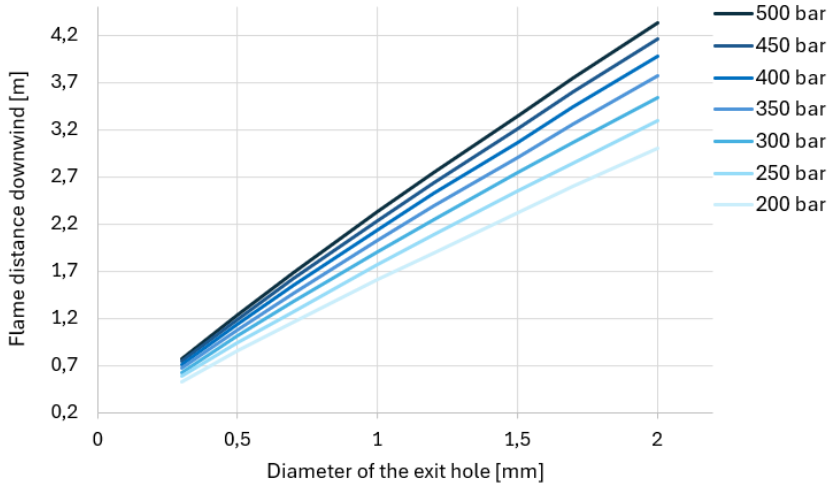

Figure 4.30: Flame length trend as the outlet hole diameter and storage pressure vary, under 1.5D atmospheric conditions.

The results obtained for the maximum radiation and its distance from the release point have been reported only for the pressures of 200 bar, in **Figure 4.31**, and 500 bar, in **Figure 4.32**, since the analysis of the other pressure conditions studied has highlighted similar trends. The main variation concerns the values of the maximum thermal radiation and the distance at which it propagates, while the general behaviour of the phenomenon remains unchanged. For this reason, it was chosen to present only the cases of minimum and maximum pressure considered, in order to provide a representative picture without redundancy in the data.

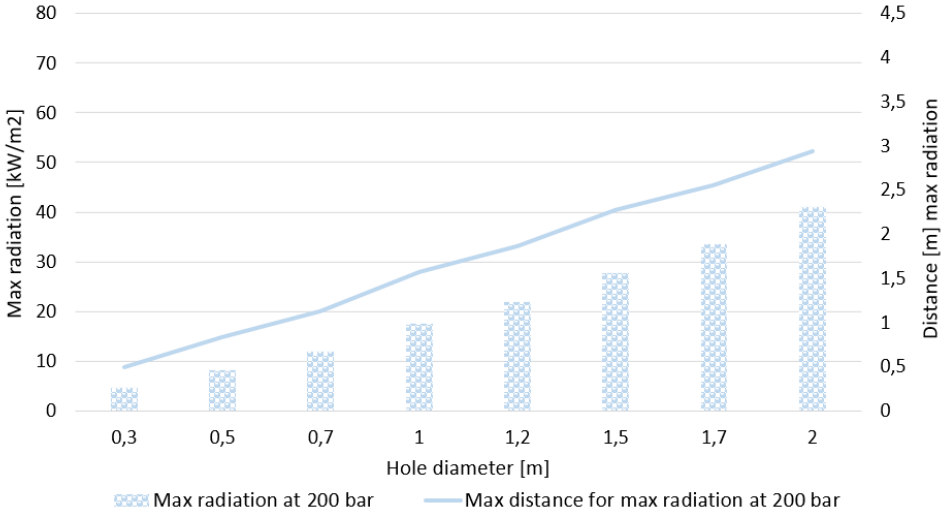

Figure 4.31: Trend of the maximum thermal radiation of the jet fire (blue dotted bars, left axis) and the distance at which this radiation is detected (blue solid line, right axis) as a function of the diameter of the exit hole following a release of hydrogen stored at 200 bar under 1.5D atmospheric conditions.

The analysis of the results shows that both the maximum thermal radiation and the distance at which it is detected along the release axis increase with rising storage pressure and outlet hole diameter. The dependence of the maximum thermal radiation of the jet fire on these two parameters can be explained through the principles of fluid dynamics. The emitted thermal radiation is strictly related to the mass flow rate of the hydrogen exiting. According to the study by Yuhua et al. (2002), the mass flow rate is directly proportional to both the area of the outlet hole and the storage pressure. Therefore, at the same pressure, an increase in the diameter of the hole causes a quadratic increase in the area and, consequently, in the flow rate of the released gas. The results obtained with the PHAST software confirm a strong dependence of the radiation on the diameter, with the maximum radiation increasing by 7.8 times with rising hole diameter. On the contrary, the mass flow rate of the exit gas is directly proportional to the pressure, but the effect of the latter on the radiation is less evident. Indeed, the maximum radiation increases only by 0.68 times as the pressure increases.

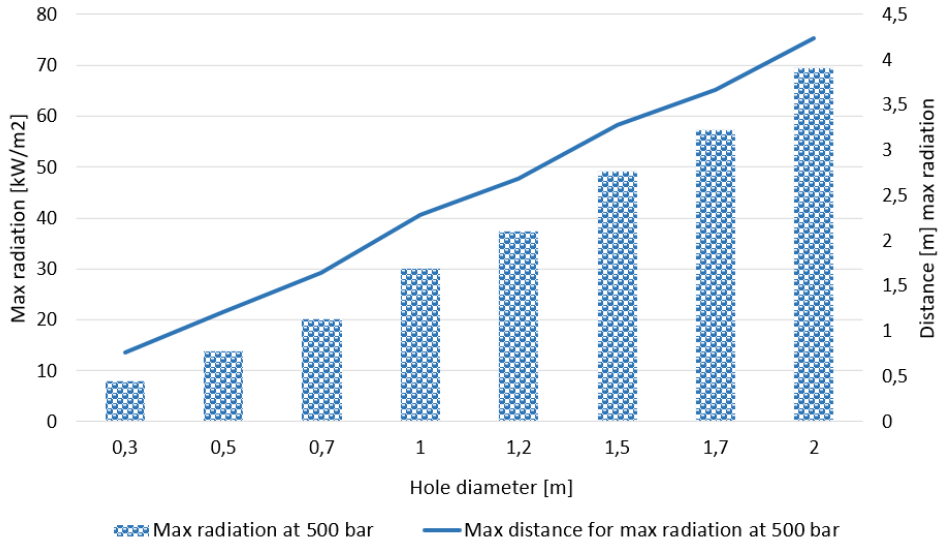

Figure 4.32: Trend of the maximum thermal radiation of the jet fire (blue dotted bars,

left axis) and the distance at which this radiation is detected (blue solid line, right axis) as a function of the diameter of the exit hole following a release of hydrogen stored at 500 bar under 1.5D atmospheric conditions.

Furthermore, the data indicate that atmospheric conditions do not significantly influence these values; indeed, no substantial variations in distance or radiation are observed with changes in either wind speed or atmospheric stability.

Explosion Results

The Ministry of Public Works (Ministero dei Lavori Pubblici, 2001) indicates threshold values of overpressure for effects: 0.3 bar for high lethality, 0.14 bar for early lethality and 0.03 bar for reversible lesions. In the context of dispersion and ignition of high-pressure gas jets, the PHAST software allows the estimation of the distances at which such overpressure values occur in the event of an explosion. The analysis shows that for holes with diameters up to 1.5 mm, no explosive event is recorded, since the amount of gas released is not sufficient to cause a significant deflagration. However, for diameters of 1.5 mm, the explosion becomes possible when the storage pressure exceeds 300 bar, suggesting that at lower pressures the release does not generate conditions favourable to the transition from combustion to detonation. For diameters of 1.7 mm or more, the explosion can also occur at lower pressures. This behaviour can be explained by considering that a larger diameter hole allows an increase in the mass flow rate of the exiting gas, favouring a larger formation of a mixture of hydrogen with air. These results confirm that the risk of explosion does not depend only on the storage pressure, but also on the diameter of the release orifice, which directly influences the dynamics of the dispersion and the possibility of ignition in critical conditions.

The results obtained with the PHAST software are presented below, showing the distance reached by the overpressure waves of 0.3 bar, 0.14 bar and 0.03 bar, in relation to the diameter of the outlet hole and the storage pressure. These data are illustrated in **Figures 4.31**, **4.32**, and **4.33**, respectively. The distance reached by the overpressure waves is influenced by both the storage pressure and the diameter of the outlet hole, with a dependence that appears linear for both parameters. This behaviour is highlighted by the presence of straight lines with constant slope in the graphs, which indicate a proportional relationship between the distance of the shock waves and the diameter of the hole. Furthermore, the equality of the slope between the different straight lines suggests that the effect of the pressure also follows a linear law, confirming that an increase in the storage pressure leads to a proportional increase in the distance reached by the overpressure waves.

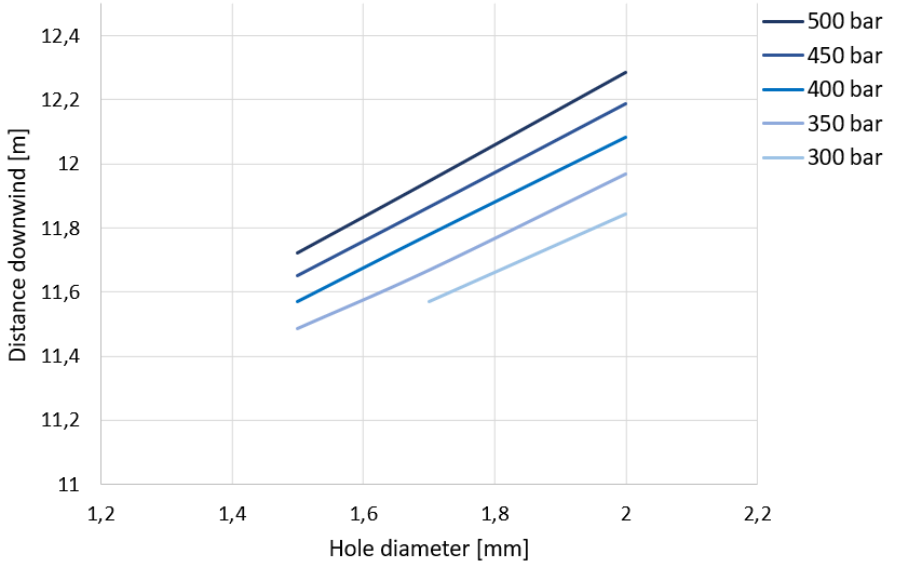

Figure 4.33: Trend of the distance reached by the 0.3 bar overpressure wave as a function of the diameter of the outlet hole and the hydrogen storage pressure in the event of an explosion, under 1.5D atmospheric conditions.

Overpressure waves propagate over longer distances under more stable atmospheric conditions. This is probably because, in a stable atmosphere, gas dispersion is slower and the mixture remains confined long enough to generate a stronger explosion, capable of producing a more intense shock wave. On the contrary, in conditions of atmospheric turbulence, the released gas disperses more rapidly. In these scenarios, overpressure waves are less intense, reaching shorter distances. This aspect is important to understand the impact of environmental conditions on the propagation of shock waves: in the presence of atmospheric stability, the shock wave travels further, while in more turbulent conditions, the dispersion of the gas limits the formation of a significant overpressure wave. It can be seen from the figures that, if the same overpressure values are considered, the shock wave propagates over longer distances at higher storage pressures and larger hole diameters. It is noteworthy that, as overpressure increases, the distance reached by the shock wave decreases linearly, indicating an inverse proportionality between the two variables. In particular, as the overpressure decreases from 0.3 bar to 0.13 bar, it is observed that the storage pressure must be reduced by about 2.3 times. However, under the same operating conditions (pressure and orifice diameter), the shock wave propagation distance increases slightly, by about 1.06 times. A similar behaviour is found in the transition from 0.13 bar to 0.03 bar, where the storage pressure is reduced by a factor of 4, while the distance travelled by the shock wave doubles. This behaviour can be explained by considering that less intense shock waves tend to dissipate energy more slowly in stable environments, thus being able to propagate over greater distances, although with less intensity. On the contrary, more intense waves, although generating high overpressures, tend to lose energy more rapidly due to the greater interaction with the surrounding environment. It is essential to underline that these results derive from simulations conducted in ideal conditions, in the absence of physical obstacles. The presence of buildings, structures or natural elements can significantly influence the propagation of the shock wave, altering the effective

distances at which the overpressures occur. Therefore, the values obtained represent a theoretical limit useful for comparative analysis but must be interpreted with caution in the practical application phase.

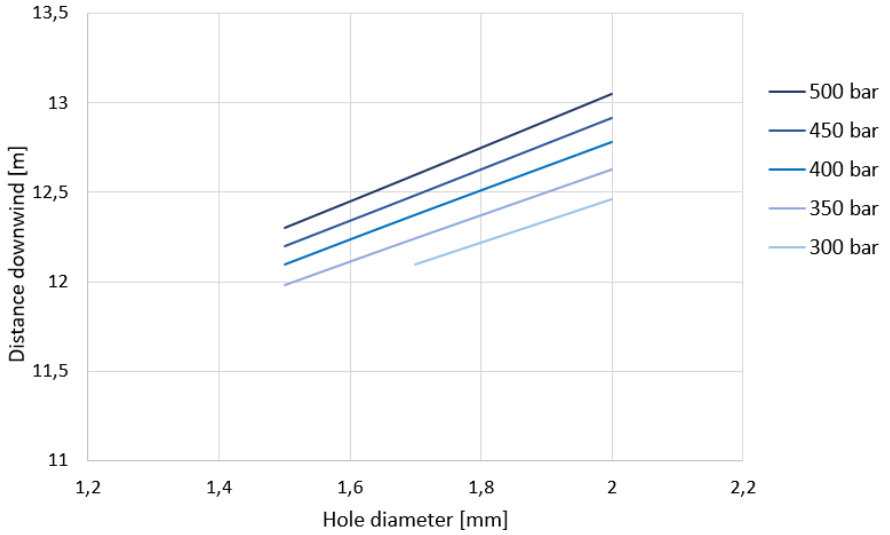

Figure 4.34: Trend of the distance reached by the 0.14 bar overpressure wave as a function of the diameter of the outlet hole and the hydrogen storage pressure in the event of an explosion, under 1.5D atmospheric conditions.

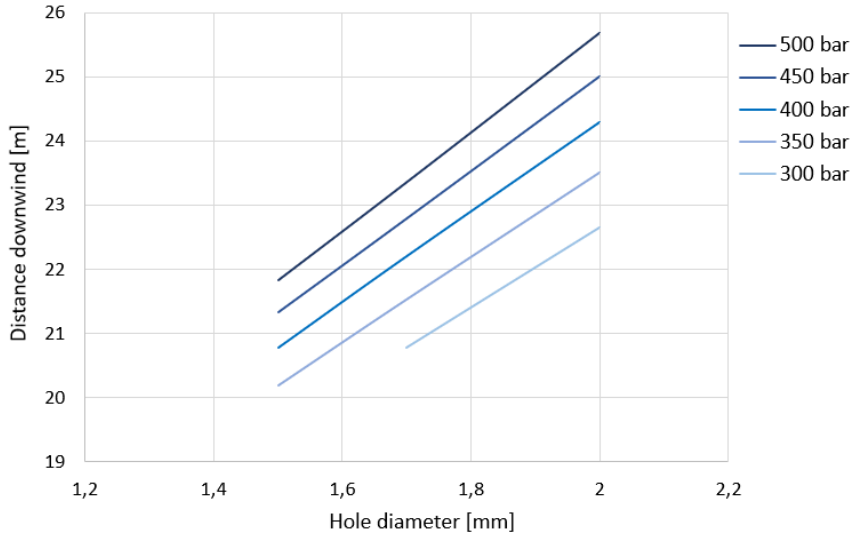

Figure 4.35: Trend of the distance reached by the 0.03 bar overpressure wave as a function of the diameter of the outlet hole and the hydrogen storage pressure in the event of an explosion under 1.5D atmospheric conditions.

4.5 Proposed Approach for Hydrogen Leak Detection

The methodology explored in this study considers the use of drones for the detection of hydrogen leaks, with the installation of specific sensors. As already discussed, the choice of the sensor depends on the application and the gas to be detected, but the solution with the highest risk is the one with the installation of a concentration detector that requires flying in contact with the gas. For this reason, in this work, a drone with a concentration detector will be considered, and the aim is to evaluate how to have a safe flight. **Figure 4.36** shows the flight pattern of the drone used for the tank inspection. The image shows, in lateral view, on the right,

the drone flying over a predefined trajectory, indicated by a dotted line, with the data acquisition points marked by "x" symbols. The top view, on the left, allows the visualization the planimetric layout of the path with respect to the geometry of the tank, providing a complementary view useful for understanding the coverage strategy adopted.

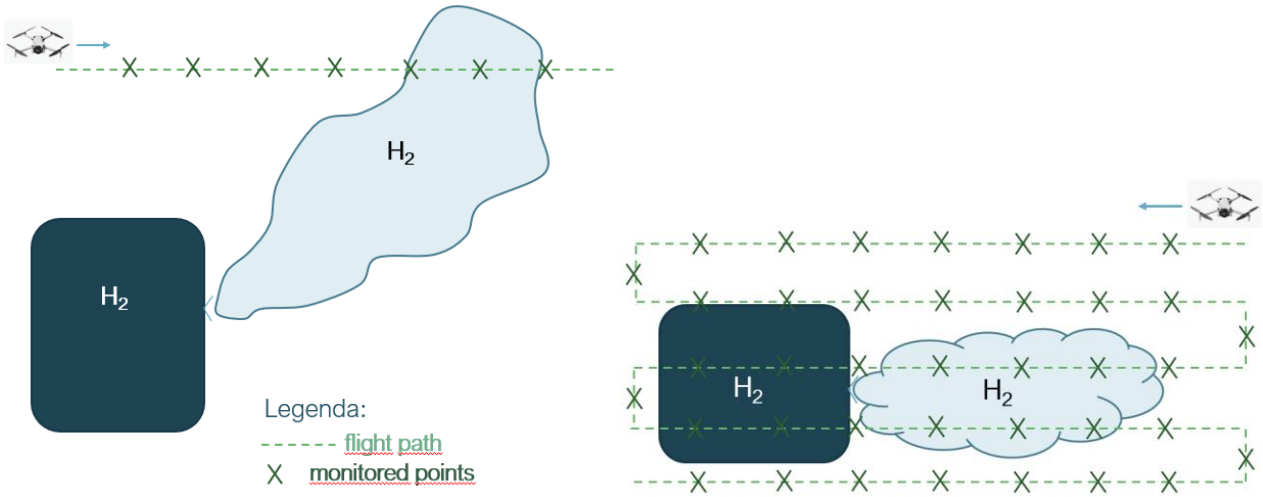

Figure 4.36: Schematic of a drone overflight mission for tank inspection. On the right, side view with dashed flight path and detection points marked with "x". On the left, the same scene in top view.

For this purpose, the proposed methodology is based on a systematic approach for the detection of hydrogen in the environment, taking into account critical factors such as safety and monitoring effectiveness. The methodology in question, illustrated in **Figure 4.37**, provides for an initial phase in which a precautionary flight height is set for the monitoring device that allows obtaining an overview of the environmental conditions and the possible dispersion of the gas in the air. The initial flight altitude is selected based on prior studies concerning the distribution and behaviour of hydrogen in the atmosphere. In the absence of detectable hydrogen in the air, the methodology involves a gradual reduction of the flight altitude, thus adapting the monitoring process to real environmental conditions. The height will be progressively reduced until a concentration of hydrogen in the air equal to 500 ppm is detected. This threshold value was selected based on the considerations reported in **Section 4.4.2** of this study. This approach allows for a reduction in the risk associated with possible sources of danger, optimizing resources and improving the efficiency of the detection system. The height decrease is a dynamic response that provides a more detailed mapping of the area without compromising safety, ensuring that there are no undetected hydrogen leaks.

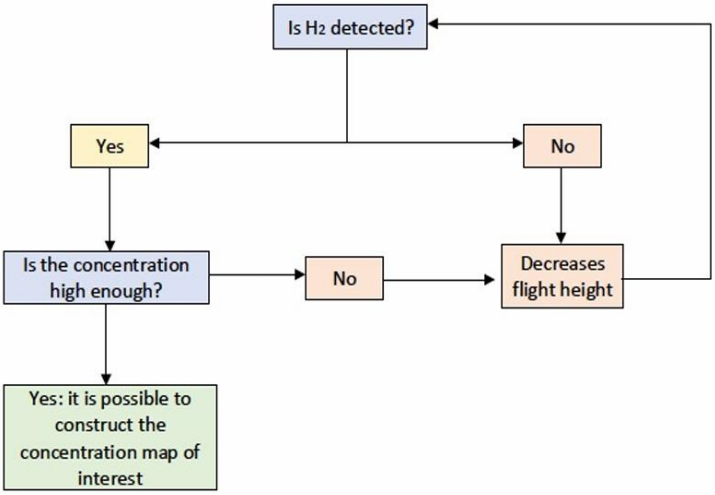

Figure 4.37: Proposed methodology for hydrogen detection using a drone equipped with a concentration detector.

In this preliminary phase, it is assumed that the hydrogen does not ignite, a necessary condition for detecting the gas. Consequently, the drone minimum flight altitude is constrained by the presence of plant equipment, in order to avoid collisions or interference with structures.

When hydrogen is detected, the sensor measures the concentration of the gas at multiple points in the surrounding space. This approach enables the generation of a detailed concentration map, providing insights into the spatial distribution of hydrogen in the environment and supporting a thorough risk assessment. Mapping hydrogen concentrations has several limitations, mainly due to the physical nature of the gas and the variable environmental conditions. Hydrogen, being a very light gas, tends to disperse rapidly in the environment, and concentrations can undergo significant changes in short times. This rapid dispersion makes it difficult to establish a stable concentration map, as the gas can vary considerably with location and time. The influence of wind is a determining factor in the distribution of hydrogen in the atmosphere: wind direction and speed can quickly move the gas, causing concentrations to vary on a spatial and temporal scale. Then the variability induced by the detection system itself, as the movement of the drone can locally alter the cloud, changing its shape and distribution. Furthermore, the size and height of the hole from which the gas is released are factors that influence the amount of hydrogen emitted and the speed at which it disperses into the environment. It is important to underline that this work represents a first exploratory analysis, and that the analytical evaluation is still open, as it is subject to numerous uncertainties reported previously.

Considerations on the flight height decrease and assessments on the location of the release point in space from the concentration map are discussed below.

4.5.1 Flight Path Optimization

In order to ensure a safe flight of the drone, studies were conducted always with the aid of the PHAST software to evaluate how much it was possible to decrease the flight height. For this purpose, a release of hydrogen under pressure

at 300 bar was simulated from a 1mm diameter hole at a height of 1m at room temperature. The height of the concentration curves was plotted as a function of the distance downwind, shown in **Figure 4.38.** The height shown in the graphs corresponds to the maximum altitude reached by the indicated concentration.

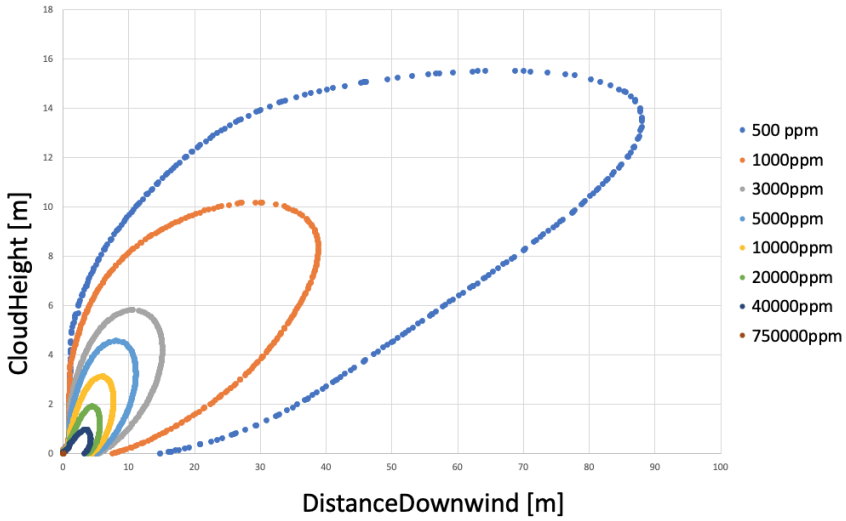

Figure 4.38: Height of concentration curves following a release of gaseous hydrogen from a 300 bar pressurized tank and from a 1 mm diameter hole.

The figure shows the vertical evolution of the hydrogen cloud at different concentrations. At greater distances from the release point, the curves tend to flatten and become closer together, indicating a reduction in concentration gradients. This behaviour can provide useful information for defining the minimum safe flight altitude of the drone, avoiding intersections with areas of significant concentration.

This observation implies that when the sensor detects low concentrations of hydrogen in the air, the flight altitude must be progressively reduced in a controlled way to intercept any areas of sufficiently high concentration before the drone enters a potentially dangerous area. This value allows changes in concentrations in the transition zones between safe and potentially hazardous areas to be monitored more accurately. By reducing the height in a controlled manner, the ability to detect any peaks in concentration is improved, reducing the risk of operating in areas with hydrogen levels that are too high for the integrity of the equipment. The flight path scheme is shown in **Figure 4.39.**

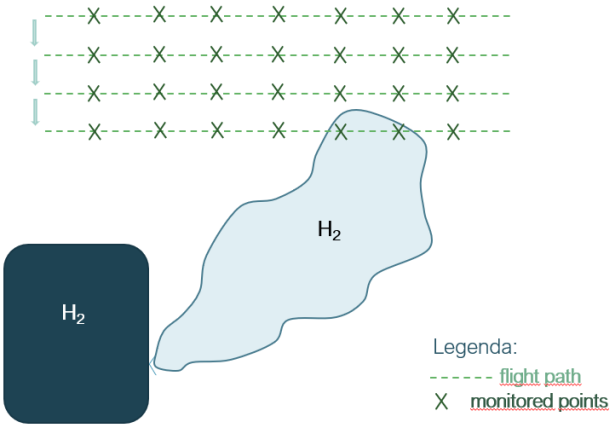

Figure 4.39: Schematic of the release of gaseous hydrogen from a tank. The drone

performs a progressive descent until the hydrogen cloud, at which point the gas concentration is detected.

4.5.2 Evaluation of the Release Point

To obtain a concentration map, the drone should fly over the tank during the release phase, while the operator manually controls its altitude, decreasing the flight height in 0.5 m intervals. This process allows the identification of the hydrogen cloud, that is, the area in which the gas concentration is high enough to be detected by the onboard sensor, but still lower than the flammability threshold, so as to guarantee safe operating conditions. Once the drone detects the presence of hydrogen, it can proceed to detect the concentrations at several points uniformly distributed across the detection plane, thus obtaining a detailed map of the cloud. This step allows for the reconstruction of the dispersion geometry and supports the analysis for localizing the release point. Once the scan is completed, a concentration map is obtained that ideally assumes a configuration similar to the one shown in **Figure 4.40**. In particular, the figure shows the iso-concentration curves generated by a release from a tank stored at 300 bar, with a hole with a diameter of 1 mm, in the presence of wind at 1.5 m/s and stable atmospheric conditions. The detection was carried out at a height of 1 meter from the release point. It can be observed that each curve at equal concentration can be geometrically approximated to an ellipse. **Figure 4.41** shows a generic ellipse defined by the semi-axes a and b, with the centre in the coordinates (x_0, y_0).

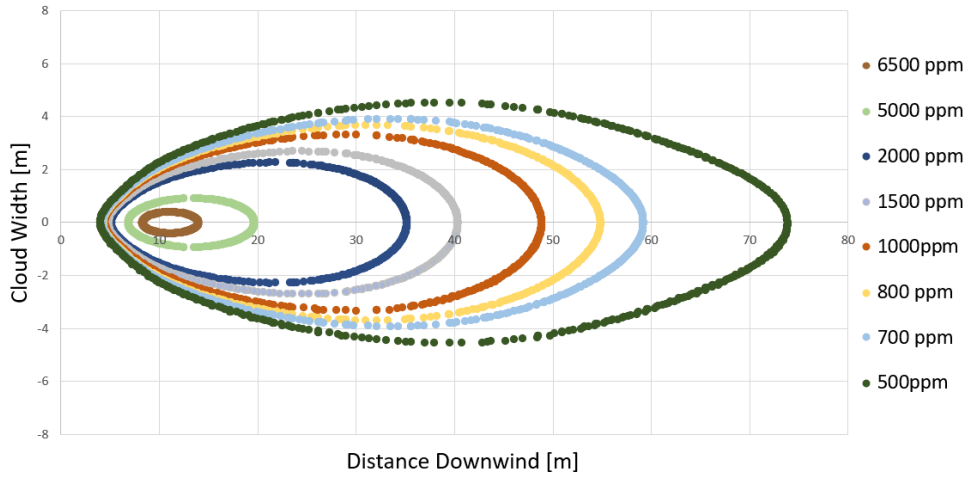

Figure 4.40: Iso-concentration curves obtained from a hydrogen release (300 bar, 1 mm hole, 1.5 m/s wind, stable conditions). Detection at 1 m height. The curves show an elliptical distribution of the cloud.

The point A_0 (x_{A0} ; y_{A0}) represents the point of the ellipse closest to the release along the main direction of dispersion. Since the point of maximum detected concentration (A_0) does not coincide with the actual point of release (x_R; y_R), it is necessary to estimate the distance α that separates them, considering the operating and environmental conditions. Assuming that we have at least four points in space, identified by the coordinates (x_1,y_1), (x_2,y_2), (x_3,y_3), (x_4,y_4) which lie on the same iso-concentration curve, and on the same ellipse, it is possible to determine the coordinates of the centre of the ellipse by solving a system of nonlinear equations.

The generic equation of an ellipse is given below:

$$\frac{[(x-x_0)cos\theta+(y-y_0)sen\theta]^2}{a^2}+\frac{[(x-x_0)sen\theta+(y-y_0)cos\theta]^2}{b^2}=1 \quad \textbf{(4.5)}$$

where θ is the angle of rotation of the ellipse with respect to the x-axis. For simplicity, the analysis assumed that the rotation angle of the ellipse was zero, meaning that the major axis was aligned with the x-axis, corresponding to the prevailing wind direction. However, this assumption can be overcome by changing the variables to include a rotation angle θ, making the model more general and suitable for scenarios in which the cloud develops in directions that are not orthogonal to the Cartesian axes. A limitation is related to the dynamic nature of the hydrogen cloud: being a light and highly diffusive gas, its shape and position can vary rapidly over time, making it difficult to obtain well-defined and stable iso-concentration curves. A possible solution, which could be explored in future developments, consists of integrating a fixed-time cloud reconstruction model, using wind speed as a measurable parameter. Knowing the wind direction and intensity, it would theoretically be possible to correct the positions detected by the drone, bringing them back to a common temporal reference. Although this approach was not implemented in this work, it represents an interesting prospect for improving the spatial and temporal consistency of concentration maps, especially under variable environmental conditions.

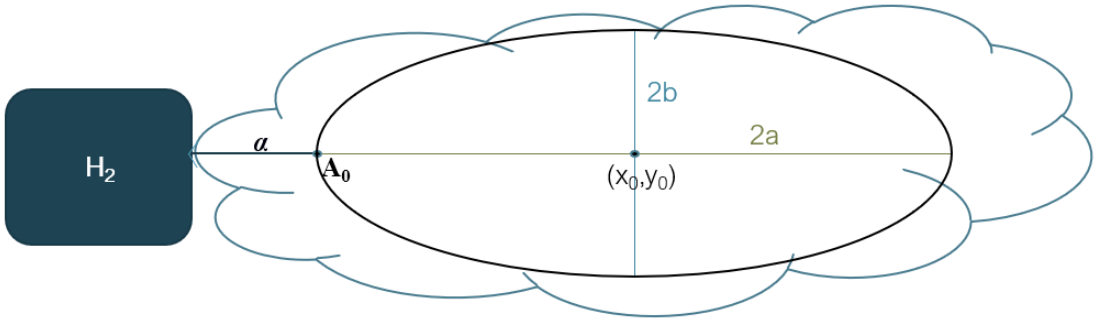

Figure 4.41: Generic ellipse with semi-axes a and b, and centre (x0, y0).

To solve the system of nonlinear equations that allows estimation of the main parameters of the ellipse, namely, semi-axes and centre coordinates, a dedicated spreadsheet was developed. This tool allows, starting from the coordinates of four uniformly distributed points belonging to the same isoconcentration curve, to automatically determine the values of the semi-axes and centre of the ellipse that approximates the spatial distribution of the cloud. Once these parameters are known, it is also possible to calculate the coordinates of point A_0, i.e., the point on the ellipse closest to the release source. For greater clarity, all the equations used to solve the system have been reported in the **Annex 2**.

It is important to underline that the point A0, obtained as a projection along the main axis of the ellipse, does not coincide exactly with the real point of release of hydrogen. Between these two points, there is a distance, indicated by the symbol α, which represents a systematic deviation influenced by various physical and environmental factors. In particular, the distance α depends on the atmospheric conditions, the gas release pressure, the difference in altitude between the release point and the measurement plane, as well as the diameter of the hole through which the release occurs. However, calculating the exact distance α is

unrealistic in a real-world scenario, as the parameters it depends on are generally unknown at the time of detection. Nevertheless, the proposed approach still provides important information for emergency management.

Geometric analysis of iso-concentration curves allows the identification of the cloud direction, which is generally aligned with the wind direction. A more operational and less uncertain approach is proposed: draw a line along the major axis, passing through the cloud centre, and extend it in both directions. In this context, the wind direction provides crucial information for determining which side of the line to proceed with the analysis, correctly orienting the search for the release point. The line, superimposed on the plant map, allows the identification of potentially affected structures. If the line passes through a single equipment, identification is immediate, as shown in **Figure 4.42**. If it crosses a larger area of the plant, a progressive analysis is performed, starting from the most likely point and moving away, with the support of intelligent systems that guide the operator through the investigation. This approach is particularly useful in complex plants, where knowledge of the spatial configuration narrows the investigation and allows for targeted interventions.

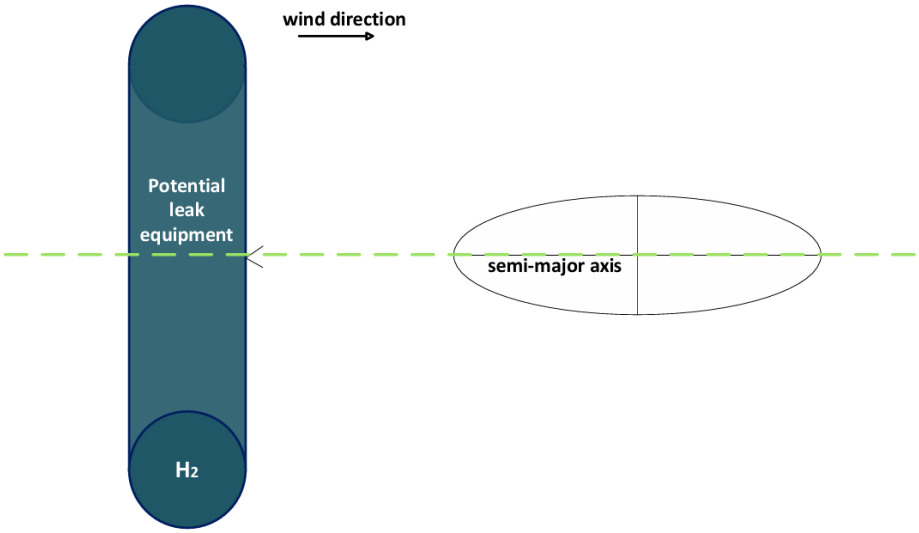

Figure 4.42: Identification of the potential release area in the event of a pipeline leak. The direction of the release is obtained by following the semi-major axis of the ellipse towards the affected equipment (indicated in the figure by the green dashed line).

To facilitate understanding of the proposed method, the main steps for estimating the possible release area from the concentration map are reported below.

Phase 1. Hydrogen Detection at the Plant

The drone flies with progressively decreasing altitude until a hydrogen concentration of 500 ppm is detected.

Phase 2. Data Collection:

The hydrogen concentration map is generated at the selected height, and at least four points with identical concentration levels are subsequently chosen.

Phase 3. Ellipse Construction:

The selected points are used to calculate the semi-axes and the centre of the ellipse that approximates the iso-concentration curve.

Phase 4. Identifying the affected equipment

By tracing the line oriented according to the semi-major axis of the ellipse on the plant, it is possible to identify the equipment it intersects and select the most likely affected one.

For completeness, a qualitative study was conducted on the α parameter, with the aim of analysing its dependencies on other physical and environmental parameters. Specifically, the relationships between α and variables such as the diameter of the release hole, storage pressure, height (as the height distance between the detection plane and the release point), and atmospheric conditions were considered. The results obtained can support the localization of the release area and the identification of the equipment involved, even with data unknown a priori. The analysis initially considered the effect of release pressure and orifice diameter and then extended to the influence of height and environmental conditions. The aim was to understand how α varies as these parameters vary. To this end, a contour plot was used, which is a two-dimensional graphic representation of a three-dimensional surface, in which level lines, the contours, connect points with the same value of the dependent variable. In this case, the lines represent constant values of α as a function of the pressure and the diameter of the hole. The contour plot shown in **Figure 4.43** was obtained following a campaign of numerical simulations conducted using the PHAST software, systematically varying the release pressure and the hole diameter, while keeping the environmental conditions (atmospheric stability and wind speed) and the height distance between the detection plane and the release point constant. This methodology allowed for the individual assessment of each parameter influence on the distance α. From the analysis of the graph, it clearly emerges that α tends to increase as both the release pressure and the hole diameter decrease, highlighting a significant sensitivity of the α parameter with respect to these two operating variables. The values of α are represented by contour lines and a colour scale ranging from dark blue (minimum values, about 5.25 m) to yellow (maximum values, about 8.75 m). From the contour plot, it is clearly observed that:

- α increases as the hole diameter decreases; the regions with higher values of α (lighter colours) are concentrated in the left part of the graph, where the diameter is smaller.
- α also tends to increase as the pressure decreases, although with a less marked variation compared to the diameter, the contour lines show a gentler gradient along the pressure axis.
- The distribution of contour lines suggests a greater sensitivity of α to the hole diameter, compared to the pressure.

This representation visually confirms the quantitative results obtained through the correlation analysis, highlighting that the hole diameter has a more significant impact on the distance α than the release pressure.

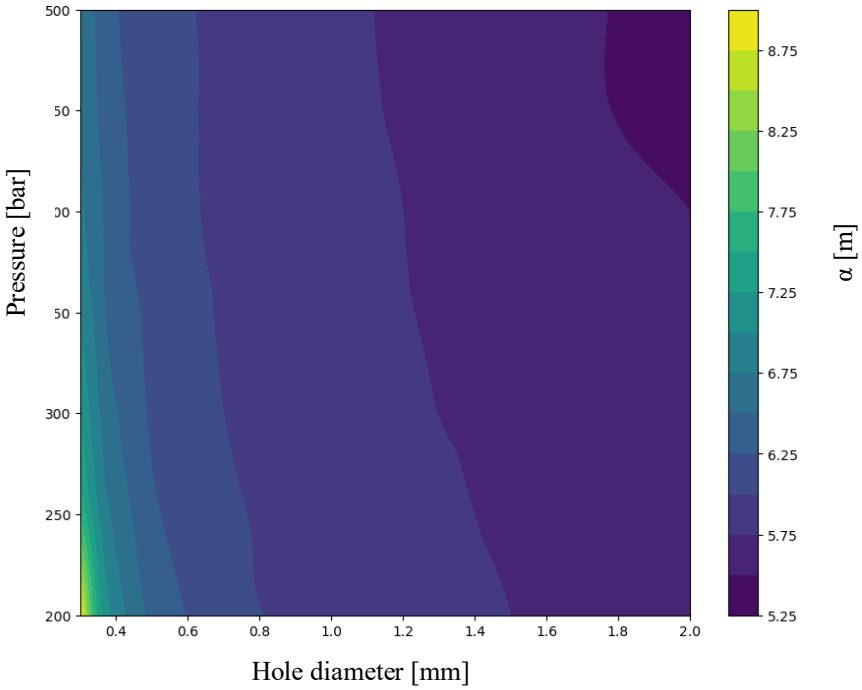

Figure 4.43: Contour plot of distance α as a function of release pressure and hole diameter.

To quantitatively investigate these relationships, the Pearson correlation between α and each parameter was calculated, using the formula reported in the Pearson (1895) and statistical analysis tools. Pearson correlation is a statistical index that measures the strength and direction of the linear relationship between two variables. The coefficient varies between -1 and +1:

- a value close to +1 indicates a strong positive correlation (the variables grow together),
- a value close to -1 indicates a strong negative correlation (one variable grows while the other decreases),
- a value close to 0 indicates no linear correlation.

The statistical analysis conducted by calculating the Pearson correlation coefficient (Nancarrow et al., 2021) allowed the quantification of the linear relationship between the distance α and the main physical parameters considered, such as the hole diameter and the release pressure. The results, summarized in **Table 4.6**, highlight a strong negative correlation between α and the hole diameter, with a coefficient equal to -0.758, statistically significant at a confidence level higher than 99% ($p < 0.001$). In this context, the p-value represents the probability that the observed correlation is due to chance: a very low value, as in this case, indicates that the correlation is highly significant from a statistical point of view. As regards the pressure, a weaker negative correlation is observed, equal to -0.247, however significant at the 95% level ($p = 0.023$), suggesting that even an increase in pressure contributes, albeit to a lesser extent, to a reduction in the distance α. Finally, the absence of correlation between diameter and pressure confirms that the two parameters were varied independently in the simulations. These results support the hypothesis that the distance α is influenced more significantly by the hole diameter than by the pressure, providing useful indications for the calibration of dispersion models as a function of operating

conditions.

Table 4.6: Pearson correlation coefficients between three variables: hole diameter (Dhole), release pressure (Pressure) and distance α (Alpha), calculated on a sample of 84 simulations.

		Dhole	Pressure	Alfa
Dhole	Pearson Correlation	1	.000	-.758**
	Sig. (2-tailed)		1.000	<.001
	N	84	84	84
Pressure	Pearson Correlation	.000	1	-.247*
	Sig. (2-tailed)	1.000		.023
	N	84	84	84
Alfa	Pearson Correlation	-.758**	-.247*	1
	Sig. (2-tailed)	<.001	.023	
	N	84	84	84

A further series of simulations was conducted keeping the release pressure and the hole diameter constant, in order to isolate the effect of the environmental conditions and the height distance between the detection plane and the release point on the distance α. The graph reported in **Figure 4.44** represents the results obtained, showing the variation of α as a function of the height of the release point (H_{loc}), with the points coloured according to the specific combination of atmospheric stability class and wind speed. In particular, the green colour represents the most stable conditions (class F) with a wind speed of 1.5 m/s; blue indicates class D with the same speed; while yellow corresponds to class D associated with a higher wind speed of 5 m/s. It is important to highlight that, as described in **Section 4.4.2**, to eliminate the dependence of the release height from the ground, the height H_{loc} is defined as the distance between the detection plane and the exit hole. The colour scale, from blue to yellow, reflects the increasing influence of the atmospheric conditions, with values ranging from 1.5D to 5D. The graph shows a general tendency for the distance α to increase with the increase of H_{loc} and the wind speed; on the contrary, with the increase of the atmospheric stability, the value of α decreases.

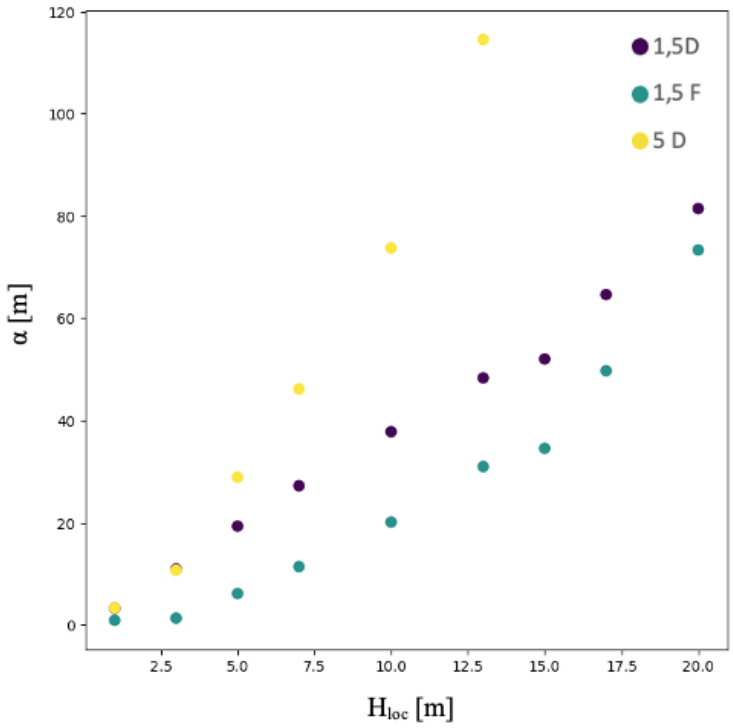

Figure 4.44: Contour plot of distance α as a function of atmospheric condition and height distance between the detection plane and the release point.

The correlation table reported in **Table 4.7** summarizes the Pearson coefficients calculated to evaluate the linear relationship between the distance α, the height and the atmospheric conditions. In calculating the Pearson coefficient, atmospheric conditions were numerically coded based on the combination of stability class and wind speed, thus obtaining a representative quantitative variable. This coding allowed the evaluation of the correlation between these conditions and the distance α. The results show a strong positive correlation between α and H_{loc}, with a coefficient equal to 0.784, statistically significant at a confidence level higher than 99%. This indicates that as the distance between the detection plane and the release point increases, the distance α tends to increase significantly. The correlation between α and atmospheric conditions is negative and weaker, with a coefficient equal to 0.283, not statistically significant ($p = 0.181$), suggesting that, in the range of conditions analysed, the effect of atmospheric conditions on the distance α is less marked and not systematic. Finally, the correlation between H_{loc} and atmospheric conditions is also negative and weak ($r = -0.218$, $p = 0.305$), confirming that the two parameters were varied independently. These results reinforce the evidence that the release height represents a determining factor in the localization of the cloud centre, while the influence of atmospheric conditions appears more contained in this specific simulation context.

Table 4.7: Pearson correlation coefficients between three variables: height (Hloc), Atmospheric condition and distance α (Alpha), calculated on a sample of 24 simulations.

Correlations

		Hloc	Atm. Condition	alfa
Hloc	Pearson Correlation	1	-0.218	.784**
	Sig. (2-tailed)		0.305	0.000
	N	24	24	24
Atm. Condition	Pearson Correlation	-0.218	1	0.283
	Sig. (2-tailed)	0.305		0.181
	N	24	24	24
alfa	Pearson Correlation	.784**	0.283	1
	Sig. (2-tailed)	0.000	0.181	

The overall analysis shows that α has a quadratic dependence on the hole diameter and on the height, and a linear dependence on the pressure, so there is a stronger dependence on parameters that are generally not known a priori. For this reason, a graphical representation of the dependence of α on D_{hole} for different values of H_{loc} was created to visualize the combined effect of these variables and support the definition of release localization strategies.

Figure 4.45 shows the dependence of the parameter α on the hole diameter for different detection heights (H_{loc}), defined as the vertical distance between the gas release point and the measurement plane. The data reported were obtained through simulations conducted with the PHAST software, under stable atmospheric conditions (classified as "D"), as these conditions are among the most common during daytime hours in industrial environments, according to the Pasquill classification, with a constant wind speed of 1.5 m/s and a storage pressure of 500 bar. It is observed that, for Hloc values of 1.5 m, α is almost constant as D varies, indicating a low sensitivity of the parameter when the detection is close to the release point. Conversely, as the detection height increases, the dependence of α on the diameter becomes progressively more marked. In particular, a decreasing trend in the α parameter is observed as the hole diameter increases, with a more marked variation for smaller diameters. However, for values greater than 2 mm, α tends to stabilize, showing substantial independence from the diameter at least up to a release height of 15 m. This behaviour confirms that, in detection conditions further from the release point, the hole diameter significantly affects the distance α.

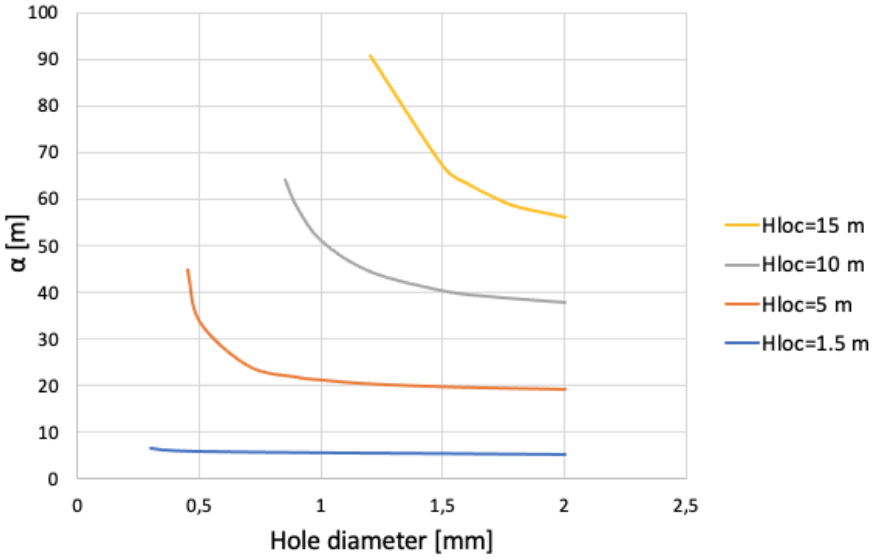

Figure 4.45: Trend of the α distance from the hole diameter at different height distance between the detection plane and the release point at 500 bar and environmental condition of 1.5D.

This behaviour confirms the need to adopt an approach based on identifying the release area, rather than on a precise estimate of the α parameter. Indeed, in the range of diameters considered in the study, the value of α shows significant variability at the highest detection heights, and these parameters are generally not known a priori. This consideration guided the development of the proposed model. For completeness, a correlation of the α parameter as a function of the four variables just discussed has been derived in **Annex 2**. This correlation can be used as a support when it is necessary to estimate the diameter and height of the release through iterative calculations.

Recent studies (Papadaki et al., 2025) have demonstrated the effectiveness of data-driven models for estimating safety distances in toxic dispersion scenarios, even in the presence of unknown variables. These approaches, based on PHAST simulations and machine learning algorithms, offer a flexible and adaptable methodology that can be integrated with dynamic monitoring systems using drones. Similarly, this work proposes a model for hydrogen release source localization based on the geometric reconstruction of the curves. In line with the previous study, further developments could include the implementation of machine learning techniques to improve the system's predictive and adaptive capacity.

In summary, the proposed model allows for the localization of the hydrogen release source even under uncertain conditions, integrating numerical simulations and dynamic monitoring techniques. This approach represents an innovative contribution to industrial risk management, with potential applications in complex, real-time scenarios. The results obtained can be integrated into monitoring systems and forecasting models to optimize sensor positioning, improve the timeliness of interventions, and increase the reliability of safety procedures, in line with the objectives of operational resilience and energy sustainability.

Chapter 4 Partial Conclusions

In conclusion, this chapter explored the issues related to hydrogen management in the industrial sector, highlighting how its unique physical and chemical characteristics make it complex to manage under real-world operating conditions. Specifically, the vulnerability of industrial infrastructure to material degradation was analysed, with a focus on the phenomenon of embrittlement and its implications for plant safety, contributing to the answer to RQ1 through a historical analysis of accidents and the identification of the components most susceptible to degradation.

To introduce a methodology for detecting and identifying small hydrogen leaks, the PHAST software was preliminarily tested through comparison with experimental data. The results obtained confirmed the validity of the numerical model, with a low mean absolute error, demonstrating the reliability of the software in reproducing small-scale release scenarios. Validation was necessary because, although PHAST is widely used in the literature for simulating hydrogen release scenarios, no studies confirming its accuracy were identified. Subsequently, a systematic study of pressurized hydrogen release was conducted, with the aim of analysing cloud propagation and the parameters that influence its dispersion. Based on these results, an operational methodology was developed to identify the release source using sensor-equipped drones. The proposed strategy involves a progressively descending flight until the cloud is intercepted, mapping the concentrations, and extracting the cloud geometry. Subsequently, it is possible to identify a probable release equipment.

This approach represents an initial qualitative analysis, useful for narrowing the research area and guiding emergency response operations. The information obtained can be integrated into monitoring systems and forecasting models to optimize sensor positioning, improve the timeliness of interventions, and increase the reliability of safety procedures in complex industrial scenarios.

A direct comparison between the CFD simulations and the modeling approaches adopted in this work would be useful for further validation and analysis of the results obtained. In particular, such a comparison would allow for a more detailed assessment of the differences and complementarities between the modeling tools. This analysis will be developed in future research.

This chapter contributes to achieving objective SG3 by evaluating the effectiveness of dynamic monitoring technologies for real-time detection of hydrogen leaks and proposing innovative solutions for the prevention and management of risks associated with highly flammable gases. Furthermore, the chapter addresses RQ3 by analysing the main challenges in hydrogen leak detection and proposing an operational approach based on dynamic monitoring, numerical simulations, and dispersion analysis, useful for locating the release source and defining safe flight paths. Thus, the work provides a theoretical and applied contribution to the construction of more resilient plants, in line with the Seveso III objectives and the needs of a safe and sustainable energy transition.

Chapter 4 References

Acar, C., and Dincer, I. (2019). Review and evaluation of hydrogen production options for better environment. Journal of Cleaner Production, 218, 835–849. https://doi.org/10.1016/j.jclepro.2019.02.046

Alfarizi, M. G., Ustolin, F., Vatn, J., Yin, S., and Paltrinieri, N. (2023). Towards accident prevention on liquid hydrogen: A data-driven approach for releases prediction. Reliability Engineering & System Safety, 236, 109276. https://doi.org/10.1016/j.ress.2023.109276

Andersson, J., and Grönkvist, S. (2019). Large-scale storage of hydrogen. International Journal of Hydrogen Energy, 44(23), 11901-11919.https://doi.org/10.1016/j.ijhydene.2019.03.063

Bade, S. O. and Tomomewo, O. S. (2024). A review of governance strategies, policy measures, and regulatory framework for hydrogen energy in the United States. International Journal of Hydrogen Energy, 78, 1363–1381. https://doi.org/10.1016/j.ijhydene.2024.06.338

Barchyn, T. E., Hugenholtz, C. H., and Fox, T. A. (2019). Plume detection modeling of a drone-based natural gas leak detection system. Elementa: Science of the Anthropocene, 7, 41. https://doi.org/10.1525/elementa.379

BARPI (2022). The ARIA database [WWW Document], The French Bureau for Analysis of Industrial Risks and Pollutions (BARPI). URL: https://www.aria.developpement-durable.gouv.fr (Accessed 10.23).

Bel Hadj Ali, N., Abichou, T., and Green, R. (2020). Comparing estimates of fugitive landfill methane emissions using inverse plume modeling obtained with Surface Emission Monitoring (SEM), Drone Emission Monitoring (DEM), and Downwind Plume Emission Monitoring (DWPEM). Journal of The Air & Waste Management Association, 70(4), 410–424. https://doi.org/10.1080/10962247.2020.1728423

Byrom, R., and Shine, K. (2022). Methane's Solar Radiative Forcing. Geophysical Research Letters, 49. https://doi.org/10.1029/2022GL098270.

Birch, A. D., Brown, D. R., Dodson, M. G., and Swaffield, F. (1984). The structure and concentration decay of high pressure jets of natural gas. Combustion Science and Technology, 36(5-6), 249–261. https://doi.org/10.1080/00102208408923739

Burgués, J., Hernández, V., Lilienthal, A. J., and Marco, S. (2019). Smelling nano aerial vehicle for gas source localization and mapping. Sensors, 19(3), 478. https://doi.org/10.3390/s19030478

Burgués, J., and Marco, S. (2020). Environmental chemical sensing using small drones: A review. Science of The Total Environment, 748, 141172. https://doi.org/10.1016/j.scitotenv.2020.141172

Burgués, J., Doñate, S., Esclapez, M. D., Saúco, L., and Marco, S. (2022). Characterization of odour emissions in a wastewater treatment plant using a drone-based chemical sensor system. Science of The Total Environment, 846, 157290. https://doi.org/10.1016/j.scitotenv.2022.157290

Buttner, W. J., Post, M. B., Burgess, R., and Rivkin, C. (2011). An overview of hydrogen safety sensors and requirements. International Journal of Hydrogen Energy, 36(3), 2462–2470. https://doi.org/10.1016/j.ijhydene.2010.04.176

Calabrese, M., Portarapillo, M., Di Nardo, A., Venezia, V., Turco, M., Luciani, G., and Di Benedetto, A. (2024). Hydrogen safety challenges: a comprehensive review on production, storage, transport, utilization, and CFD-based consequence and risk assessment. Energies, 17(6), 1350. https://doi.org/10.3390/en17061350

Campari, A., Bennici, M., Tzioutzios, D., and Liu, Y. (2023). Optimization of Leak Detectors' Positioning in a Hydrogen Refueling Station. Chemical Engineering Transactions, 105, 115–120. https://doi.org/10.3303/CET23105020

Casabona, M. (2020). Deep learning basato su immagini da drone per la super risoluzione di scene multispettrali acquisite da satellite. Master Thesis, Politecnico di Torino. https://webthesis.biblio.polito.it/15640/

Castro Rodriguez, D.J., Tufano, C., Vitale, M., Mietkiewicz, J., Baldissone, G., Barresi, A.A., and Demichela, M. (2023). Dataset of NaTech events triggered by lightning within the Process Industry, Mendeley Data, V2. https://doi.org/10.17632/fff64w3rzn.2

Castro Rodriguez, D.J., Mietkiewicz, J., Vitale, M., Baldissone, G., Barresi, A.A., and Demichela, M. (2024). NaTech triggered by lightning: Novel insights from past events in the process industry. Heliyon 10, e31610. https://doi.org/10.1016/j.heliyon.2024.e31610

Chae, C. K., Park, B. H., Huh, Y. S., Kang, S. K., Kang, S. Y., and Kim, H. N. (2020). Development of a new real time responding hydrogen fueling protocol. International Journal of Hydrogen Energy, 45(30), 15390-15401. https://doi.org/10.1016/j.ijhydene.2020.04.012

Chemsafe (2024). Database for safety characteristics in explosion protection version 08/24 [WWW Document]. URL: https://www.chemsafe.ptb.de/home

Cole, T. J., and Altman, D. G. (2017). Statistics Notes: What is a percentage difference? Bmj, 358: j3663. https://doi.org/10.1136/bmj.j3663

Daponte, P., De Vito, L., Glielmo, L., Iannelli, L., Liuzza, D., Picariello, F., and Silano, G. (2019). A review on the use of drones for precision agriculture. In IOP conference series: earth and environmental science, 275(1), 012022. IOP Publishing. https://doi.org/10.1088/1755-1315/275/1/012022

Demirbas, A. (2017). Future hydrogen economy and policy. Energy Sources, Part B: Economics, Planning, and Policy, 12(2), 172–181. https://doi.org/10.1080/15567249.2014.950394

DNV (2018). Phast and phast lite tutorial manual. [WWW Document]. URL: https://mysoftware.dnv.com/download/public/phast/Tutorials/PhastandPhastLiteTutorials.pdf (Accessed 03/2025).

DNV (2025). Phast and Safeti Technical Documentation – Dispersion Modelling. [WWW Document]. URL : https://mysoftware.dnv.com/knowledge-centre/phast-and-safeti/tech-doc/05dispersion/(Accessed: 07/2025).

Doz, S., Foucher, P. Y., and Watremez, X. (2018). Methane leak near real time quantification with a hyperspectral infrared camera. In Thermosense: Thermal Infrared Applications XL (Vol. 10661, p. 1066103). SPIE. https://doi.org/10.1117/12.2304819

Druart G., Foucher P.-Y., Doz S., Watremez X., Jourdan S., Vanneau E., Pinot H. (2021). Test of SIMAGAZ: a LWIR cryogenic multispectral infrared camera for methane gas leak detection and quantification, in: SPIE Defense + Commercial Sensing, Algorithms, Technologies, and Applications for Multispectral and Hyperspectral Imaging XXVII. SPIE, Online, United States, p. 117270G. https://doi.org/10.1117/12.2586933

Dutta, S. (2014). A review on production, storage of hydrogen and its utilization as an energy resource. Journal of Industrial and Engineering Chemistry, 20(4), 1148–1156. https://doi.org/10.1016/j.jiec.2013.07.037

Dwivedi, S.K. and Vishwakarma, M. (2018). Hydrogen embrittlement in different materials: A review. International Journal of Hydrogen Energy 43, 21603–21616. https://doi.org/10.1016/j.ijhydene.2018.09.201

Ekerold, E. N. (2014). Interpretation of geometrical effects in consequence modelling. Comparison study between the commercial consequence assessment tools FLACS and PHAST for flammable gas dispersion. Master Thesis, The University of Bergen. https://bora.uib.no/bora-xmlui/handle/1956/8039

Elaoud, S., Hadj-Taïeb, L., and Hadj-Taïeb, E. (2010). Leak detection of hydrogen–natural gas mixtures in pipes using the characteristics method of specified time intervals. Journal of Loss Prevention in The Process Industries, 23(5), 637–645. https://doi.org/10.1016/j.jlp.2010.06.015

eMARS (2022). EUROPA - eMARS Accidents Search - European Commission [WWW Document]. URL: https://emars.jrc.ec.europa.eu/en/emars/accident/search (Accessed 10.23).

European Commission (2015). Directive 2012/18/EU of the European Parliament and of the Council of 4 July 2012 on the control of Major-Accident Hazards involving dangerous substances, amending and subsequently repealing Council Directive 96/82/EC. URL: https://eur-lex.europa.eu/legal-content/ EN/TXT/PDF/?uri=CELEX:32012L0018

(Accessed 10.23).

JRC (2023): HIAD 2.1. European Commission, Joint Research Centre (JRC) Dataset [WWW Document]. URL: http://data.europa.eu/89h/1d6b06e9-3a89-4ec2-b051-3fb8a28eab9f (Accessed 10.23).

Ferriso, C. (1962). High-Temperature Spectral Absorption of the 4.3-Micron CO2 Band. Journal of Chemical Physics, 37, 1955–1961. https://doi.org/10.1063/1.1733412

Ganci, F., Carpignano, A., Mattei, N., and Carcassi, M. N. (2011). Hydrogen release and atmospheric dispersion: Experimental studies and comparison with parametric simulations. International Journal of Hydrogen Energy, 36(3), 2445–2454. https://doi.org/10.1016/j.ijhydene.2010.04.006

Giannissi, S. G., Hoyes, J. R., Chernyavskiy, B., Hooker, P., Hall, J., Venetsanos, A. G., and Molkov, V. (2015). CFD benchmark on hydrogen release and dispersion in a ventilated enclosure: Passive ventilation and the role of an external wind. International Journal of Hydrogen Energy, 40(19), 6465-6477. https://doi.org/10.1016/j.ijhydene.2015.03.072

Giannissi, S. G., Tolias, I. C., Melideo, D., Baraldi, D., Shentsov, V., Makarov, D., Molkov, V., and Venetsanos, A. G. (2021). On the CFD modelling of hydrogen dispersion at low-Reynolds number release in closed facility. International Journal of Hydrogen Energy, 46(57), 29745-29761. http://doi.org/ 10.1016/j.ijhydene.2020.09.078

Gnoni, M.G., Andriulo, S., Maggio, G., and Nardone, P. (2013). "Lean occupational" safety: An application for a Near-miss Management System Design, Safety Science, 53, 96–104. https://doi.org/10.1016/j.ssci.2012.09.012

Gong, L., Yang, S., Han, Y., Jin, K., Lu, L., Gao, Y., and Zhang, Y. (2022). Experimental investigation on the dispersion characteristics and concentration distribution of unignited low-temperature hydrogen release. Process Safety and Environmental Protection, 160, 676–682. https://doi.org/10.1016/j.psep.2022.02.055

Greenwood, W. W., Lynch, J. P., and Zekkos, D. (2019). Applications of UAVs in civil infrastructure. Journal of Infrastructure Systems, 25(2), 04019002. https://doi.org/10.1061/(ASCE)IS.1943-555X.000046

Han, S. H., Chang, D., and Kim, J. S. (2014). Experimental investigation of highly pressurized hydrogen release through a small hole. International Journal of Hydrogen Energy, 39(17), 9552–9561. https://doi.org/10.1016/j.ijhydene.2014.03.044

Hansler, R.J., Bellamy, L.J., and Akkermans, H.A. (2022) Ageing assets at major hazard chemical sites–The Dutch experience. Safety Science, 153, 105788. https://doi.org/10.1016/j.ssci.2022.105788

Hecht, E., Panda, P., Roy C., B., and Ye, D. (2019). Characteristics of Cryogenic

Hydrogen Releases Under Unignited and Ignited Conditions. OSTI.GOV, Technical Report, Sandia National Lab. (SNL-CA), Livermore, CA (United States); Sandia National Lab. (SNL-NM), Albuquerque, NM (United States). https://doi.org/10.2172/1763216

Hopfield, J., and Dieke, G. (1926). Absorption Spectrum of the Hydrogen Molecule. Nature, 118, 592–592. https://doi.org/10.1038/118592C0.

Hosch M. J. (2019). Hydrogen and fire safety: Detecting the most flammable element on earth. Det-tronics. URL: https://www.det-tronics.com/content/documents/AR-1132-Hydrogen-and-fire-safety.pdf (Accessed 11/2024).

Howard, J., Burch, D., and Williams, D. (1956). Infrared Transmission of Synthetic Atmospheres.* II. Absorption by Carbon Dioxide. Journal of The Optical Society of America, 46, 237–241. https://doi.org/10.1364/JOSA.46.000237.

Hyndman, R. J., and Koehler, A. B. (2006). Another look at measures of forecast accuracy. International Journal of Forecasting, 22(4), 679-688. https://doi.org/10.1016/j.ijforecast.2006.03.001

Hu, C., Thomasson, J. A., Reberg-Horton, C., Mirsky, S. B., and Bagavathiannan, M. V. (2022). Modeling realistic 3D agricultural vegetations using a photometric-based approach and its application to weed detection. Computers and Electronics in Agriculture, 198, 107020. https://doi.org/10.1016/j.compag.2022.107020

International Energy Agency (2021). [WWW Document]. National Hydrogen Strategy Preliminary Guidelines. URL: https://www.iea.org/policies/13087-national-hydrogen-strategy-preliminary-guidelines (Accessed 02/2025).

Kahl, J. D. W., and Chapman, H. L. (2018). Atmospheric stability characterization using the Pasquill method: A critical evaluation. Atmospheric Environment, 187, 196–209. https://doi.org/10.1016/j.atmosenv.2018.05.058

Khodadadi-Mousiri, A., Yaghoot-Nezhada, A., Sadeghi-Yarandi, M., and Soltanzadeh, A. (2023). Consequence modeling and root cause analysis (RCA) of the real explosion of a methane pressure vessel in a gas refinery. Heliyon, 9(4). https://doi.org/10.1016/j.heliyon.2023.e14628

Khorram, R. (2020). Modeling the consequences release of cyanogen agents in bushehr nuclear power plant neighborhood using PHAST, ALOHA and WISER software. Iran Occupational Health, 17(4), 37–49.

Koutsourakis, N., Tolias, I. C., Giannissi, S. G., and Venetsanos, A. G. (2023). Numerical investigation of hydrogen jet dispersion below and around a car in a tunnel. Energies, 16(18), 6483. https://doi.org/10.3390/en16186483

Koval A., Irigoyen E. and Koval T. (2017). AR. Drone as a platform for

measurements. 2017 IEEE 37th International Conference on Electronics and Nanotechnology (ELNANO) (pp. 424–427). IEEE.

Laadel, N. E., El Mansori, M., Kang, N., Marlin, S., and Boussant-Roux, Y. (2022). Permeation barriers for hydrogen embrittlement prevention in metals–a review on mechanisms, materials suitability and efficiency. International Journal of Hydrogen Energy, 47(76), 32707–32731. https://doi.org/10.1016/j.ijhydene.2022.07.164

Lackner M. (2007). Tunable diode laser absorption spectroscopy (tdlas) in the process industries – A review. Reviews in Chemical Engineering 23, 65–147. https://doi.org/10.1515/REVCE.2007.23.2.65

Lee, C. C., Wan, T. J., Kuo, C. Y., and Chung, C. Y. (2006). Estimating air quality in a traffic tunnel using a forecasting combination model. Environmental Monitoring and Assessment, 112, 327–345. https://doi.org/10.1007/s10661-006-1073-x

Lee, H. E., Sohn, J. R., Byeon, S. H., Yoon, S. J., and Moon, K. W. (2018). Altenative risk assessment for dangerous chemicals in South Korea regulation: Comparing three modelling programs. International Journal of Environmental Research and Public Health, 15(8), 1600. https://doi.org/10.3390/ijerph15081600

Li X., Ma X., Zhang J., Akiyama E., Wang Y., and Song X. (2020). Review of hydrogen embrittlement in metals: hydrogen diffusion, hydrogen characterization, hydrogen embrittlement mechanism and prevention. Acta Metallurgica Sinica (English Letters), 33, 759–773. https://doi.org/10.1007/s40195-020-01039-7

Li K., Hu Y., Wang L., Yang Z., Wang B., Yuan M., Li W., Yu C., Zheng W. (2023). Detecting unknown gas clouds with multispectral imagery based on spectral angle matching, in: Conference on Infrared, Millimeter, Terahertz Waves and Applications (IMT2022), SPIE, pp. 660–665. https://doi.org/10.1117/12.2662678

MacNguyen, R. (2023). Comparison of hydrogen and hydrocarbon fuels hazards and practical risk management strategies. Process Safety Progress, 42(2), 225-241. https://doi.org/10.1002/prs.12460

Makarov, D., Verbecke, F., Molkov, V., Roe, O., Skotenne, M., Kotchourko, A., Lelyakin, A., Yanez, J., Hansen, O., Middha, P., Ledin, S.,Baraldi, D., Heitsch, M., Efimenko, A., and Gavrikov, A. (2009). An inter-comparison exercise on CFD model capabilities to predict a hydrogen explosion in a simulated vehicle refuelling environment. International Journal of Hydrogen Energy, 34(6), 2800-2814. https://doi.org/10.1016/j.ijhydene.2008.12.067

Ministero dei Lavori Pubblici (2001). Requisiti minimi di sicurezza in materia di pianificazione urbanistica e territoriale per le zone interessate da stabilimenti a rischio di incidente rilevante, Decreto Ministeriale 9 Maggio 2001, Supplemento ordinario Nr 151 alla “Gazzetta Ufficiale” n. 138 del

16 giugno 2001 - Serie generale. Italia.

Murugan, D., Garg, A., and Singh, D. (2017). Development of an adaptive approach for precision agriculture monitoring with drone and satellite data. IEEE Journal of Selected Topics in Applied Earth Observations and Remote Sensing, 10(12), 5322–5328. https://doi.org/10.1109/JSTARS.2017.2746185

Nancarrow, P., Al-Othman, A., Mital, D.K. and Döpking, S. (2021). Comprehensive analysis and correlation of ionic liquid conductivity data for energy applications. Energy, 220, 119761. https://doi.org/10.1016/j.energy.2021.119761

Okino, T., Yamahira, S., Yamada, S., Hirose, Y., Odagawa, A., Kato, Y., and Tanaka, T. (2017). Ultraviolet and visible spectral imaging of hydrogen flames using an organic photoconductive film CMOS imager. In Proceedings of the International Image Sensor Workshop (pp. 188–191).

Palacios, A., and Rengel, B. (2020). Computational analysis of vertical and horizontal jet fires. Journal of Loss Prevention in The Process Industries, 65, 104096. https://doi.org/10.1016/j.jlp.2020.104096

Pandya, N., Marsden, E., Floquet, P. and Gabas, N. (2008). Toxic release dispersion modelling with PHAST: parametric sensitivity analysis. In: CISAP - 3rd International Conference on Safety & Environment in Process Industry, 12–14 May 2008, Rome, Italy, pp. 179–186. Available at: https://hal.science/hal-04030478 (Accessed: 07/2025).

Papadaki, A., Àgueda, A., and Planas, E. (2025). Machine learning for safety distances prediction during emergency response of toxic dispersion accidental scenarios. Journal of Loss Prevention in the Process Industries, 95, 105604. https://doi.org/10.1016/j.jlp.2025.105604

Pearson, K. (1895). VII. Note on regression and inheritance in the case of two parents. Proceedings of the Royal Society of London, 58(347-352), 240-242. https://doi.org/10.1098/rspl.1895.0041

Pillosu, M. (2020). Very deep super resolution (VDSR): applicazione su dati acquisiti da UAV e da satellite in ambito agricoltura di precisione. Master Thesis, Politecnico di Torino. https://webthesis.biblio.polito.it/16263/

Portarapillo, M., Polidoro, F., and Di Benedetto, A. (2025). CFD-based risk assessment of underground hydrogen storage in salt caverns. Journal of Energy Storage, 128, 117192. https://doi.org/10.1016/j.est.2025.117192

Post, M. B., Buttner, W. J., Hartmann, K., Thorson, J., Pearman, D., and Wischmeyer, T. (2021). The NREL Sensor Laboratory: Status and Future Directions for Hydrogen Detection. Paper presented at the International Conference on Hydrogen Safety (ICHS 2021), Edinburgh, Scotland, 21–24 September. https://hysafe.info/uploads/papers/2021/176.pdf

Prakash, A., Kumar, U., Kumar, K., and Jain, V. K. (2011). A wavelet-based

neural network model to predict ambient air pollutants' concentration. Environmental Modeling & Assessment, 16, 503–517. https://doi.org/10.1007/s10666-011-9270-6

Qanbar, M. W., and Hong, Z. (2024). A review of hydrogen leak detection regulations and technologies. Energies, 17(16), 4059. https://doi.org/10.3390/en17164059

Rejeb, A., Abdollahi, A., Rejeb, K., and Treiblmaier, H. (2022). Drones in agriculture: A review and bibliometric analysis. Computers and Electronics in Agriculture, 198, 107017. https://doi.org/10.1016/j.compag.2022.107017

Ricci, F., Casson Moreno, V., and Cozzani, V. (2021). A comprehensive analysis of the occurrence of Natech events in the process industry. Process Safety and Environmental Protection, 147, 703–713. https://doi.org/10.1016/j.psep.2020.12.031

Roberts, P., Shirvill, L. C., Roberts, T. A., Butler, C. J., and Royle, M. (2006). Dispersion of hydrogen from high pressure sources. Hazards XIX - Process Safety and Environmental Protection, 151, 410–421.

Roes, A. L., and Patel, M. K. (2011). Ex-ante environmental assessments of novel technologies–Improved caprolactam catalysis and hydrogen storage. Journal of Cleaner Production, 19(14), 1659–1667. https://doi.org/10.1016/j.jclepro.2011.05.010

Russo P., Marra F., Mazzaro M., Pilo F., Marini D., Vianello C., Pulci G. (2020). Spatial and Radiative Characteristics of Large Scale Hydrogen Jet-fires. Chemical Engineering Transactions, 82, 217–222. https://doi.org/10.3303/CET2082037

Shelke, A., and Wen, J. (2020). The burning characteristics and flame evolution of hydrocarbon and hydrogen flash fires. Proceedings of the Combustion Institute. https://doi.org/10.1016/j.proci.2020.05.013

Spalevic, Z., Ilic, M., and Savija, V. (2018). The use of drones in agriculture-ICT policy, legal and economical aspects. Ekonomika, Journal for Economic Theory and Practice and Social Issues, 64(4), 93–107. https://doi.org/10.22004/ag.econ.290358

Sugimoto, S., Asahi, I., and Shiina, T. (2021). A practical-use hydrogen gas leak detector using CARS. International Journal of Hydrogen Energy, 46(37), 19693–19703. https://doi.org/10.1016/j.ijhydene.2021.03.101

Taj, G., Anand, S., Haneefi, A., Kanishka, R. P., and Mythra, D. H. A. (2020). Monitoring of historical structures using drones. In IOP Conference Series: Materials Science and Engineering 955(1), 012008. IOP Publishing. https://doi.org/10.1088/1757-899X/955/1/012008

UNECE (2021). Globally harmonized system of classification and labelling of chemicals (GHS), ST/SG/AC.10/30/Rev.9. United Nations Economic

Commission for Europe (UNECE).

Vitale, M., Barresi, A., and Demichela, M. (2024a). The Use of Aerial Platforms for Identification of Loss of Containment. Chemical Engineering Transactions, 111, 73-78. https://doi.org/10.3303/CET24111013

Vitale, M., Shi, H., Castro Rodriguez, D.J., Barresi, A. and Demichela, M. (2024b) Ageing in process industry: Identification of material degradation from past accidents analysis. IFAC-PapersOnLine 58(4), 568–573. https://doi.org/10.1016/j.ifacol.2024.07.279.

Vitale, M., Castro Rodriguez, D. J., Barresi, A., and Demichela, M. (2025a). Database of material degradation event within process industry, Mendeley Data, V1. https://doi.org/10.17632/6hd3xky6kb.1

Vitale, M., Rodriguez, D. J. C., Barresi, A. A., and Demichela, M. (2025b). Hydrogen Safety in Process Industry: Systematization of Past Lessons. Chemical Engineering Transactions, 116, 403–408. https://doi.org/ 10.3303/CET25116068

Wang T., Yang F., Hu Q., Hu S., Li Y. and Ouyang M. (2022). Experimental and simulation research on hydrogen leakage of double ferrule joints. Process Safety and Environmental Protection, 160, 839–846. https://doi.org/10.1016/j.psep.2022.02.056

Wang, X., and Ma, X. (2021). Risk control analysis of safety accident in hydrogen refueling station based on PHAST software. In IOP Conference Series: Earth and Environmental Science, 680(1), 012119.

Watremez, X., Marblé, A., Baron, T., Marcarian, X., Dubucq, D., Donnat, L., Cazes, L., Foucher, P., Danno, R., Elie, D., Chamberland, M., Gagnon, J.P., Gay, L. P., Dobler, J., Østrem, R., Russu, A., Schmidt, M., and Olivier Z. (2018). Remote sensing technologies for detecting, visualizing and quantifying gas leaks. In SPE International Conference and Exhibition on Health, Safety, Security, Environment, and Social Responsibility. SPE-190496-MS. https://doi.org/10.2118/190496-MS

Xiao, J., Travis, J. R., and Breitung, W. (2011). Hydrogen release from a high pressure gaseous hydrogen reservoir in case of a small leak. International Journal of Hydrogen Energy, 36(3), 2545–2554. https://doi.org/10.1016/j.ijhydene.2010.05.069

Yang, S., Talbot, R. W., Frish, M. B., Golston, L. M., Aubut, N. F., Zondlo, M. A., Gretencord, C., and McSpiritt, J. (2018). Natural gas fugitive leak detection using an unmanned aerial vehicle: Measurement system description and mass balance approach. Atmosphere, 9(10), 383. https://doi.org/10.3390/atmos9100383

Yuhua, D., Huilin, G., Jing'en, Z., and Yaorong, F. (2002). Evaluation of gas release rate through holes in pipelines. Journal of Loss Prevention in The Process Industries, 15(6), 423–428. https://doi.org/10.1016/S0950-4230(02)00041-4

Züttel, A. (2004). Hydrogen storage methods. Naturwissenschaften 91, 157–172. https://doi.org/10.1007/s00114-004-0516-x

5. Liquid Hydrogen and Risk Assessment

For storage and transportation, liquid hydrogen is seen as a good alternative to gaseous hydrogen due to its high energy density and relatively low weight (Tamburini et al., 2024). Indeed, in liquefied form, it has a density three orders of magnitude higher than atmospheric conditions, equal to 70.9 kg/m3. This makes it a promising fuel in the automotive and marine sectors (Ustolin et al., 2022). However, liquid hydrogen presents several safety challenges. Primarily, hydrogen has a very low boiling point compared to that of common hydrocarbons, equal to -253°C. Therefore, it is important to design the equipment to minimize heat losses and avoid boil-off gas (BOG) that would lead to an increase in pressure inside the tank. To prevent this phenomenon, gaseous hydrogen is vented into the atmosphere (Schiaroli et al., 2025). This means that liquid hydrogen equipment is still limited and expensive. In addition to its high flammability, liquid hydrogen presents other challenges. In humans, the risk of cryogenic burns and asphyxiation. Furthermore, low-temperature hydrogen embrittlement and the solidification of atmospheric oxygen can pose significant hazards to equipment and the surrounding environment. Roblin et al. (1997) document burns caused by cryogenic gases, highlighting how direct exposure can cause significant, even fatal, injuries. The extent of the injury depends on the area of adipose tissue involved, the amount of cryogenic fluid, the proximity to the fluid, the type of contact, and the duration. Zheng et al. (2023) studied the solidification behaviour of oxygen. Indeed, due to the low temperature of liquid hydrogen, the air components in contact with hydrogen can solidify, having both oxygen and nitrogen solidification temperatures higher than that of liquid hydrogen. The study highlights how, when the oxygen concentration reaches a certain threshold, the liquid hydrogen and solid air system can lead to an explosion.

As highlighted in the literature, numerous studies have focused on liquid hydrogen and its applications, with the aim of ensuring its safe management, storage, and transport, considering the associated risks. Therefore, the aim of the following research was to find suitable methods for the analysis of the consequences of a liquid hydrogen release on an industrial scale to increase awareness and knowledge of these events. Firstly, the ability of the PHAST Software to simulate liquid hydrogen release was tested, comparing the results with experimental analyses and verifying their reliability. The use of PHAST software in this study stems from the need to identify reliable and easily applicable tools for modelling the consequences associated with the release of liquid hydrogen. Due to the complexity of the physical phenomena involved, such as cryogenic evaporation, pooling, dispersion, and combustion, simulating accident scenarios with LH_2 requires advanced models, which are often difficult to

implement in industrial settings. To verify its reliability even under cryogenic conditions, the predictive performance of PHAST software, commonly used for accident consequence analysis, was analysed The validation was conducted by comparing simulation results with experimental data available in the literature, with the aim of verifying whether PHAST can be used as a support tool in defining safety measures and designing liquid hydrogen plants. Looking ahead, the use of validated PHAST could facilitate future studies and risk assessments, contributing to a more informed and resilient management of hydrogen-related accident scenarios. Subsequently, the methods proposed by the Center for Chemical Process Safety (CCPS) for the evaluation of thermal effects caused by fires were applied. These methods are particularly useful in the preliminary risk assessment phases, or in industrial settings where advanced numerical simulations are not possible. Comparison with experimental data highlighted the limitations and potential of each model, contributing to a broader reflection on the integrated use of analytical and numerical tools in safety assessment.

5.1 Analysis of LH2 release Experiments

A detailed analysis was carried out on experimental data of liquid hydrogen release test, to characterize the spatial and temporal evolution of gas concentrations, thermal radiation and overpressure phenomena following a release.

The main experimental studies on liquid hydrogen releases available in the literature (Ustolin et al., 2021) include tests conducted by NASA (Witcofski and Chirivella, 1984) in 1981 at the White Sands Test Facility involved continuous releases of LH_2 lasting about 35 seconds. The liquid flowed through a 30-meter-long insulated tube with an internal diameter of 152 mm, terminating on a steel plate placed in the centre of a sand tank. The test conducted by Federal Institute for Materials Research (Verfondern and Dienhart, 1997) in 1994 within the Testing Euro-Qu6bec Hydro-Hydrogen Pilot Project to study continuous 60-second releases of LH_2 from a 50 mm nozzle, positioned 0.5 m above an aluminium plate. In a second test, the release occurred in a cylindrical container to study the formation of pools, even on liquid surfaces such as water. The HSL experiments (Willoughby and Royle, 2012; Hall, 2014) in 2010, which included ignited and non-ignited releases of LH_2 from a 25.4 mm nozzle, oriented vertically and horizontally. Release occurred at 60 litres per minute, with durations ranging from 215 to 561 seconds, from a 1 bar tank. Experiments conducted at Kawasaki Heavy Industries (Unno et al, 2015) in 2015 to evaluate the safety of maritime transportation of liquid hydrogen (LH_2). The test involved the controlled release of LH_2 and liquefied natural gas (LNG) onto surfaces of different materials, with the aim of comparing the dispersion and propagation of the two fuels. The tests conducted by Sandia National Laboratories (Panda and Hecht, 2017; Cirrone et al., 2019; Hecht and Panda, 2019) in 2017 cryogenic hydrogen release experiments were conducted to simulate real storage conditions in low-pressure (2–6 bar absolute) and very low-temperature (23–28 K) tanks. The experiments aimed to study cryogenic under-released jet flames and measure the maximum

ignition distance, flame length and radiative heat flux. The Bundesanstalt für Materialforschung und prüfung (BAM) tests (Tamburini et al., 2024) in 2020 under the SH2IFT project, the experiments were conducted to study the behaviour of liquid hydrogen released above and below the water surface. Cryogenic release occurred above and below water to assess the possibility of rapid phase transitions (RPT) in contact with water, analyse the risk of spontaneous ignition in the absence of theoretical ignition sources, and measure pressures generated in air and underwater during releases. Most recently, the experiments for the PRESHLY project in 2021 (Jordan and Kuznetsov, 2021), experiments on cryogenic hydrogen release and dispersion, including rainout tests. They were used to validate theoretical models of release and emptying dynamics of cryogenically compressed tanks. At the same time, the NREL Hydrogen Sensor Laboratory contributed to the same research program by developing and implementing a Hydrogen Wide Area Monitoring (HyWAM) system for three-dimensional monitoring of liquid hydrogen (LH_2) releases in order to characterize the cold hydrogen plume (Buttner et al., 2021).

The selection of the experimental data used for the comparison was guided by the availability of data characterized by a high level of detail and by an accurate documentation of the initial conditions. These features enabled a faithful reproduction of the experimental conditions, making a consistent and reliable comparison possible with the obtained results using the PHAST software and the methods proposed by the Center for Chemical Process Safety (CCPS) line guide for thermal radiations. For the purposes of the comparison on the evolution of the concentration of hydrogen in the space and the pool downstream of the release, the study conducted by NASA (Witcofski and Chirivella, 1984) was taken as references. Regarding the analysis of thermal radiation, the results of experiments at Sandia National Laboratories were used (Cirrone et al., 2019).

5.2 Validation of PHAST software for Liquid Hydrogen

In this section, the results obtained from the comparison between experimental data on liquid hydrogen releases and simulations carried out using the PHAST software are analysed. The aim of this comparison is to evaluate the accuracy of the software in reproducing complex physical phenomena associated with hydrogen accident scenarios, in particular for dispersion and thermal radiation.

In **Subsection 5.2.1**, the experimental conditions of the studies conducted by NASA are described, with particular emphasis on the dispersion of gaseous hydrogen downstream of the release and on the formation of the cryogenic pool. The results obtained were compared with the simulated ones, paying attention to the spatial trend of the concentrations and the diameter of the liquid hydrogen pool.

In **Subsection 5.2.2**, the experimental conditions of the experiments on jet fires conducted by the Sandia National Laboratories are illustrated. In this case, the comparison focused on the thermal radiation generated by the combustion of hydrogen, comparing the experimental values with those obtained with PHAST

software.

5.2.1 Comparison with NASA Experiment

NASA conducted a series of seven experiments to study the behaviour of liquid hydrogen under controlled release conditions. A total mass of 402 kg of hydrogen was used in each test. Nine instrumented towers, positioned downwind of the release point, equipped with sensors to measure the concentration of gaseous hydrogen and air temperature, were used to collect the experimental data. The spatial arrangement of the towers with respect to the release point is illustrated in **Figure 5.1**:

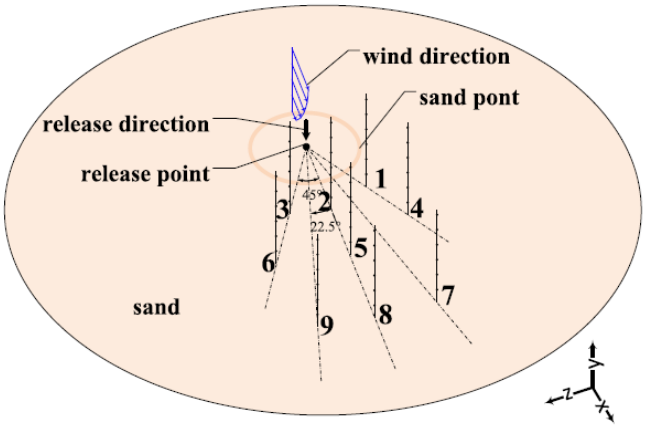

Figure 5.1: NASA experiment number 6 setup. Image from Jäkel et al. (2019).

This study focuses on the analysis of the sixth experiment of the campaign, characterized by a vertical release of liquid hydrogen lasting 38 seconds, carried out at a height of 100 mm above the ground. The release occurred at a flow rate of 9.5 kg/s inside a containment tank with a diameter of 9.1 m, delimited by 60 cm high clay walls and with a bottom made of compacted sand. The atmospheric conditions at the time of the experiment were characterized by a wind speed of 2.2 m/s, measured at 10 m height, and an ambient temperature of 15 °C. Since the PHAST software returns the results as a function of the downwind distance, the values recorded by tower 2, located 3 m from the release point and at a height of 1 m from the ground, were considered for comparison with the experimental data. The parameters used for the numerical simulation are reported in **Table 5.1**:

Table 5.1: Input parameters used on PHAST for the simulation of a liquid hydrogen release.

Simulated conditions	
Equipment	Storage tank
Release orientation	Vertical
Release mass flow rate [kg/s]	9.5
Hole diameter [mm]	199
Release height [mm]	100
Time of release [s]	38

Hydrogen mass [kg]	402
Storage temperature H_2 [K]	20
Wind velocity [m/s]	2.2
Atmospheric stability	Atmospheric class F
Room temperature [°C]	15

Side view of the hydrogen cloud

The first data analysed concern the spatial distribution of the hydrogen concentration as a function of the distance downwind from the release point. **Figure 5.2a** shows the results obtained by simulation with the PHAST software, while **Figure 5.2b** shows the experimental data from the study by Witcofski and Chirivella (1984).

The analysis of the experimental data indicates that the hydrogen cloud at a concentration of 4% by volume, corresponding to the lower flammability limit (LFL), extends to a distance exceeding 35 meters from the release point, attaining a vertical height of approximately 15 meters. As the volumetric concentration of hydrogen increases, the corresponding isoconcentration contours exhibit a progressive and nearly linear contraction in both horizontal and vertical dimensions. At the highest examined concentration of 52% by volume, the cloud's spatial extent is reduced to just over 10 meters in length, with a vertical rise limited to only a few meters.

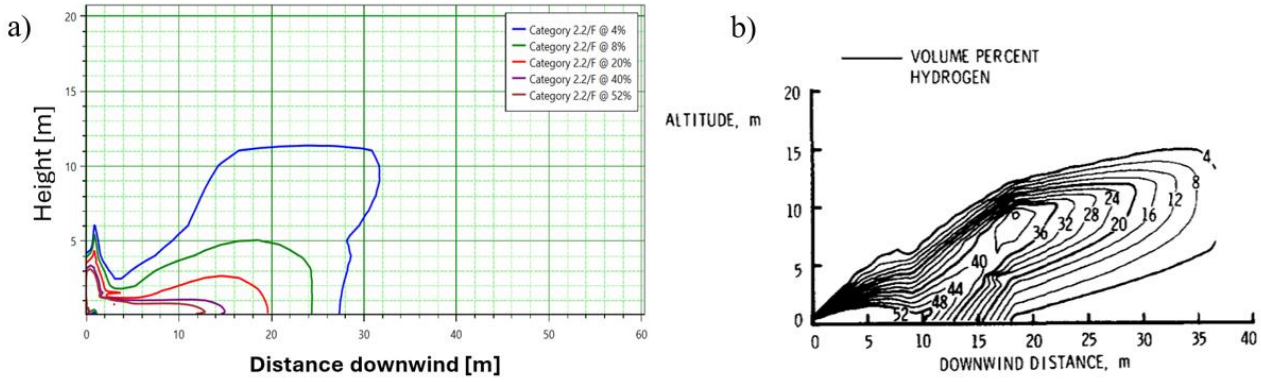

Figure 5.2: A) Concentration curves obtained by the PHAST software as a function of the downwind distance. B) Experimental concentration curves reported in the study by Witcofski and Chirivella (1984).

Two notable features observed in the experimental concentration profiles are: the detachment of the cloud from the ground at a distance of about 18 m from the release and a slight decrease in the upper part of the cloud around 8 m away. This feature is also reproduced in the results simulated by PHAST, although more markedly than in the real case. In the simulation results, the simulated 4% curve extends for a little more than 30 m, slightly underestimating the experimentally observed distance. However, the most significant discrepancy concerns the reduction of the spatial expansion with increasing concentration: in the PHAST results, the isoconcentrations are much less expanded than in the experimental data. For example, the 8% curve reaches only 24 m in distance and 5 m in height,

while experimentally it extends up to 35 m with a height close to 15 m. The curves relating to the highest concentrations are instead more consistent between simulation and experimental data. Finally, it is observed that, in the PHAST results, the detachment of the cloud from the ground occurs at greater distances than what was detected experimentally.

The observed discrepancies can be attributed to several modelling factors. In particular, the underestimation of simulated concentrations could result from an incomplete or simplified representation of the heat exchange between the liquid hydrogen pool and the soil. This heat exchange is a mechanism that favours the evaporation of the cryogenic liquid. If the model does not adequately consider this heat transfer, a significant fraction of the evaporated hydrogen may not be accounted for in the mass balance of the release, leading to an underestimation of the amount of gas available for atmospheric dispersion.

Concentration during the time

Subsequently, a comparative analysis was performed between the experimental and simulated data relating to the temporal trend of the hydrogen concentration detected by sensor no. 2, positioned 3 meters away from the release point and at a height of 1 meter. The results of this comparison are shown in **Figure 5.3**.

From the experimental data, it is observed that the hydrogen concentration varies irregularly over time, without following a defined trend. This behaviour can be attributed to the non-linear dynamics of the evaporation of the liquid hydrogen pool, which involves a variation in the radius of the pool itself over time, thus influencing the amount of gas released into the atmosphere. The results obtained from, PHAST simulation initially show a behaviour consistent with the experimental data, before stabilizing at a concentration of approximately 60% after 27 seconds.

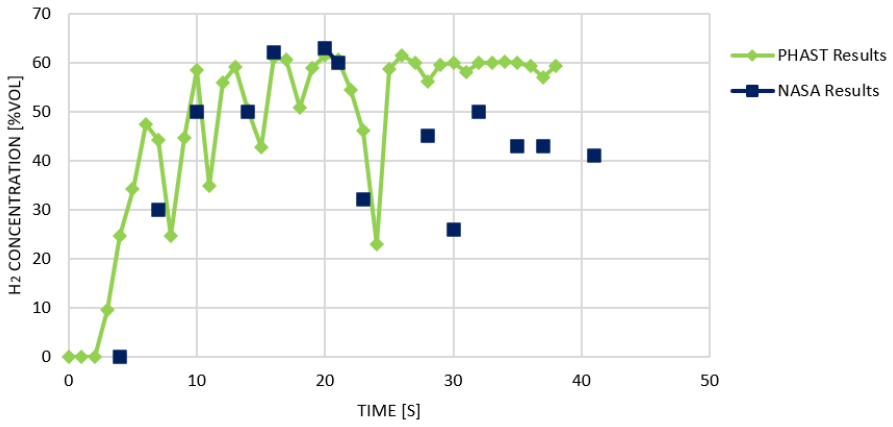

Figure 5.3: Concentration over time at 3 meters from the release and at a height of 2 meters. Experimental results in blue and the concentration over time curve obtained with the PHAST software in green.

Radius of the liquid hydrogen pool

The experimental data do not provide specific values of the radius of the

liquid hydrogen pool but indicate a range of variability within which it is located, highlighting a non-linear evolution over time. In **Figure 5.4**, the grey area represents the experimental range of the radius observed during the experiment, while the red curve shows the trend simulated by PHAST.

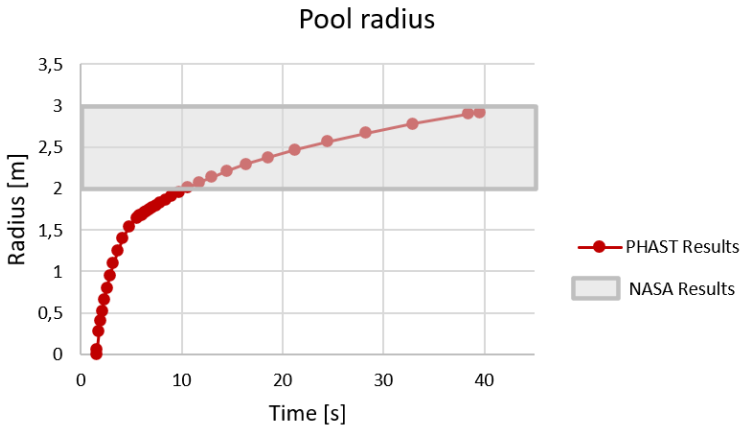

Figure 5.4: Temporal evolution of the hydrogen pool radius. The grey-shaded area represents the experimental range of the pool radius, while the red curve corresponds to the simulated radius over time as computed by the PHAST software.

It can be observed that the pool radius simulated by PHAST falls within the experimental range, yet it exhibits an increasing and smooth temporal evolution in line with CFD application conducted by Middha and al. (2011), which deviates from the nonlinear and fluctuating behaviour observed in experimental condition. As reported in previous studies (Friedrich et al., 2023), the radius of a liquid hydrogen pool does not increase uniformly over time but is instead subject to temporal fluctuations. These are primarily driven by variable heat exchange dynamics with both the ambient atmosphere and the ground surface, which directly influence the evaporation rate. This non-linear dynamic is particularly marked for liquid hydrogen, compared to other cryogenic fuels such as hydrocarbons, due to its high evaporation rate and low gas density. The results obtained show that this behaviour is not adequately represented in the PHAST model, suggesting the need for an improvement in the modelling of cryogenic release.

5.2.2 Comparison with SNL Experiment

Among the experimental campaigns conducted at Sandia National Laboratories, a series of tests involved vertical hydrogen releases through nozzles with diameters of 0.75 mm, 1.00 mm, and 1.25 mm, under varying thermodynamic conditions. The experiment described in the study concerns a cryogenic hydrogen jet fire in a non-premixed configuration: the hydrogen is released into the air and ignites subsequently. This implies a diffusive combustion, with a longer and less intense flame than in a premixed case (Mastri et al., 2023). The release temperatures ranged from 37K (cryogenic conditions) to 295K (ambient conditions), while the injection pressures varied between 2 bar and 6 bar. The experimental setup, illustrated in **Figure 5.5**, features a vertical release configuration, with optical sensors strategically positioned along the axis of the

jet. These sensors were employed to measure the radiative emission associated with the jet fire, enabling the characterization of the flame structure and intensity under different release conditions.

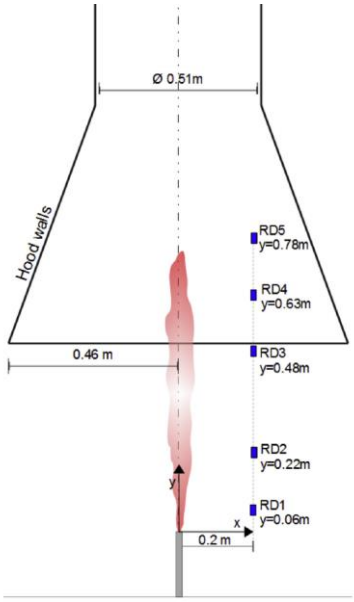

Figure 5.5: Experiment setup conducted by National Sandia Laboratories. Image taken from Cirrone et al. (2019).

Five experiments were conducted, but in this study, only the first one was considered as it is the only one for which complete and detailed results are available. Therefore, a vertical release of hydrogen was simulated with a flow rate of 0.33 g/s stored at 2 bar and 64K. The results are reported as a function of the distance on the jet axis at a distance of 0.2 meters from the release. The parameters related to the simulation are reported in **Table 5.2**:

Table 5.2: Input parameters used on PHAST for the simulation of a liquid hydrogen jet fire.

Simulated conditions	
Release orientation	Vertical
Release mass flow rate [g/s]	0.33
Hole diameter [mm]	1.15
Storage temperature H_2 [K]	64
Storage pressure H_2 [bar]	2
Room temperature [°C]	15

Thermal radiations results

The results of the analysis are presented in **Figure 5.6**. The experimental data exhibit a slight increase in thermal radiation intensity, followed by a gradual decrease beyond approximately 0.4 meters from the release point. A similar trend is observed in the PHAST simulation, which also displays a bell-shaped radiation profile. However, the experimental curve appears narrower compared to the one predicted by PHAST, indicating a more localized radiation peak in the real

scenario.

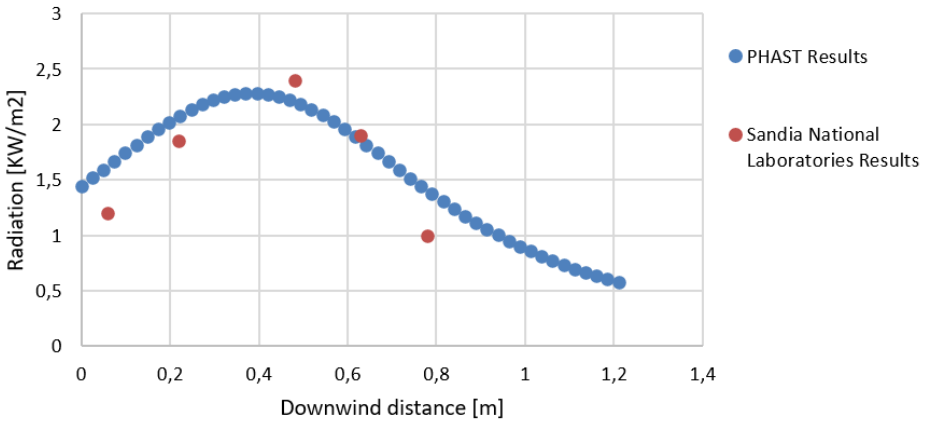

Figure 5.6: Thermal radiation profile along the release axis at 0.2 m from the release point. The experimental data are represented by the red points, while the blue curve corresponds to the simulation results obtained using the PHAST software.

Overall, the PHAST software demonstrates a reasonably accurate representation of the liquid hydrogen jet fire behaviour under low release rate conditions, capturing the general shape and magnitude of the thermal radiation distribution.

5.3 Validation Thermal Radiations Methods for Liquid Hydrogen

In addition to the PHAST simulation, the analytical methods proposed by CCPS for estimating thermal radiation were also considered. These approaches, although based on simplified assumptions, require limited input data and limited computational resources, making them particularly useful for preliminary assessments.

The next section analyses the applicability of the analytical methods proposed by CCPS (2010), through a comparison with experimental data relating to liquid hydrogen fires, with the aim of enhancing the understanding of hazard zones and thermal radiation associated with these events. These insights can serve as a valuable support tool in quantitative risk assessments for industrial facilities handling liquid hydrogen. Rather than aiming to reproduce the full complexity of accident scenarios, the purpose of this comparison is to evaluate the reliability and accuracy of the CCPS methods in estimating key safety parameters, specifically, thermal radiation levels, at selected distances from the release. This parameter is important for defining safety areas and designing protective measures in hydrogen applications.

The heat generated by combustion processes is transferred through three primary mechanisms: conduction, convection, and thermal radiation. In the case of large-scale fires, where high temperatures are reached, thermal radiation becomes the dominant hazard due to its potential to cause damage to people, structures, and equipment in the surrounding environment. The Center for Chemical Process Safety (CCPS) outlines two general approaches for estimating the radiative effects at a given distance from the flame: the Point-Source Model

and the Surface Emitter Model, also known as the Solid-Flame Model (CCPS,2010).

5.3.1 Point-Source Model (PSM)

The Point-Source Model simplifies the heat source as a single point that emits thermal radiation uniformly in all directions. This assumption allows for the estimation of thermal radiation intensity at various distances from the source without accounting for directional dependence. The model is particularly useful for preliminary hazard assessments due to its computational simplicity and conservative nature. The model assumes that only a fraction (f) of the heat of combustion is emitted as radiation in all directions; the radiation per unit area and per unit time (q) can be calculated from **Equation 5.1**:

$$q = \frac{f\dot{m}H_{comb}\tau_a}{4\pi x^2} \quad \textbf{(5.1)}$$

$\dot{m}$ is the combustion rate, H_{comb} is the heat of combustion of the fuel considered, τ_a is the transmissivity, and x is the distance from the point source.

The model assumes that the target surface is oriented toward the radiation source to receive the maximum incident heat flux. For a pool fire involving a fuel with a boiling point (T_b) higher than room temperature (T_a), the combustion rate can be estimated using the empirical relationship:

$$\dot{m} = \frac{0.001H_{comb}A}{H_v + C_v(T_b - T_a)} \quad \textbf{(5.2)}$$

A is the area of the liquid fuel pool, H_v the heat of evaporation and C_v the specific heat of fuel. Transmissivity represents the proportion of energy that is either absorbed or scattered by the atmosphere before it reaches the target surface. This proportion tends to increase with the distance between the source and the target, as well as with atmospheric parameters that enhance absorption and scattering, most notably, relative humidity. A graphical representation of transmissivity is presented as a function solely of air relative humidity. These graphs can be approximated by the following expression:

$$\tau_a = \ln(14.1RH^{0.108}x^{-0.13}) \quad \textbf{(5.3)}$$

RH represents the relative humidity.

This method has been applied to the hydrogen jet fire reproducing the experiment analysed by Cirrone et al. (2019), the input data considered are reported in **Table 5.3**:

Table 5.3: Input parameters used for the Point-Source model.

Parameter	Value	Reference
f	0.05	Bernardy et al. (2025)
$\dot{m}$ [kg/s]	0.00033	-
H_{comb} [MJ/kg]	140	Zheng et al. (2019)
τ_a	2.37	-
x [m]	0.2	-
A [m^2]	0.0026	-

H_v [kJ/kg]	449	Zheng et al. (2019)
c_v [kJ/kg·K]	1.47	Timmerhaus and Flynn (1989)
T_a[K]	288	-
T_b[K]	20	Timmerhaus and Flynn (1989)
RH	90%	-

The parameters employed in the calculations were obtained from the literature, with the corresponding references listed in **Table 5.3**. The remaining values were derived from the experimental setup described by Cirrone et al. (2019). From **Equation 5.1**, the following results is obtained based on the data:

$$q = \frac{f\dot{m}H_c\tau_a}{4\pi x^2} = 10.9\frac{kW}{m^2}$$

The study conducted by Cirrone et al. (2019) presents the spatial distribution of thermal radiation, as illustrated in **Figure 5.6**. This distribution clearly demonstrates how radiation intensity varies along the flame axis, a consequence of the non-uniform temperature field within the flame. Such variability highlights a significant limitation of the Point Source Model, which inherently assumes a simplified representation of the flame as a singular radiative point. This model is highly sensitive to the type and quantity of fuel used, yet it neglects critical aspects such as the physical extent of the flame and the presence of temperature gradients. Moreover, the PSM tends to significantly overestimate the radiative heat flux received by a target. Indeed, the predicted values are an order of magnitude higher than those observed experimentally. This discrepancy can be attributed to the model's assumption that all emitted radiation is directed toward and absorbed by the target, an idealization that does not reflect the complex interactions and losses occurring in real fire scenarios. These findings underscore that the Point Source Model is not suitable for estimating the radiative heat flux from a cryogenic hydrogen jet fire, where the flame structure and thermal field are highly anisotropic and dynamic.

5.3.2 Solid-Flame Model (SFM)

The solid flame model assumes that the fire can be represented as a solid body with a simple geometric shape, from whose surface all thermal radiation is emitted. This approach offers the advantage of accounting for the geometries of both the fire and the target, as well as their relative positions. The geometric relationship between the radiating surface and the receiving target is quantified through the view factor (F), which represents the fraction of the total emitted radiation that is directly received on the target. The view factor depends on the shapes of both the flame and the receiving surface, as well as on the distance and orientation between them, and is determined through purely geometric analysis. The radiation per unit area and per unit time (q) can be calculated from **Equation 5.4**:

$$q = FE\tau_a \quad \textbf{(5.4)}$$

E is the surface emissive power. The emissive power represents the radiative heat flux emitted from the surface of the fire. It can be calculated using the

Stefan–Boltzmann law, reported in **Equation 5.5**, which defines the radiative emission of an ideal blackbody as a function of its absolute temperature. For real surfaces, which do not behave as perfect blackbodies, the equation is modified by introducing the emissivity factor (ε), which quantifies the efficiency of a material in emitting thermal radiation relative to an ideal blackbody. Emissivity values range from 0 to 1, and the actual radiative power is obtained by multiplying the blackbody emission by the material's emissivity.

$$E = \varepsilon\sigma T^4 \quad \textbf{(5.5)}$$

σ is the Stefan–Boltzmann constant and T is the temperature of the flame. Emissivity is determined by the absorption of radiation by combustion products within the flame and by the wavelength of the emitted radiation. This dependency can be described by **Equation 5.6**:

$$\varepsilon = 1 - \exp(-kx_f) \quad \textbf{(5.6)}$$

The view factor depends on the geometry of the emitting surface, the distance between the emitting and receiving surfaces, and their relative orientation. In the context of fire modelling, the flame generated by a pool fire or a jet fire can be idealized as a cylindrical surface with height (h) and a radius (r) corresponding either to the pool radius or to the nozzle exit radius, respectively. Let x denote the distance between the flame and the receiving body:

$$h_r = \frac{h}{r} \quad \textbf{(5.7)}$$

$$X_r = \frac{x}{r} \quad \textbf{(5.8)}$$

$$A = (X_r + 1)^2 + h_r^2 \quad \textbf{(5.9)}$$

$$B = (X_r - 1)^2 + h_r^2 \quad \textbf{(5.10)}$$

The view factor is calculated by considering separately the radiation emitted by the lateral surface and the bases of the cylinder representing the flame. To this end, two distinct components are introduced: the view factor F_v, associated with the lateral surface of the cylinder, and the view factor F_h, related to the bases. These two contributions are then combined to obtain a single maximum view factor, as predicted by **Equation 5.13**, which allows the estimation of the radiant fraction that reaches a point of interest.

$$F_h = \frac{1}{\pi}\left[\tan^{-1}\left\{\left(\frac{X_r-1}{X_r+1}\right)^{1/2}\right\} + \frac{{X_r}^2-1+h_r^2}{\sqrt{AB}}\tan^{-1}\left\{\left(\frac{(X_r-1)A}{(X_r+1)B}\right)^{1/2}\right\}\right] \quad \textbf{(5.11)}$$

$$F_v = \frac{1}{\pi X_r}\tan^{-1}\left\{\left(\frac{h_r^2}{{X_r}^2-1}\right)^{1/2}\right\} + \frac{h_r^2(A-2X_r)}{\pi X_r\sqrt{AB}}\tan^{-1}\left\{\left(\frac{(X_r-1)A}{(X_r+1)B}\right)^{1/2}\right\} - \frac{h_r}{\pi X_r}\tan^{-1}\left\{\left(\frac{X_r-1}{X_r+1}\right)^{1/2}\right\} \quad \textbf{(5.12)}$$

$$F_{max} = ({F_v}^2 + {F_h}^2)^{0.5} \quad \textbf{(5.13)}$$

This method has been applied to the hydrogen jet fire reproducing the experiment analysed by Cirrone et al. (2019), the input data considered are reported in **Table 5.4**:

Table 5.4: Input parameters used for the Solid-Flame Model.

Parameter	Value	Reference
F	0.18	-
F_v	0.0015	-
F_h	0.18	-

τ_a	2.37	-
ε	0.0089	-
σ [$W/m^2 K^4$]	5.67 x 10^{-8}	CCPS (2010)
k [m^{-1}]	7	Mudan (1984)
x_f [m]	0.0013	-
X_r	314.96	-
h_r	1039.37	-
r [m]	0.000635	-
h [m]	0.66	-
x [m]	0.2	-
A	1180121	-
B	1178861	-

The parameters employed in the calculations were obtained from the literature, with the corresponding references listed in the table. The remaining values were derived from the experimental setup described by Cirrone et al. (2019) or obtained from the aforementioned equations.

To calculate the thermal radiation, the adopted method requires knowledge of the flame temperature at specific points along its axis. To this end, the data reported by Cirrone et al. (2019) were used, which provide a temperature profile as a function of the axial distance from the base of the flame (x_b), which corresponds to the distance from the exit hole. Based on these values, the local emissive power was determined using the Stefan-Boltzmann law. Subsequently, the thermal radiation per unit area was calculated, considering the emissivity and geometry of the radiant source. The results are reported in **Table 5.5**:

Table 5.5: Results obtained from the Solid-Flame Model.

x_b	T(x)	E [W/m^2]	q [kW/m^2]
0.06	1350	1666.83	0.73
0.22	1650	3719.56	1.62
0.48	1800	5268.00	2.29
0.63	1500	2540.50	1.11
0.78	1250	1225.17	0.53

The results obtained were compared with those reported by Cirrone et al. (2019), using the graph shown in **Figure 5.7**. The comparison shows that the Solid Flame Model consistently reproduces the trend of the thermal radiation generated by a cryogenic hydrogen jet fire. However, a slight underestimation of the calculated values is observed compared to the experimental ones, with a relative error equal to 28%.

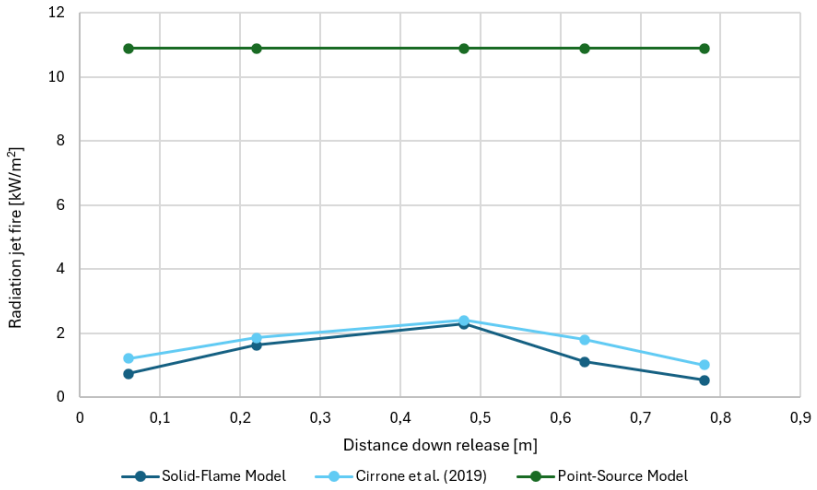

Figure 5.7: Radiation emitted by the liquid hydrogen jet fire at a distance of 0.2 m along the flame axis direction. In light blue, the experimental data presented by Cirrone et al. (2019), in blue, the results of the Solid-Flame Model, and in green, the results of the Point-Source Model.

This deviation indicates that, although the model is useful for obtaining an estimate of the order of magnitude of the thermal radiation, it has limitations in terms of quantitative accuracy. Therefore, for applications in which greater precision in the evaluation of the thermal impact is required, it is necessary to use more advanced models, capable of describing with greater fidelity the spatial distribution and intensity of the emitted radiation. Among the most advanced models are CFD simulations that allow for the solution of the energy, momentum, and mass balance equations, considering turbulence, domain geometry, and the thermophysical properties of the fuel (Cirrone et al., 2019; C. Jäkel et al., 2019). These models are more complex to implement but particularly suitable for detailed engineering analyses and the design of safety systems.

Chapter 5 Partial Conclusions

This chapter analysed the behaviour of liquid hydrogen under accidental release conditions, focusing on dispersion phenomena and the thermal effects associated with combustion. Comparison of experimental data with simulations conducted using the PHAST software highlighted significant limitations in ability of the software to accurately reproduce the spatial distribution of hydrogen concentrations in cryogenic scenarios. However, the results for thermal radiation generated by jet fires showed good consistency with experimental data, confirming the software's partial reliability in specific contexts.

To complete the analysis, the analytical methods proposed by the CCPS for estimating thermal radiation were also applied. Despite their simplified nature, these approaches proved useful for preliminary assessments and for defining thermal impact zones, especially in contexts where computational resources are limited. Comparison with experimental data highlighted the strengths and weaknesses of each method, suggesting the possibility of using more advanced models, such as CFD simulations, for high-fidelity analyses.

The results obtained in this chapter contribute to the achievement of scientific objective SG4, to evaluate the effectiveness of detection and modelling technologies for the prevention and management of hydrogen leaks. Specifically, the validation of the PHAST software for liquid hydrogen release scenarios has verified its applicability in complex cryogenic conditions, offering a potentially useful tool for defining safety measures and designing systems. At the same time, the analysis of the methods proposed by the CCPS has provided an overview of the possibilities offered by simplified analytical approaches, which can be employed in industrial contexts where the use of advanced numerical models is not always feasible.

This dual approach, numerical and analytical, has allowed us to explore the limitations and potential of each methodology, contributing to a broader reflection on the integration of different tools in risk assessment. This work partially addresses RQ4 by addressing the specific challenges associated with hydrogen release management, with particular attention to the complexity of phenomena associated with liquid hydrogen. Furthermore, the path followed reinforces the importance of integrated and scalable modelling strategies, in line with the resilient approach promoted by this research, which aims to provide operational solutions adaptable to different levels of complexity and available resources.

Chapter 5 References

Bernardy, C., Habib, A. K., Kluge, M., Schalau, B., Kant, H., Schulze, M., and Orchini, A. (2025). Large-scale investigations of the thermal radiation of hydrogen jet flames. Journal of Loss Prevention in The Process Industries, 94, 105491. https://doi.org/10.1016/j.jlp.2024.105491

Buttner, W., Hall, J., Coldrick, S., Hooker, P., and Wischmeyer, T. (2021). Hydrogen wide area monitoring of LH2 releases. International Journal of Hydrogen Energy, 46(23), 12497–12510. https://doi.org/10.1016/j.ijhydene.2020.08.266

CCPS (2010). Guidelines for Vapor Cloud Explosion, Pressure Vessel Burst, BLEVE, and Flash Fire Hazards. Center for Chemical Process Safety. 2nd ed. Hoboken, NJ: Wiley-AIChE.

Cirrone, D. M. C., Makarov, D., and Molkov, V. (2019). Thermal radiation from cryogenic hydrogen jet fires. International Journal of Hydrogen Energy, 44(17), 8874–8885. https://doi.org/10.1016/j.ijhydene.2018.08.107

Friedrich, A., Veser, A., Jordan, T., Kuznetsov, M., Kotchourko, N. (2023). Dataset: Preslhy experiment series 4.4; material of the ground: concrete. https://doi.org/10.35097/1321

Hall J. (2014). Ignited release of liquid hydrogen. Hsl rr987, technical report, HSL, UK.

Hecht, E. S., and Panda, P. P. (2019). Mixing and warming of cryogenic hydrogen releases. International Journal of Hydrogen Energy, 44(17), 8960–8970. https://doi.org/10.1016/j.ijhydene.2018.07.058

Jäkel, C., Kelm, S., Verfondern, K., and Allelein, H. J. (2019). Validation of a 3D multiphase-multicomponent CFD model for accidental liquid and gaseous hydrogen releases. International Journal of Hydrogen Energy, 44(17), 8807–8818. https://doi.org/10.1016/j.ijhydene.2018.10.024

Jordan, T., and Kuznetsov, M. (2021). Experimental Investigation of Pre-Mixed Systems with Cryogenic Hydrogen. PRESLHY Project Deliverable 5.3, D20.

Mastri, A.R., Cleary, M.J. and Dunn, M.J. (2023). Turbulent Flames of Hydrogen. In: E.A. Tingas, ed. Hydrogen for Future Thermal Engines. Green Energy and Technology. Cham: Springer. https://doi.org/10.1007/978-3-031-28412-0_4

Middha, P., Ichard, M., and Arntzen, B. J. (2011). Validation of CFD modelling of LH2 spread and evaporation against large-scale spill experiments. International Journal of Hydrogen Energy, 36(3), 2620-2627. https://doi.org/10.1016/j.ijhydene.2010.03.122

Mudan, K.S. (1984). Thermal radiation hazards from hydrocarbon pool fires.

Progress in Energy and Combustion Science, 10, pp.59–80. https://doi.org/10.1016/0360-1285(84)90119-9

Panda, P. P., and MacNguyen, E. S. (2017). Ignition and flame characteristics of cryogenic hydrogen releases. International Journal Of Hydrogen Energy, 42(1), 775–785. https://doi.org/10.1016/j.ijhydene.2016.08.051

Roblin, P., Richards, A., and Cole, R. (1997). Liquid nitrogen injury: a case report. Burns, 23(7-8), 638–640. https://doi.org/10.1016/S0305-4179(97)00082-X

Schiaroli, A., Claussner, L., Campari, A., Cirrone, D., Linseisen, B., Friedrich, A., Torres de Ritter E.L., Kuznetsov M., and Ustolin, F. (2025). A comprehensive review on liquid hydrogen transfer operations and safety considerations for mobile applications. International Journal of Hydrogen Energy, 107, 164–182. https://doi.org/10.1016/j.ijhydene.2024.12.266

Tamburini, F., Kluge, M., Habib, A. K., Ustolin, F., Cozzani, V., and Paltrinieri, N. (2024). Exploring experimental tests concerning liquid hydrogen releases. Process Safety and Environmental Protection, 192, 1330-1343. https://doi.org/10.1016/j.psep.2024.11.014

Timmerhaus, K.D. and Flynn, T.M. (1989). Properties of Cryogenic Fluids. In: Cryogenic Process Engineering. The International Cryogenics Monograph Series. Springer, Boston, MA. https://doi.org/10.1007/978-1-4684-8756-5_2

Unno S., Takakoka Y., Kihimoto A., Suga H.,Kamiya S., Miida Y.,and Oyama S. (2015). A study on dispersion resulting from liquefied hydrogen spilling. In: Proceedings of the 6th international conference on hydrogen safety.

Ustolin, F., Åsholt, H. Ø., Zdravistch, F., Niemi, R., and Paltrinieri, N. (2021). Computational fluid dynamics modeling of liquid hydrogen release and dispersion in gas refuelling stations. Chemical Engineering Transactions, 86, 223–228. https://doi.org/10.3303/CET2186038

Ustolin, F., Campari, A., and Taccani, R. (2022). An extensive review of liquid hydrogen in transportation with focus on the maritime sector. Journal of Marine Science and Engineering, 10(9), 1222. https://doi.org/10.3390/jmse10091222

Verfondern, K., and Dienhart, B. (1997). Experimental and theoretical investigation of liquid hydrogen pool spreading and vaporization. International Journal of Hydrogen Energy, 22(7), 649–660. https://doi.org/10.1016/S0360-3199(96)00204-2

Willoughby D, and Royle M. (2012). Release of unignited liquid hydrogen. Hsl report rr986, technical report, HSL, UK.

Witcofski R, and Chirivella J (1984). Experimental and analytical analyses of the mechanisms governing the dispersion of flammable clouds formed by liquid hydrogen spills. International Journal of Hydrogen Energy,

9(5):425–35. https://doi.org/10.1016/0360-3199(84)90064-8.

Zheng, J., Chen, L., Xu, X., Guo, L., Zhou, Y., and Wang, J. (2019). A novel insulation system based on active cooling without power input for liquid hydrogen storage. Energy, 182, 1–10. https://doi.org/10.1016/j.energy.2019.06.050

Zheng, X., Dai, W., Shu, Z., Zhao, D., Liang, W., Lei, G., and Qian, H. (2023). Numerical simulation of air solidification process in liquid hydrogen with LBM-CA coupled method. International Journal of Hydrogen Energy, 48(30), 11567–11577. https://doi.org/10.1016/j.ijhydene.2022.05.026

6. Validation CCPS Explosion Methods for Hydrogen

Following the analysis of thermal effects associated with hydrogen releases in the previous chapter, this chapter focuses on the evaluation of the mechanical effects, specifically the overpressures generated by explosive scenarios. It analyses the predictive capacity of the methods proposed by the Center for Chemical Process Safety (CCPS, 2010) for estimating overpressures generated by hydrogen cloud explosions, both in the gaseous and cryogenic phases. The CCPS classifies the methods for forecasting explosive effects from vapour clouds into three main categories: the TNT equivalence method, numerical simulations and methods based on explosion curves. The present study focuses on the identification of simplified methodologies for the estimation of overpressures generated by these events. To this end, the analysis has been limited to TNT equivalence methods and methods based on explosion curves, as they do not require the use of advanced computational resources and are therefore more suitable for preliminary applications or in contexts with limited availability of computational tools. The objective is to verify the reliability and application limitations of the three simplified approaches by comparing the results obtained with experimental data available in the literature.

The following sections present the application of three methodologies commonly used for the estimation of explosive effects: the Multi-Energy method developed by the Netherlands Organisation for Applied Scientific Research (TNO), the Trinitrotoluene (TNT) equivalence method, and the Baker-Strehlow-Tang (BST) model. These approaches have been applied to hydrogen explosion scenarios to evaluate their suitability in predicting the generated overpressures. The aim is to identify which of these models provides a sufficiently accurate and conservative estimate of the overpressure effects, considering the specific characteristics of hydrogen as a fuel.

The application of these methods has been compared with available experimental data, in particular with the results of the European project PRESLHY (Jordan and Kuznetsov, 2021), which has conducted tests on cryogenic hydrogen release explosions. For a more complete evaluation, experiments conducted with gaseous hydrogen have also been considered. The main studies available in the literature include the tests of SRI International on behalf of the Institute of Applied Energy (IAE), within the New Energy and Industrial Technology Development Organization (NEDO) program in 2007 involving the analysis of deflagrations and detonations in open spaces, experiments in small-scale tunnels, tests with obstacles to simulate turbulence effects, controlled

releases of hydrogen with and without ventilation and tests with protective walls to evaluate the reduction of overpressure (Sato et al., 2006; Groethe et al., 2007); and the tests of the Research Center for Explosion Safety, National Institute of Advanced Industrial Science and Technology (AIST) where experimental tests were conducted in open fields to study the explosive force generated by stoichiometric mixtures of hydrogen and air (Wakabayashi et al., 2007). This comparison has allowed the evaluation of the robustness and the limits of the simplified methods in representing real explosion scenarios.

Experimental validation is based on a series of large-scale tests conducted in various geometric configurations, including tunnels, partially confined spaces, and protective barriers. Each experiment is analysed in the following sections to assess the accuracy of the selected models.

The experiments analysed for cryogenic hydrogen are part of the PRESLHY campaign (Jordan et al., 2023) and were designed to study the overpressure generated by hydrogen release ignitions under controlled conditions. The experiments, at the DisCha facility of the Karlsruhe Institute of Technology (KIT) in Germany, involved a hydrogen release from a 2.8-litre tank through a 4 mm diameter nozzle, with an initial pressure of 50 or 200 bar.

6.1 TNO Multi-Energy Method

The Multi-Energy method is an empirical approach developed for the estimation of overpressures generated by vapour cloud explosions (VCE). The Multi-Energy method considers the distribution of explosive energy within the cloud and the geometric configuration of the surrounding environment. In particular, it is assumed that only a portion of the cloud actively participates in the explosion, thus allowing for more realistic scenarios, taking into account the non-homogeneity of the fuel-air mixture and the degree of confinement. The method allows the subdivision of the environment involved in the explosion into portions characterized by different levels of confinement and congestion, in order to more accurately evaluate the overall effects of the event. However, since the experiments considered were conducted in environments with uniform conditions of congestion and confinement, the subdivision is not necessary in this analysis.

Overpressures are estimated using empirical curves associated with different energy levels, which depend on the distance from the explosion. The intensity of the explosion is represented by a numerical index between 1 (low energy) and 10 (detonating behaviour). Therefore, the method involves the identification of the volume of gas involved in the explosion, the characterization of its intensity as a function of the type of fuel, the confinement and the presence of obstacles, and finally the calculation of the expected overpressure at a given distance.

Once the volume of the cloud V_c is defined, the total energy of combustion E is calculated from **Equation 6.1**:

$$E = E_{comb} \times \rho_{gas} \times V_c \quad \textbf{(6.1)}$$

E_{comb} is the combustion energy of the fuel per unit mass. Thus, it is possible to calculate the Sachs-scale distance from charge $\bar{R}$ following **Equation 6.2**:

$$\bar{R} = \frac{R}{(E/P_0)^{1/3}} \quad \textbf{(6.2)}$$

R is the distance between the source of the explosion and the receiving body, and P_0 is the ambient pressure. From the value of $\bar{R}$, it is possible to evaluate the Sachs-scale peak overpressure $\Delta\overline{P_s}$ at distance R using **Figure 6.1**, and evaluate the overpressure P_s from **Equation 6.3**:

$$P_s = \Delta\overline{P_s} \times P_0 \quad \textbf{(6.3)}$$

The curves reported in **Figure 6.1** are characterized by a numerical parameter between 1 and 10, which represents the intensity level of the explosion. This value reflects the violence of the deflagration and depends on several factors, including the reactivity of the fuel and the environmental conditions. Hydrogen is the fuel analysed in this study, known for its high reactivity, which makes it particularly relevant in the analysis of explosive scenarios. However, parameters such as the degree of congestion and confinement of the experimental environment, also significantly influence the choice of the energy level associated. The selection of the intensity adopted for each case will be discussed in detail in the following sections.

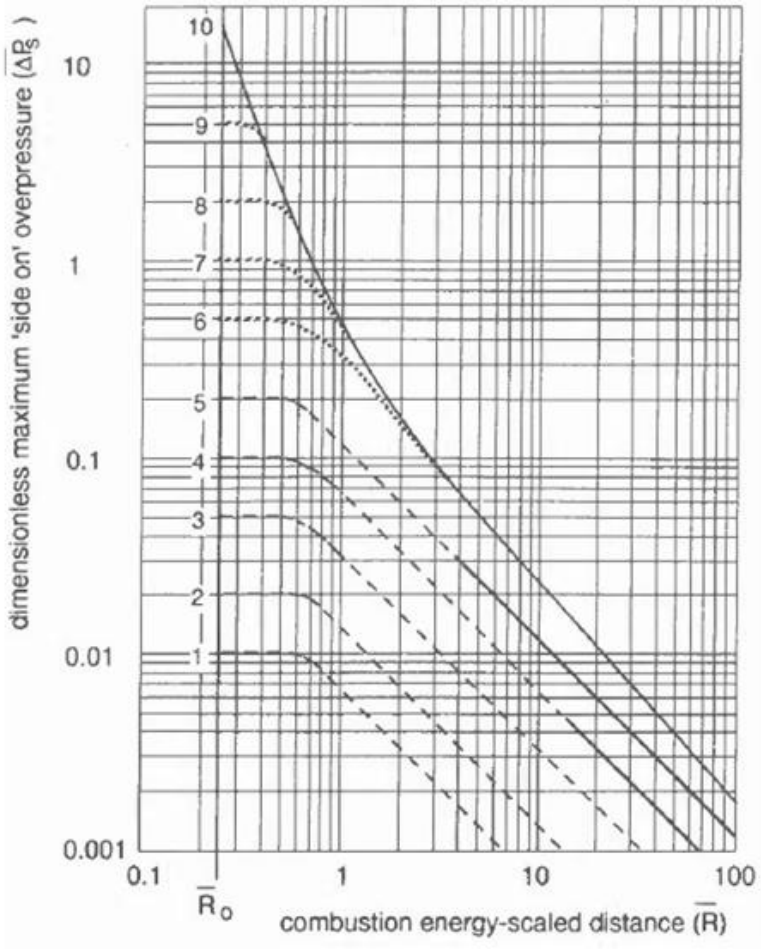

Figure 6.1: Multi Energy method explosion curves. Image taken from CCPS (2010).

Gaseous Hydrogen Explosion

This method has been applied to the gaseous hydrogen explosion reproducing the experiment analysed by Groethe et al. (2007), the data considered are reported in **Table 6.1**:

Table 6.1: Parameters used for the TNO Multi-Energy method for gaseous hydrogen

explosion.

Parameter	Value
P_0 [Pa]	101325
ρ_{gas} [kg/m3]	0.0899
E_{comb} [MJ/kg]	140

In the **first experiment**, conducted in a confined volume of 300 m³ initially closed, a mixture composed of 30% hydrogen by volume was used, corresponding to a total hydrogen volume of 90 m³. The ignition was by a spark, and it occurred in the lower part of the structure. The plastic film was cut shortly before the ignition to avoid total confinement of the mixture. The energy released by the explosion was estimated to be 1.13×10^9 J. From these data, the Sachs-scaled distance $\bar{R}$ was calculated as a function of the real distance R from the release point. For each value of R, the peak overpressure was determined using the data reported in **Figure 6.1**. The application of the Multi-Energy method requires the preliminary definition of the explosive source intensity level. In this scenario, a homogeneous mixture of air and hydrogen with a concentration of 30% by volume of hydrogen is considered, a value included within the flammability range of the gas. The presence of a trigger guarantees the activation of the explosive reaction, which is expected to be of significant intensity. However, it is important to note that immediately before the trigger, the confined environment is partially opened following the breaking of a plastic film, partially reducing the effect of the confinement. Taking these factors into account, it was considered appropriate to adopt an intensity level equal to 5, in accordance with the CCPS (2010).

Table 6.2: Sachs-scale distance and overpressure values obtained with the TNO method for a hydrogen explosion in a space of 300 m3, initially closed. Intensity level adopted: 5.

R [m]	$\bar{R}$	ΔP [kPa]
3	0.13	20
5	0.22	20
7	0.31	20
10	0.45	20
12	0.54	19
15	0.67	18
20	0.76	16
25	0.89	13
30	1.12	10

The trend is shown in **Figure 6.2**.

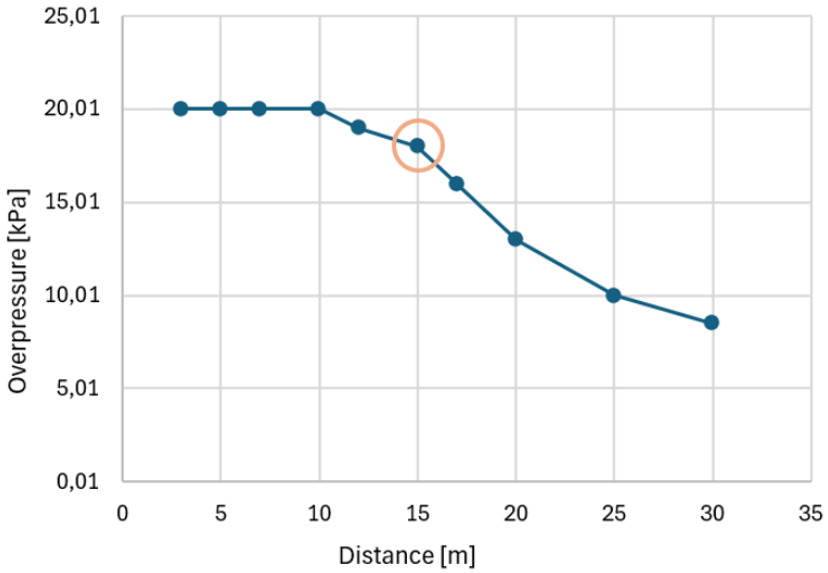

Figure 6.2: Overpressure trend as a function of distance from the charge obtained with the TNO method for an explosion which involved 90 m^3 of hydrogen in a 300 m^3 space. The red circle highlights the point 15 m from the release, where the measured experimental overpressure peak is compared with the maximum value predicted by the TNO model at the same distance.

The results obtained with the TNO method were compared with the experimental data reported by Groethe et al. (2007) (**Figure 6.3**), which include the temporal profile of the overpressure measured at a distance of 15 m from the trigger point (blue and red continuous curves). Specifically, the temporal profile of the overpressure recorded during the experiment is shown, while the TNO model provides the maximum overpressure expected in space at the same distance.

Although the two approaches provide different information, one temporal and the other spatial, it is possible to compare the experimental peak value with the calculated one. The TNO method estimates a maximum overpressure of 18 kPa at 15 m, a value that is in good agreement with the experimentally observed peak, confirming the validity of the model under similar conditions.

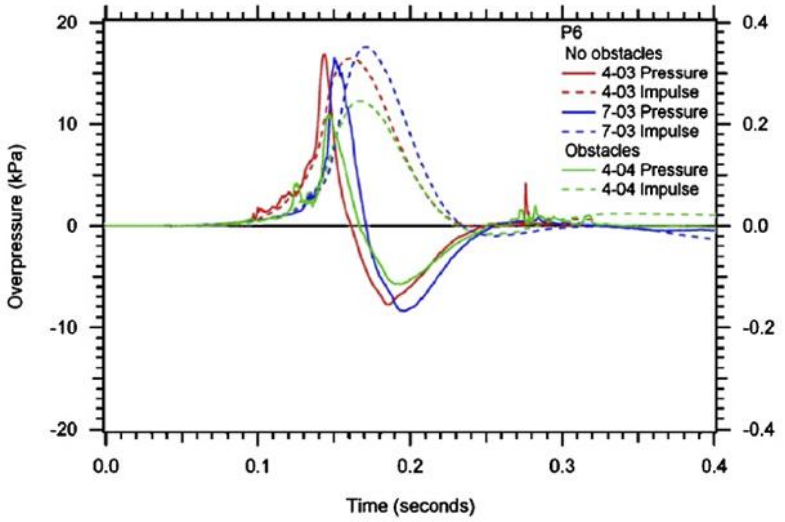

Figure 6.3: Overpressure time profile at 15 m for an explosion involving 90 m^3 of hydrogen in a space of 300 m^3. Experimental results reported by Groethe et al. (2007).

The **second experiment** involved a hydrogen gas explosion inside a tunnel. The explosion occurred in a confined space along a single direction in a tunnel volume of 293.6 m³, of which 30% was filled with hydrogen gas. In this case, the explosion occurred in a confined space along a single direction, which resulted in much more violent dynamics than in less constrained scenarios. Consequently, the total volume of hydrogen considered in the experiment was about 88 m³. The ignition was by spark. The energy released by the explosion was estimated to be 1.11×10^9 J. From these data, the Sachs-scaled distance $\bar{R}$ was calculated as a function of the real distance R from the release point. For each value of R, the peak overpressure was determined using the data reported in **Figure 6.1**. In the second scenario analysed, the explosion occurs inside a tunnel, in a highly confined environment. Considering the above mentioned factors, an intensity level of 10 was adopted, corresponding to the maximum foreseen by the Multi-Energy method, in order to conservatively and realistically represent the severity of the explosive event.

Table 6.3: Sachs-scale distance and overpressure values obtained with the TNO method for a hydrogen explosion for a hydrogen explosion in a 1D confined space. Intensity level adopted: 10.

R [m]	$\bar{R}$	ΔP [kPa]
3	0.14	1100
5	0.23	1080
7	0.32	500
10	0.45	250
12	0.54	160
15	0.68	100
20	0.77	80
25	0.90	56
30	1.13	34

The trend is shown in **Figure 6.4**.

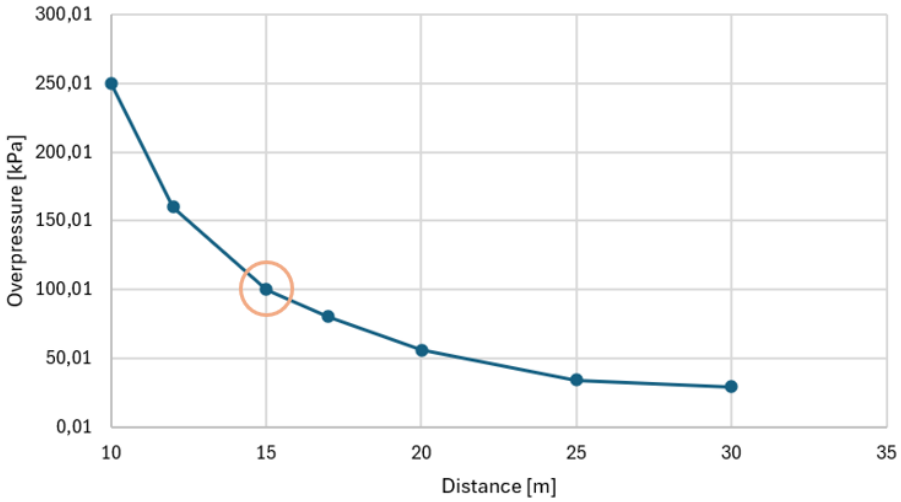

Figure 6.4: Overpressure trend as a function of distance from the charge obtained with

the TNO method for an explosion which involved 88 m^3 of hydrogen in a confined space along a single direction. The red circle highlights the point 15 m from the release, where the measured experimental overpressure peak is compared with the maximum value predicted by the TNO model at the same distance.

For the second experiment, it was also possible to compare the results obtained with the TNO method with the experimental results reported in **Figure 6.5** by Groethe et al. (2007).

The analysis conducted with the TNO model returned a maximum overpressure of 100 kPa at 15 meters, a value consistent with the peak recorded in the experimental data. This agreement confirms the validity of the model even under different experimental conditions, strengthening its applicability for estimating explosive effects in real-world scenarios.

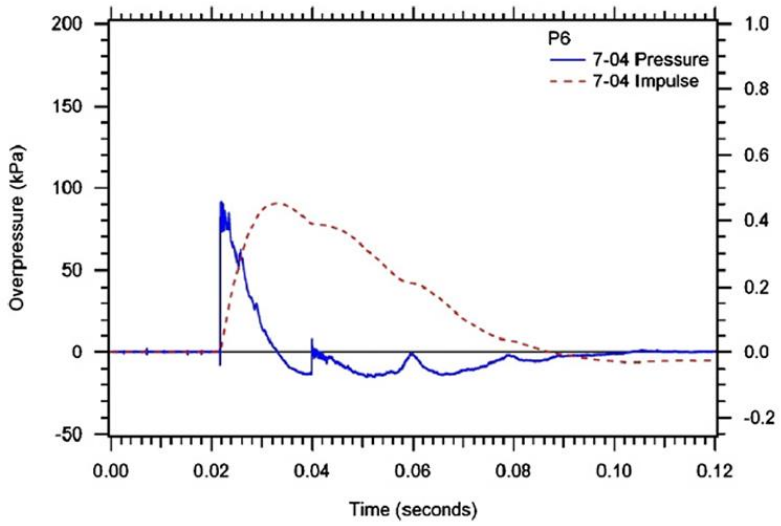

Figure 6.5: Overpressure time profile at 15 m for a hydrogen explosion in a 1D confined space. Experimental results reported by Groethe et al. (2007).

The **third experiment** was conducted in a confined volume of 37 m^3, between two aluminium plates placed in parallel, in a space of 10 mm. In this cavity, a homogeneous mixture of air and hydrogen was prepared, with a concentration of 30% by volume of hydrogen, corresponding to a total volume of about 30 litres and ignited by a spark. However, the geometric configuration of the system, consisting of two parallel plates separated by a small space, determines a confinement defined as 2D according to CCPS (2010), which limits the propagation of the shock wave. Furthermore, the overall volume of hydrogen involved in the explosion was relatively small. Considering these elements, it was considered appropriate to adopt an intensity level equal to 3, in line with what was reported by CCPS (2010).

Table 6.4: Sachs-scale distance and overpressure values obtained with the TNO method for a hydrogen explosion for a hydrogen explosion in a 2D confined space. Intensity level adopted: 3.

R [m]	$\bar{R}$	ΔP [kPa]
0.2	0.14	5
0.8	0.54	4.9
1	0.68	4.4

3	2.03	1.9
5	3.39	0.95
7	4.75	0.7
10	6.78	0.41
12	8.14	0.35
15	10.17	0.3
17	11.53	0.15

The trend is shown in **Figure 6.6**.

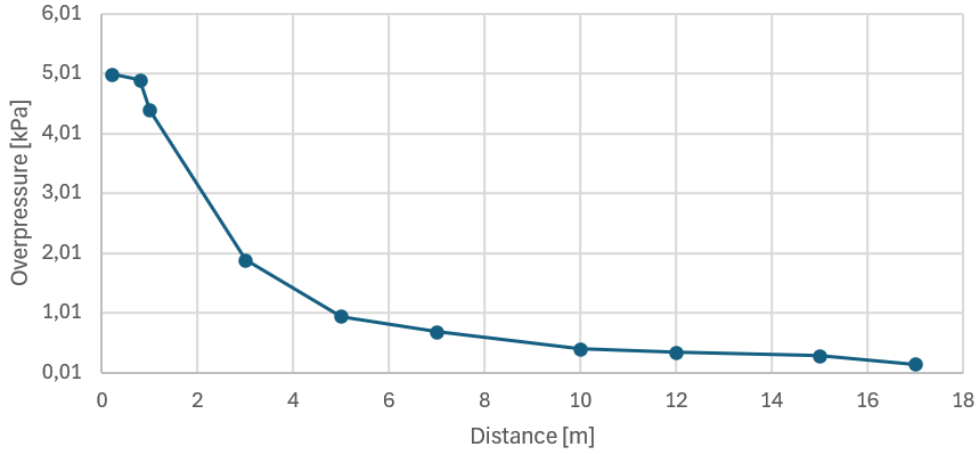

Figure 6.6: Overpressure trend as a function of distance from the charge obtained with the TNO method for an explosion which involved 0.03 m^3 of hydrogen in a confined space 2D.

Since the results of this experiment, reported in the study by Groethe et al. (2007), are not expressed as overpressure as a function of time, but as overpressure scaled as a function of the scaled distance in logarithmic scale the results obtained using the TNO model are reported below in **Figure 6.7**, converted to the same scale, in order to allow a direct comparison with the experimental data. The comparison between the scaled overpressure values shows that the results obtained by the TNO model are comparable with the experimental ones reported by Groethe et al. (2007). A good coherence is observed between the trend predicted by the model and the experimental data: both show an initial plateau phase, with scaled overpressure values close to 0.05, which extends up to a scaled distance between 0.5 and 0.6. Beyond this range, the overpressure progressively decreases. This behaviour suggests that the TNO model is able to describe with good accuracy the distribution of the overpressure generated by a hydrogen explosion in 2D confinement conditions.

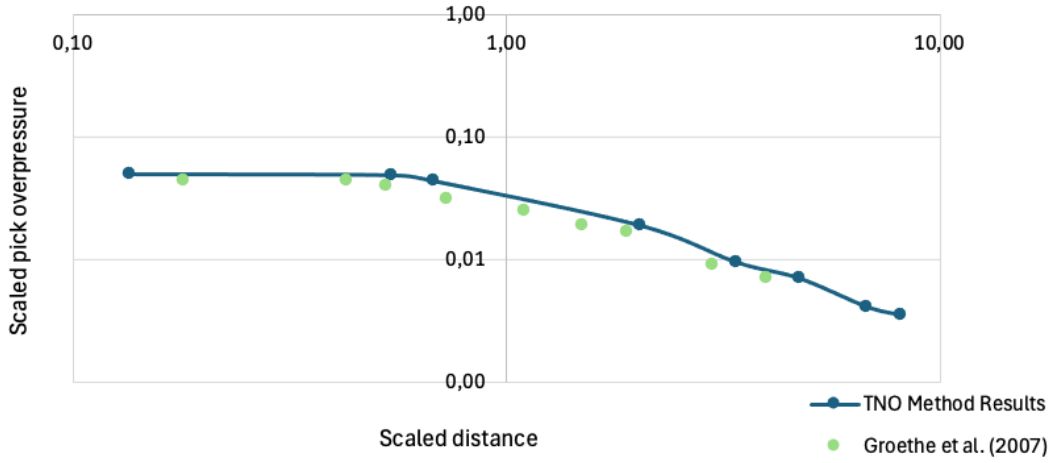

Figure 6.7: Overpressure trend as a function of Sachs-scale distance obtained from the TNO method compared with Groethe et al. (2007) experimental results, for an explosion which involved 0.03 m^3 of hydrogen in a confined space 2D.

The **fourth experiment** analysed in this study, based on the work of Groethe et al. (2007), was conducted in an open environment, with the presence of a protective barrier designed to attenuate the propagation of shock waves. This structure, 4 meters high and 10 meters wide, was positioned at a distance of 4 meters from the explosive source, consisting of a stoichiometric mixture of hydrogen and air, with a total volume of 5.26 m^3. The objective was to evaluate the reduction of overpressure and impulse behind the barrier, in conditions similar to those of an urban filling station. The energy released by the explosion was estimated to be 6.67×10^7 J. From these data, the Sachs-scaled distance $\bar{R}$ was calculated as a function of the real distance R from the release point. For each value of R, the peak overpressure was determined using the data reported in **Figure 6.1**. To choose the intensity, it must be considered that the explosion occurs in an open environment, the absence of geometric confinement allows a rapid dispersion of the shock wave, reducing the amplification of the explosive effects. Considering the high amount of fuel involved, but also the unconfined nature of the scenario, it was deemed appropriate to adopt an intensity level of 2.5, in accordance with CCPS (2010).

Table 6.5: Sachs-scale distance and overpressure values obtained with the TNO method for a hydrogen explosion in an open space. Intensity level adopted: 2.5.

R [m]	$\bar{R}$	ΔPs [kPa]
3	0.34	3
5	0.57	3
7	0.80	3
10	1.15	3
12	1.38	2.9
15	1.72	2.6
17	1.95	2.3
20	2.30	2

25	2.87	1.6
30	3.45	1.3

The trend is shown in **Figure 6.8**.

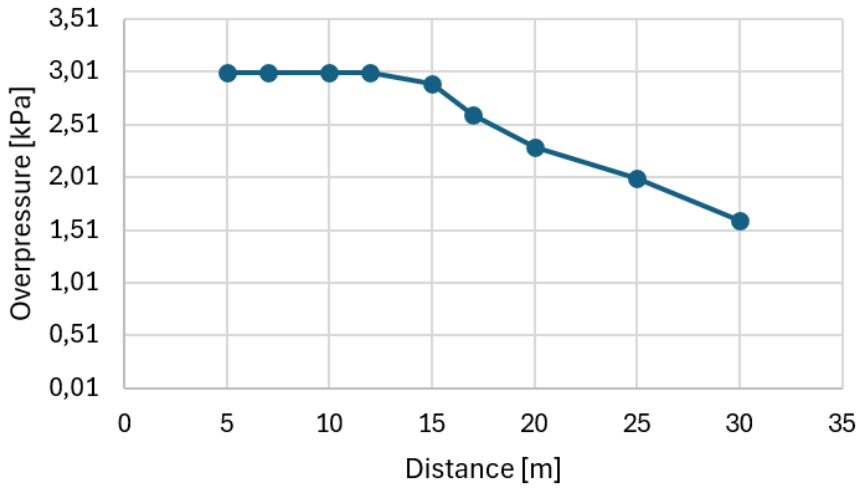

Figure 6.8: Overpressure trend as a function of distance from the charge obtained with the TNO method for an explosion which involved 5.26 m^3 of hydrogen in an open space.

Even for this last experiment, the experimental results and those obtained with the TNO model in **Figure 6.9** are reported as overpressure scaled as a function of the scaled distance, represented in logarithmic scale. From the comparison between the data obtained from the TNO model and the experimental ones, it is possible to note how both profiles exhibit comparable trends, characterized by an overpressure plateau of about 0.03. In the experimental results, having no continuous results in space, it is possible to see how this value is maintained up to a distance between 0.5 and 0.6, then the overpressure results are directly reported at a scaled distance of about 0.9 near the wall. Instead, in the results of the TNO method, since the presence of the wall is not considered, a gradual decrease is observed, which begins at a scaled distance of about 0.6.

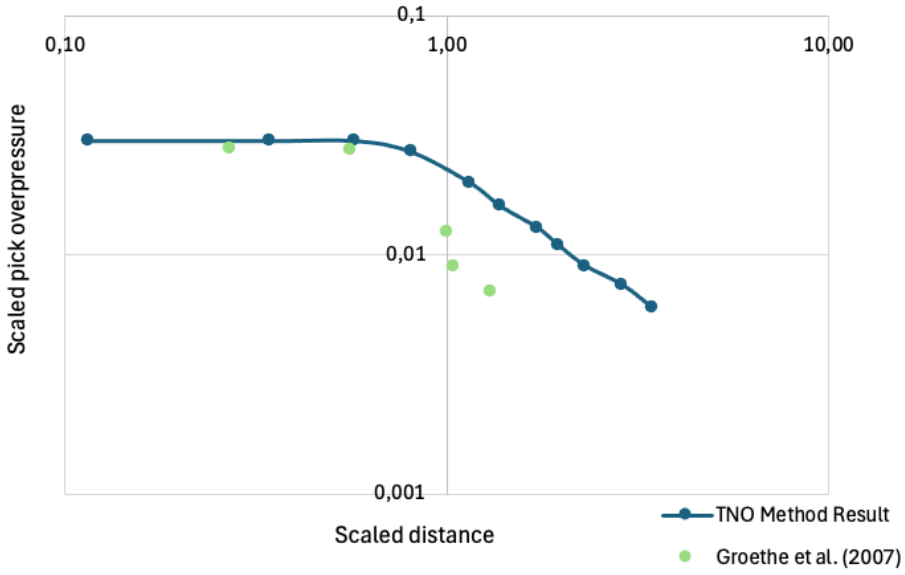

Figure 6.9: Overpressure trend as a function of Sachs-scale distance obtained from the TNO method compared with Groethe et al. (2007) experimental results, for an explosion which involved 5.26 m^3 of hydrogen in an open space.

Cryogenic Hydrogen Explosion

This method has been applied to the cryogenic hydrogen explosion reproducing the PRESLHY experiments reported in Jordan et al. (2023). Tests were performed both in ambient conditions and at low temperature (80 K), to simulate liquid or cryogenic hydrogen release scenarios. Our study focused on these cryogenic tests, both at 50 and 200 bar, as they represent the most extreme and relevant conditions for the evaluation of overpressures generated by cryogenic hydrogen releases. The trigger was positioned at 39.5 cm from the nozzle. The measurement system included high-frequency pressure sensors positioned along the jet axis at distances of 50, 75, 100 and 175 cm. Although the volume of the tank was the same in both cases, 2.8-litre, and the release hole was 4 mm, the mass of hydrogen contained was different due to the variation in density. In this regard, **Table 6.6** was taken from Jordan et al. (2023), which reports the trend of hydrogen density as a function of pressure and temperature, considered in the experiments. The values of ambient pressure and combustion energy per unit mass used in this analysis are the same as those used in the previous study on gaseous hydrogen, and they are reported in **Table 6.1**.

Table 6.6: Density and mass variation in PRESLHY experiments with pressure and temperature. Table taken from Jordan et al. (2023).

Temperature [K]	Pressure [bar]	1	5	10	20	50	100	150	200
293.15	Ideal Density [g/l]	0.083	0.414	0.827	1.654	4.136	8.271	12.407	16.542
	Z-factor @ 300K	1.000	1.000	1.008	1.013	1.030	1.060	1.090	1.120
	Density [g/l]	0.083	0.414	0.821	1.633	4.015	7.803	11.382	14.770
	H2 mass in DisCha [g]	0.233	1.164	2.310	4.597	11.303	21.966	32.042	41.587
77	Ideal Density [g/l]	0.315	1.574	3.149	6.298	15.745	31.490	47.235	62.980
	Z-factor @ 80K	1.000	0.990	0.980	0.970	0.960	1.020	1.130	1.260
	Density [g/l]	0.315	1.590	3.213	6.493	16.401	30.872	41.801	49.984
	H2 mass in DisCha [g]	0.886	4.477	9.045	18.277	46.169	86.906	117.669	140.704

The **first case** analysed is the one with a storage pressure equal to 50 bar, for which the hydrogen density is 16.401 g/l (**Table 6.6**). From these data, the combustion energy was calculated, which was found to be equal to 6.46×10^6 J. Subsequently, the values of the Sachs-scaled distance were determined at different points in space, in order to obtain the associated overpressure values through **Figure 6.1**. The distances selected for the calculation were chosen in coherence with the experimental setup adopted by Jordan et al. (2023), who placed the sensors at 0.5 m, 0.75 m, 1 m and 1.75 m away from the explosion release point. The application of the multi-energy method requires the preliminary definition of the intensity level of the explosive source. In this scenario, a release of cryogenic hydrogen from a 2.8-litre pressurized tank, stored at 50 bar and at a temperature of 80 K, in an open environment is considered. Although the total amount of hydrogen released is lower than in the previously analysed case, the gas density under the cryogenic conditions considered is about three orders of magnitude

higher, resulting in a significantly higher energy content per unit volume. The presence of a trigger ensures the activation of the explosive reaction, while the absence of confinement limits the propagation of the shock wave. Taking these factors into account, it was considered appropriate to adopt an intensity level equal to 3. The results are reported below.

Table 6.7: Sachs-scale distance and overpressure values obtained with the TNO method for a hydrogen explosion of cryogenic hydrogen stored at 80 K and 50 bar. Intensity level adopted: 3.

R [m]	$\bar{R}$	ΔP [kPa]
0.5	0.13	5
0.75	0.19	5
1	0.25	5
1.75	0.44	5

The experimental data reported by Jordan et al. (2023) consist of temporal pressure profiles measured at different points in space. From these profiles, it was possible to extrapolate, for each position, the maximum overpressure value recorded over time. These peak values were used for comparison with the results obtained from the TNO model shown in **Figure 6.10**, which directly provides the maximum overpressure expected in space at the same distances. The comparison shows that the curve produced by the TNO model reproduces in an overall accurate way the general trend observed experimentally. Although the experimental curve shown in **Figure 6.10** has a smooth, bell-shaped shape, the raw data available in the PRESLHY database show oscillatory behaviour in the maximum overpressure values measured at different points in space. However, not all available experimental data have been reported, as in some cases the precise measurement location was missing, making a consistent comparison with the TNO model results impossible. However, such fluctuations are not present in the model results. The curves obtained with the TNO method show a more regular trend, characterized by a constant plateau for the distances analysed. Based on the normalized curves shown in **Figure 6.1**, it is expected that the overpressure progressively decreases as one moves away from the explosion point.

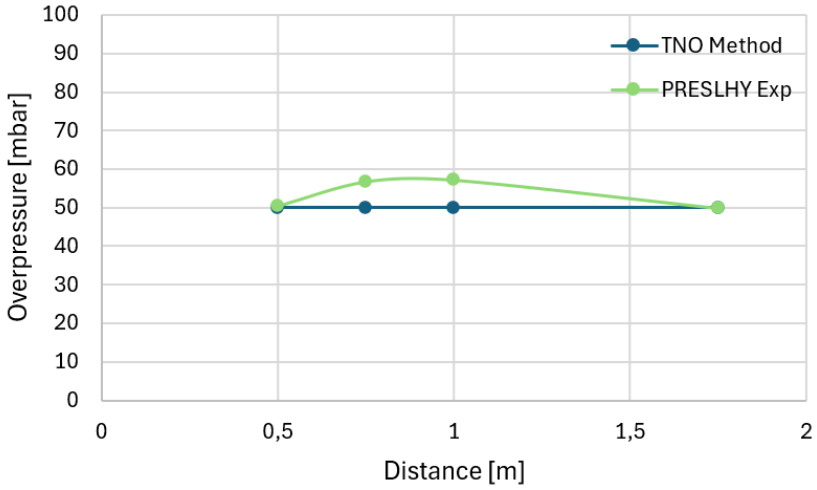

Figure 6.10: Overpressure trend as a function of distance from the charge for an

explosion which involved cryogenic hydrogen released from a tank at 50 bar pressure and 80K. The blue line represents the TNT Method results, the green line the experimental results.

To quantitatively evaluate the accuracy of the model with respect to the experimental data, the mean absolute percentage error was calculated using the formula reported in **Equation 4.4**. The value obtained is equal to 6.4%, indicating a good correspondence between the numerical and experimental results, with limited deviations and distributed in a contained way along the analysed range.

The **second case** analysed is the one with a storage pressure equal to 200 bar, for which the hydrogen density is 49.984 g/l. From these data, the combustion energy was calculated, which was found to be equal to 1.97×10^7 J. Subsequently, the values of the Sachs-scaled distance were determined at different points in space, in order to obtain the associated overpressure values through **Figure 6.1**. Compared to the case previously analysed with the same volume of hydrogen at 50 bar, the increase in pressure leads to an even higher density of the fuel, with a consequent increase in the energy content per unit volume. Taking these factors into account, it was considered appropriate to adopt an intensity level between 3.5 and 4, equal to 3.8. The results are reported below.

Table 6.8: Sachs-scale distance and overpressure values obtained with the TNO method for a hydrogen explosion of cryogenic hydrogen stored at 80 K and 200 bar. Intensity level adopted: 3.8.

R [m]	$\bar{R}$	ΔP [kPa]
0.5	0.09	9
0.75	0.13	9
1	0.17	9
1.75	0.3	9

The evolution of the numerical results obtained by applying the TNO model is shown in **Figure 6.11**. These results have been compared with the experimental data published by Jordan et al. (2023). The comparison highlights that the curve generated by the TNO model reproduces with good accuracy the overall trend observed experimentally. However, in this case as well, the experimental results do not exhibit a clear spatial dependence, unlike the predictions provided by the TNO model, for the distances considered.

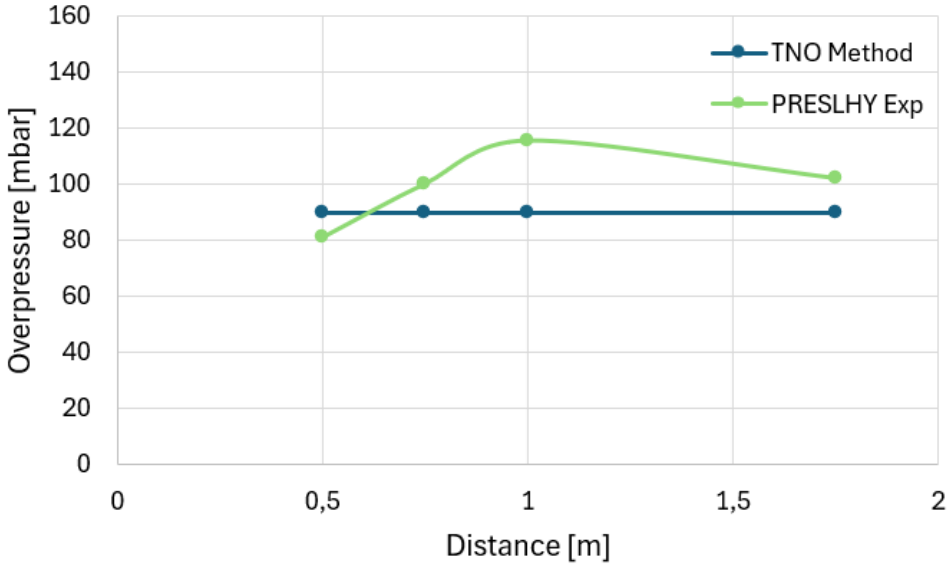

Figure 6.11: Overpressure trend as a function of distance from the charge for an explosion which involved cryogenic hydrogen released from a tank at 200 bar pressure and 80K. The blue line represents the TNT Method results, the green line the experimental results.

Also in this case, the accuracy of the model with respect to the experimental data was quantitatively evaluated by calculating the mean absolute percentage error, using the formula reported in **Equation 4.4**. The value obtained, equal to 13.7%, suggests that the model is able to reproduce the phenomenon with a moderate accuracy: the error is not negligible, but falls within an acceptable range for preliminary engineering applications.

In conclusion, during the analysis, the TNO Multi-Energy model was applied to different hydrogen explosion scenarios, varying the confinement conditions, the geometry of the environment and the volume of gas involved. The results obtained showed a good qualitative consistency with the experimental. The strengths found in the model were:

The simplicity and speed of application.

The possibility of varying the intensity of the explosion allows the reproduction of complex scenarios.

The limitations found are instead:

Absence of modelling of the geometric confinement: the model does not take into account the presence of obstacles, walls or openings, leading to underestimations or overestimations in real scenarios.

The model reports a simplified overpressure trend.

A particularly relevant aspect is the choice of the source intensity, which represents both a strength and a potential criticality of the method. On the one hand, the possibility of modulating this parameter allows for the consideration of fuel reactivity in the analysis, the quantity of released gas, its density and the degree of confinement and congestion, thus offering a certain flexibility in the representation of the phenomenon. On the other hand, the selection of an appropriate value requires a thorough knowledge of the method and of its application modalities to the specific type of fuel considered. There is a risk of introducing significant uncertainties in the estimation of the explosive effects.

Therefore, the TNO model proved to be a useful tool for a preliminary assessment of the explosive effects in scenarios with hydrogen but presents significant limitations in the presence of obstacles or complex geometries. It can be used as a support for a preliminary analysis of the consequences of a hydrogen explosion.

6.2 TNT Equivalence Method

The use of the TNT equivalence method to predict the effects of an explosion is particularly simple and immediate from an applicative point of view. This approach consists of evaluating the energy available inside a vapour cloud and converting it into an equivalent mass of trinitrotoluene, assuming that the explosion of the cloud produces effects similar to those generated by a conventional TNT detonation. Once the equivalent mass of TNT has been determined, it is possible to estimate the characteristics of the explosion, particularly the peak of lateral overpressure of the shock wave, at different distances from the point of origin. This estimate is carried out by using scaled graphs, derived from experimental data, which correlate the scaled distance with the main parameters of the shock wave.

TNT equivalence can be interpreted as a conversion coefficient that allows the available thermal energy, resulting from the combustion of the vapour cloud, to be transformed into an equivalent explosive energy. The CCPS guidelines indicate a value for this coefficient (α_c) equal to 0.03, which implies that only a fraction of the total combustion heat contributes to the generation of the shock wave. Based on this assumption, the equivalent mass of TNT (W_{TNT}) can be calculated using the following expression:

$$W_{TNT} = \alpha_c \frac{W_f H_f}{H_{TNT}} \quad \textbf{(6.4)}$$

H_f and W_f are the heat and the mass of fuel in the cloud, respectively, and H_{TNT} is the bast energy of the trinitrotoluene. To calculate the equivalent mass of TNT, it is necessary to preliminarily determine the mass of fuel actually involved in the formation of the explosive cloud W_f. This represents only a fraction of the total mass of fuel W released into the atmosphere, as not all the fuel contributes to the generation of the explosion. This fraction is defined as the flash fraction F and represents the percentage of fuel that mixes with the air in flammable concentrations. Therefore, the mass of fuel involved is determined by multiplying the total mass by the flash fraction:

$$F = 1 - exp[\frac{-c_p \Delta T}{L}] \quad \textbf{(6.5)}$$

L is the latent heat of vaporization, ΔT the temperature difference between the vessel temperature and the boiling temperature at ambient pressure, and c_p is the mean specific heat of the fuel. Once the equivalent mass of TNT has been determined, it is possible to calculate the Hopkinson-scaled distance ($\bar{R}$), defined as the ratio of the actual distance between the explosion point and the receiving body (x) to the cube root of the equivalent mass of TNT. This parameter can be used to estimate the effects of the shock wave, and it is defined by the following relation:

$$\bar{R} = \frac{x}{W_{TNT}{}^{1/3}} \quad \textbf{(6.6)}$$

With $\bar{R}$ value, it is possible to obtain from **Figure 6.12** the scaled peak overpressure value p_s at distance x.

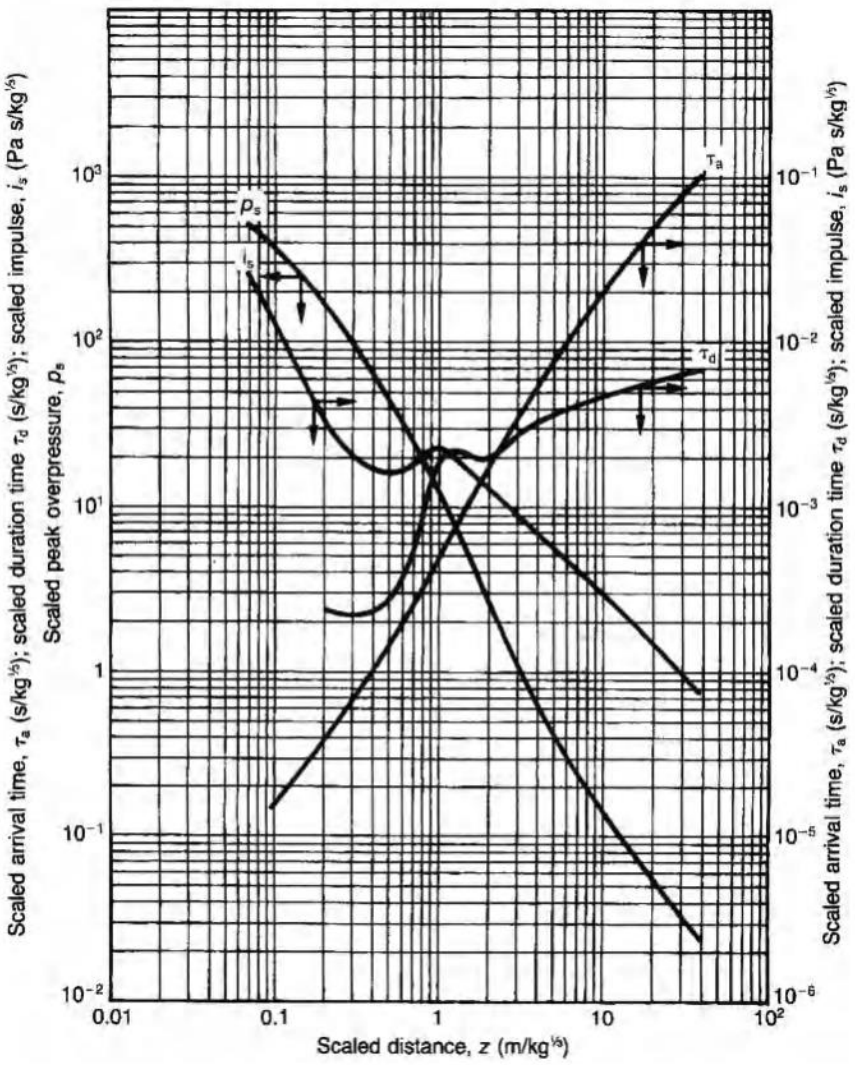

Figure 6.12: Experimental parameters related to a TNT explosion. Image taken from CCPS (2010).

The TNT method was compared with available experimental results for hydrogen explosions in both the gaseous and cryogenic phases. The analysis highlighted that this approach is not suitable for correctly representing the explosive effects of hydrogen. In particular, the model shows poor sensitivity to confinement conditions and environmental geometry, providing nearly identical results for scenarios with very different explosive dynamics. Furthermore, the highly reactive nature of hydrogen and its physicochemical properties, especially in the liquid phase, differ significantly from those of conventional explosives such as TNT, making the energy equivalence assumption inappropriate. Consequently, the method tends to significantly underestimate or overestimate the generated overpressures, making it unreliable for engineering applications in the context of hydrogen.

Detailed simulation results and comparisons with experimental data are

reported in the **Annex 3**, in order to streamline the main body of the text and focus attention on the most relevant critical and comparative considerations.

6.3 Baker-Strehlow-Tang (BST) Method

The Baker–Strehlow–Tang model is based on empirical results and is used to estimate overpressures generated by vapour cloud explosions, with particular attention to the effects of confinement and congestion of the environment. In contrast to models based on energy equivalence, the BST considers the propagation of the pressure wave as a function of the flame speed, therefore of the fuel reactivity, of the site geometry and of the presence of obstacles, which influence the combustion acceleration. Starting from these parameters, the model calculates the resulting overpressure as a function of the distance of the explosion. The BST is particularly useful for complex industrial scenarios, where the presence of structures and plants can amplify the effects of the explosion.

The estimation of the peak overpressure generated by the explosion with the BST method depends on the apparent flame propagation speed, indicated by the parameter M_f. This parameter represents an indicator of the violence of the explosion and is determined as a function of three main factors: the reactivity of the fuel, the degree of congestion and the level of confinement of the environment in which the explosion occurs. To support the selection of the value of M_f, the CCPS provides a table that allows estimating this parameter based on the specific conditions of the system. The table is reported below and constitutes a practical tool for the application of the BST model in real scenarios.

Table 6.9: Flame propagation speed values as a function of fuel reactivity, confinement and congestion in the region where the explosion occurs. Table taken from CCPS (2010).

Confinement	*Reactivity*	*Congestion*		
		High	*Medium*	*Low*
2-D	High	DDT	DDT	0.59
	Medium	1.6	0.66	0.47
	Low	0.66	0.47	0.079
2.5-D	High	DDT	DDT	0.47
	Medium	1.0	0.55	0.29
	Low	0.50	0.35	0.053
3-D	High	DDT	DDT	0.36
	Medium	0.50	0.44	0.11
	Low	0.34	0.23	0.026

Once the value of the M_f parameter has been defined, it is necessary to determine the energy term E, which represents the energy released by the explosion. This energy is then corrected by a ground reflection factor, as the BST model curves are based on the assumption of a spherical explosion. However, in vapour cloud explosions that occur in contact with the ground, the energy is reflected upwards, effectively doubling the perceived explosive effect. For this

reason, a reflection factor of 2 is commonly applied. It is important to underline that the BST model was developed for the evaluation of external explosions. To obtain the peak overpressure, the stand-off scaled distance $\bar{R}$ is calculated by **Equation 6.7**:

$$\bar{R} = R \times (\frac{P_0}{E})^{1/3} \quad \textbf{(6.7)}$$

R is the distance between the source of the explosion and the receiving body, and P_0 is the ambient pressure. To determine the combustion energy E using **Formula 6.10**, it is first necessary to calculate the stoichiometric concentration η via **Formula 6.8**, followed by calculating the number of moles of gas n using **Formula 6.9**.

$$\eta = \frac{moles\ fuel}{moles\ fuel\ and\ air} \quad \textbf{(6.8)}$$

$$n = \frac{PV}{RT} \quad \textbf{(6.9)}$$

$$E = 2 \times \eta \times n \times MW \times E_{comb} \quad \textbf{(6.10)}$$

where P is the gas pressure, V the volume, R the universal gas constant, T the temperature and MW the molecular weight.

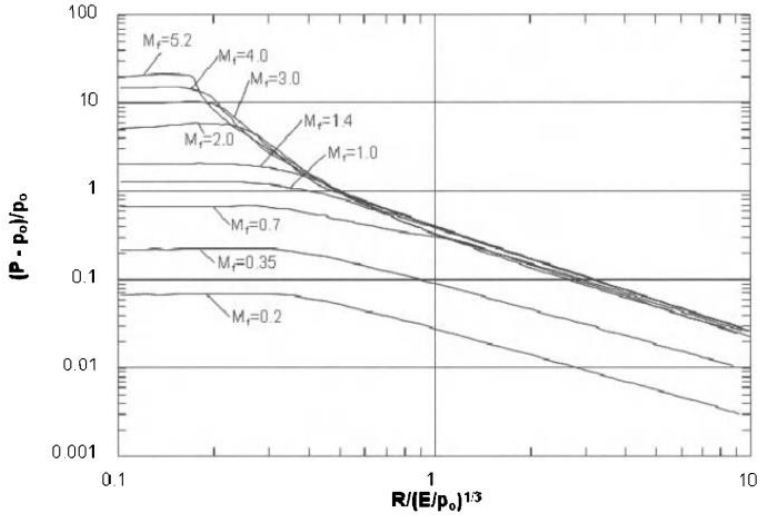

Figure 6.13: Baker-Strehlow-Tang method explosion curves. Image taken from CCPS (2010).

The BST method was also compared with experimental data from gaseous and cryogenic hydrogen explosions. The results show a systematic overestimation of overpressures, with values significantly higher than those measured. This behaviour is attributable to the simplified structure of the model, which does not explicitly consider key parameters such as the actual amount of fuel, storage conditions, or release geometry. Furthermore, the overpressure curve used does not vary with operating conditions, leading to poor model sensitivity. These limitations make the BST unsuitable for simulating explosive scenarios with hydrogen, especially in the presence of complex geometries or liquid-phase fluids.

Again, the numerical results and comparisons with experimental data are reported in the **Annex 3**.

6.4CCPS Case Study Application

From the results obtained in the model validation phase, it emerged that the Multi-Energy method developed by TNO represents the most effective tool to describe the consequences of a hydrogen cloud explosion, regarding the estimation of the generated overpressures. Unlike other simplified approaches, the TNO model allows for the consideration of the degree of confinement and congestion of the environment, as well as the reactivity of the fuel, providing a more realistic and conservative representation of the explosive effects.

For this reason, the TNO model was selected for the analysis of a real case study, in order to apply the method in a real-world operational context and evaluate its effectiveness in predicting the danger zones. The case study analysed concerns a real-life accidental release of liquid hydrogen that occurred at the AC Transit refuelling station in Emeryville, California, in 2012. Although the event did not result in the ignition of the gas or serious consequences, it represents a significant near miss, useful for assessing the potential consequences in a cloud triggered event.

The objective of the analysis is therefore not to reconstruct an actual explosion, but to assess the potential explosive effects in a hypothetical scenario consistent with the actual conditions of the release. This approach allows for the estimation of the danger zones associated with a worst-case scenario, providing useful insights for designing safety measures, defining safety distances, and planning mitigation interventions.

In this context, the TNO method was applied to simulate the explosion of the cloud generated by the release, in order to verify its effectiveness in predicting overpressures and support the adoption of preventive strategies in similar facilities.

6.4.1 Event description

The incident analysed occurred at the AC Transit hydrogen refuelling station in Emeryville, California, a facility designed to support the refuelling of fuel cell buses with liquid hydrogen (Harris et al., 2012). The storage system consisted of a vertical, double-walled, vacuum-insulated cryogenic tank containing liquid hydrogen at approximately 20 K at low pressure. The tank was connected to a distribution system that fed refuelling pumps and transfer lines to the vehicles.

On May 4, 2012, a malfunctioning pressure relief valve (PRV) caused an uncontrolled release of liquid hydrogen. The failure led to the valve being opened unintentionally, resulting in the release of LH_2 into the open air. According to the official report by Sandia National Laboratories, the total amount of hydrogen released was estimated to be approximately 300 kg. The release occurred over a relatively short period of time, generating a visible cryogenic cloud that rapidly expanded and dispersed into the atmosphere.

The environmental conditions at the time of the event were not described in detail, but they were assumed to be consistent with a temperate and stable climate, typical of the California coastal area. Despite the absence of ignition, the event led to the evacuation of the plant and the interruption of operations, highlighting the criticality of an uncontrolled release of LH_2 even in the absence of combustion.

For the purposes of the analysis, it is assumed that the release occurred in stable atmospheric conditions (class F), with a wind speed of 2 m/s and an ambient temperature of 15 °C. The release was considered instantaneous and localized at ground level, in proximity to the tank. The total mass of 300 kg of liquid hydrogen was used as input for the simulation of explosive effects by means of the TNO model, to estimate the overpressures generated in case of ignition of the cloud and to define the related danger zones.

6.4.2 Multi-Energy Method Application

The Multi-Energy model developed by TNO was applied to simulate the explosive effects of an accidental release of liquid hydrogen at the AC Transit plant in Emeryville. This approach allows estimating the overpressures generated by a vapour cloud explosion, taking into account the available energy, fuel reactivity and environmental conditions. The parameters considered in the analysis are reported in **Table 6.10**:

Table 6.10: Parameters used for the TNO method for the case study.

Parameter	Value
P_0 [Pa]	101325
E [J]	4.20×10^{10}
E_{comb} [MJ/kg]	140
m_{H2} [kg]	300

In the present case study, the fuel involved is liquid hydrogen, known for its high reactivity and for its ability to generate flammable mixtures even at low concentrations. The released mass, equal to about 300 kg, is significantly higher than that considered in other documented experiments, such as those of the PRESLHY project, where masses between 0.04 kg and 0.14 kg were associated with intensity levels between 3.0 and 3.8. Furthermore, while the PRESLHY experiments were conducted in open and well-ventilated environments, the release at the Emeryville plant occurred in proximity to industrial structures, in a semi-confined context, with the potential presence of obstacles and complex geometries that can favour turbulence and flame acceleration. Considering the higher amount of hydrogen released, the liquid form of the fuel, its high reactivity and the characteristics of the environment, it was considered appropriate to adopt an intensity level of 7. This value represents a compromise between a conservative approach and a realistic risk assessment, consistent with the TNO model guidelines for industrial scenarios with light fuels and partially confined environments. The results are reported below.

Table 6.11: Sachs-scale distance and overpressure values obtained with the TNO method for a hydrogen explosion of liquid hydrogen stored at 20 K in a refuelling station. Intensity level adopted: 7.

R [m]	$\bar{R}$	ΔP [kPa]
5	0.07	100

10	0.13	100
15	0.2	100
20	0.27	100
25	0.34	100
30	0.40	100
40	0.54	90
50	0.67	80
60	0.80	65
70	0.94	49
80	1.07	40
90	1.21	38
100	1.34	30
170	2.28	14
200	2.68	11
300	4.02	7
600	8.05	3

In the context of the analysis of the effects of an explosion, the threshold values of overpressure established by the Ministero dei Lavori Pubblici (2001) were taken into consideration. These values represent the limits beyond which significant physiological effects on the human body occur. The thresholds identified are 0.3 bar, 0.14 bar and 0.03 bar, which correspond to 30 kPa, 14 kPa and 3 kPa, respectively. Each threshold is associated with a different level of severity. The value of 30 kPa represents a condition of high lethality, in which the probability of death due to the shock wave is very high. At 14 kPa, the beginning of lethality is observed, a threshold beyond which the first cases of death are recorded, although with a lower probability than the upper threshold. Finally, the value of 3 kPa is considered the minimum limit beyond which reversible lesions occur, such as physical damage that does not permanently compromise the health of the individual.

The spatial analysis of the explosive event shows that the effects of the overpressure wave extend over a considerable radius. It is observed that the threshold of 3 kPa is already reached at a distance of approximately 600 meters from the charge, emphasizing that the overpressure wave is capable of causing physiological damage even at relatively large distances. This result highlights the importance of evaluating the safety zones. The data trend is shown in **Figure 6.14**.

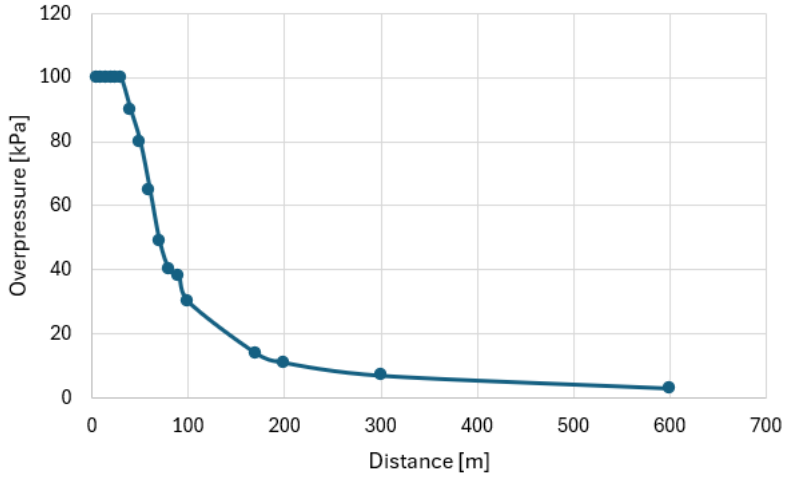

Figure 6.14: Overpressure trend as a function of distance from the charge obtained with the TNO method for an explosion which involved 300 kg of liquid hydrogen in a partially open space.

The analysis conducted using the Multi-Energy model of the TNO highlighted a characteristic behaviour of the overpressure generated by the explosion of a hydrogen cloud in a semi-confined environment. In particular, the presence of an initial plateau is observed, in which the overpressure remains almost constant at around 100 kPa up to a distance of about 40 meters from the release point. Once this threshold is exceeded, the overpressure begins to decrease gradually and continuously, following the typical trend of the TNO curves for medium-high intensity levels. Despite the progressive decrease, the effect of the explosion extends over considerable distances: at 600 meters from the charge, the residual overpressure is still equal to about 3 kPa, a value sufficient to cause damage to light structures or to cause injuries to unprotected exposed subjects.

It is important to underline that the analysed scenario represents a hypothetical and conservative case, in which it is assumed that the entire mass of liquid hydrogen released participates in the explosion, without having the time to disperse into the environment. Atmospheric dispersion and cloud dilution could significantly reduce the amount of fuel actually involved in the combustion. However, the adoption of this approach allows the evaluation of the worst-case scenario, useful for the definition of safety distances and for the design of adequate mitigation measures. The results obtained from this simulation offer valuable insights for the risk assessment associated with the management of liquid hydrogen in the industrial sector. Therefore, the application of the TNO model allows the realistically estimation of the extension of the impact zones in the event of an explosion, thus supporting the definition of safety distances, the design of protective barriers and the adoption of effective mitigation measures. The study is part of the broader objective of promoting a quantitative and evidence-based approach for the prevention of major accidents, contributing to the strengthening of the safety culture in emerging sectors related to hydrogen as an energy vector.

This simulation is part of a resilient approach to risk management, which is not limited to incident response but includes the preventive assessment of possible critical scenarios and the design of protective measures based on quantitative evidence.

Chapter 6 Partial Conclusions

This chapter critically analysed three simplified methodologies proposed by the CCPS for estimating the explosive effects generated by hydrogen clouds: the Multi-Energy (TNO) method, the TNT equivalent method, and the Baker-Strehlow-Tang (BST) model. The objective was to evaluate their reliability in predicting the overpressures generated by explosive scenarios, both in the gaseous and cryogenic phases, through comparison with experimental data available in the literature.

The results showed that the TNO method represents the most robust and flexible approach among those analysed, thanks to the ability to modulate the explosion intensity as a function of confinement, congestion, and fuel reactivity conditions. The model showed good consistency with experimental data, both qualitatively and quantitatively, proving suitable for preliminary engineering applications.

Conversely, the TNT and BST methods showed significant limitations. The former showed poor sensitivity to geometry and confinement, providing similar results for very different scenarios. The second method systematically overestimated overpressures, demonstrating a poor adaptation to real operating conditions.

The analysis conducted in this chapter directly contributes to the achievement of the research's scientific objectives. Specifically, the chapter contributed to achieving objective SG4 through the application and validation of simplified methodologies for estimating the overpressure generated by hydrogen cloud explosions. The analysis identified the TNO method as an effective tool for the preliminary assessment of explosive scenarios, useful for planning prevention measures and defining safety distances. Furthermore, the chapter addressed RQ4 by demonstrating how the use of predictive models, even simplified ones, can support proactive risk management in industrial environments, contributing to the construction of more resilient plants. The approach adopted highlighted the importance of selecting calculation tools consistent with the characteristics of the fuel and the operating context, in order to ensure a realistic and conservative assessment of explosive effects. In summary, the chapter has provided a solid methodological basis for the selection and application of hydrogen explosion analysis tools, contributing to strengthening the resilience of industrial plants and defining more effective prevention strategies.

Chapter 6 References

CCPS (2010). Guidelines for Vapor Cloud Explosion, Pressure Vessel Burst, BLEVE, and Flash Fire Hazards. Center for Chemical Process Safety. 2nd ed. Hoboken, NJ: Wiley-AIChE.

Groethe, M., Merilo, E., Colton, J., Chiba, S., Sato, Y., Iwabuchi, H. (2007). Large-scale hydrogen deflagrations and detonations. International Journal of Hydrogen Energy, 32(13), 2125–2133. https://doi.org/10.1016/j.ijhydene.2007.04.016

Harris, A.P., San Marchi, C.W., Levin, J. and Butler, D. (2012). Investigation of the hydrogen release incident at the AC Transit Emeryville Facility. Sandia National Laboratories. URL: https://www.osti.gov/biblio/1121962 (Accessed July 2025).

Jordan, T., and Kuznetsov, M. (2021). Experimental Investigation of Pre-Mixed Systems with Cryogenic Hydrogen. PRESLHY Project Deliverable 5.3, D20.

Jordan, T., Friedrich, A., Veser, A. and Kotchourko, N. (2023). PRESLHY Experiment series E5.1 (Ignited Discharge) results – Benchmarking. Karlsruhe Institute of Technology. URL, https://www.radar-service.eu/radar/en/dataset/uzDLoVtvVFILFwGQ (Accessed June 2025).

Ministero dei Lavori Pubblici (2001). Requisiti minimi di sicurezza in materia di pianificazione urbanistica e territoriale per le zone interessate da stabilimenti a rischio di incidente rilevante, Decreto Ministeriale 9 Maggio 2001, Supplemento ordinario Nr 151 alla “Gazzetta Ufficiale” n. 138 del 16 giugno 2001 - Serie generale. Italia.

Sato, Y., Iwabuchi, H., Groethe, M., Merilo, E., and Chiba, S. (2006). Experiments on hydrogen deflagration. Journal of Power Sources, 159(1), 144–148. https://doi.org/10.1016/j.jpowsour.2006.04.062

Wakabayashi, K., Nakayama, Y., Mogi, T., Kim, D., Abe, T., Ishikawa, K., Kuroda, E., Matsumura, T., Horiguchi, S., Oya, M., and Fujiwara, S. (2007). Experimental study on blast wave generated by deflagration of hydrogen-air mixture up to 200 m3. Science and Technology of Energetic Materials, 68(1), 25.

General Conclusions

Managing technological risk in the industrial sector requires an integrated approach, combining historical analysis, predictive modelling, and advanced monitoring technologies. This work developed a methodological framework oriented towards operational resilience, with particular attention to material degradation, loss of containment, and safety management in hydrogen-based systems.

The analysis of a large set of historical events allowed the study of the relations between material degradation and the process industry. The most common failure mechanisms included corrosion, vibration, fatigue, and erosion. The equipment most affected was primary containment systems, frequently subjected to severe operating conditions and thermomechanical cycles that accelerate their deterioration. The most affected industrial sectors were chemical and petrochemical industries and pipeline transportation networks. A clear correlation also emerged between the age of the systems and the probability of failure, with a higher incidence of events in older systems. In many cases, the events required a revision of inspection plans, highlighting the inadequacy of the preventive control systems in place.

The application of Bayesian Networks allowed the estimation of scenarios even in the presence of incomplete data, providing a quantitative basis for risk classification and prioritization of inspection and maintenance interventions. A risk-consequence matrix model was also developed, useful for supporting operational decisions in complex contexts.

The analysis also highlighted how degradation phenomena can interact with external events, generating complex and amplified scenarios. In particular, the role of structural failures as predisposing factors in cases of accidental escalation was explored, with reference to historical events in which degradation acted as a latent element, triggered by unfavourable environmental or operational conditions. This highlighted the importance of an integrated risk assessment, which considers not only the static conditions of the plant, but also its evolution over time and its interaction with the context.

Then, the issue of loss of containment, which emerged as the primary cause from the analysis of material degradation, was addressed, with particular reference to hydrogen, a strategic energy carrier characterized by high reactivity and difficult to contain. An operational methodology was proposed for the dynamic detection of leaks using sensor-equipped drones, integrating geometric modelling to locate the release source. This approach allows the estimation of the location of the release point from the concentration map, even in complex scenarios.

Validation of the PHAST software confirmed its reliability in simulating the thermal effects associated with liquid hydrogen releases, while analysis of the methodologies proposed by the CCPS for estimating explosive effects highlighted that the Multi-Energy (TNO) model is the only one among those analysed capable of consistently representing real-world scenarios. This model was applied to the AC Transit refuelling station in Emeryville, California, where an accidental release of liquid hydrogen occurred following the malfunction of a safety valve.

Although the event did not result in the ignition of the gas, it was used as a case study to simulate a potential explosion and assess the associated hazard areas. The analysis allowed the estimation of the overpressures generated and the evaluation of safety distances, providing useful insights for designing mitigation measures and emergency planning.

Overall, the work provided a methodological and applicative contribution to the construction of a resilience-oriented risk management system capable of integrating historical data, predictive models, and advanced monitoring technologies. The results obtained support the adoption of proactive strategies for the prevention of major accidents, in line with the principles of the Seveso III Directive and the safety requirements of new energy scenarios.

Annexes

Annex 1: Further PHAST Results from Hydrogen Release Simulation

Below are the maximum concentration profiles obtained from simulations of hydrogen release through holes of different diameters, with an analysis of the effect of temperature on the spatial distribution of the gas.

The concentration profiles for the simulations of releases from holes of 1.5 mm (**Figure A-1.1**) and 1 mm diameter (**Figure A-1.2**) are shown below. From

what has been observed, the trend of the concentration follows that described for releases from holes of 2 mm diameter. Indeed, even with lower flow rates at lower temperatures, the concentration is higher. Furthermore, even in these two scenarios, the concentration decreases rapidly from almost 100% in volume to less than 10% in 0.5 m. Regarding the percentage difference between the concentrations at different storage temperatures, the results for a hole diameter of 1.5 mm are reported in **Table A-1.1,** while the results for a hole diameter of 1 mm are reported in **Table A-1.2**.

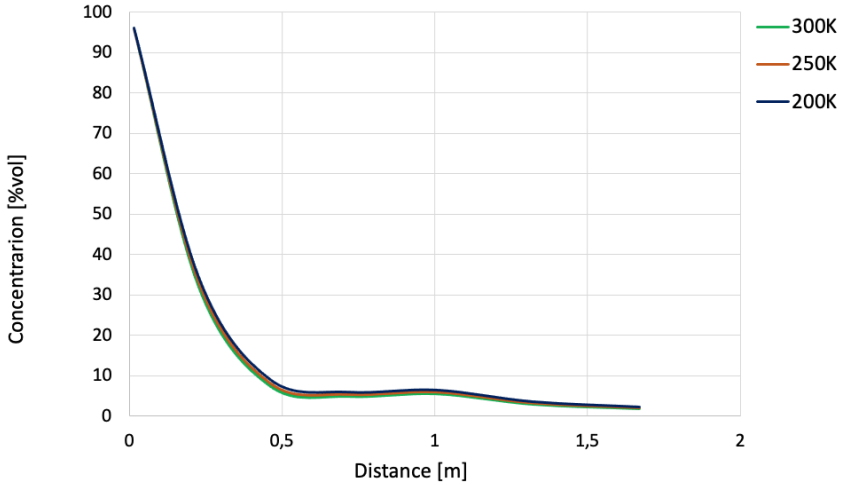

Figure A-1.1: Maximum concentration as a function of distance following a release of hydrogen from a 1.5 mm hole from a 5-bar storage tank at three different temperatures. Green is 300K, orange is 250K, and blue is 200K. Simulation performed with PHAST software.

Table A-1.1.: Percentage difference between concentrations in space following a release from a 5-bar tank with a 1.5 mm diameter hole at 200K and 250K in the second column. Percentage difference between concentrations at 200K and 300K in the third column, at a distance from the release point reported in the first column.

Distance [m]	$\Delta\%_{200K-250K}$	$\Delta\%_{200K-300K}$
0.01	0.08	0.15
0.23	3.81	7.21
0.46	11.37	21.50
0.72	11.56	21.89
1.00	9.06	16.78
1.32	11.54	21.54
1.67	12.59	23.30

For both scenarios, the ratio between $\Delta\%_{200K-300K}$ and $\Delta\%_{200K-250K}$ remains almost constant, with the former being approximately twice the latter. However, in the case of the release from a 1 mm hole, the concentrations initially move apart as the temperature varies, with an increase in the percentage differences, $\Delta\%_{200K-300K}$ and $\Delta\%_{200K-250K}$, but unlike the other two scenarios, at a distance of about one meter these differences tend to decrease, suggesting that the concentration curves come closer together again.

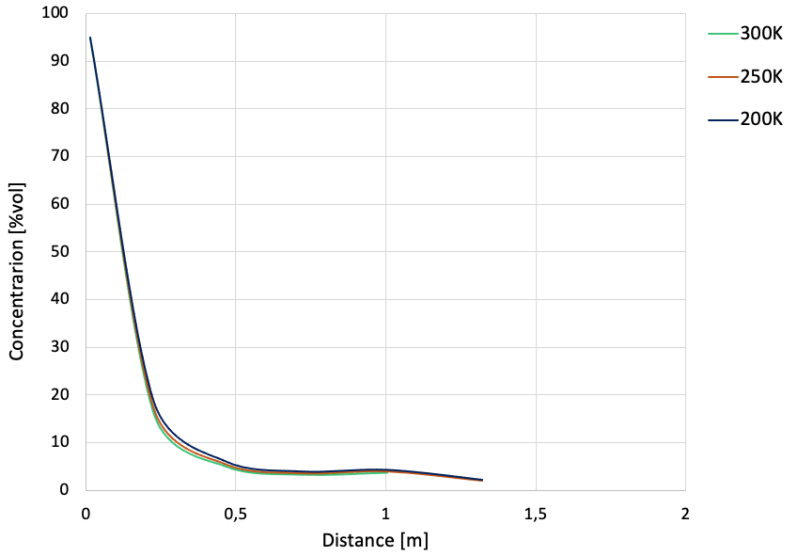

Figure A-1.2: Maximum concentration as a function of distance following a release of hydrogen from a 1 mm hole from a 5-bar storage tank at three different temperatures. In green 300K, in orange 250K and in blue 200K. Simulation conducted with the PHAST software.

Table A-1.2: Percentage difference between concentrations in space following a release from a 5-bar tank with a 1mm diameter hole at 200K and 250K in the second column. Percentage difference between concentrations at 200K and 300K in the third column, at a distance from the release point reported in the first column.

Distance [m]	$\Delta\%_{200K-250K}$	$\Delta\%_{200K-300K}$
0.01	0.10	0.163
0.23	8.85	15.76
0.46	11.53	21,81
0.72	11.70	22.15
1.00	9.27	17.68

Annex 2 Analytical Development of the Geometric Parameters from Concentration Curves

Below are the equations used to estimate the parameters of the ellipse, semi-axes and centre, starting from four points belonging to the same iso-concentration curve**.** It is possible to formulate a system of four equations in four unknowns, a, b, x_0, and y_0, using the coordinates of four points belonging to the same curve with equal concentration. The resolution of this system allows the estimation of the position of the centre and the main dimensions of the ellipse that approximates the spatial distribution of the cloud:

$$\frac{(x_1-x_0)^2}{a^2}+\frac{(y_1-y_0)^2}{b^2}=1 \quad \textbf{(A-2.1)}$$

$$\frac{(x_2-x_0)^2}{a^2}+\frac{(y_2-y_0)^2}{b^2}=1 \quad \textbf{(A-2.2)}$$

$$\frac{(x_3-x_0)^2}{a^2}+\frac{(y_3-y_0)^2}{b^2}=1 \quad \textbf{(A-2.3)}$$

$$\frac{(x_4-x_0)^2}{a^2}+\frac{(y_4-y_0)^2}{b^2}=1 \quad \textbf{(A-2.4)}$$

The solution of the system yields the following estimates for the unknown parameters:

$$x_0=\frac{({x_2}^2-{x_3}^2)-\left[({x_1}^2-{x_2}^2)\times(\frac{{y_3}^2-{y_2}^2}{{y_2}^2-{y_1}^2})\right]}{\left[(2x_2-2x_1)\times(\frac{{y_3}^2-{y_2}^2}{{y_2}^2-{y_1}^2})\right]-(2x_3-2x_2)} \quad \textbf{(A-2.5)}$$

$$\mathrm{y_0}=\frac{-(\mathrm{kh+rg-fc-de})\pm\sqrt{(\mathrm{kh+rg-fc-de})^2-4(\mathrm{rh-fd})(\mathrm{kg-ec})}}{2(\mathrm{rh-fd})} \quad \textbf{(A-2.6)}$$

$$a=\sqrt{\frac{(x_1-x_0)^2}{1-\frac{(y_1-y_0)^2}{b^2}}} \quad \textbf{(A-2.7)}$$

$$b=\sqrt{\frac{\left[(y_2-y_0)^2-\frac{(y_1-y_0)^2(x_2-x_0)^2}{(x_1-x_0)^2}\right]}{1-\frac{(x_2-x_0)^2}{(x_1-x_0)^2}}} \quad \textbf{(A-2.8)}$$

parameterized for simplicity as follows:

$$k=(x_2^2-x_3^2)(y_2^2-y_1^2)-(x_1^2-x_2^2)(y_3^2-y_2^2) \quad \textbf{(A-2.9)}$$

$$r=(x_2^2-x_3^2)(2y_1-2y_2)-(x_1^2-x_2^2)(2y_2-2y_3) \quad \textbf{(A-2.10)}$$

$$c=(2x_2-2x_1)(y_3^2-y_2^2)-(2x_3-2x_2)(y_2^2-y_1^2) \quad \textbf{(A-2.11)}$$

$$d=(2x_2-2x_1)(2y_2-2y_3)-(2x_3-2x_2)(2y_1-2y_2) \quad \textbf{(A-2.12)}$$

$$e=(x_3^2-x_4^2)(y_3^2-y_2^2)-(x_2^2-x_3^2)(y_4^2-y_3^2) \quad \textbf{(A-2.13)}$$

$$f=(x_3^2-x_4^2)(2y_2-2y_3)-(x_2^2-x_3^2)(2y_3-2y_4) \quad \textbf{(A-2.14)}$$

$$g=(2x_3-2x_2)(y_4^2-y_3^2)-(2x_4-2x_3)(y_3^2-y_2^2) \quad \textbf{(A-2.15)}$$

$$h=(2x_3-2x_2)(2y_3-2y_4)-(2x_4-2x_3)(2y_2-2y_3) \quad \textbf{(A-2.16)}$$

Based on the geometric representation of the ellipse, a spreadsheet was developed that allows estimating the main parameters of the iso-concentration curve. By entering the coordinates of four experimental points belonging to the same ellipse, the spreadsheet solves the system of equations, returning the values of the coordinates of the centre and semi-axes of the ellipse. Once these parameters have been determined, the spreadsheet also returns the value of the

coordinates of point A_0 (x_{a0}, y_{a0}), according to the equations:

$$x_{a0} = x_0 - a \quad \textbf{(A-2.17)}$$

$$y_{a0} = y_0 \quad \textbf{(A-2.18)}$$

For completeness, a predictive model based on second-order polynomial regression was developed in order to find a correlation between α and the main parameters on which this length depends. The analysis was conducted considering only stable atmospheric conditions (classified as "D"). Furthermore, the "atmospheric conditions" variable is categorical and not continuous and modelling it within a single predictive function would have required the introduction of dummy variables and could have reduced the readability and interpretability of the resulting formula. Focusing on a single atmospheric scenario allowed the simplification of the model structure while maintaining high predictive accuracy. The model takes four input variables; the output variable is the distance between point A_0 and the actual release source. The subset of the polynomial regression model was trained using the following independent variables:

i) the hole diameter D_{hole} (mm)

ii) the storage pressure P (bar)

iii) the distance height between the detection plane and the release H_{loc} (m)

iv) the wind speed v (m/s).

The dependent variable is the distance α (m), obtained from numerical simulations.

The approximate function obtained through second-degree polynomial regression has a MAPE of 6.5%, calculated by **Equation 4.3** reported in **Chapter 4**, indicating a quite good predictive capacity. The model for condition D showed significant dependence on all variables considered, including interactions between them. The resulting approximate function is as follows:

$$\alpha = 6.614 - (0.776 \times D_{hole}) - (0.014 \times P) + (0.000052 \times H_{loc}) + (0{,}000035 \times v) - (1.047 \times D_{hole}^{2}) - (0.00365 \times D_{hole} \times P) - (1.149 \times D_{hole} \times H_{loc}) + (1.149 \times D_{hole} \times v) + (0.000012 \times P^{2}) + (0.00468 \times P \times H_{loc}) - (0.0038 \times P \times v) + (0.0693 \times H_{loc}^{2}) + (1.659 \times H_{loc} \times v) + (0.000226 \times v^{2})$$

(A-2.19)

Once the equipment involved in the release has been identified and the value of α has been obtained, **Equation A-2.19** can be used to iteratively estimate the hole diameter and the height of the release. This approach may be useful in scenarios where it is necessary to identify the height and diameter of the leak from the data obtained by the drone. Furthermore, the ability to implement the function in spreadsheets broadens its applicability even in contexts where computational resources are limited or where a real-time response is required. Thus, the model represents a valuable tool for supporting emergency management and the timely location of hydrogen leaks in complex industrial environments.

Annex 3 TNO and BST Methods Applied to Hydrogen Explosions

Detailed results of simulations conducted with the TNT and BST methods, applied to gaseous and cryogenic hydrogen explosion scenarios, are reported, with comparison with available experimental data.

TNT Methods calculations

Gaseous Hydrogen Explosion

This method has been applied to the gaseous hydrogen explosion reproducing the experiment analysed by Groethe et al. (2007), the data considered are reported in **Table A-3.1**:

Table A-3.1: Parameters used for the TNT equivalence method for gaseous hydrogen explosion.

Parameter	Value
F	0.997
c_p [kJ/kg K]	9.69
ΔT [K]	267.7
L [kJ/kg]	449
α_c	0.03
H_f [MJ/kg]	140
H_{TNT}[MJ/kg]	4.68

The results of the **first experiment** are reported in **Table A-3.2**:

Table A-3.2: Parameters used for the TNT equivalence method for the first experiment conducted by Groethe et al. (2007).

Parameter	Value
W_{TNT} [kg]	7.24
W [kg]	8.091
W_f [kg]	8.066

From these data, the Hopkinson-scaled distance $\bar{R}$ as a function of the distance R from the release point were calculated, and for each value of R, the peak overpressure was determined using **Figure 6.12**, reported in **Chapter 6**.

Table A-3.3: Hopkinson-scaled distances and overpressure values obtained with the TNT method for a hydrogen explosion in a space of 300 m3, initially closed.

R [m]	$\bar{R}$ [m/kg$^{1/3}$]	ΔP [kPa]
3	1.55	500
5	2.58	170

7	3.62	80
10	5.17	42
12	6.20	30
15	7.75	20
20	10.34	12
25	12.92	9,5
30	15.51	8

The trend is shown in **Figure A-3.1**.

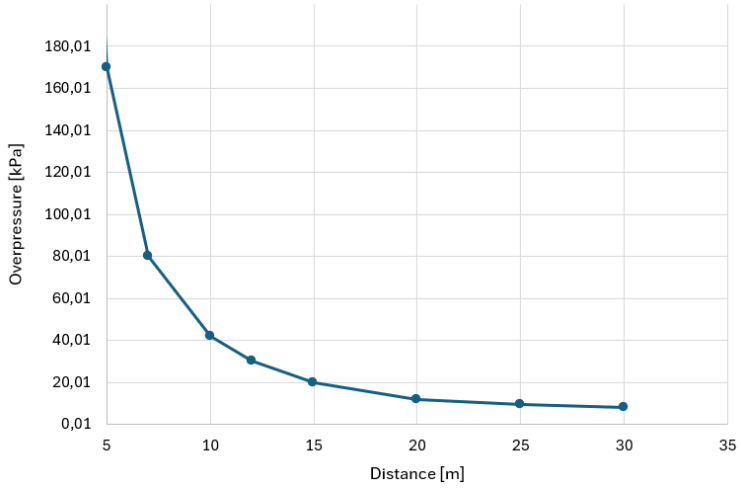

Figure A-3.1: Overpressure trend as a function of distance from the charge obtained with the TNT method for an explosion which involved 90 m^3 of hydrogen in a 300 m^3 space.

It was possible to compare the maximum overpressures obtained in space with the experimental data reported by Groethe et al. (2007), relating to the overpressure measured at 15 meters from the explosion point. In particular, the study presents the temporal trend of the overpressure at this distance, as illustrated in **Figure 6.3** reported in **Chapter 6**, which allows the identification of the peak value to be compared with the one calculated using the model. From the analysis, it is observed that, in the experiment, the maximum peak of overpressure reached a value just below 20 kPa after about 0.15 seconds. Applying the TNT model, the overpressure calculated at the same distance is equal to 20 kPa, indicating a slight overestimation compared to the experimental data.

The **second experiment** reported the following results:

Table A-3.4: Parameters used for the TNT equivalence method for the second experiment conducted by Groethe et al. (2007).

Parameter	Value
W_{TNT} [kg]	7.084
W [kg]	7.92
W_f [kg]	7.89

From these data, the Hopkinson-scaled distance $\bar{R}$ as a function of the distance

R from the release point were calculated, and for each value of R, the peak overpressure was determined using **Figure 6.12**, reported in **Chapter 6**.

Table A-3.5: Overpressure peak as a function of Hopkinson-scaled distance obtained with the TNT method for a hydrogen explosion in a 1D confined space.

R [m]	$\bar{R}$ [m/kg$^{1/3}$]	ΔP [kPa]
3	1.56	500
5	2.60	170
7	3.64	80
10	5.21	42
12	6.25	30
15	7.81	20
20	10.41	12
25	13.02	9.5
30	15.62	8

The trend is shown in **Figure A-3.2**.

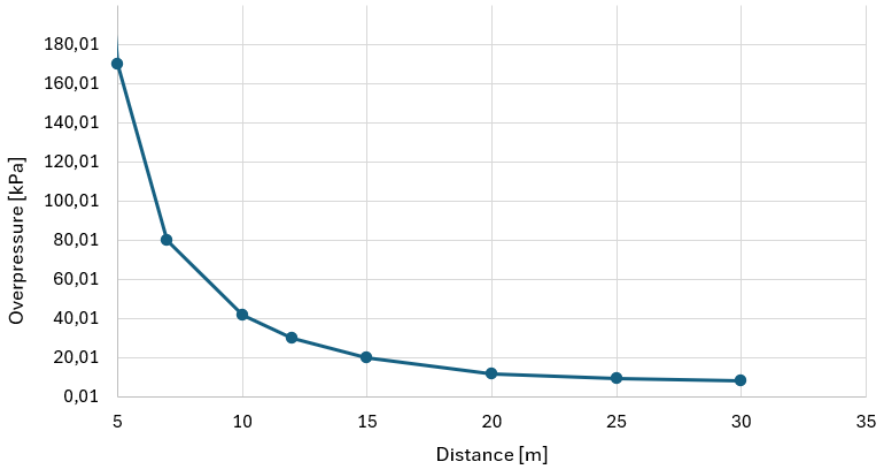

Figure A-3.2: Overpressure trend as a function of distance from the charge for an explosion obtained with the TNT method, which involved 88 m^3 of hydrogen in a confined space along a single direction.

The results obtained were compared with those reported in the study, which shows the temporal trend of the overpressure at 15 meters from the explosion, as illustrated in **Figure 6.5** in **Chapter 6**.

The TNT model, based exclusively on the mass of the fuel involved and on the combustion energy, does not take into account the confinement or congestion conditions of the environment. Consequently, given the similarity in the hydrogen masses involved in experiments 1 and 2, the model provides almost identical results for both cases, with overpressures of about 20 kPa at a distance of 15 meters from the explosion.

This discrepancy highlights a significant limitation of the TNT model: its inability to consider the influence of spatial confinement and the geometry of the

environment on the intensity of the explosion. In real scenarios, the presence of structures, obstacles or closed spaces can significantly increase the violence of the event, generating overpressures much higher than those predicted by simplified models. Therefore, the application of the TNT model in confined contexts can lead to a significant underestimation of the consequences, making it less suitable for hydrogen explosions.

Cryogenic Hydrogen Explosion

This method has been applied to the cryogenic hydrogen explosion reproducing the PRESLHY experiments reported in Jordan et al. (2023), the data considered are outlined in **Table A-3.6**:

Table A-3.6: Parameters used for the TNT equivalence method for cryogenic hydrogen explosion.

Parameter	Value
F	0.99
c_p [kJ/kg K]	9.69
ΔT [K]	208
L [kJ/kg]	449
α_c	0.03
H_f [MJ/kg]	140
H_{TNT}[MJ/kg]	4.68

The **first case** analysed is the one with a storage pressure equal to 50 bar, for which the hydrogen density is 16.401 g/l. The results relating to this scenario are reported in **Table A-3.7**.

Table A-3.7: Parameters used for the application of the TNT equivalence method, relating to an explosion of cryogenic hydrogen stored at 80 K and 50 bar, contained in a 2.8 litres tank and released through a 4 mm hole.

Parameter	Value
W_{TNT} [kg]	0.041
W [kg]	0.046
W_f [kg]	0.046

From these data, the Hopkinson-scaled distance $\bar{R}$ as a function of the distance R from the release point were calculated, and for each value of R, the peak overpressure was determined using **Figure 6.12**, reported in **Chapter 6**.

Table A-3.8: Overpressure peak as a function of Hopkinson-scaled distance obtained with the TNT method for a hydrogen explosion of cryogenic hydrogen stored at 80 K and 50 bar.

R [m]	$\bar{R}$ [m/kg$^{1/3}$]	ΔP [kPa]

0.5	1.44	500
0.75	2.17	190
1	2.89	120
1.75	5.06	41

The trend of the numerical results is reported in **Figure A-3.3**. These results have been compared with the experimental data obtained by Jordan et al. (2023). The comparative analysis highlights that, in this case, the model based on the TNT equivalent is unable to represent the phenomenon, producing overpressure values that are significantly higher and strongly discordant with respect to the experimental measurements. In particular, the TNT model shows a marked decrease in overpressure, which goes from 500 kPa to 41 kPa in a range of 1.25 m. On the contrary, the experimental data show a much more contained variation, with values that decrease from 5.04 kPa to 4.98 kPa in the same spatial range.

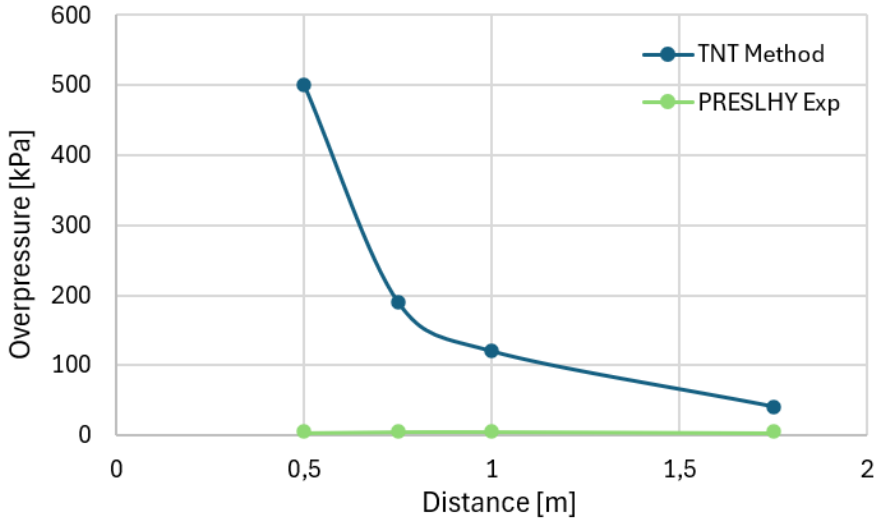

Figure A-3.3: Overpressure trend as a function of distance from the charge for an explosion which involved cryogenic hydrogen released from a tank at 50 bar pressure and 80K. The blue line represents the TNT Method results, the green line the experimental results.

The **second case** analysed is the one with a storage pressure equal to 200 bar, for which the hydrogen density is 49.984 g/l. The results relating to this scenario are reported in **Table A-3.9**.

Table A-3.9: Parameters used for the application of the TNT equivalence method, relating to an explosion of cryogenic hydrogen stored at 80 K and 200 bar, contained in a 2.8-litre tank and released through a 4 mm hole.

Parameter	Value
W_{TNT} [kg]	0.13
W [kg]	0.14
W_f [kg]	0.139

From these data, the Hopkinson-scaled distance $\bar{R}$ as a function of the distance R from the release point were calculated, and for each value of R, the peak

overpressure was determined using **Figure 6.12**, reported in **Chapter 6**.

Table A-3.10: Overpressure peak as a function of Hopkinson-scaled distance obtained with the TNT method for a hydrogen explosion of cryogenic hydrogen stored at 80 K and 200 bar.

R [m]	$\bar{R}$ [m/kg$^{1/3}$]	ΔP [kPa]
0.5	1	2000
0.75	1.49	500
1	1.99	290
1.75	3.48	79

The trend of the numerical results is reported in **Figure A-3.4**. These results have been compared with the experimental data obtained by Jordan et al. (2023). The TNT model shows a marked decrease in overpressure, which goes from 2000 kPa to 79 kPa in a range of 1.25 m. On the contrary, the experimental data show a much more contained variation, with values that decrease from 8.11 kPa to 10.2 kPa in the same spatial range. This behaviour indicates that the method based on the TNT equivalent is not suitable to represent the distribution of when the fuel used is cryogenic hydrogen. This suggests that, due to the highly reactive nature and the physical-chemical characteristics of liquid hydrogen, they differ significantly from those of conventional explosives, making the simplified approach of the TNT model inadequate to describe shock wave propagation phenomena under such conditions.

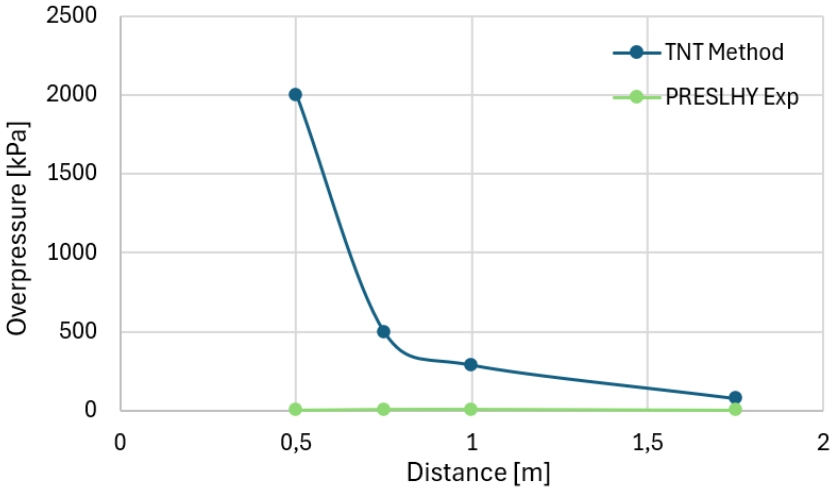

Figure A-3.4: Overpressure trend as a function of distance from the charge for an explosion which involved cryogenic hydrogen released from a tank at 200 bar pressure and 80K. The blue line represents the TNT Method results, the green line the experimental results.

In conclusion, the analysis highlights the significant limitations of the TNT-equivalent model in the context of hydrogen explosions, particularly in confined or complex scenarios. The inability of the model to consider the influence of geometry, confinement and specific properties of hydrogen leads to a marked underestimation of the generated overpressures. Such simplifications make the

model unsuitable for an accurate assessment of explosive effects in real contexts, where environmental conditions play a decisive role in the propagation of the shock wave. Therefore, the adoption of more advanced and hydrogen-specific models, able to consider the confinement, the congestion and thermophysical characteristics of the fuel, is necessary.

BST Methods calculations

Gaseous Hydrogen Explosion

This method has been applied to the gaseous hydrogen explosion reproducing the experiment analysed by Groethe et al. (2007). The analysis first considered the low explosive intensity case, corresponding to the release of 5.3 m³ of hydrogen mixed with air in an open environment. In accordance with the indications of the CCPS (2010), hydrogen was treated as a highly reactive fuel, in conditions of the absence of confinement and low congestion. Based on the data reported in **Chapter 6** in **Table 6.9**, a flame propagation velocity value of 0.36 was adopted. The parameters for the implementation of the method in the selected case study are presented in **Table A-3.11**.

Table A-3.11: Parameters used for the BST method for a hydrogen explosion in an open space.

Parameter	Value
P_0 [Pa]	101325
ρ_{gas} [kg/m3]	0.0899
E_{comb} [MJ/kg]	140
n	0.22
V [m^3]	5.30
T [K]	288
R [J/kmol K]	8314
η	0.67
MW [kg/kmol]	2.016
E [J]	8.44×10^7

Once this value has been determined, the scaled stand-off distance can be calculated using **Equation 6.7** reported in **Chapter 6**. The corresponding scaled overpressure values can then be obtained by referring to **Figure 6.13**.

Table A-3.12: Stand-off scaled distance and overpressure values obtained with the BST method for a hydrogen explosion in an open space.

R [m]	$\bar{R}$	ΔP [kPa]
3	0.32	21
5	0.53	19

7	0.74	16
10	1.06	10
12	1.28	9
15	1.59	7
17	1.81	6
20	2.13	5
25	2.66	4.2
30	3.19	3.9

The results reported by Groethe et al. (2007) are not expressed as overpressure as a function of time, but as overpressure scaled as a function of the scaled distance, represented in logarithmic scale. To allow a direct comparison, the results obtained with the BST model have been converted into the same form and reported in **Figure A-3.5,** which highlights an overestimation of the model. However, it must be underlined that a wall was positioned in the experiments to evaluate its effects, for this reason a decrease in the scaled overpressure is noted at a scaled distance of approximately 1.

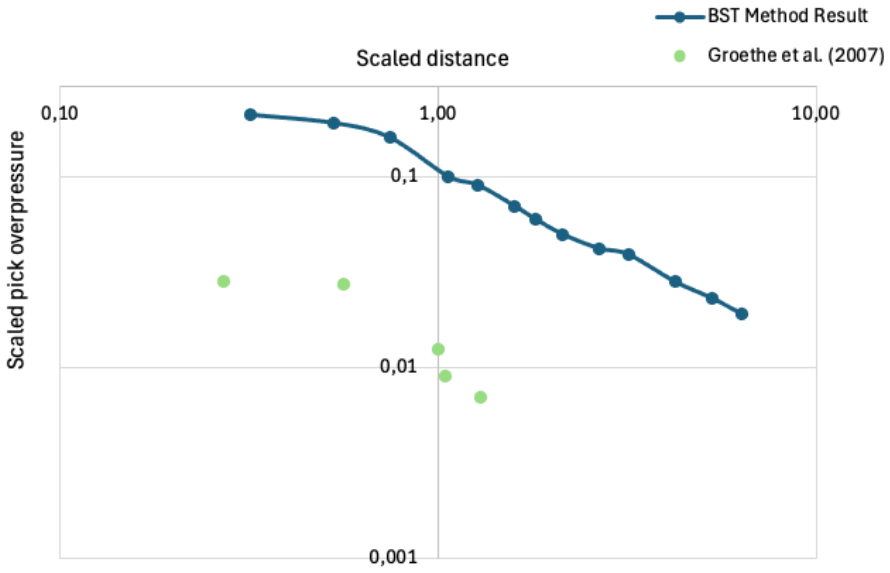

Figure A-3.5: Overpressure trend as a function of stand-off scaled distance obtained from the BST method compared with Groethe et al. (2007) experimental results, for an explosion which involved 5.26 m^3 of hydrogen in an open space.

The overpressure curve as a function of distance, obtained by applying the BST method, is shown below. In order to carry out a comparative evaluation of the results, they were compared with those previously obtained using the TNO model (in **Figure 6.8)**, which proved to be adequate in estimating peak overpressures.

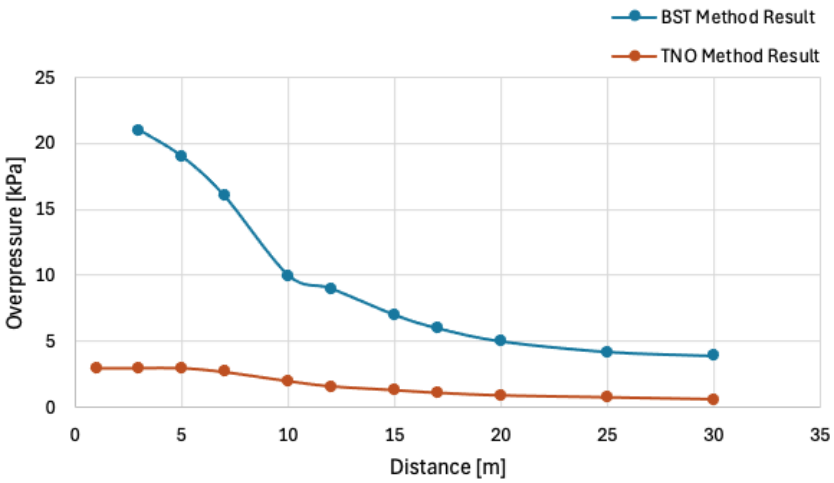

Figure A-3.6: Overpressure trend as a function of distance from the charge obtained with the BST method compared with TNO method results for an explosion which involved 5.26 m^3 of hydrogen in an open space.

From the analysis of the presented results, it emerges that the BST method tends to overestimate the peak overpressures associated with hydrogen explosions in open environments. In particular, it is observed that the scaled overpressure is higher than 0.1 for scaled distance values lower than 1, while the experimental data indicate significantly lower values, of the order of 0.03. The comparison with other models highlights further discrepancies: the BST method returns overpressure values higher than 21 kPa, while the TNO model, which has demonstrated a good ability to faithfully reproduce the peak overpressures in conditions of release in open and unconfined space, provides for the same scenario a value of about 3 kPa. Due to the discrepancy shown with the application to this case study, it was decided not to proceed with the other experiments, considering the model not suitable to reproduce overpressures generated by gaseous hydrogen explosions.

Cryogenic Hydrogen Explosion

Finally, the method was applied to the case of cryogenic hydrogen explosion, replicating the experiments conducted in the PRESLHY project, as reported in Jordan et al. (2023). The ambient pressure and combustion energy per unit mass values used in this analysis are consistent with those used in the study on gaseous hydrogen.

The **first case** analysed was the 2.8 litres tank maintained at 80 K and 50 bar, from which is possible to calculate a total combustion energy of 1.29×10^7 J. Subsequently, the values of the stand-off scaled distance were determined at different points in space to estimate the associated overpressures using **Figure 6.13**. The distances selected for the calculation (0.5 m, 0.75 m, 1 m and 1.75 m from the release point) were chosen in coherence with the experimental setup adopted by Jordan et al. (2023), which involved the positioning of the sensors at these distances for the detection of the explosive parameters. The value of the flame propagation speed is always 0.36, since the fluid involved is the same and

the confinement and congestion conditions are unchanged compared to the application of the method in the presence of gaseous hydrogen.

Table A-3.13: Stand-off scale distance and overpressure values obtained with the BST method for a hydrogen explosion of cryogenic hydrogen stored at 80 K and 50 bar.

R [m]	$\bar{R}$	ΔP [kPa]
0.5	0.1	20
0.75	0.15	20
1	0.2	20
1.75	0.35	18

The trend of the numerical results obtained using the BST method is shown in **Figure A-3.7**.

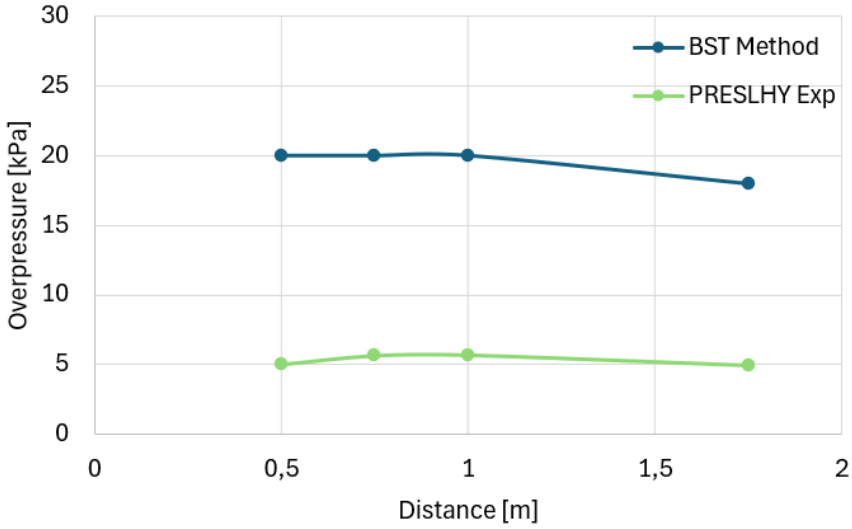

Figure A-3.7: Overpressure trend as a function of distance from the charge for an explosion which involved cryogenic hydrogen released from a tank at 50 bar pressure and 80K. The blue line represents the BST Method results, the green line the experimental results.

The results show that, even for cryogenic hydrogen stored at 50 bar, the BST method tends to overestimate the explosion intensity. In particular, the model predicts peak overpressures up to 20 kPa, while the experimental data relating to the real scenario indicate significantly lower values, around 5 kPa.

For the **second case** involving the tank containing cryogenic hydrogen stored at 200 bar and 80 K, with a volume of 2.8 litres, the total combustion energy calculated is equal to 3.94×10^7 J. Subsequently, the values of the scaled stand-off distance at different points in the space were determined, in order to estimate the associated overpressures using **Figure 6.13**. The value of the flame propagation speed is maintained at 0.36 m/s, since the fluid involved is the same and the confinement and congestion conditions are unchanged compared to the application of the method with gaseous hydrogen.

Table A-3.14: Stand-off scale distance and overpressure values obtained with the BST method for a hydrogen explosion of cryogenic hydrogen stored at 80 K

and 200 bar.

R [m]	$\bar{R}$	ΔP [kPa]
0.5	0.07	20
0.75	0.10	20
1	0.14	20
1.75	0.24	20

The trend of the numerical results obtained using the BST method is shown in **Figure A-3.8**.

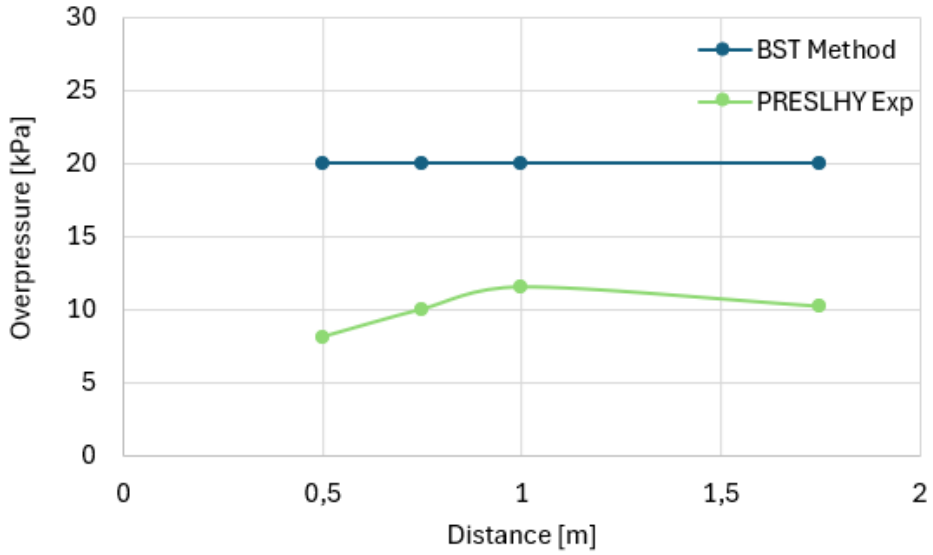

Figure A-3.8: Overpressure trend as a function of distance from the charge for an explosion which involved cryogenic hydrogen released from a tank at 200 bar pressure and 80K. The blue line represents the BST Method results, the green line the experimental results.

The overpressures calculated for the 200 bar and 50 bar cases show minimal variations, indicating a limited sensitivity of the model with respect to the storage pressure. This behaviour is attributable to an intrinsic limitation of the BST method, which does not take into account the storage conditions or the actual amount of fuel present in the determination of the flame propagation speed. These parameters only influence the calculation of the total combustion energy and, consequently, the scaled distance, but do not modify the reference curve used to estimate the overpressure.

The application of the BST method to estimate overpressures generated by hydrogen explosions has highlighted significant limitations in the presence of hydrogen. The model shows a systematic tendency to overestimate peak overpressures, with values that are significantly higher than those obtained from experimental data. As opposed to the TNT model, which is based on a single reference curve, the BST method uses differentiated curves as a function of the flame propagation speed, approaching in this aspect the behaviour of the TNO model. However, the BST does not explicitly consider important variables in the determination of the speed, such as the actual amount of fuel. These parameters

only influence the calculation of the total energy and the scaled distance, but do not determine any variation in the overpressure curve used. Consequently, even when these parameters vary, the estimated value of the overpressure does not change, which represents an unrealistic simplification. This oversimplification leads to a poor sensitivity of the model to real operating conditions, as demonstrated by the comparison between the 200 bar and 50 bar cases, whose results closely overlap. Consequently, the BST method is not suitable for analyses or for the design of safety systems in the presence of hydrogen.

Annex 4 Collaboration with ARPA Piemonte as Part of LEPTA 4 Project

This section documents the activities conducted in collaboration with ARPA Piemonte, as part of the project "LEPTA 4 – Participation in Emergencies, Crises, and Civil Protection Activities," formalized by the National System for Environmental Protection (SNPA).

The collaboration was carried out at the SS03.04 "Industrial Plants and Energy" Simple Structure and focused on the analysis of anthropogenic fires, with particular reference to waste treatment and storage facilities and industrial warehouses.

This activity was an integral part of the PhD program's training program, in accordance with Ministerial Decree No. 351 of April 9, 2022, which promotes the inclusion of PhD students in collaborative projects with public bodies and national institutions.

Fire in waste treatment plants in Piedmont Region: case studies and comparison[20]

As a first step, a historical analysis of fires that occurred in Piedmont, Italy, between March 2014 and October 2024 was conducted, based on the ARPA internal database. The analysis included over 400 recorded events, classified according to the type of activity involved, combustible materials, and geographical location. Furthermore, a categorization of the materials involved was performed, with particular attention to waste, chemicals, and tires, which are frequently present in the cases analysed.

Based on the results of the historical analysis, a representative case study was selected: a fire in a tire storage warehouse, a material with a high calorific value and environmental impact. The study involved the integrated application of PHAST and CFAST software, compared to the Index Method described in the Decreto del Presidente del Consiglio dei Ministri (2021). The modelling approach allowed the simulation of the combustion dynamics, the dispersion of toxic fumes, the thermal power released, and the lethality associated with the event, comparing the results obtained with those derived from the Index Method, which provides a semi-quantitative estimate of risk and the required distance.

Historical Analysis in Piedmont

ARPA Piedmont manages a rapid response service for emergencies of both anthropogenic and natural origin, conducting sampling of various environmental matrices (air, water, soil). For this purpose, it has adopted a specific technical procedure (ARPA Piemonte, 2023). Specifically, during fires, environmental analyses are conducted to collect data on specific substances that act as tracers, such as carbon monoxide (CO), nitrogen oxides (NOx), fine particulate matter (PM2.5 and PM10), and volatile organic compounds (VOCs). These parameters help identifying and characterize fires and assess their impact on the environment and public health.

To manage the rapid response service, the Agency has been developing the Unscheduled Checks application since 2014. It is available on the company intranet and allows for the recording of reports from citizens, operators, and other emergency agencies regarding various types of pollution. This application generates a database that can be used to analyse event trends, respond consistently to emergencies, and plan future interventions related to the events that occurred.

This document focuses on reports of fires that occurred in Piedmont from March 2014 to October 2024. A database extraction was performed containing a total of 436 records. Each record includes a series of information, including the report ID, the event description, the territorial department (Northwest Department,

[20] Portions of this Annex have been published in preliminary form in: Manuguerra, F., Vitale, M., Carpegna, C., and Basso, B. (2025). Fire in waste treatment plants in Piedmont Region: case studies and comparison. In ICSI 2025 International Conference on Safety & Innovation (pp. 670-681), Rome, 11-13 March 2025.

Northeast Department, Southwest Department, and Southeast Department), the date and method of reporting, and the entity or person who reported it. For the specific needs of the project, the data extracted from the database was processed and structured to facilitate subsequent analysis and interpretation. The report ID, department, and reporting date columns were retained, and new fields were added to include the type of business where the fire occurred, the location, a description of the material/product involved, and an indication of whether the event occurred inside or outside a building.

The activities include Industrial Establishments, that include production and manufacturing plants, Waste Treatment and Storage Facilities, as collection, selection, treatment and disposal centres for both hazardous and non-hazardous waste, Warehouse, referring to spaces or structures for storing materials or goods, Agricultural, that involves non-urbanized areas, and Other, a generic category that includes all activities not included in the previous. A detailed classification was adopted to describe the burned material to facilitate analysis of the substances. The categories are Substance, to classify fires in which the material involved is an identifiable chemical substance, Waste, Structures Containing Asbestos, Vehicle when the fire involves cars or trucks, Electronics for electronic devices or electrical components, Wood, Tires, and finally, Tissue.

In this regard, to improve the quality and consistency of the recorded information, when an event involved multiple substances from the same category or materials from different categories, it was decided to report only the material considered to have the greatest impact on the atmosphere (for example, in the case of a fire in an asbestos structure containing bales of hay, asbestos was chosen as category). Furthermore, to avoid data redundancies and ensure more effective analysis, all duplicate reports have been eliminated, retaining only the most complete version available for each event. Subsequently, the "Unknown" category has been added to handle events where the data is reported incompletely or where the activity or material involved in the event cannot be precisely determined. This addition allows for data consistency in the database even when the information is not fully available, improving overall report management and analysis.

Following the restructuring of the dataset, the updated database was refined from an initial total of 436 records to 361 distinct fire events selected for analysis. This data was examined through a graphical analysis aimed at highlighting any similarities, differences, and correlations, as detailed below.

Figure A-4.1a shows the trend in fires that occurred between March 2014 and October 2024, divided by the four territorial departments. The department with the highest number of fires is the Northwest, followed by the Southeast, the Northeast, and finally the Southwest, as also highlighted in **Figure A-4.1b**. In quantitative terms, the Northwest department recorded an average of approximately 18 fires per year, with a significant peak in 2017, which saw an increase to 26 fires. As for the Northeast department, the average number of fires is approximately 6 per year, with a significant increase in the 2018-2019 period, during which approximately 10 fires were recorded for each year. The Southeast department has an average of approximately 6 fires per year, but has three peaks,

in 2016, 2019, and 2022, with approximately 9 fires recorded in each year. Finally, the Southwest department has an average of four fires per year, with slight increases observed in 2015 and 2017, but without significant fluctuations compared to other departments.

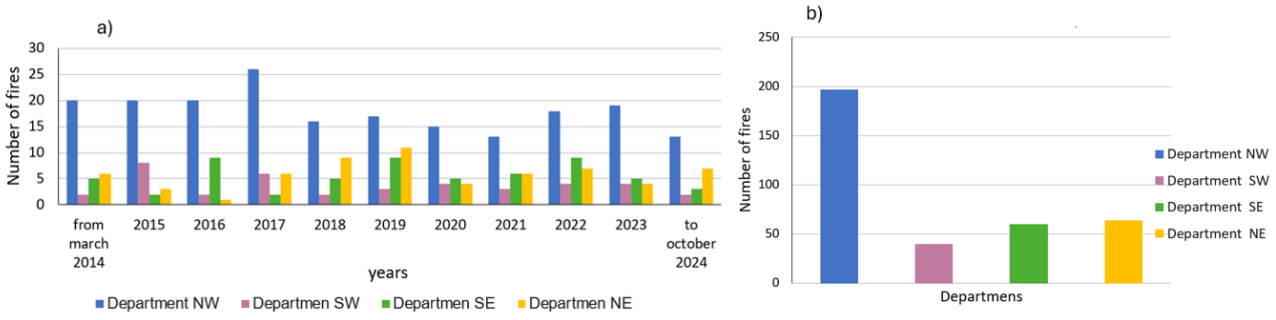

Figure A-4.1: Fires analysed. A) Number of fires in the period March 2014 - October 2024 divided by Department. B) Total number of fires in the four Departments.

Figure A-4.2 below shows the number of fires recorded in the period examined in the Piedmont provinces, with the exception of Turin and Cuneo, for which the data correspond to the totals reported for the Northwest and Southwest departments, respectively, in **Figure A-4.1a**. An analysis of the graph reveals an overall Gaussian trend for the number of fires between 2017 and 2020, with a significant peak in 2019 in the provinces of Alessandria and Novara, indicating an anomalous increase in fire events in that year. A further peak is observed for Alessandria between 2020 and 2024, with a trend similar to a Gaussian distribution, suggesting a regular increase in fires over this period. For the remaining provinces the number of fires follows a fluctuating trend, indicating more variable behaviour over the years.

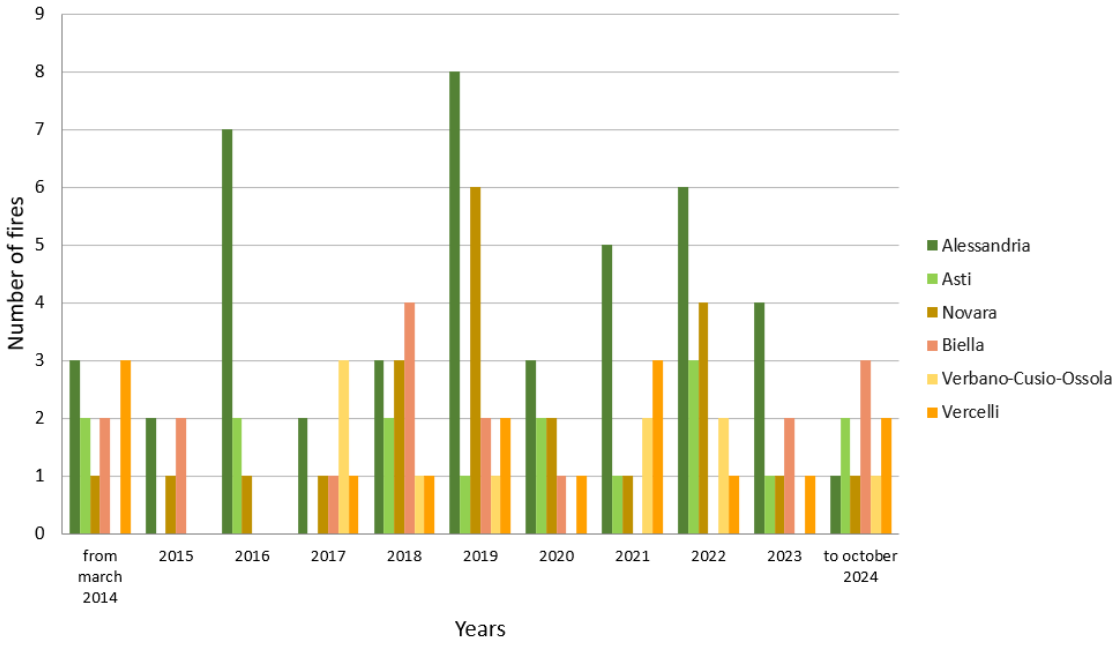

Figure A-4.2: Number of fires in the provinces, excluding Turin and Cuneo, between March 2014 and October 2024.

Figure A-4.3a illustrates the distribution of activities recorded in the modified database, providing a detailed view of the main categories present. The analysis

shows that the Other category is the most prevalent, representing 36% of reports, followed by the Unknown category with a percentage of 7%. Since these two categories do not contribute significantly to a precise understanding of the most relevant activities, it was decided to exclude them from the analysis to focus on those with the greatest impact and better defined.

Figure A-4.3b, which shows the data excluding Other and Unknown, shows that the categories of industrial plants and waste treatment and storage facilities are those with the highest incidence, with 35% and 27% of reports, respectively.

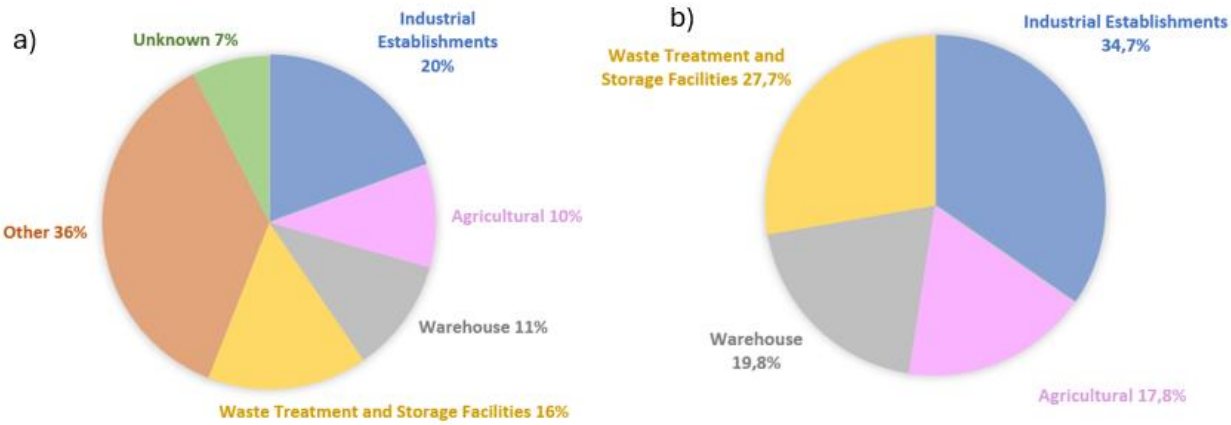

Figure A-4.3: A) Activities involved in the fire cases studied. B) Activities involved in the fire cases studied excluding the Other and Unknown categories.

Figure A-4.4 shows the percentage of business types affected by fires, broken down by province, excluding Other category to keep the analysis focused exclusively on manufacturing activities. The province of Turin shows a higher incidence of fires affecting Industrial Establishments and Waste Treatment and Storage Facilities. This data is consistent with expectations, as Turin is a major industrial area and, as a large urban centre, has numerous waste treatment and storage facilities and landfills. In the province of Novara, home to a significant industrial hub, 50% of the fires affected Industrial Establishments. Conversely, the province of Alessandria, despite also having a significant industrial presence, recorded a higher number of fires in Waste Treatment and Storage Facilities, than in Industrial Establishments. Finally, in the provinces of Cuneo and Vercelli, a higher frequency of fires involving Agricultural category is observed, closely related to the geomorphological characteristics and land use in these areas.

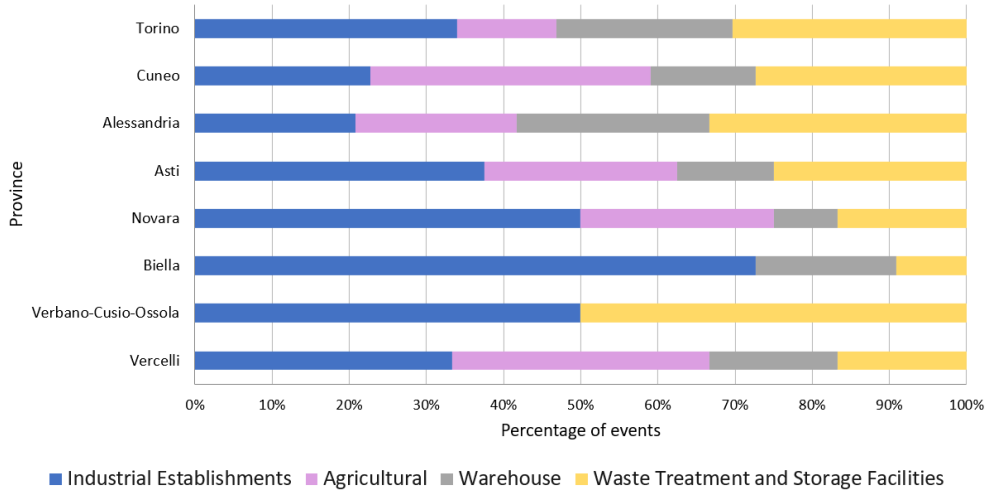

Figure A-4.4: Percentage of fires occurring in different types of businesses, excluding the Other category, for each province.

Based on the outcomes of the above analysis, attention was directed toward the two activity types most frequently impacted by fire events: Industrial Establishments and Waste Treatment and Storage Facilities, examining their distribution at the provincial level. Regarding Industrial Establishments, the analysis, illustrated in **Figure A-4.5**, shows that the number of fires was highest in the province of Turin, followed by Biella and Novara. Similarly, for Waste Treatment and Storage Facilities, the data highlighted that the province with the highest number of fires was Turin, followed by Alessandria and Cuneo. **Figure A-4.6a** illustrates the distribution of materials involved in the analysed fire events. The analysis shows that, excluding the Unknown category, the materials most affected are Waste and Substance. This result is consistent with what was previously observed, namely that fires occur more frequently in Industrial Establishments and Waste Treatment and Storage Facilities. **Figure A-4.6b** illustrates the main sources relating to the reports received by ARPA, from which it emerges that the agencies most involved are Emergency Health Service 118 and the National Fire Brigade (VVF).

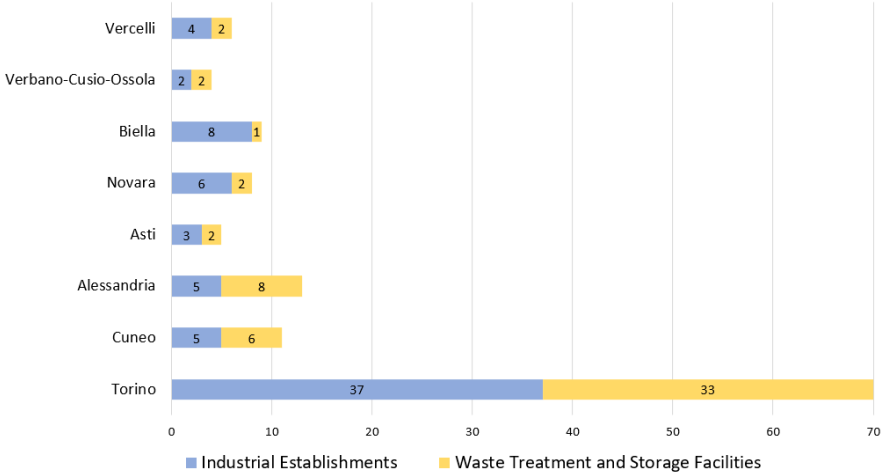

Figure A-4.5: Number of fires involving Industrial Establishments and Waste Treatment and Storage Facilities, divided by province.

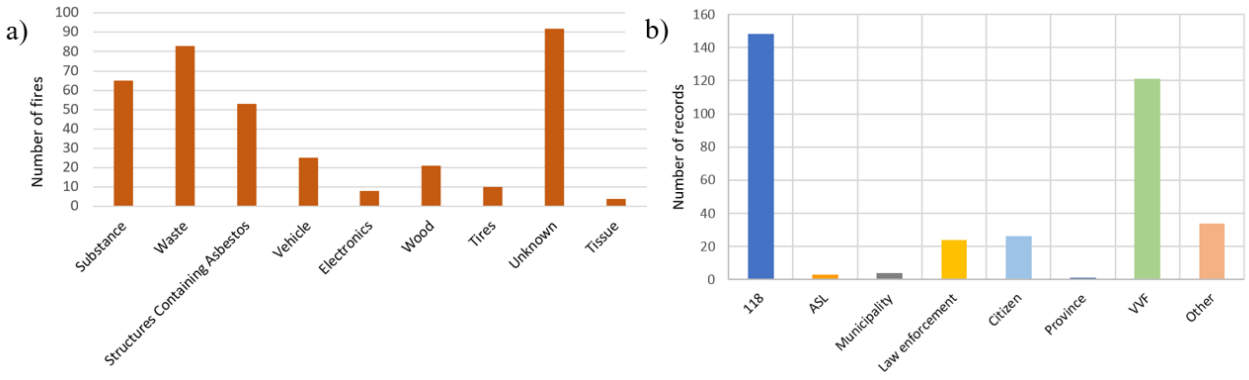

Figure A-4.6: Further analysis. A) Combustible materials involved in the analyzed fires. B) Reporting body of the records.

Regulatory and methodological framework

In recent years, the increasing incidence of fires in industrial plants and storage sites has led to the introduction of new regulatory provisions aimed at strengthening prevention and risk management. Specifically, Law No. 132/2018[21] extended the requirement to draft Internal Emergency Plans (IEPs) and required Prefectures to prepare External Emergency Plans (EEPs) for waste treatment and storage facilities, similarly to what is already required for facilities subject to the Legislative Decree 105/2015. In response to this need, the Decree of the President of the Council of Ministers (Decreto del Presidente del Consiglio dei Ministri, 2021) introduced an index method for the semi-quantitative assessment of fire risk, useful for external emergency planning and public information. The method is based on the assignment of scores to various risk and protection factors, which contribute to the calculation of the Fire Risk Index (FIR) according to the **Formula A-4.1**:

$$FIR = Pr + Pt - FC + FD \quad \textbf{(A-4.1)}$$

Pr represents waste storage and is calculated based on the specific fire load; Pt refers to the processing and treatment processes present in the facility; FC indicates the credit factor, associated with the protective measures adopted, such as extinguishing systems or physical barriers; finally, FD corresponds to the debit factor, which considers the health and environmental hazard related to the facility location relative to sensitive areas. It should be noted that the Pr index is determined by the specific fire load (q_f), which in turn depends on various factors: the mass of the combustible material (g_i), its calorific value (H_i), the surface area of the operating area (A) and parameters which consider, for example, the participation in combustion (m_i and Ψ_i), according to the following **Formula A-4.2**:

[21]Italia (2018). Legge 1 dicembre 2018, n. 132 "Conversione in legge, con modificazioni, del decreto-legge 4 ottobre 2018, n. 113, recante disposizioni urgenti in materia di protezione internazionale e immigrazione, sicurezza pubblica, nonché misure per la funzionalità del Ministero dell'interno e l'organizzazione e il funzionamento dell'Agenzia nazionale per l'amministrazione e la destinazione dei beni sequestrati e confiscati alla criminalità organizzata. Delega al Governo in materia di riordino dei ruoli e delle carriere del personale delle Forze di polizia e delle Forze armate". Art. 26 bis. Gazzetta Ufficiale della Repubblica Italiana, n. 281, 3 dicembre 2018.

$$q_f = \frac{\sum_{i=1}^{n} g_i \cdot H_i \cdot m_i \cdot \Psi_i}{A} \left[\frac{MJ}{m^2}\right] \quad \textbf{(A-4.2)}$$

The FC credit factor is the sum of four components representing the prevention and protection measures adopted: Pre indicates management prevention measures, such as staff training and operating procedures; Proa represents active protection, including detection, alarm, and automatic shutdown systems; Prop concerns passive protection, such as structural and system measures, compartmentalization and physical barriers; finally, Sec evaluates perimeter security, including access control and external area surveillance.

The Decree of the President of the Council of Ministers (Decreto del Presidente del Consiglio dei Ministri, 2021) defines in detail the criteria for assigning scores to each index, using tables and evaluation grids that allow the numerical value of the fire risk index to be calculated. The final FIR index value is associated with a qualitative risk level, which corresponds to a warning distance, reported in **Table A-4.1**: this represents the maximum area around the facility within which the effects of a fire could manifest. In the absence of more detailed technical assessments, this distance can be used as a reference for external emergency planning.

Table A-4.1: Correlation between risk level and attention distance. Table taken from Law No. 132/2018.

FIR	Risk Level	Attention Distance [m]
0-400	Low Risk	100
401-700	Medium-Low Risk	200
701-1100	Medium Risk	300
1101-1500	Medium-High Risk	400
>1500	High Risk	500

In parallel, for a more detailed and dynamic assessment of the accident scenarios, two specialized simulation software programs were used: PHAST, described in **Chapter 4**, and CFAST (Consolidated Model of Fire Growth and Smoke Transport). The CFAST software is a simulation model developed by the National Institute of Standards and Technology (NIST, 2023), designed to analyse the dynamics of fires in confined spaces. Its structure is based on a zone model, which divides each compartment into two main layers, an upper and a lower one, allowing for a good approximation of the thermal and fluid dynamic behaviour within enclosed spaces. This approach makes it particularly suitable for environments with simple geometries, such as rectangular or square rooms. CFAST allows modelling of fire evolution, smoke and combustion gas transport, as well as temperature variations over time. The input data required by the software mainly concern the characteristics of the stored material, such as mass, empirical formula, and net calorific value; the properties of the building; and finally, the properties of the fire, including ignition time and theoretical energy release rate (HRR). The simulation results include the mass flow rate of the fumes emitted during combustion, the quantity of each product, and the pyrolysis mass flow rate expressed in kg/s. The energy release rate is also calculated as a function of time, compared to the expected heat output, along with the intensity and height of the flame. Finally, the software provides indications on the activation times of

the fire prevention systems, allowing the effectiveness of the protective measures adopted to be assessed.

The integration of the Index Method and numerical models allows for a comparison between simplified approaches and advanced simulations, offering a more comprehensive perspective on risk assessment. In this work, these tools were applied to a representative case study, with the aim of analysing the potential and critical aspects of each approach, contributing to the definition of an integrated methodology for fire risk management in industrial settings.

Fire Behaviour Theory

For this study, the theoretical framework used was Quintiere (2016), which provides the conceptual basis for interpreting the parameters used in simulation software. One of the key aspects in describing fire dynamics is the burning rate ($\dot{m}$), which represents the amount of fuel consumed per unit of time. In large fires, not all vaporized fuel reacts immediately with oxygen: combustion may be partial or delayed, especially in environments with limited ventilation. For this reason, it is important to distinguish between the fuel that vaporizes and the fuel that participates in the chemical reaction.

The burning rate can be expressed as the product $\dot{m}'' \times A$ where $\dot{m}''$ is the combustion rate per unit area and depends on the properties of the fuel, while A represents the area involved in the combustion.

Another fundamental parameter of combustion is the effective heat of combustion ΔH_c, which represents the chemical energy released per unit mass of vaporized fuel participating in the reaction.

The energy release rate ($\dot{Q} = \text{HRR}$) is a parameter that measures the energy released per unit time during combustion. This indicator is important for assessing the intensity and growth of a fire, as it reflects both the amount of energy generated and its ability to spread throughout the affected area. This parameter depends on the mass flow of burning fuel and the fuel vaporization area, and is described by the following relationship:

$$\dot{Q}_{\max} = \text{HRR}_{max} = \dot{m}'' \cdot A \cdot \Delta \text{H}_\text{c} \qquad \textbf{(A-4.3)}$$

In Quintiere (2016), the maximum value of the combustion rate per unit area $\dot{m}''$ and the effective heat of combustion ΔH_c. are tabulated, as reported in **Table A-4.2**:

Table A-4.2: Values of the combustion rate per unit area and the effective heat of combustion. Table taken from Quintiere (2016).

Fuel	$\dot{m}''$ (g/m²-s)
Liquified propane	100–130
Liquified natural gas	80–100
Benzene	90
Butane	80
Hexane	70–80
Xylene	70
JP-4	50–70
Heptane	65–75
Gasoline	50–60
Acetone	40
Methanol	22
Polystyrene (granular)	38
Polymethyl methacrylate (granular)	28
Polyethylene (granular)	26
Polypropylene (granular)	24
Rigid polyurethane foam	22–25
Flexible polyurethane foam	21–27
Polyvinyl chloride (granular)	16
Corrugated paper cartons	14
Wood crib	11

Methane	50.0
Ethane	47.5
Ethene	50.4
Propane	46.5
Carbon monoxide	10.1
n-Butane	45.7
c-Hexane	43.8
Heptane	44.6
Gasoline	43.7
Kerosene	43.2
Benzene	40.0
Acetone	30.8
Ethanol	26.8
Methanol	19.8
Polyethylene	43.3
Polypropylene	43.3
Polystyrene	39.8
Polycarbonate	29.7
Nylon 6/6	29.6
Polymethyl methacrylate	24.9
Polyvinyl chloride	16.4
Cellulose	16.1
Glucose	15.4
Wood	13–15

With these values, it is then possible to calculate the maximum value of the energy release power $\dot{Q}_{\max}$. The energy release rate (HRR) also depends on other factors, the ignition process, flame spread, and the mass flow of fuel consumed during the fire. Each material or object has a characteristic growth rate, which represents the time required for the fire to reach significant strength. The energy release rate (HRR) follows a quadratic relationship with time, expressed by the formula:

$$\dot{Q} = \text{HRR} = \alpha' \cdot t^2 \quad \textbf{(A-4.4)}$$

where α' is a constant that depends on the specific characteristics of the fuel and t is time. Fire growth rates are classified into four main categories, based on the speed at which a reference power of 1 MW is reached: slow (600 seconds), medium (300 seconds), fast (150 seconds), and ultrafast (75 seconds). From **Equation A-4.4**, α' can be calculated by considering the hypothetical growth time of the fire, considering the four categories just described. It is then possible to calculate the actual t_{peak} using the previously calculated HRR_{max}. This quadratic relationship is useful for describing the growth phase of the fire until its full development.

After this phase, combustion is limited by the exhaustion of the produced material. To calculate the time in the steady state phase of the fire (t_{steady}), the total energy released (E_{tot}) is first determined by considering the mass of the material and its effective heat of combustion (ΔH_c), which is then divided by the $\text{HRR}_{\max}$.

When the air flow rate is limited, as in a closed warehouse, combustion is limited. The maximum air flow rate $\dot{m}_{air,\max}$ through an opening depends on the temperature difference and the size of the opening. For a ventilation with height H_0 and cross-sectional area A_0, the maximum air flow rate is expressed as:

$$\dot{m}_{air,\max} = 0.5 \cdot A_0 \cdot \sqrt{H_0} \quad \textbf{(A-4.5)}$$

In this scenario, the maximum energy release power inside the room is determined by the amount of available oxygen, given by the **Formula A-4.6**:

$$\dot{Q}_{max} = \dot{m}_{air,max} \cdot 3000\ \mathrm{kJ/kg_{reacted\ air}} \quad \textbf{(A-4.6)}$$

where $3000\ \mathrm{kJ/kg_{reacted\ air}}$ is a constant value used for almost all common fuels.

To calculate the total energy ($E_{steady,closed}$) released in the closed warehouse and hence the time in the stationary phase ($t_{steady,closed}$), the proportion was considered:

$$E_{steady,closed} : HRR_{max,closed} = E_{steady,open} : HRR_{max,open} \quad \textbf{(A-4.7)}$$

Warehouse Fire Analysis

Based on the historical analysis and the needs of ARPA Piemonte, the project focused on studying tire warehouse fires and analysing the effects of combustion fumes. Specifically, a case study was conducted on a 10x10.8x7 m^3 storage warehouse with a storage capacity of 72,000 kg of tires, corresponding to 200 pallets, each containing 36 tires with an average weight of approximately 10 kg. Due to their chemical composition and high calorific value, tires are a particularly critical type of material in the event of a fire, both because they are difficult to extinguish and because they produce toxic substances. The net calorific value of tires was assumed to be 25 MJ/kg (Certifico Srl, 2021), a value chosen because of its similarity to that of rigid polyurethane foam, which has comparable energy characteristics. For the simulation of the fire in the closed compartment, specific input parameters calculated based on the equations reported by Quintiere (2016) were adopted, referring to the fire growth and the ventilation of the system. The maximum air flow rate was estimated to be 7.79 kg/s, while the maximum heat release rate (HRR_{max}) reached 23,382.69 kW. The growth constant α', equal to 0.044 kW/s^2, describes the initial increase of the fire up to the peak time, set at 725.33 seconds. The steady-state phase was extended up to 26,666.67 seconds. Two scenarios were hypothesized: a real case with all the prevention and protection measures present in a similar real warehouse for which ARPA had all the necessary documentation, and a simplified case in which the obligations set out in Legislative Decree 81/08 and the plan for maintaining the fire safety level were considered. The structure was considered to have brick masonry walls, with a 3×3 m door. To characterize the combustible material, we used data reported by Quintiere (2016), comparing the thermal behaviour of tires to that of rigid polyurethane foam due to their low conductivity and high-temperature resistance, characteristics shared by vulcanized rubber. The crude chemical formula of the polymer was $C_9H_{12}N_2O_3$ (Gustin et al., 2017), representing a repetitive unit. Environmental and ventilation conditions were set to a wind speed of 1.5 m/s, with atmospheric stability ranging from class F (most stable) to class D (least stable), to represent realistic dispersion scenarios.

The most significant results from each approach are summarized below, with particular attention to the differences between the two hypothesized scenarios.

The internal warehouse results obtained by CFast software concern the temperatures reached, illustrated in **Figure A-4.7**, and the heat release rate over time, reported in **Figure A-4.8**. In the simplified case, a gradual increase was

observed, with temperatures reaching approximately 800°C in the upper layer and 350°C in the lower one, followed by a slow cooling to room temperature. In the real case, the activation of the sprinklers when the temperature exceeded 100°C resulted in a rapid reduction in temperature, stabilizing around 20°C in the upper layer and 40°C in the lower one, highlighting the system's effectiveness in containing the fire. Analysis of the Heat Release Rate curves showed, in the simplified case, a discrepancy between the theoretical and experimental values, with a maximum peak of 1×10^4 kW for the real curve and 6.52×10^3 kW for the convective component. In the real case, the theoretical and experimental curves are superimposable, with peaks of 2.40×10^3 kW and 1.50×10^3 kW for the total and convective HRR respectively, confirming the consistency between model and observed data and the effectiveness of the active protection system in mitigating the thermal effects of the fire.

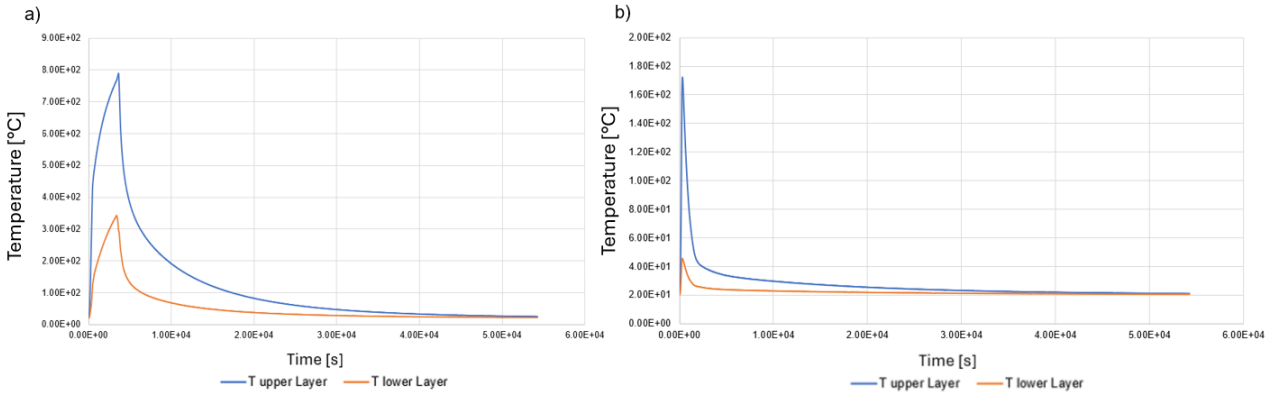

Figure A-4.7: Temperature trends over time inside the warehouse. A) Simplified case. B) Real case.

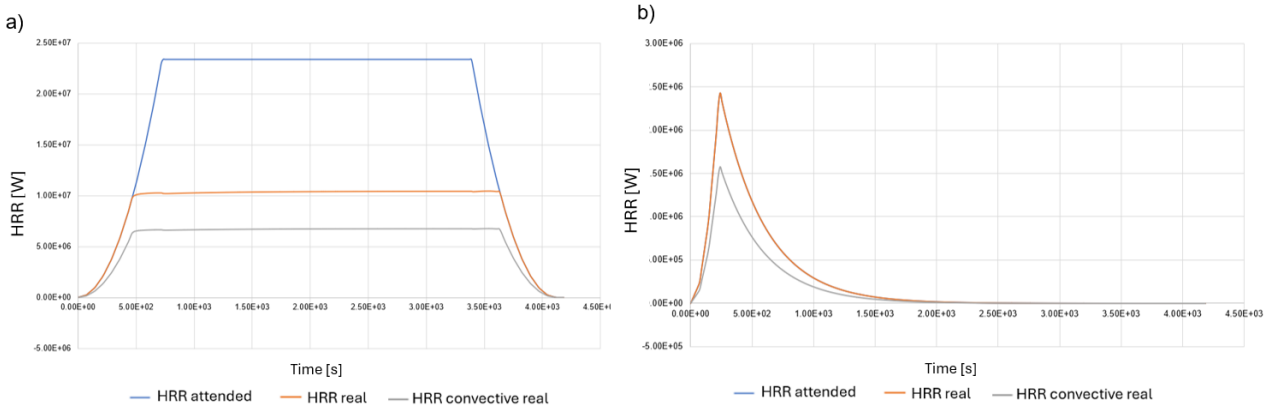

Figure A-4.8: Heat release rate over time. A) Simplified case. B) Real case.

The results of the smoke cloud coming out of the warehouse obtained by PHAST software concern the concentrations and distances reached in space. The simulation highlighted how atmospheric stability significantly influences the dispersion of the toxic cloud generated by the fire, illustrated in in **Figure A-4.9**. In the simplified case, class F produced a maximum concentration of approximately 800 ppm at the warehouse exit, higher than the 650 ppm observed in class D. Furthermore, the class D cloud dispersed more rapidly, with a more marked decrease in concentration along the downwind direction. The spatial distribution of the cloud, illustrated in **Figure A-4.10**, also showed differences: in

class F, the cloud reached 600 m in horizontal extension and 14 m in height, while in class D it was limited to 200 m, while maintaining the same height. These results indicate that greater atmospheric stability favours wider horizontal dispersion, increasing the risk for areas distant from the point of origin. In the real case, the simulations confirmed the same concentration and distribution profiles observed in the simplified case, suggesting that the protective measures present in the real warehouse do not significantly modify the external dispersion of the toxic cloud. This result can be attributed to the fact that the protective measures in place in the real case primarily affect the internal fire dynamics, limiting its spread and reducing smoke production, but do not directly impact the atmospheric dispersion phase once the contaminants have been released outside. It should be noted that meteorological conditions, particularly atmospheric stability and wind speed, exert a predominant influence on the distribution of the toxic cloud, overriding the effects of internal containment measures. These aspects highlight the need for a more detailed characterization of the emission source and the interactions between the compartment and the external environment, to improve the accuracy of simulations and the environmental risk assessment.

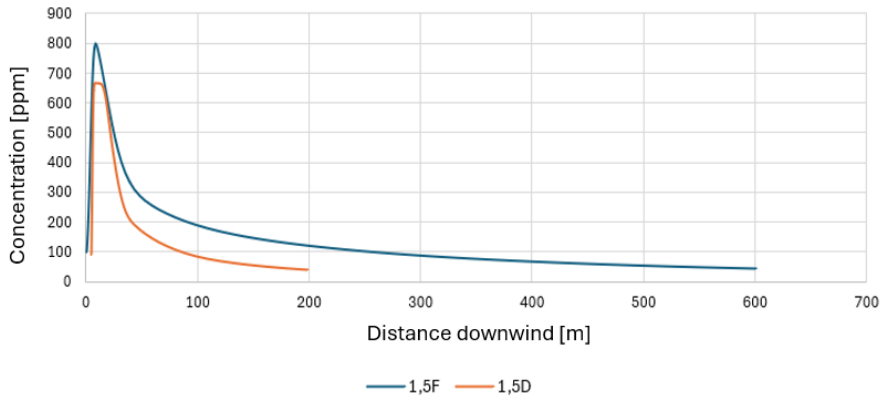

Figure A-4.9: Maximum concentration of the toxic cloud in space generated by the fire in a tire warehouse.

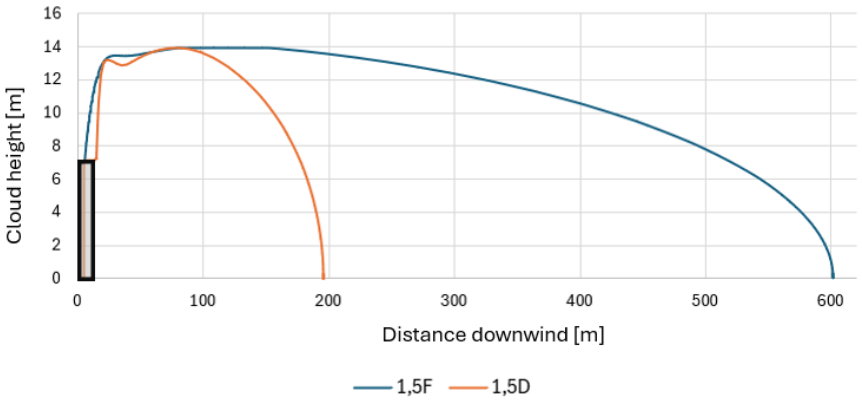

Figure A-4.10: Side view of the height of the toxic cloud in space generated by the fire in a tire warehouse highlighted in black in the figure.

The Index Method was also applied to the distances reached by the smoke cloud, to compare the results with those obtained by the PHAST software. The analysis was developed on two configurations: the real scenario, which considers

all the measures present in the plant, and the simplified scenario, constructed by including only the minimum legal requirements. In both cases, a FD factor of 20 was assumed due to the presence of an adjacent watercourse, while the Pt factor was zero because the plant does not include waste treatment activities. The calculation of the specific fire load, equal to 12,971.83 MJ/m², was identical for the two configurations, as it depends on the physical-chemical parameters of the stored materials, their calorific value, and the size of the warehouse, assuming combustion participation coefficients equal to one.

In the real scenario, the score reflected the presence of a structured prevention system, which included both management and plant measures. The prevention measures Pre received the highest score (175), as the company adopts consolidated organizational procedures and safety management plans. Similarly, the active protection measures Proa achieved the highest score (200), thanks to the presence of comprehensive fire prevention systems, including detectors, alarms, and automatic extinguishing devices. The security system Sec achieved the highest score (70), demonstrating a high level of surveillance and access control. In contrast, the passive protection system Prop was limited to the presence of fire water collection tanks, with a score of 30. This configuration resulted in an overall fire risk index of 1045, corresponding to a medium risk level and an attention distance of 300 meters.

In the simplified case, however, the values assigned to the indices reflect a minimal approach. The Pre was assigned a score of 100, as it was limited to the obligations set forth in Legislative Decree 81/08 and the fire prevention maintenance plan. The Proa was assigned a score of 100, as it assumed only the presence of internal and external fire hydrants and portable fire extinguishers, without any other advanced systems. The Sec and Prop measures remained unchanged compared to the real scenario. The calculated fire risk index in this case was 1220, corresponding to a medium-high risk level and a warning distance of 400 meters.

The results are shown in **Table A-4.3.**

Table A-4.3: Input and output data for the Index method, real case and simplified case.

Parameter	Real Case	Simplified Case
q_f [MJ/m^2]	12971.83	12971.83
Pr	1500	1500
Pt	-	-
FC = Pre + Proa + Prop + Sec	475 = 175+200+30+70	300 = 100+100+30+70
FD	20	20
FIR	1045	1220
Risk Level	Medium	Medium-High
Attention Distance	300 m	400 m

Comparing the results obtained in the simplified tire warehouse scenario using both the Index Method and the PHAST software reveals significant differences in the distances reached by the smoke cloud. PHAST provides maximum dispersion distances of approximately 600 m in class F atmospheric conditions and approximately 200 m in class D, as shown in Figure A-4.10, while the Index Method provides a warning distance of approximately 400 m from the plant perimeter for the same scenario. It should be noted that the two approaches are not directly comparable: the PHAST software calculates the cloud dispersion starting from the area immediately outside the warehouse, while the Index Method defines the warning distance using the plant boundary as a reference. In terms of application, PHAST proves to be a more suitable tool for emergency planning, as it allows for an assessment of the impact of toxic smoke from combustion. The Index Method, while representing a possible alternative, is limited to providing a general indication of areas of concern and has several limitations. Among these, incorporating all the prevention and protection systems envisaged by the method does not lead to a significant reduction in the risk level, contrary to what one might expect. Furthermore, the fire risk index remains unchanged whether the warehouse is open or closed, thus failing to consider structural configurations that could significantly influence the spread of the fire. A further critical issue concerns the failure to distinguish between different active protection systems: for example, automatic extinguishing systems do not differentiate between water-based and foam-based ones, although this distinction may be relevant in terms of effectiveness. Finally, a limitation arises in determining the FD index, which only considers the distance between the perimeter of the facility and the sensitive external target, without considering the actual location of the warehouse affected by the fire. Unlike the Index Method, the CFAST software is not intended for emergency planning, but finds application in the detailed study of fire dynamics within a structure, proving useful in the design of buildings and fire prevention systems.

Annex 5: Analysis of NaTech Events Caused by Lightning in the Industrial Sector

This section fits within the methodological framework outlined in Chapter 2 of the thesis, which focuses on analysing the systemic vulnerability of industrial infrastructure exposed to extreme natural events. Specifically, the chapter introduced the concept of bidirectional vulnerability, highlighting how material degradation can both amplify the effects of natural events and be accelerated by such events, generating critical operating conditions.

Continuing these considerations, Annex 5 delves into the specific case of NaTech events triggered by lightning, one of the most recurrent and impactful types of events in the industrial sector. The analysis reported here was developed as part of a collaborative scientific project:

Castro Rodriguez, D.J., Mietkiewicz, J., Vitale, M., Baldissone, G., Barresi, A.A., and Demichela, M. (2024). NaTech triggered by lightning: Novel insights from past events in the process industry. Heliyon, 10, e31610. https://doi.org/10.1016/j.heliyon.2024.e31610

This contribution is part of the research activities envisaged for the doctoral program and aimed to systematically analyse industrial accidents caused by lightning, through the development of a dedicated dataset and the application of probabilistic models for vulnerability assessment. Furthermore, the work described in this appendix contributed to refining the analysis methodology, subsequently applied in Chapter 1 of the thesis and in the related scientific article.

My specific contribution to the work involved the collection, selection, and structuring of data relating to NaTech lightning events, extracted from international industrial accident databases. This activity required careful review of information quality, removal of duplicates, and technical classification of events according to criteria consistent with scientific literature and European regulations.

The article represents an original contribution to understanding the vulnerability of industrial infrastructure to lightning strikes and integrates with the interpretative model proposed in Chapter 2, strengthening the multidisciplinary and predictive approach to technological risk management in contexts exposed to natural factors.

Annexes References

ARPA Piemonte (2023). Gestione delle emergenze ambientali. Codice: U.RP.T170. Revisione 4.

CCPS (2010). Guidelines for Vapor Cloud Explosion, Pressure Vessel Burst, BLEVE, and Flash Fire Hazards. Center for Chemical Process Safety. 2nd ed. Hoboken, NJ: Wiley-AIChE.

Certifico Srl (2021). Potere calorifico materiali (Hi) [MJ/kg]. [WWW Document] URL: https://www.certifico.com/id/14854 (Accessed 12/2024).

Decreto del Presidente del Consiglio dei Ministri (2021) "Approvazione delle linee guida per la predisposizione del piano di emergenza esterna e per la relativa informazione della popolazione per gli impianti di stoccaggio e trattamento dei rifiuti". Gazzetta Ufficiale della Repubblica Italiana, n. 204, 30 agosto 2021.

Groethe, M., Merilo, E., Colton, J., Chiba, S., Sato, Y., Iwabuchi, H. (2007). Large-scale hydrogen deflagrations and detonations. International Journal of Hydrogen Energy, 32(13), 2125–2133. https://doi.org/10.1016/j.ijhydene.2007.04.016

Gustin D., Colbassi M., Lepre E., Anastasio A., Contus D. and Pitacco D. (2017). Chimica delle Macromolecole Introduzione ai polimeri Breve introduzione alla caratterizzazione, polimerizzazione e alle proprietà dei polimeri. Moodle2 units. URL: https://moodle2.units.it/pluginfile.php/112553/mod_resource/content/1/l%20relaz%20blended.pdf (Accessed 12/2024)

Jordan, T., Friedrich, A., Veser, A. and Kotchourko, N. (2023). PRESLHY Experiment series E5.1 (Ignited Discharge) results – Benchmarking. Karlsruhe Institute of Technology. URL, https://www.radar-service.eu/radar/en/dataset/uzDLoVtvVFILFwGQ (Accessed June 2025).

NIST (2023). CFAST: Consolidated Fire and Smoke Transport. [WWW Document]. URL: https://pages.nist.gov/cfast/manuals.html (Accessed 12/2024).

Quintiere, J.G. (2016). Principles of fire behavior. 2nd ed. Boca Raton: CRC Press.